A measurement of the 2 neutrino double beta decay rate of ^{130}Te in the CUORICINO experiment

Laura Katherine Kogler
Ph.D. Thesis

Department of Physics
University of California, Berkeley
Berkeley, CA 94720

and

Nuclear Science Division
Lawrence Berkeley National Laboratory
One Cyclotron Road
Berkeley, CA 94720

Committee in charge:

Professor Stuart J. Freedman, Chair

Professor Yury G. Kolomensky

Professor Eric B. Norman

Fall 2011

DISCLAIMER

This work supported by the Director, Office of Science, Office of Nuclear Physics of the U.S. Department of Energy under Contract No. DE-AC02-05CH11231.

A measurement of the 2 neutrino double beta decay rate of ^{130}Te in the CUORICINO experiment

Laura Katherine Kogler

Abstract

A measurement of the 2 neutrino double beta decay rate of ^{130}Te in the CUORICINO experiment

by

Laura Katherine Kogler

Doctor of Philosophy in Physics

University of California, Berkeley

Professor Stuart J. Freedman, Chair

CUORICINO was a cryogenic bolometer experiment designed to search for neutrinoless double beta decay and other rare processes, including double beta decay with two neutrinos ($2\nu\beta\beta$). The experiment was located at Laboratori Nazionali del Gran Sasso and ran for a period of about 5 years, from 2003 to 2008. The detector consisted of an array of 62 TeO_2 crystals arranged in a tower and operated at a temperature of $\sim$10 mK. Events depositing energy in the detectors, such as radioactive decays or impinging particles, produced thermal pulses in the crystals which were read out using sensitive thermistors.

The experiment included 4 enriched crystals, 2 enriched with ^{130}Te and 2 with ^{128}Te, in order to aid in the measurement of the $2\nu\beta\beta$ rate. The enriched crystals contained a total of $\sim$350 g ^{130}Te. The 128-enriched (130-depleted) crystals were used as background monitors, so that the shared backgrounds could be subtracted from the energy spectrum of the 130-enriched crystals. Residual backgrounds in the subtracted spectrum were fit using spectra generated by Monte-Carlo simulations of natural radioactive contaminants located in and on the crystals. The $2\nu\beta\beta$ half-life was measured to be $T^{2\nu}_{1/2} = [9.81 \pm 0.96(\text{stat}) \pm 0.49(\text{syst})] \times 10^{20}$ y.

To my family

Contents

List of Figures

List of Tables

Acknowledgments

I would like to express my sincere gratitude to the following individuals, who contributed substantially to the completion of this work:

To my advisor, Stuart Freedman, for supporting me through my graduate career, for giving me the freedom to pursue my own investigations, and for all the bits of wisdom slyly couched in deadpan anecdotes.

To my committee members Yury Kolomensky and Rick Norman for their invaluable expertise and guidance on data analysis and nuclear physics, and for their careful reading and feedback on this document.

To Maura Pavan for sharing her extensive knowledge about the intricacies, subtleties and quirks of CUORICINO data analysis, gained from years of experience on CUORICINO and its predecessor experiments.

To the current and former LBNL post-docs and staff, Elena Guardincerri, Patrick Decowski, Ke Han, Thomas Bloxham, Richard Kadel, Tom Banks, and Jason Detweiler for useful conversations, technical advice, and collaborations.

To Oliviero Cremonesi and Silvia Capelli for assistance with the Monte Carlo simulations.

To Marco Vignati for his leadership on the Diana project and for setting an example which has challenged and inspired me to improve the quality of my code.

To my fellow graduate students and office mates, Adam Bryant, Michelle Dolinski, Tommy O'Donnell, and Lindley Winslow, for showing me that it is possible to reach the light at the end of the tunnel, and for countless tips, pointers, helpful conversations and commiserations along the way.

To my European collaborators for welcoming me into the collaboration and to Italy, in particular Iulian Bandac, Fabio Bellini, Marisa Pedretti, Cecilia Maiano, Marco Carrettoni, Chiara Salvioni, and Maria Martinez for their warmth and hospitality.

To the women of SWPS, Lauren Tompkins, Jessica Kirkpatrick, Jennie Guzman, Cindy Keeler, Candace Gilet, and many others: you have truly been an inspiration to me, and a crucial source of support and encouragement.

To my family, and to Anna Schneider and Lester Hedges for supporting me through the thesis writing process and making our home a happy one.

And of course, most sincere thanks to the entire CUORICINO collaboration, without whom this work would not have been possible.

Chapter 1

Introduction

Ever since their birth as Pauli's "desperate remedy" to explain the beta decay spectrum, neutrinos have been a surprising and enigmatic addition to the world of particle physics. Electrically neutral and nearly massless, neutrinos are observable only through their weak interactions, making them among the most difficult standard model particles to study. Great strides have been made in understanding neutrino properties in the past few decades, but major questions still remain.

Perhaps the most fundamental of these questions is whether the neutrino is a Majorana or a Dirac particle. A Dirac particle is a particle which has a distinct antiparticle, while a Majorana particle is identical to its antiparticle. Charged particles are distinguished from their antiparticles by opposite charge; neutrinos, being electrically neutral, are the only leptons which could potentially be Majorana particles.

The only known experimentally feasible method to distinguish these two possibilities involves a rare nuclear process called double beta ($\beta\beta$) decay. Double beta decay is a second order weak process in which a nucleus (A, Z) decays into a daughter (A, Z+2) via the emission of two electrons. In general, this decay is accompanied by the emission of two electron (anti-)neutrinos (Fig. 1.1(a)). However, if the neutrino is a massive Majorana particle, it is also possible for the decay to proceed without the emission of any neutrinos (Fig. 1.1(b)). The observation of neutrinoless double beta decay ($0\nu\beta\beta$) would show that the neutrino is a Majorana particle and would provide information about the absolute mass scale of the neutrino. Measuring the associated two-neutrino beta decay rates ($2\nu\beta\beta$) is also important for understanding the nuclear physics of $\beta\beta$ decay and the background contribution to $0\nu\beta\beta$ measurements from $2\nu\beta\beta$.

1.1 Neutrino properties

1.1.1 Neutrino oscillations

The Standard Model includes three charged leptons, $\ell = e, \mu, \tau$, each of which is coupled to a corresponding neutrino state ν_ℓ via the W vector boson of the weak interaction. The

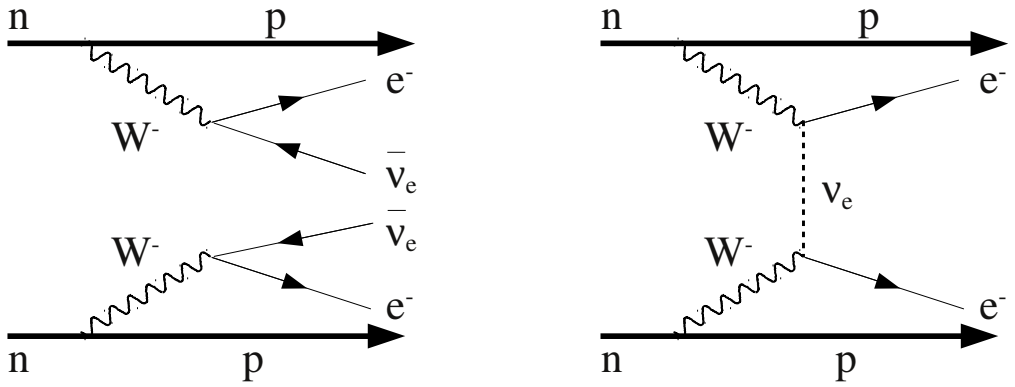

(a) Double beta decay with two neutrinos

(b) Neutrinoless double beta decay

Figure 1.1: Two possible modes for double beta decay.

states $\{\nu_\ell\}$ are referred to as the "flavor" eigenstates of the neutrino. In the minimal Standard Model, these neutrino states are massless. However, recent experimental evidence suggests that neutrinos have nonzero mass with eigenstates $\{\nu_m\}$, related to the flavor eigenstates via a (3×3) unitary mixing matrix $\mathbf{U}$:

$$\nu_\ell = \sum_m U_{\ell m} \nu_m. \tag{1.1}$$

The matrix $\mathbf{U}$ is known as the Pontecorvo-Maki-Nakagawa-Sakata (PMNS) matrix, and may be written as:

$$\mathbf{U} = \begin{pmatrix} c_{12}c_{13} & s_{12}c_{13} & s_{13}e^{-i\delta} \\ -s_{12}c_{23} - c_{12}s_{23}s_{13}e^{i\delta} & c_{12}c_{23} - s_{12}s_{23}s_{13}e^{1\delta} & s_{23}c_{13} \\ s_{12}s_{23} - c_{12}s_{23}s_{13}e^{i\delta} & -c_{12}s_{23} - s_{12}c_{23}s_{13}e^{1\delta} & c_{23}c_{13} \end{pmatrix} \begin{pmatrix} e^{i\alpha_1/2} & 0 & 0 \\ 0 & e^{i\alpha_2/2} & 0 \\ 0 & 0 & 1 \end{pmatrix}, \tag{1.2}$$

where s_{ij} and c_{ij} refer to $\sin(\theta_{ij})$ and $\cos(\theta_{ij})$. This matrix contains six parameters: the mixing angles θ_{12}, θ_{23}, and θ_{13}; a CP-violating phase δ; and two "Majorana" phases α_1 and α_2, which are only physically meaningful if the neutrino is a Majorana particle.

A non-diagonal mixing matrix $\mathbf{U}$ leads to a phenomenon known as neutrino oscillation: when a neutrino is produced in a flavor eigenstate of the weak interaction (i.e. a superposition of mass eigenstates), the probability of later detecting that neutrino in the same flavor eigenstate oscillates with the distance traveled (L) over the energy of the neutrino (E). For the simplified case of only two neutrino states (approximately valid in most experimental

situations), and assuming CP conservation, this probability is given by:

$$P_{\nu_\ell \to \nu_\ell} = 1 - \sin^2(2\theta)\sin^2\left(1.27 \cdot \Delta m^2[\,\mathrm{eV}^2] \cdot \frac{L[\,\mathrm{m}]}{E[\,\mathrm{MeV}]}\right), \tag{1.3}$$

where θ is the mixing angle and $\Delta m^2 = |m_1^2 - m_2^2|$ is the mass-squared difference between the two neutrino states [1].

Neutrino oscillations were first proposed by Bruno Pontecorvo in 1957 [2], and are historically associated with the "solar neutrino problem" — a deficit in the measured flux of neutrinos from the sun, first observed by Ray Davis in the Homestake experiment [3]. The solar neutrino problem was finally resolved in 2001 when the SNO experiment measured the total neutrino flux from the sun, using flavor-insensitive neutral-current reactions [4]. This flux was consistent with the predictions of the standard solar model; the apparent deficit was due to the oscillation of electron-type neutrinos produced in nuclear reactions in the sun oscillating into other flavor states, which were not detectable by previous experiments.

Perhaps the most striking evidence for neutrino oscillations comes from the KamLAND experiment, which measured the flux of anti-neutrinos from nearby nuclear reactors. The KamLAND results show a clear oscillation pattern in the energy spectrum of the detected neutrinos, shown in Fig. 1.2.

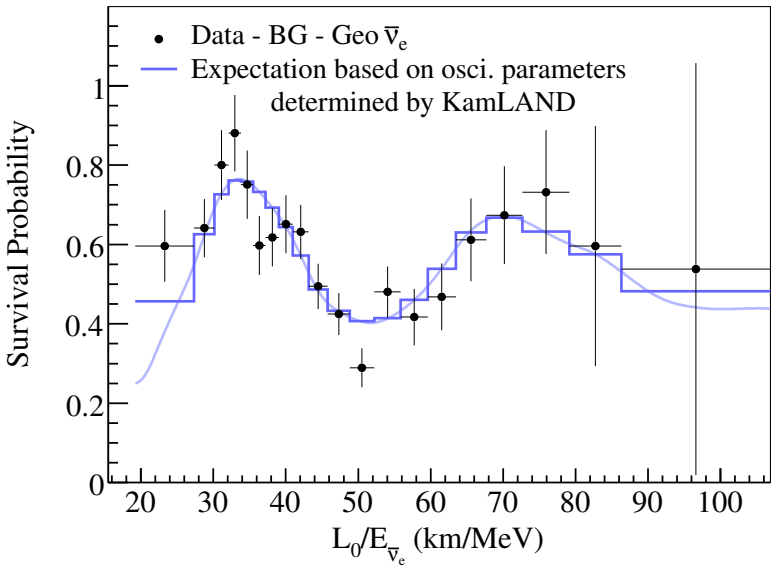

Figure 1.2: Neutrino oscillation results from KamLAND [5]

Table 1.1: Experimental best values for the neutrino mixing parameters [8].

Parameter	Value
$\sin^2(2\theta_{12})$	0.87 ± 0.03
$\sin^2(2\theta_{23})$	> 0.92
$\sin^2(2\theta_{13})$	< 0.15
Δm^2_{21}	$(7.59 \pm 0.20) \times 10^{-5}\,\mathrm{eV}^2$
Δm^2_{32}	$(2.43 \pm 0.13) \times 10^{-3}\,\mathrm{eV}^2$

Neutrino oscillations are now experimentally well-established, having been observed in neutrinos originating from the sun [4], the atmosphere [6], nuclear reactors [5] and accelerators [7]. A summary of current experimental best values for the neutrino oscillation parameters is shown in Table 1.1. It has not yet been experimentally determined whether m_2 is larger or smaller than m_3, leaving open the question of the neutrino mass hierarchy; that is: are the neutrino masses ordered similarly to the charged leptons and quarks, such that the closely-spaced mass pair has a smaller mass than the third mass state (the so-called "normal" hierarchy)? Alternatively, if m_2 is greater than m_3, neutrino masses would follow an "inverted" hierarchy (Fig. 1.3). Although the splittings between the neutrino mass eigenstates may be measured precisely by neutrino oscillation experiments, oscillation experiments are unable to probe the absolute value of the neutrino masses. The situation where the offset between zero and the smallest neutrino mass state is large compared to the differences between states is referred to as the quasi-degenerate mass hierarchy.

Although the neutrino mass is too small to (yet) be detected directly, neutrino oscillations provide compelling evidence that neutrinos have (at least two) non-zero mass eigenvalues. Consequently, the minimal Standard Model must be extended to include mass terms for the neutrino. The ways in which this could be done are the topic of the next section.

1.1.2 Dirac and Majorana neutrinos

A neutrino field may be represented as a four-component spinor ψ, which satisfies the Dirac equation:

$$(-i\gamma^\mu \partial_\mu + m)\psi = 0. \tag{1.4}$$

Its charge conjugate field ψ^c is defined as:

$$\psi^c = \eta_C C \bar{\psi}^T, \tag{1.5}$$

where C is the charge-conjugation matrix, η_C is a phase factor, the superscript T indicates a transposed matrix, and $\bar{\psi} = \psi^\dagger \gamma^0$ is the Hermitian conjugate field times the 0th Dirac matrix. Given the requirements that the Lagrangian must be Lorentz invariant and hermitian, the

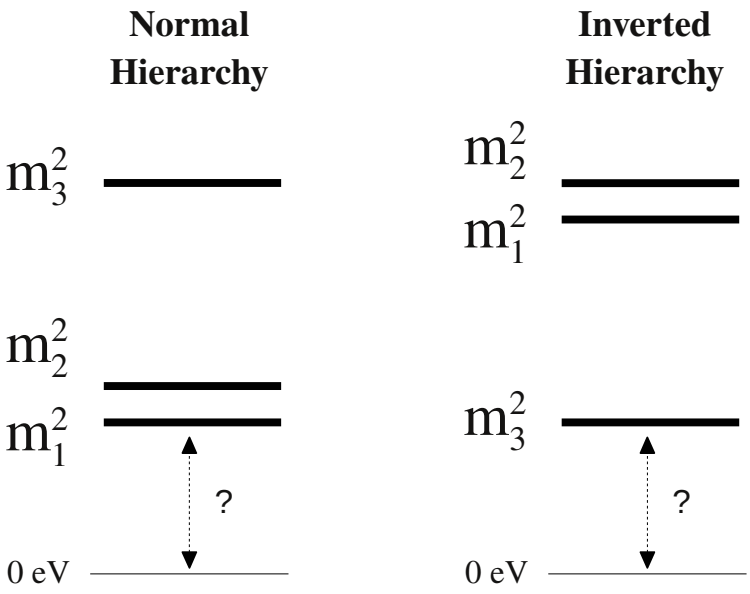

Figure 1.3: Possible arrangements for the neutrino mass eigenstates.

most general mass term that can be constructed is:

$$-4\mathcal{L}_m = \underbrace{\bar{\psi} m_D \psi + \bar{\psi}^c m_D \psi^c}_{\mathcal{L}_m^D} + \underbrace{\bar{\psi} m_M \psi^c + \bar{\psi}^c m_M^* \psi}_{\mathcal{L}_m^M}, \tag{1.6}$$

where m_D is a real-valued mass parameter, and m_M is complex. The first part of Eq. (1.6) ($\mathcal{L}_m^D$) has the form of a Dirac mass term, analogous to the charged leptons. Unlike $\mathcal{L}_m^M$, it is invariant under the global gauge transformation $\psi \rightarrow e^{i\alpha}\psi$, which is a mathematical expression of the fact that Dirac mass terms conserve lepton number, but Majorana mass terms do not.

Since neutrinos participate in (parity-violating) weak interactions, it is convenient to work in terms of the left and right chiral projections of the neutrino field:

$$\begin{aligned} \psi_L &= \left(\frac{1-\gamma_5}{2}\right)\psi \\ \psi_R &= \left(\frac{1+\gamma_5}{2}\right)\psi. \end{aligned} \tag{1.7}$$

In that case, Eq. (1.6) can be re-written as:

$$-\mathcal{L}_m = M_D \bar{\psi}_L \psi_R + \frac{M_L}{2}(\bar{\psi_L})^c \psi_L + \frac{M_R}{2}(\bar{\psi_R})^c \psi_R + h.c. \tag{1.8}$$

Following the discussion found in reference [9], we define two new fields:

$$\begin{aligned} f &= \frac{\psi_L + (\psi_L)^c}{\sqrt{2}} \\ F &= \frac{\psi_R + (\psi_R)^c}{\sqrt{2}}. \end{aligned} \tag{1.9}$$

In terms of these new fields, the Lagrangian becomes:

$$-\mathcal{L} = \bar{f}\gamma_\mu \partial_\mu f + \bar{F}\gamma_\mu \partial_\mu F + \left(\bar{f}, \bar{F}\right) \begin{pmatrix} M_L & M_D \\ M_D & M_R \end{pmatrix} \begin{pmatrix} f \\ F \end{pmatrix}. \tag{1.10}$$

The mass matrix in Eq. (1.10) must be diagonalized to find states of definite mass. The resulting mass eigenstates (ν and N) are also eigenstates of charge-conjugation; i.e., they describe Majorana particles. Effectively, the Dirac spinor ψ, with four mass-degenerate components describing the spin up and down states of a particle and its (distinct) anti-particle, has been broken into two two-state particles with non-degenerate mass.

One reason Majorana neutrinos are favored by theorists is their potential to explain the unusually small value of the neutrino mass relative to other standard-model particles, via a mechanism known as the "see-saw" mechanism. The see-saw mechanism arises if there is a hierarchy among the mass matrix elements in Eq. (1.10), such that $M_L \ll M_D \ll M_R$. In

many theories, M_L is expected to be zero, while M_R is expected to be very large, on the order of the symmetry-breaking scale. The Dirac mass term, M_D, on the other hand should arise via the same mechanism as the charged fermions, and may be taken to be of the same order as the quark or charged lepton masses. In this limit, the mass eigenvalues of the neutrino are given by:

$$M_N \simeq M_R \qquad M_\nu \simeq \frac{M_D^2}{M_R}. \tag{1.11}$$

In this way, we end up with one extremely light neutrino (consistent with experiment) and one extremely heavy neutrino (yet to be observed).

The previous discussion treated only one neutrino flavor; however, the mass term can be generalized to an arbitrary number of neutrino species (n), by replacing the field ψ by an n-dimensional vector $\Psi = (\psi_e, \psi_\mu, \psi_\tau, ...)$, and replacing the mass parameters m_D and m_M by $(n \times n)$ matrices (see, for example, reference [10]).

1.2 Double beta decay

In principle, $\beta\beta$ decay occurs in any nucleus for which it is kinematically allowed, in competition with all other decay modes. However, in practice, because it is an extremely rare process, it is only observable when competing decay modes are forbidden or highly suppressed. Because of the pairing force between like nucleons, the situation can arise in even-even nuclei that a single β decay is energetically forbidden, leaving the $\beta\beta$ decay as the first allowed decay mode (Fig. 1.4). Table 1.2 lists some naturally occurring isotopes for which $\beta\beta$ is expected to be the dominant decay mode.

1.2.1 Two-neutrino double beta decay

The decay rate for $2\nu\beta\beta$ was first calculated by Goeppert-Mayer in 1935 [18]. It is a standard second order weak decay, which does not depend on the Dirac or Majorana nature of the neutrino, and may be modeled as two successive single beta transitions which proceed via virtual intermediate nuclear states. In principle, both the Fermi and Gamow-Teller operators can contribute to the transition; however, because the Fermi component is strongly suppressed for $2\nu\beta\beta$ by isospin symmetry, only the Gamow-Teller component is usually considered in practice. Following the derivation of [19], we can write the half-life for the ground-state to ground-state (i.e., for even-even nuclei, $0^+ \rightarrow 0^+$) $2\nu\beta\beta$ transition in second order perturbation theory as

$$\begin{aligned}\frac{1}{T_{1/2}^{2\nu}} = \frac{G^4 g_A^4}{32\pi^7 m_e \ln 2} \int_{m_e}^{Q+m_e} \mathcal{F}(Z,\varepsilon_1) k_1 \varepsilon_1 \mathrm{d}\varepsilon_1 \int_{m_e}^{Q+2m_e-\varepsilon_1} \mathcal{F}(Z,\varepsilon_2) k_2 \varepsilon_2 \mathrm{d}\varepsilon_2 \\ \times \int_0^{Q+2m_e-\varepsilon_1-\varepsilon_2} \nu_1 \nu_2 \mathrm{d}\nu_1 \sum_{a,a'} A_{aa'},\end{aligned} \tag{1.12}$$

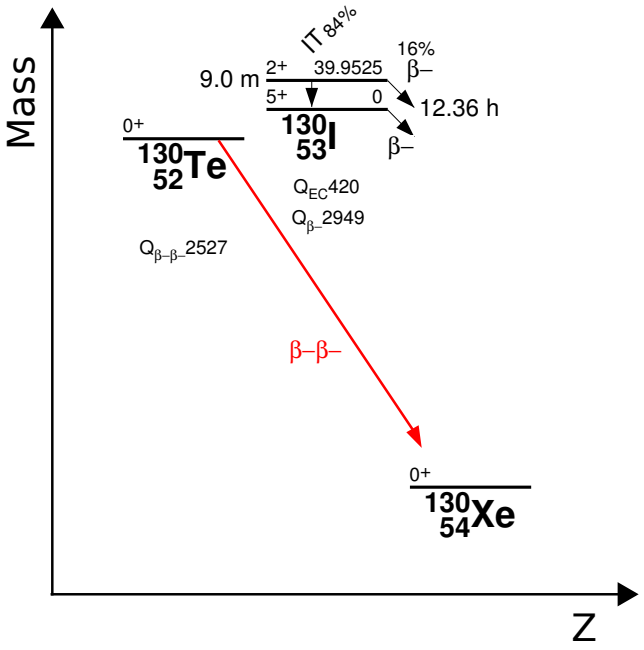

Figure 1.4: When a single β decay would put the nucleus in a higher mass state, $\beta\beta$ decay may be the first allowed decay mode, as seen in the case of ^{130}Te [11].

Table 1.2: Some commonly studied $\beta\beta$ decay isotopes and their properties. Isotopic abundances taken from [12], phase space factors $G^{2\nu}$ and $G^{0\nu}$ from [1], and Q values from [13], except (a) [14], (b) [15], (c) [16] and [15], and (d) [17]

$\beta\beta$ Decay Reaction	Isotopic Abundance (atomic %)	Q-value (keV)	$[G^{2\nu}]^{-1}$ (y)	$[G^{0\nu}]^{-1}$ (y)
^{48}Ca→^{48}Ti	0.2	4274	8.71e21	7.16e26
^{76}Ge→^{76}Se	7.6	2039	7.66e18	4.09e25
^{82}Se→^{82}Kr	8.7	2996	2.30e17	9.27e24
^{96}Zr→^{96}Mo	2.8	3348	5.19e16	4.46e24
^{100}Mo→^{100}Ru	9.6	3034$^{(a)}$	1.06e17	5.70e24
^{116}Cd→^{116}Sn	7.5	2809	1.25e17	5.28e24
^{124}Sn→^{124}Te	5.8	2288	5.93e17	9.48e24
^{128}Te→^{128}Xe	31.8	866$^{(b)}$	1.18e21	1.43e26
^{130}Te→^{130}Xe	34.2	2527$^{(c)}$	2.08e17	5.89e24
^{136}Xe→^{136}Ba	8.9	2458$^{(d)}$	2.07e17	5.52e24
^{150}Nd→^{150}Sm	5.6	3368	8.41e15	1.25e24

where ε_i and ν_i are the energies of the outgoing electrons and neutrinos, respectively, $k_i = \sqrt{\varepsilon_i^2 - m_e^2}$ are the electron momenta, Q is the maximum available kinetic energy, or Q-value, of the decay, and G and g_A are weak interaction coupling constants. The function $\mathcal{F}$ is the Fermi factor, which describes the effect of the coulomb field of the daughter nucleus on the emitted electrons. The quantity $A_{aa'}$ contains the nuclear Gamow-Teller transition matrix elements and energy denominators, which are summed over the intermediate 1^+ nuclear states indexed by a and a':

$$A_{aa'} = \langle 0_f^+|\tau_-\sigma|1_a^+\rangle\langle 1_a^+|\tau_-\sigma|0_i^+\rangle\langle 0_i^+|\tau_-\sigma|1_{a'}^+\rangle\langle 1_{a'}^+|\tau_-\sigma|0_f^+\rangle \times \frac{1}{3}\left(K_aK_{a'} + L_aL_{a'} + \frac{1}{2}K_aL_{a'} + \frac{1}{2}L_aK_{a'}\right) \tag{1.13}$$

where

$$K_a = \frac{1}{E_a + \varepsilon_1 + \nu_1 - E_i} + \frac{1}{E_a + \varepsilon_2 + \nu_2 - E_i} \tag{1.14a}$$

$$L_a = \frac{1}{E_a + \varepsilon_1 + \nu_2 - E_i} + \frac{1}{E_a + \varepsilon_2 + \nu_1 - E_i}. \tag{1.14b}$$

Since $A_{aa'}$ depends on the energies of both the leptons and the intermediate nuclear states, the integration over lepton energies should be carried out individually for each intermediate nuclear state. However, it is generally a good approximation to replace the lepton energy $\varepsilon + \nu$ in Eq. (1.14) with the average value, $Q/2 + m_e$, in which case

$$K_a \approx L_a \approx \frac{1}{E_a - E_i + Q/2 + m_e}. \tag{1.15}$$

Under this approximation, the half-life expression can then be factorized as:

$$\frac{1}{T_{1/2}^{2\nu}} = G^{2\nu}(Q, Z)|M^{2\nu}|^2, \tag{1.16}$$

where $G^{2\nu}$ is the (accurately calculable) lepton phase-space integral, which depends on the Q value of the decay and the charge of the final state nucleus (Z), and

$$M^{2\nu} = \sum_a \frac{\langle 0_f^+|\tau_-\sigma|1_a^+\rangle\langle 1_a^+|\tau_-\sigma|0_i^+\rangle}{E_a - E_i + Q/2 + m_e} \tag{1.17}$$

is the nuclear matrix element containing all of the nuclear physics information. The nuclear matrix elements are not easily calculable, but have been computed by various groups using different nuclear models, as discussed in Sect. 1.2.3.

A qualitative view of the spectrum shape can be obtained by using a non-relativistic approximation for the the Fermi factor $\mathcal{F}$ in Eq. (1.12):

$$\mathcal{F}(Z, E) = \frac{E}{p}\frac{2\pi Z\alpha}{1 - e^{-2\pi Z\alpha}}. \tag{1.18}$$

This approximation, introduced by Primakoff and Rosen [20], allows the phase space integral to be solved analytically, yielding the following commonly used expression for the differential decay rate:

$$\frac{dN}{dE} \sim E(Q-E)^5 \left(1 + 2E + \frac{4E^2}{3} + \frac{E^3}{3} + \frac{E^4}{30}\right), \tag{1.19}$$

where E refers to the total kinetic energy of the two emitted electrons, in units of the electron mass. This equation describes the black curve plotted in Fig. 1.8. In this approximation, the phase space factor $G^{2\nu}$ scales as Q^{11}; more precise calculations are described in Appendix B and tabulated for various isotopes in Table 1.2.

1.2.2 Neutrinoless double beta decay

In the case that the $0\nu\beta\beta$ is mediated by a light Majorana neutrino[1], as pictured in Fig. 1.1(b), the ground-state to ground-state $0\nu\beta\beta$ decay rate can be written as:

$$\frac{1}{T^{0\nu}_{1/2}} = G^{0\nu}(Q,Z)|M^{0\nu}|^2 \left(\frac{\langle m_{\beta\beta}\rangle}{m_e}\right)^2. \tag{1.20}$$

This expression is similar in form to that for $2\nu\beta\beta$ (Eq. (1.16)), containing a phase space factor $G^{0\nu}$ (which scales approximately as Q^5) and a matrix element $M^{0\nu}$. However, the $0\nu\beta\beta$ rate contains an additional component, which is the effective Majorana neutrino mass, $\langle m_{\beta\beta}\rangle$, given by

$$\begin{aligned} \langle m_{\beta\beta}\rangle &= \left|\sum_i m_i U_{ei}^2\right| \\ &= \left|u_{e1}^2 e^{i\alpha_1} m_1 + u_{e2}^2 e^{i\alpha_2} m_2 + u_{e3}^2 m_3\right|, \end{aligned} \tag{1.21}$$

where m_i are the neutrino mass eigenstates and

$$\mathbf{U} \equiv \mathbf{u} \times \begin{pmatrix} e^{i\alpha_1/2} & 0 & 0 \\ 0 & e^{i\alpha_2/2} & 0 \\ 0 & 0 & 1 \end{pmatrix} \tag{1.22}$$

is the neutrino mixing matrix defined in Eq. (1.2). If CP is conserved, the u_{ei} are real and the Majorana phase factors $e^{i\alpha_i}$ are ± 1. Cancellation may occur between the terms in Eq. (1.21); in principle, the terms could cancel completely, which would cause the $0\nu\beta\beta$ rate to be zero, even if the neutrino were a Majorana particle. However, in the absence of any underlying symmetry or physical principle forbidding the decay, complete "accidental" cancellation seems unlikely.

[1] A variety of other mechanisms for $0\nu\beta\beta$ have been proposed (for example, right handed currents, exchange of a heavy Majorana neutrino, or exchange of supersymmetric particles); regardless of the mechanism, the observation of $0\nu\beta\beta$ implies a Majorana mass term for the neutrino [21].

Measured values for the elements of **u** from neutrino oscillation experiments place a constraint on the possible values of $\langle m_{\beta\beta} \rangle$. Using the current experimental best values for the neutrino mixing parameters and letting the Majorana phases vary through their allowed ranges of 0 to 2π, the possible values of $\langle m_{\beta\beta} \rangle$ are shown in Fig. 1.5. This kind of plot is often used to compare the results of different neutrino mass experiments. Direct neutrino mass measurements (beta decay endpoint experiments or cosmological measurements) exclude area from the right side of the plot inward, while $0\nu\beta\beta$ experiments exclude area from the top down. However, there is a large uncertainty in translating the measured half-life limits from $0\nu\beta\beta$ experiments into limits on $\langle m_{\beta\beta} \rangle$ due to the difficulty of calculating the nuclear matrix elements $M^{0\nu}$, discussed in the next section.

1.2.3 Nuclear matrix elements for $\beta\beta$ decay

The nuclear matrix elements $M^{0\nu}$ and $M^{2\nu}$ are similar in form. They generically consist of a wavefunction describing the 0^+ ground state of the even-even parent nucleus, a wavefunction describing the final state of the even-even daughter nucleus (usually also the ground state), and an operator connecting those states. The matrix elements for $\beta\beta$ decay can be broken down into Fermi and Gamow-Teller components[2], as:

$$|M|^2 = \left| M_{GT} - \frac{g_V^2}{g_A^2} M_F \right|^2 , \tag{1.23}$$

where M_{GT} and M_F are the Gamow-Teller and Fermi matrix elements, and g_V and g_A are the vector and axial-vector weak interaction coupling constants, respectively. For $2\nu\beta\beta$, $M_F^{2\nu}$ is suppressed because the Fermi operator does not connect states of different isospin. Since $|M_F^{2\nu}| \ll |M_{GT}^{2\nu}|$, the contribution from $|M_F^{2\nu}|$ is usually neglected in calculations.

Although the $0\nu\beta\beta$ and $2\nu\beta\beta$ matrix elements are similar in form, there are important differences in how they are calculated, and the two are not interchangeable. One key difference is the treatment of the sum over intermediate states. In $0\nu\beta\beta$ calculations, an explicit sum over intermediate states is usually avoided by using the closure approximation. This approximation is justified because the energy of the virtual neutrino is large relative to the excitation energies of the intermediate nuclear states. The closure approximation is sometimes used for $2\nu\beta\beta$ calculations as well, but is generally considered to be a poorer approximation [1].

Historically, there have been two main methods for calculating the matrix elements for $\beta\beta$ decay: the Interacting Shell Model (ISM), and the Quasiparticle Random Phase Approximation (QRPA). These two methods are complementary in their approach, in that the QRPA uses a large number of single particle states, but in a limited number of configurations, whereas the ISM treats only a small fraction of the single particle nucleon states, but includes all possible configurations of those states. In principle, the ISM has the potential

[2]In principle, the matrix element also contains a tensor term, but it is much smaller than the others and will therefore be neglected in these discussions.

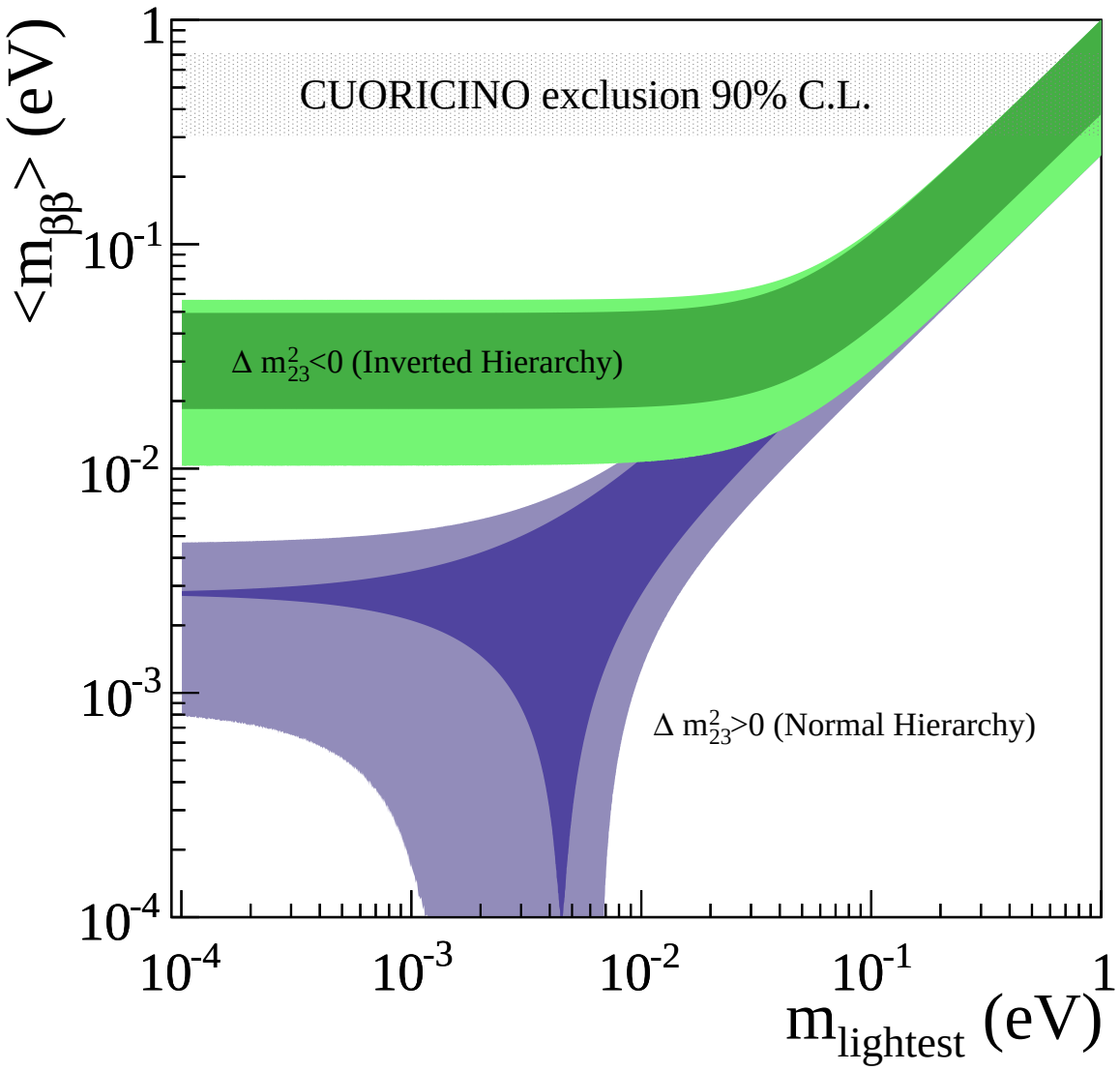

Figure 1.5: Allowed values for $\langle m_{\beta\beta} \rangle$ plotted versus the lightest neutrino mass (m_1 for the normal hierarchy, or m_3 for the inverted hierarchy), obtained using experimental values for the neutrino oscillation parameters from [22] and letting the Majorana phases vary. The lighter shaded regions correspond to the allowed regions if the oscillation parameters are allowed to vary within 3σ, where σ represents the experimental uncertainty. The CUORICINO exclusion band indicates the upper limit on $\langle m_{\beta\beta} \rangle$ set by the CUORICINO experiment; the width of the band indicates the uncertainty due to matrix element calculations.

to represent the nuclear wave function to arbitrary precision, but in practice, the technique is severely limited by available computational power. Because it is less computationally intensive, there have been many more calculations based on the QRPA model than the ISM.

Over the years, ISM and QRPA calculations have become increasingly sophisticated. There exist a large number of variations on the QRPA technique, using different treatments for the nucleon-nucleon interaction, pairing, finite nuclear size, etc. In general there are free parameters in QRPA calculations which are tuned to reproduce experimental data, such as experimental pairing energies, energy of the Gamow-Teller resonance, and other measurable nuclear properties. Recent works in both QRPA and ISM have included corrections for short-range correlations ([23], [24]), although there is no agreement on the best method for handling these correlations.

In general, there are very few experimentally measurable observables which can check the validity of $M^{0\nu}$ calculations. However, one promising new avenue of experimental input was explored by recent measurements of the neutron and proton valence occupancies in the ground states of ^{76}Ge and ^{76}Se via nucleon transfer reactions ([25], [26]). These measurements were found to be in significant disagreement with the QRPA and ISM models used for $\beta\beta$ decay calculations. When the calculations were amended to agree with the the experimental data, the discrepancy between the ISM [27] and QRPA [28] calculations decreased. Similar work investigating pair correlations and nucleon occupancies in ^{130}Te and ^{130}Xe is ongoing [29].

In addition to QRPA and ISM, a few new methods have been developed in recent years for computing $\beta\beta$ matrix elements. The Interacting Boson Model (IBM-2) treats the nucleus as a set of $J^P = 0^+$ (S) and $J^P = 2^+$ (D) bosonic pair states of identical nucleons. According to [30], the model is better able to account for nuclear deformations than QRPA or ISM, and makes use of "realistic" wave functions that well reproduce experimental nuclear data, including spectra, electromagnetic transitions, and two-nucleon transfer reactions.

The Projected Hartree-Fock-Bogoliubov (PHFB) method ([31], [32] [3], [33]) uses angular momentum projections of the HFB wave functions with a Hamiltonian which includes pairing plus quadrupole-quadrupole (PQQ) interactions. A major extension to the PHFB approach has recently been reported in [34], using Particle Number and Angular Momentum Projection (PNAMP), configuration mixing within the Generating Coordinate Method (GCM), "state-of-the-art density functional methods... and a much larger single particle basis." Recent results of $M^{0\nu}$ calculations by various groups are shown in Fig. 1.6. The calculated values of $M^{0\nu}$ for ^{130}Te agree to within approximately a factor of two.

Most of the attention devoted to $\beta\beta$ matrix elements has been focused on $M^{0\nu}$ calculations, because of their importance in extracting information about the neutrino mass from experimental half-life results. There are two main ways of viewing $2\nu\beta\beta$ in relation to the problem of $0\nu\beta\beta$ matrix elements. The first is to consider the matrix element $M^{2\nu}$, which is obtainable from experiment, as a test of the validity of nuclear models. Although correctly reproducing the value of $M^{2\nu}$ is not a guarantee that a model is valid in the 0ν case, calcula-

[3] References [31] and [32] contain a factor of two error in $M^{0\nu}$, corrected in [33]

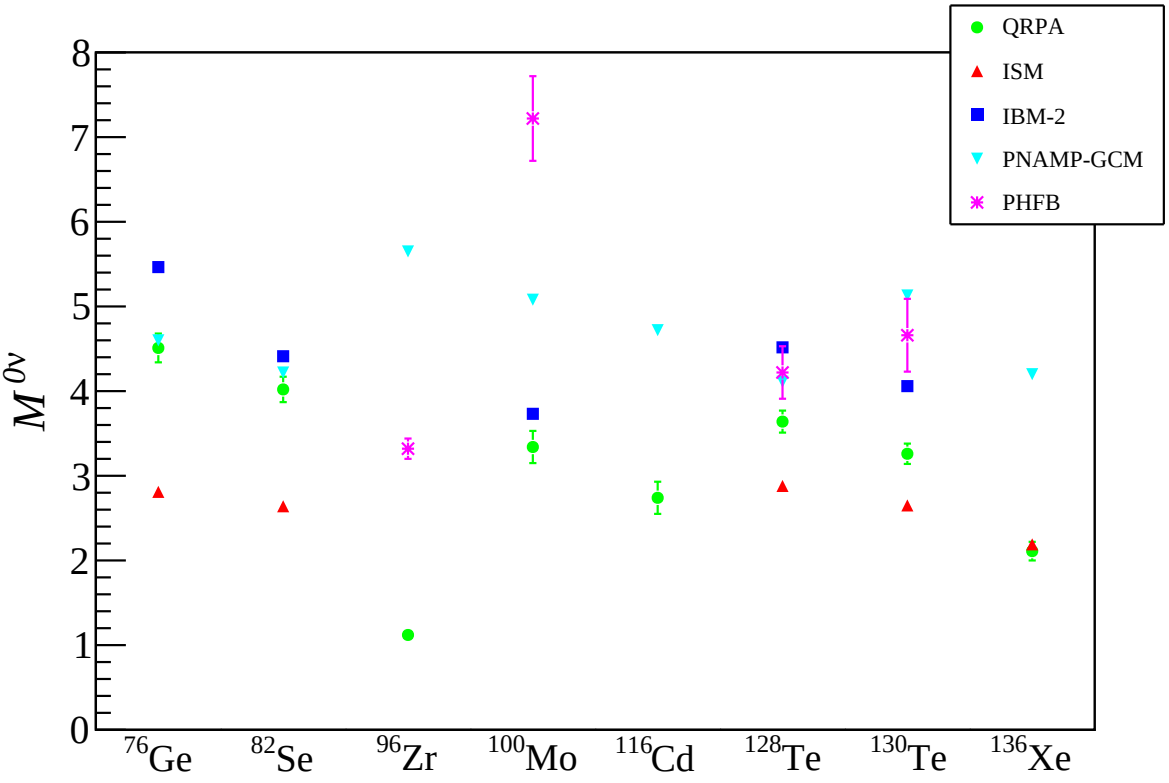

Figure 1.6: Calculated values for the $0\nu\beta\beta$ matrix elements $M^{0\nu}$ for different isotopes using a variety of models. The calculated values are taken from the following references: QRPA [35], ISM: [24], IBM-2: [30], PNAMP-GCM: [34], PHFB: [33]. All calculations used $g_A = 1.25$. The ISM results were obtained using the Unitary Correlation Operator Method (UCOM) for short-range correlations.

tions which can successfully describe $2\nu\beta\beta$ are generally viewed as more reliable. A second way of using $2\nu\beta\beta$ data is to tune a model's free parameters to agree with experimental $2\nu\beta\beta$ results before calculating $M^{0\nu}$. One notable example of this approach is described in [36] and [35]. It was found that adjusting the strength of the isoscalar particle-particle force (g_{pp}) to reproduce the measured $2\nu\beta\beta$ rates significantly reduced disagreement between different QRPA calculation methods.

There have been a few other attempts to relate the $2\nu\beta\beta$ and $0\nu\beta\beta$ matrix elements to each other. Early work by Primakoff and Rosen [20] postulated a simple proportionality between $M^{0\nu}$ and $M^{2\nu}$. This hypothesis is not supported by modern matrix element calculations and by the observed suppression of measured $2\nu\beta\beta$ rates relative to theoretical predictions. However, a recent paper by Šimkovic *et al.* [37] takes a more sophisticated approach by relating the Gamow-Teller part of the $0\nu\beta\beta$ matrix element ($M^{0\nu}_{GT}$) to the $2\nu\beta\beta$ matrix element in the closure approximation ($M^{2\nu}_{cl}$) and then relating $M^{2\nu}_{cl}$ to the true value of $M^{2\nu}$.

Early calculations of $M^{2\nu}$ (e.g. [38]) noted a serious discrepancy between measured and calculated values, with the observed half-lives being much longer than expected from theory. Later calculations in the QRPA method found that much of this observed rate suppression could be accounted for by the introduction of a particle-particle spin-isospin polarization force, represented by the parameter g_{pp} [39]. A sample of theoretical predictions for the $2\nu\beta\beta$ half-lives is found in Fig. 1.7, including ISM [38] calculations in the closure approximation, QRPA calculations made by setting the parameter g_{pp} based on single β^+/EC decays [40], QRPA calculations including Second Forbidden Corrections (SFC) [41], and more recent calculations in the PHFB framework [31], using the method described in [42] for the sum over intermediate states. A further comparison between calculated and experimental values of $M^{2\nu}$ for ^{130}Te can be found in Sect. 5.3, in the conclusion of this work.

1.2.4 Experimental searches for $\beta\beta$ decay

When choosing a $\beta\beta$ isotope for experimental study, there are several important factors to consider. A large natural isotopic abundance is beneficial to avoid the necessity of costly isotopic enrichment. Isotopic enrichment can also introduce or remove radioactive contaminants, affecting the backgrounds present in the experiment. Another desirable feature is a large Q value for the $\beta\beta$ decay, which enhances the $\beta\beta$ decay rate and places the signature of the decay in an energy region where there is less natural background gamma and beta radioactivity. The chemical properties of the element are also important in determining what kinds of experimental techniques may be used.

The isotope studied in the CUORICINO experiment is ^{130}Te, which has an isotopic abundance of 34.2% [45] and a $\beta\beta$ Q value of about 2527 keV (recent measurements report 2527.518 ± 0.013 keV [16] and 2527.01 ± 0.32 keV [15]). The properties of other $\beta\beta$ candidate isotopes are listed in Table 1.2 for comparison.

There are three experimental methods that have been used to study $\beta\beta$ decay:

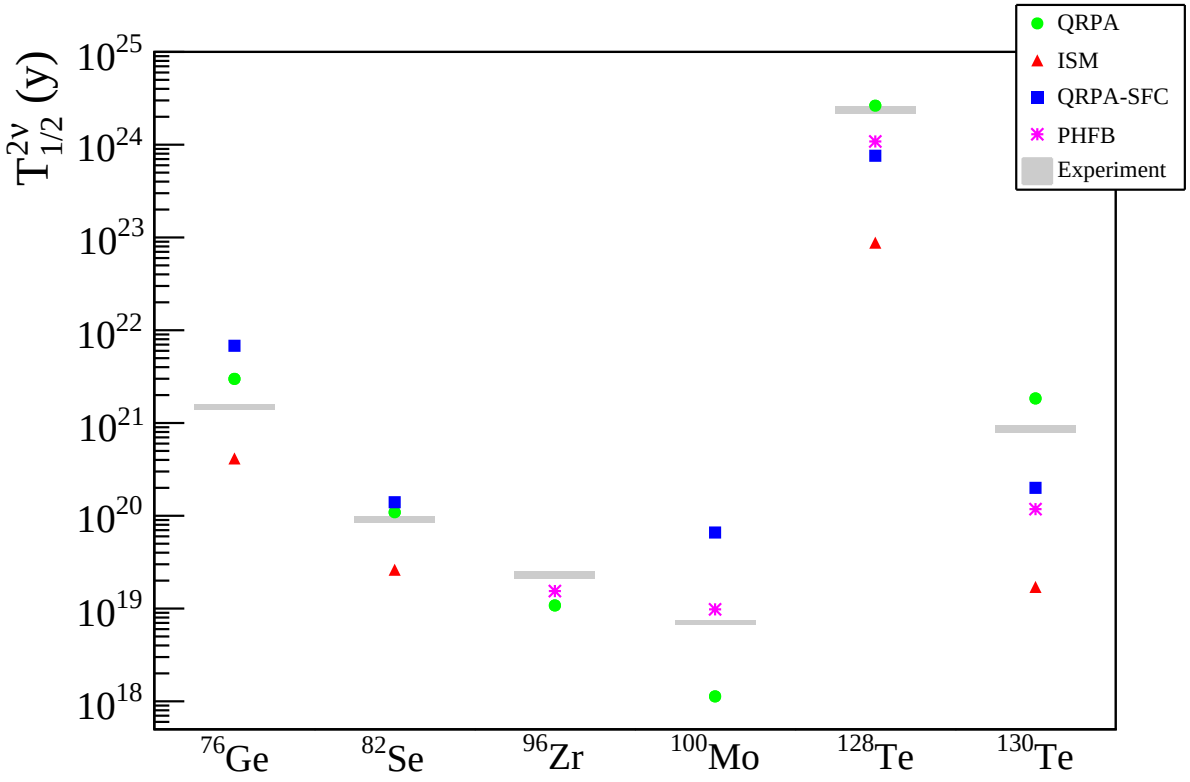

Figure 1.7: Calculated values for the $2\nu\beta\beta$ half-life for different isotopes using a variety of models. The calculated values are taken from the following references: QRPA [40], ISM: [38], QRPA-SFC: [41], and PHFB: [31]. The PHFB half-lives were obtained from the reported matrix elements using the phase space factors $G^{2\nu}$ listed in Table 1.2. The experimental results listed in Table 1.5 are represented by grey bands with a width corresponding to the 1σ uncertainties. The experimental value for ^{128}Te was obtained by scaling the ^{130}Te half life by the average of half-life ratios reported in [43] and [44].

Geochemical Measuring the isotopic abundance of daughter element in a sample of parent ore, which has been dated using independent radiochemical or geologic means.

Radiochemical Measuring the accumulation of daughter isotope in a sample of parent isotope in a laboratory setting.

Direct detection Direct detection of the emitted electrons from a $\beta\beta$ decay. The decay is identified based on spatial and/or timing coincidence of the electrons and/or their kinematic properties.

Direct detection is the only approach with the capability to distinguish between $0\nu\beta\beta$ and $2\nu\beta\beta$. The experimental signature of $0\nu\beta\beta$ is a sharp peak in the summed electron energy spectrum at the exact Q value of the decay (Fig. 1.8). In order to detect this signal, an experiment must have low background in the region near the $\beta\beta$ Q value and good energy resolution (the width of the $0\nu\beta\beta$ peak is determined by the detector resolution) to avoid losing the signal in the tail of the $2\nu\beta\beta$ spectrum.

For an equivalent half-life, the $2\nu\beta\beta$ signal is more difficult to detect, because it is spread out over a much larger energy region. The lower energy region where the $2\nu\beta\beta$ signal is found also generally contains more background from natural γ and β radioactivity. Understanding and quantifying these backgrounds is the main challenge of a $2\nu\beta\beta$ measurement.

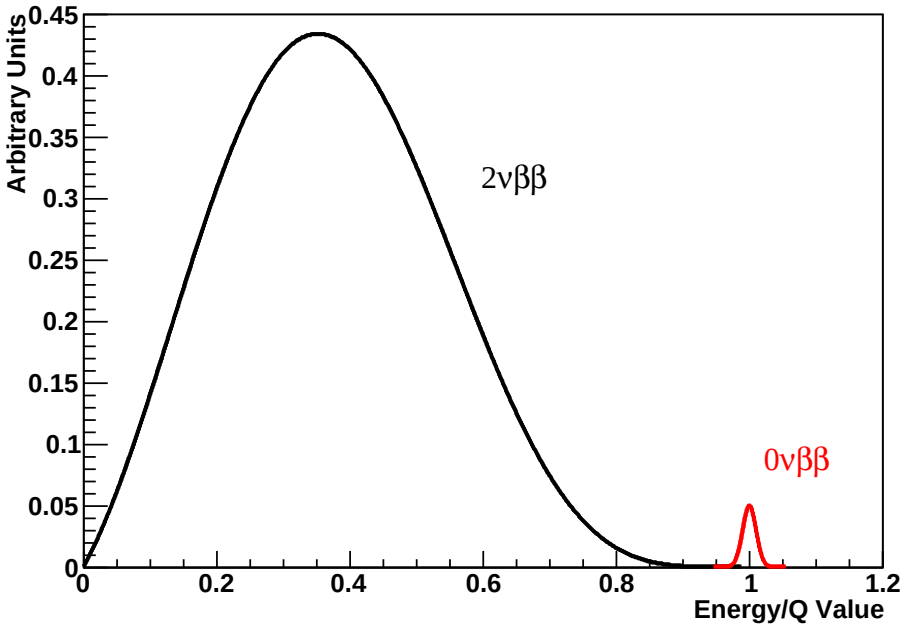

Figure 1.8: Summed electron energy spectrum for $\beta\beta$ decay.

A variety of different detector technologies have been used in $\beta\beta$ direct detection experiments. In general, these detectors measure the energy deposited by the emitted electrons in the form of ionization, scintillation, heat, or a combination of the above. Detectors which measure energy in a single mode often have better energy resolution; however, measuring a combination of two modes of energy release can help discriminate between particle types and thereby reduce backgrounds.

Detectors for $\beta\beta$ decay are often built so that the active detector volume is made of material containing the isotope of interest (the so-called "source = detector" approach). Examples of this approach include the Ge semiconductor detectors of the GERDA and Majorana experiments and the bolometric detectors used by CUORICINO (described in Chapter 2). Building the detector out of source material allows scaling up to a large mass of source material while maintaining high efficiency. Another possibility is to have the source material separate from the detector, as in the NEMO-3 experiment. The advantages of this approach are flexibility (it is easy to study many different isotopes with the same experiment) and the ability to obtain richer geometric information about decays (tracking and measuring the energy of the individual electrons). However, this type of experiment generally has much lower efficiency and worse energy resolution than "source = detector" experiments.

1.3 History and status of $\beta\beta$ decay measurements in ^{130}Te

1.3.1 Geochemical measurements

The earliest experimental evidence for $\beta\beta$ decay came from geochemical experiments, the first of which was performed in 1949 by Inghram and Reynolds [46]. The basic requirements for a geochemical $\beta\beta$ experiment are as follows:

1. A geologically old ($\sim 10^7 - 10^9$ y) sample of parent ore must be obtained.
2. The age of the sample must be able to be independently determined.
3. $\beta\beta$ decay must be the predominant source of daughter isotope in the sample.
4. The daughter isotope must not escape the parent sample, through diffusion or other means, over the geologic lifetime of the sample.

Given the long timescales involved, it is difficult to know with certainty that these criteria have been satisfied; however, the history of the samples can be inferred by their geologic environment and (radio)chemical makeup.

Historically, requirement number 3 has limited the use of geochemical methods mainly to the study of $\beta\beta$ decay processes whose products are noble gases, namely ^{130}Te $\rightarrow^{130}$ Xe, ^{128}Te $\rightarrow^{128}$ Xe, and ^{82}Se $\rightarrow^{82}$ Kr. This is because, due to the long half-lives involved, the amount of daughter isotope accumulated in any sample is so tiny that detecting it requires

the parent sample to be highly depleted in the daughter element (a factor of $\sim 10^{-7}$ or better). This condition is rarely met for any elements besides noble gasses; however, in the past decade, geochemical methods have been extended study the $\beta\beta$ decay of ^{96}Zr [47] and ^{100}Mo [48].

The typical procedure used to analyze a sample involves breaking the sample into small pieces, placing it under vacuum, heating it, and collecting the released gasses. The gasses are then subjected to isotopic analysis, and the isotope of interest is compared to a reference isotope to measure any excess. The half-life of the parent P decaying to the daughter D may then be determined by the formula:

$$T_{1/2} = t\left(\frac{P}{D^*}\right)\ln 2, \tag{1.24}$$

where t is the gas-retention age of the sample, and D^* is the excess daughter isotope measured in the sample. The main difficulty in such an experiment is accurately determining the gas-retention age, which may or may not be the same as the geologic age of the mineral deposit.

A chronology of geochemical $\beta\beta$ studies of ^{130}Te is presented in Table 1.3. The half-life results span about an order of magnitude, from $\sim 3 \times 10^{20}$ to $\sim 3 \times 10^{21}$ y. The obtained half-life values are somewhat correlated with the assumed age of the sample, as illustrated in Fig. 1.9, with older samples generally yielding longer half-lives.

Many explanations have been put forward for the disagreement among these half-life measurements. One author has even proposed that the differing values could be explained by a variation in the Fermi constant G_F over geologic time [67]. However, this hypothesis seems unlikely given the reasonably good agreement between laboratory [66] and geochemical [60] measurements of the $\beta\beta$ half-life of ^{82}Se, even those performed on very old (~ 4.5 Gy) samples [68].

A more likely explanation is an error in determining the gas-retention age of some of the samples. In general, the sample age is determined by radiochemical dating, ideally of the sample itself. However, because the Te-rich minerals under study are often highly depleted in the parent elements used for radiochemical dating, an age determination may be performed on the host rock or associated minerals. In this case, the determined ages are often treated as upper limits, since the Te mineralization may have occurred later, but is unlikely to have occurred earlier than the host rock formation. A summary of dating methods is found below:

K-Ar, U-He It is appealing to use these standard radiochemical dating methods with noble-gas products to directly estimate the gas-retention age of the sample. However, there are a number of concerns with this method:

- Lighter noble gasses undergo faster thermal diffusion, which may lead to an underestimate of the gas-retention age for xenon.
- Inclusion of excess radiogenic ^{40}Ar from precursor materials may lead to an overestimate of the sample age.

Ref.	Year	Ore source	Ore age (10^6 y)	Dating Method	Result (10^{20} y)
[46]	1950	Boliden, Sweden	1500 ± 500	geology	14
[49]	1966	Oya, Japan	90.6 ± 2.9	K-Ar	8.20 ± 0.64
[50]	1967	Boliden, Sweden	1800	K-Ar, U-Xe	3.0 ± 0.4
[51]	1967	Boliden, Sweden	530 ± 10	K-Ar,U-He	6^{+6}_{-3}
[52]	1968	Good Hope Mine, Colorado	1310 ± 140	K-Ar	$21.8^{+7.0}_{-5.3}$
[53]	1968	Kirkland Lake, Ontario	1826 ± 36	Rb-Sr	20.3 ± 3.0
[54]	1972	Boliden, Sweden	1560	U-Xe	25.1
[55]	1972	Kalgoorlie, Australia	2460 ± 80	Rb-Sr	28.3 ± 3.0
[56]	1975	Kalgoorlie, Australia	2460 ± 80	Rb-Sr	10.
[57]	1983	Good Hope Mine, Colorado	1310 ± 140	K-Ar	26.0 ± 2.8
[58]	1986	Boliden, Sweden	1800 ± 300	Se-Kr	$12.0 \pm 1.2^*$
[59]	1986	Boliden, Sweden	1560 ± 390	U-Xe	10.1 ± 2.9
[59]	1986	Good Hope Mine, Colorado	1310 ± 140	K-Ar	20.0 ± 2.5
[59]	1986	Kirkland Lake, Ontario	1830 ± 40	Rb-Sr	18.8 ± 2.8
[59]	1986	Kirkland Lake, Ontario	1830 ± 40	Rb-Sr	12.3 ± 2.2
[59]	1986	Mattagami Lake, Quebec	2750 ± 50	Pb-Pb	22.7 ± 0.8
[60]	1986	Kuusamo, Finland	2000	Se-Kr	$7.0 \pm 1.0^*$
[61]	1988	Kuusamo, Finland	1095 ± 10	U-Xe	7.5 ± 0.3
[62]	1992	American Mine, Colorado	1660	Pb-Pb	32
[62]	1992	Good Hope Mine, Colorado	1600	Pb-Pb	28
[62]	1992	Vulcan Mine, Colorado	1610	Pb-Pb	28
[62]	1992	Mattagami Lake, Quebec	2670	Pb-Pb	26
[43]	1993	Kalgoorlie, Australia	750	Pb-Pb	3.3
[43]	1993	Cripple Creek, Colorado	28	geology	9.4
[43]	1993	Cripple Creek, Colorado	28	geology	9.1
[63]	1996	Oya, Japan	93 ± 11	K-Ar	7.9 ± 1.0
[64]	1996	Suwa Mine, Japan	105	K-Ar	8.6
[65]	2008	Kochbulak, Uzbekistan	260–285	K-Ar	6.8 ± 0.8

Table 1.3: Summary of geochemical experiments to determine the $\beta\beta$ half-life of ^{130}Te. This table is an updated version of that found in [38]. *Calculated using current best value for the ^{82}Se half-life ($T^{^{82}\mathrm{Se}}_{1/2} = 9.6 \times 10^{19}$) [66].

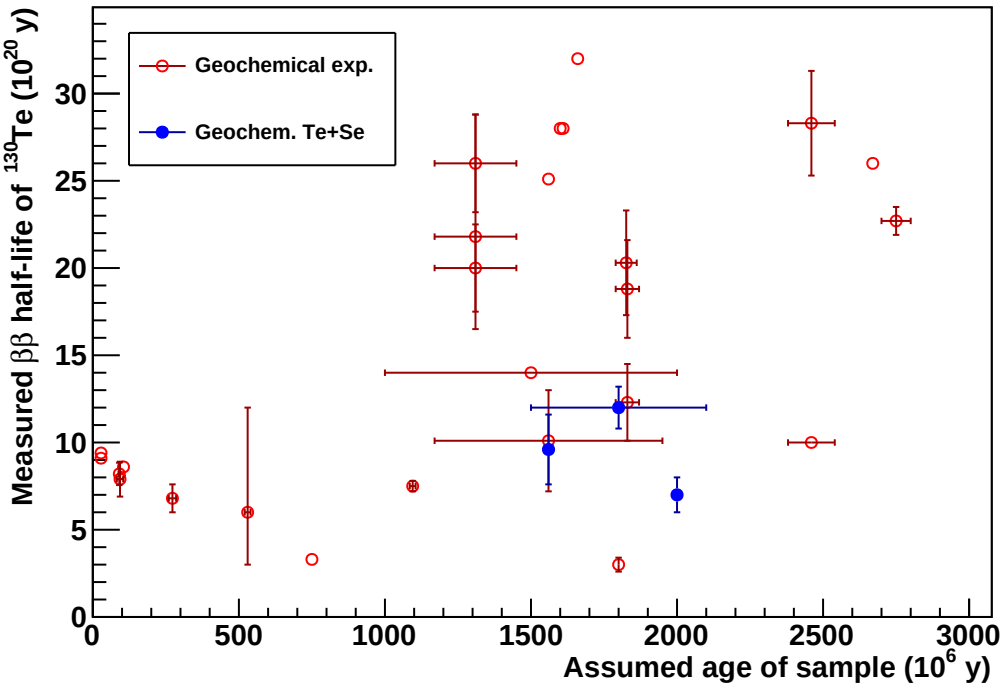

Figure 1.9: Graphical representation of geochemical measurements of the ^{130}Te $\beta\beta$ half-life. The red open circles represent the experiments presented in Table 1.3, and the blue solid circles correspond to measurements of the ratio of the $\beta\beta$ half-life of ^{82}Se to ^{130}Te (Table 1.4). These measurements may be more reliable than other geochemical experiments because the gas retention age of the sample should cancel.

Ref.	Year	Mineral	Source	Ratio ($T_{1/2}^{130\mathrm{Te}}/T_{1/2}^{82\mathrm{Se}}$)	$T_{1/2}^{130\mathrm{Te}}$ (10^{20} y)
[70]	1973	Tellurobismuthite (Bi_2Te_3)	Boliden, Sweden	10 ± 2	9.6 ± 2.0
[58]	1986	Selenokobellite $Pb_2(Bi,Sb)_2(S,Se)_5$	Boliden, Sweden	12.5 ± 0.9	12.0 ± 1.2
[60]	1986	kitkaite (NiTeSe)	Kuusamo, Finland	7.3 ± 0.9	7.0 ± 1.0

Table 1.4: Measurements on ores containing both Te and Se. (The selenokobellite sample was measured to contain 4910 ± 200 ppm of Te; the tellurobismuthite samples contained between 1.15% and 1.55% selenium.) The value of $T_{1/2}^{130\mathrm{Te}}$ was calculated by multiplying the half-life ratio by the current experimental best value for the ^{82}Se half-life ($T_{1/2}^{82\mathrm{Se}} = (9.6 \pm 0.7) \times 10^{19}$) [66].

- The Te-rich minerals under study are often highly depleted in K and U, making noble-gas age determinations difficult and unreliable.
- A number of experiments ([52], [54]) have found inconsistent results between different noble gas ages (K-Ar, U-He, U-Xe) of the same sample.

U-Xe In principle, measuring the accumulated fission Xe could directly test the Xe-retention age of the sample. However, U is often found in inclusions within Te mineral. Stepwise heating experiments [69] have indicated that these U-bearing inclusions may have better gas-retention properties than their host mineral, which could lead to an overestimate of the gas retention age for $\beta\beta$-Xe.

Se-Kr A few experiments have been performed on minerals containing both Se and Te, which allows the use of the ^{82}Se $\beta\beta$ half-life of $\approx 9.6 \times 10^{19}$ y (relatively well known from laboratory experiments [66]) to establish the gas-retention age of the material. Since both Kr and Xe are heavy noble gasses, they should have similar diffusion properties, and this method is likely to be the most accurate of the dating methods here discussed. The experiments performed on minerals containing both Se and Te are summarized in Table 1.4. Their results favor a shorter half-life for ^{130}Te.

Non-noble-gas dating (Pb-Pb, Rb-Sr) Other radiochemical dating methods have been used to establish the age of some samples. However, these methods cannot determine the onset of gas retention, and so may be treated as upper limits on the Xe accumulation time.

An additional uncertainty stems from the possibility of inclusion of "parentless" ^{130}Xe if Te minerals formed from a previous generation of Te ores. This could lead to an un-

$\beta\beta$ Decay Reaction	$T^{2\nu}_{1/2}$ (y)
^{48}Ca$\rightarrow^{48}$Ti	$(4.4^{+0.6}_{-0.5}) \times 10^{19}$
^{76}Ge$\rightarrow^{76}$Se	$(1.5 \pm 0.1) \times 10^{21}$
^{82}Se$\rightarrow^{82}$Kr	$(9.2 \pm 0.7) \times 10^{19}$
^{96}Zr$\rightarrow^{96}$Mo	$(2.3 \pm 0.2) \times 10^{19}$
^{100}Mo$\rightarrow^{100}$Ru	$(7.1 \pm 0.4) \times 10^{18}$
^{116}Cd$\rightarrow^{116}$Sn	$(2.8 \pm 0.2) \times 10^{19}$
^{130}Te$\rightarrow^{130}$Xe	$(8.6 \pm 0.8) \times 10^{20}$
^{150}Nd$\rightarrow^{150}$Sm	$(8.2 \pm 0.9) \times 10^{18}$

Table 1.5: $2\nu\beta\beta$ half-lives obtained from direct-detection experiments. Quoted values are weighted averages of positive experimental results taken from [73], except for ^{130}Te, which is a weighted average including the results of this work (see Sect. 5.1).

derestimation of the half-life for $\beta\beta$ decay. Furthermore, although its large atomic radius strongly inhibits thermal diffusion of Xe from Te minerals at "ordinary" temperatures, a recent experiment by Meshik *et al.* [69] showed that even mild heating (200-300° C) of native Te may cause rapid diffusive loss of trapped Xe. This means that a mild geothermal event could effectively reset the Te-Xe clock, without changing the apparent age as determined by Pb-Pb, Rb-Sr, or noble-gas dating performed on host rock samples.

Due to these complications, there is a large systematic uncertainty on the geochemical half-life evaluations which is not well reflected in the quoted uncertainties in Table 1.3. Ultimately, these uncertainties must be resolved by laboratory experiments, which are the topic of the next section.

1.3.2 Direct detection experiments

Unlike geochemical experiments, direct detection experiments have the ability to distinguish between the 0ν and 2ν modes of $\beta\beta$ decay; therefore, experimental half-life results for the two modes are reported separately. Aside from one controversial claim in ^{76}Ge ([71], [72]), $0\nu\beta\beta$ has never been experimentally observed. On the other hand, $2\nu\beta\beta$ has been observed for various isotopes in a number of laboratory experiments (Table 1.5).

The current best limit on $0\nu\beta\beta$ in ^{130}Te comes from the CUORICINO experiment [74], described in Chapter 2. The energy spectrum in the region near the $\beta\beta$ Q value is shown in Fig. 1.10. A best-fit to the data yields a negative decay rate of $\Gamma = (-0.2 \pm 1.4[stat] \pm 0.3[syst]) \times 10^{-25}\,\mathrm{y}^{-1}$, which corresponds to a lower limit on the half-life of $T^{0\nu}_{1/2} > 2.8 \times 10^{24}$ y (90% C.L.).

The first direct observation of the $2\nu\beta\beta$ in ^{130}Te was made by researchers from Milan in a cryogenic bolometer experiment that was the precursor to CUORICINO. The experimental setup was very similar to that of CUORICINO; in fact, the two experiments used the same set of enriched crystals.

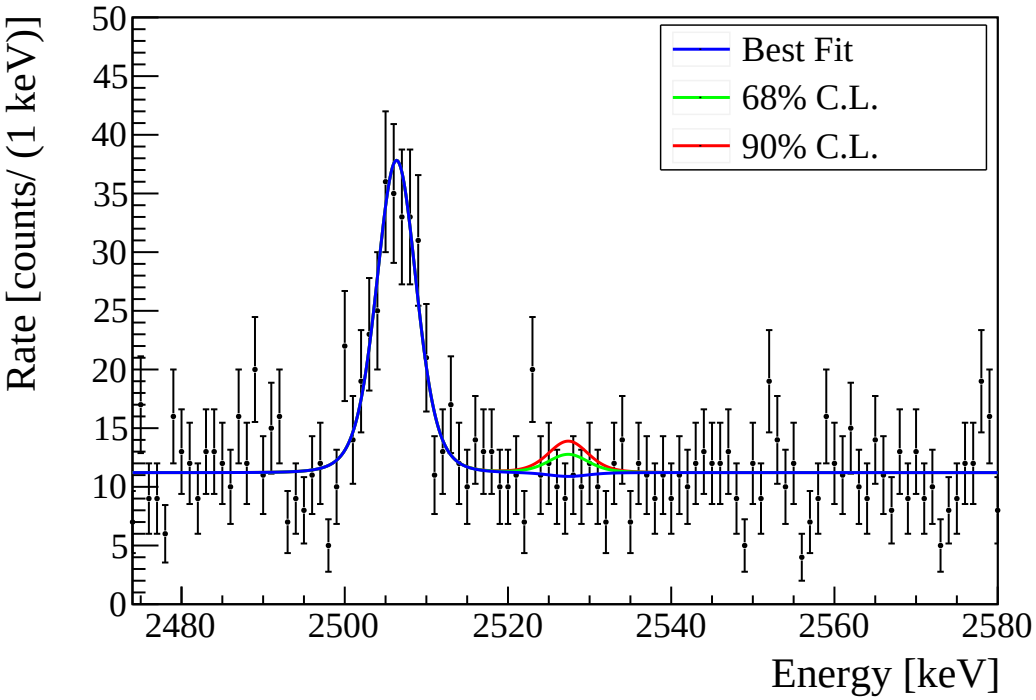

Figure 1.10: Fit of the CUORICINO energy spectrum for $0\nu\beta\beta$. [74].

The basic idea of the experiment was to record the energy spectrum of events in two pairs of crystals: one pair enriched in ^{130}Te and the other in ^{128}Te. Because the $2\nu\beta\beta$ rate of ^{128}Te is about four orders of magnitude smaller than that of ^{130}Te, the energy spectrum from the crystals enriched in ^{128}Te should have a negligible contribution from $2\nu\beta\beta$ and could be used as a "blank" for background subtraction. Unfortunately, this subtraction did not work perfectly, and there were residual background peaks observed in the subtracted spectrum that were attributed to a non-uniform distribution of radioactive contaminants in the detector or surrounding materials. In particular, evidence was found for non-uniform backgrounds from ^{40}K, which was believed to be located on copper surfaces near the detector, and contaminations of ^{238}U and ^{232}Th on the crystal surfaces. Monte-Carlo simulations were performed to determine the maximum possible contribution of these backgrounds to the $2\nu\beta\beta$ signal; this is the origin of the large systematic error on the measurement. The experiment obtained a measured half-life value of $T^{2\nu}_{1/2} = 6.1 \pm 1.4(\text{stat.})^{+2.9}_{-3.5}(\text{sys.}) \times 10^{20}$ y [75], from the background-subtracted spectrum shown in Fig. 1.11.

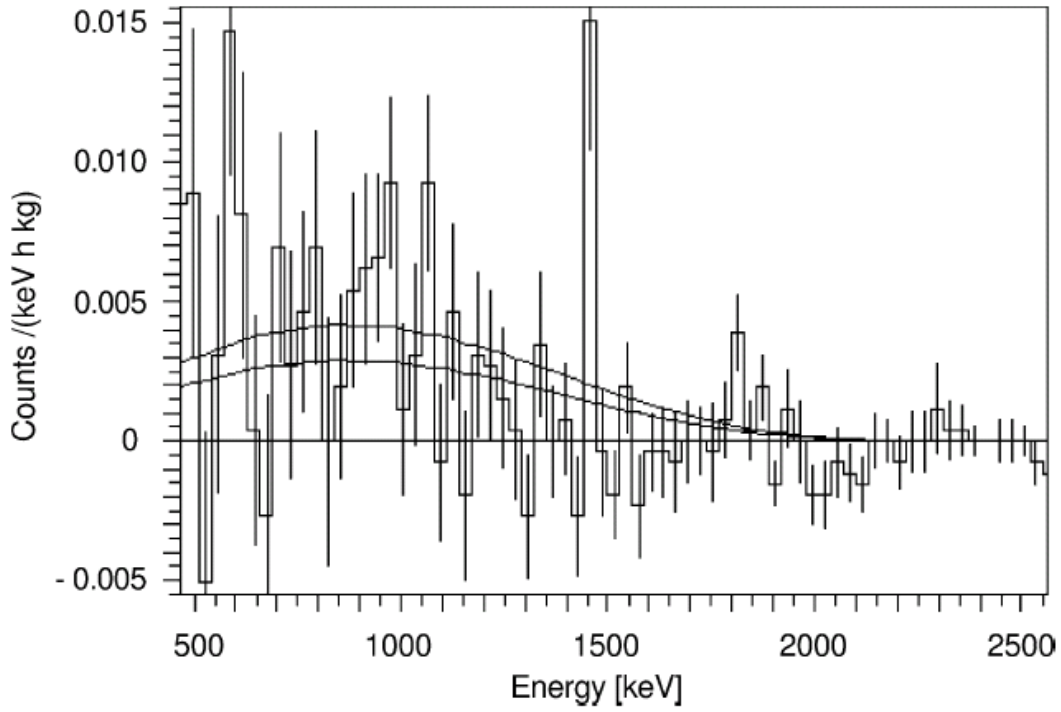

Figure 1.11: Results of a previous $\beta\beta$ experiment using cryogenic TeO_2 bolometers [75].

The only other experiment that has measured the $2\nu\beta\beta$ rate in ^{130}Te is the NEMO-3 experiment. NEMO-3 uses interchangeable source foils so that it can study many different $\beta\beta$ emitters. Three foils were used for the ^{130}Te $\beta\beta$ measurement recently reported in [76]:

one Te foil enriched to $89.4 \pm 0.5\%$ in ^{130}Te, a $^{\mathrm{nat}}$Te foil, and a very pure Cu foil. The $2\nu\beta\beta$ rate was computed using data from the enriched foil; the other two foils were used to validate the background model.

The NEMO-3 detector has both a wire-chamber tracking volume and a plastic scintillator calorimeter, which allow $\beta\beta$ events to be identified by requiring two electron-like tracks originating within a certain distance of each other in the foil and each depositing a minimum amount of energy in the calorimeter. These cuts help to reduce the background, but do not eliminate it completely. Radioactive contaminants in the foils, the tracking volume, and external to the tracking volume can all produce events which mimic the $\beta\beta$ signal in the detector. A Monte-Carlo simulation was used to extrapolate the $\beta\beta$ background rate from the measured single-β events in the detector. The resulting summed electron energy spectrum is shown in Fig. 1.12, yielding a measured half-life of $T^{2\nu}_{1/2} = (7.0 \pm 0.9(\mathrm{stat}) \pm 1.1(\mathrm{syst})) \times 10^{20}$ y.

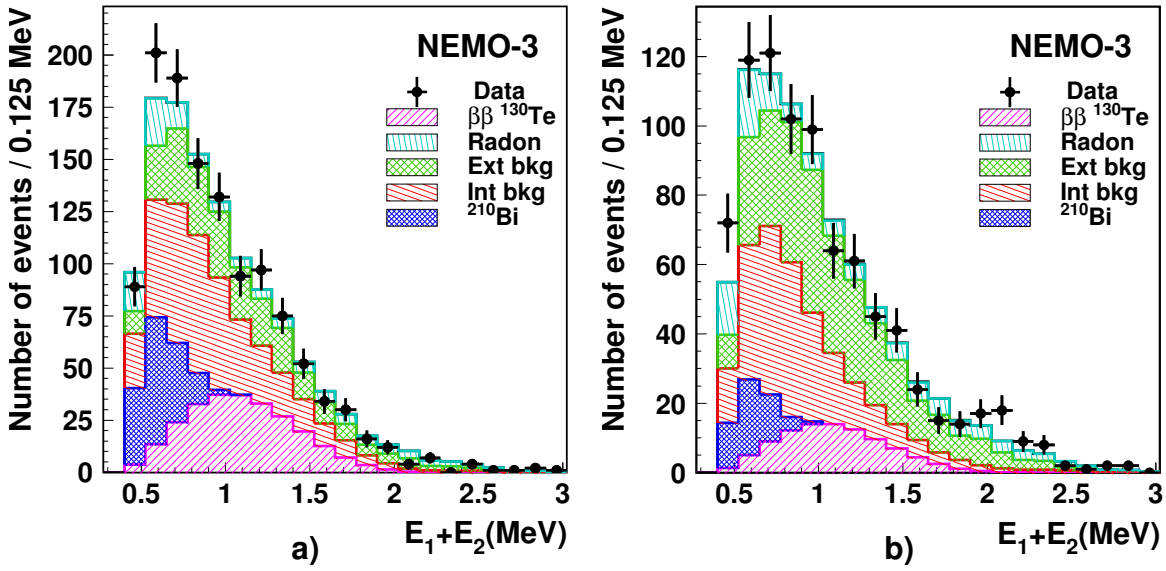

(a) Source foil enriched in ^{130}Te.

(b) Natural Te source.

Figure 1.12: Summed electron energy spectrum from the NEMO-3 experiment [76].

Chapter 2

The CUORICINO experiment

CUORICINO was a bolometric $0\nu\beta\beta$ experiment which ran at Gran Sasso National Laboratory (LNGS) in Italy from February 2003 to May 2008. CUORICINO was intended as a prototype detector for the Cryogenic Underground Observatory for Rare Events (CUORE), but was also a sensitive physics experiment on its own. Although the primary aim of CUORICINO was to search for $0\nu\beta\beta$ of ^{130}Te, the detector was also used to search for other kinds of rare events, such as dark matter interactions, $2\nu\beta\beta$, and other rare nuclear processes ([77], [78]).

2.1 CUORICINO bolometers

A bolometer is a type of particle detector that measures the energy deposited by incident radiation based on the temperature change of the detector. A bolometer generically consists of three parts: an absorber, a temperature sensor, and a weak thermal link connecting the absorber to a thermal reservoir (Fig. 2.1). A particle striking the absorber will raise its temperature by an amount ΔT, given to a good approximation by

$$\Delta T = \Delta E/C \tag{2.1}$$

where ΔE is the energy deposited and C is the heat capacity of the absorber. For a single-particle energy deposition, this temperature rise is large enough to be measured only when the heat capacity is extremely small. For dielectric, diamagnetic crystals such as those used in CUORICINO, such small heat capacities can be obtained by operating at low temperatures, for which the heat capacity is given by the Debye T^3 law [79]:

$$C = \frac{12\pi^4}{5}\frac{m}{M}N_A k_B \left(\frac{T}{\theta_D}\right)^3, \tag{2.2}$$

where m is the mass of the crystal, M is the molar mass, T is the operating temperature, and θ_D is the Debye temperature, which depends on the material.

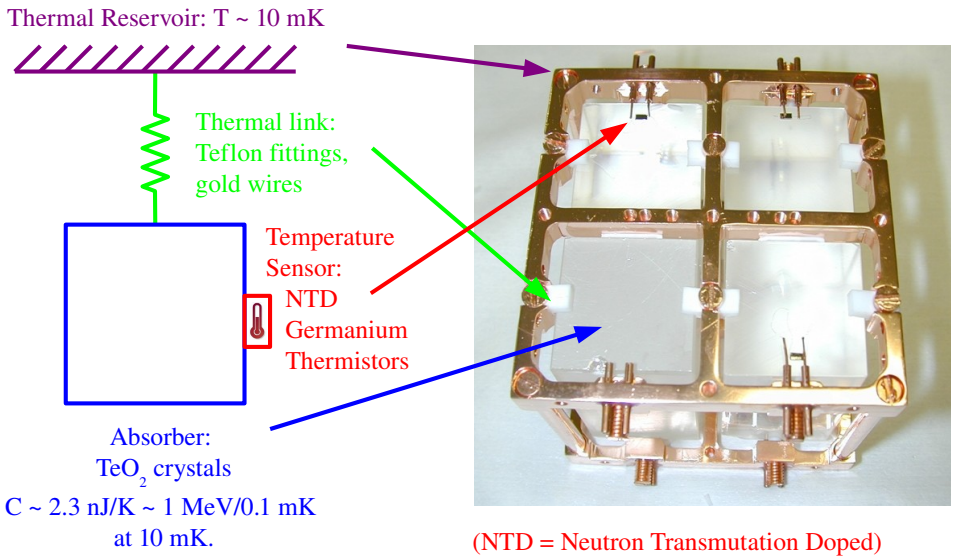

Figure 2.1: Conceptual diagram of a bolometer (left) and its implementation in CUORICINO (right).

In CUORICINO the temperature of the crystal was measured using sensitive thermistors, described in Sect. 2.1.2. As the heat produced by an energy deposition in the crystal dissipated through the weak thermal link, the temperature of the bolometer gradually returned to the baseline temperature of the thermal reservoir, resulting in a temperature pulse lasting on the order of a few seconds. The shape and duration of the recorded voltage pulse were determined by the characteristics of the thermistor and electronics as well as the thermal conductances and heat capacities of the various detector components. A typical pulse is shown in Fig. 2.2.

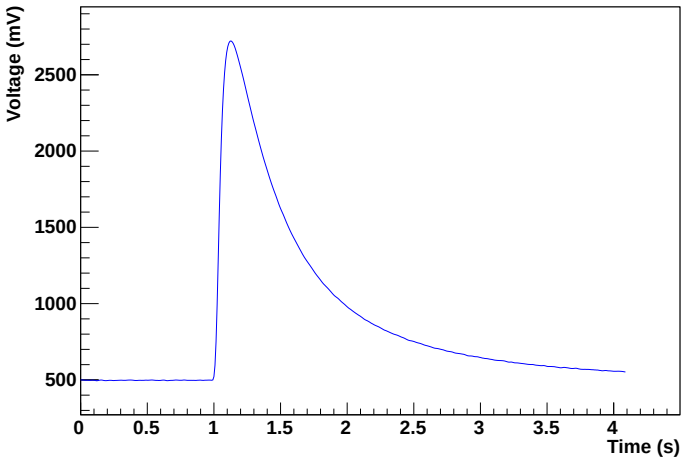

Figure 2.2: Typical voltage pulse produced by an energy deposition in a CUORICINO crystal.

2.1.1 Tellurite crystals

Each CUORICINO bolometer is made from a $5 \times 5 \times 5$ cm^3 or $3 \times 3 \times 6$ cm^3 TeO_2 crystal which functions as the absorber. As a particle enters the crystal, its energy is converted to phonons via interactions with nuclei or electrons in the crystal. Statistical fluctuations in the number of phonons exchanged with the heat sink impose a limit on the achievable energy resolution of a bolometer. Since the average energy of a phonon is given by $\epsilon = k_B T$ and the thermal energy of the absorber is $E = C(T) \cdot T$, the number of phonons can be estimated as

$$N = \frac{E}{\epsilon} = \frac{C(T)T}{k_B T} = \frac{C(T)}{k_B} \tag{2.3}$$

Assuming Poisson statistics, the fluctuation of the number of photons is $\Delta N = \sqrt{N}$, so

$$\Delta E = \epsilon \Delta N = \sqrt{C(T) k_B T^2} \tag{2.4}$$

For typical CUORICINO operating conditions, this evaluates to $\Delta E \approx 10$ eV; however, in practice, the energy resolution is limited by other sources of noise, and is several orders of magnitude above this thermodynamic limit.

The thermal and mechanical properties of TeO_2 crystals are well-suited to use as bolometers. The Debye temperature of TeO_2 is relatively high ($\theta_D = 232$ K [80]), resulting in a heat capacity on the order of 1 MeV/0.1 mK (1.6×10^{-9} J/K) at typical operating temperatures of around 10 mK. Additionally, the crystals are able to undergo repeated thermal cycling with no degradation of their performance as bolometers. Their thermal expansion coefficient is well matched with that of copper, which can therefore be used for the mechanical support structure without applying excessive force to the crystals during cooling.

The crystals used for CUORICINO were produced at the Shanghai Institute of Ceramics, Chinese Academy of Sciences (SICCAS), following the procedure outlined in [81]. The crystals must be free of defects and contaminations, both in order to ensure their proper functioning as bolometers and to reduce radioactive backgrounds for the $\beta\beta$ measurement. Strict radiopurity standards were adhered to for both the crystal raw materials and the ancillary materials used in production and handling of the crystals, such as chemical reagents, polishing powder, and plastic bags. More information about the properties and production of TeO_2 crystals can be found in [82]

2.1.2 Thermistors

The temperature sensors used in CUORICINO are Neutron Transmutation Doped (NTD) germanium thermistors. Neutron transmutation doping with reactor neutrons is a way to reproducibly and uniformly dope germanium wafers to the desired level, near but below the metal-insulator transition. When exposed to a flux of thermal neutrons from a nuclear reactor, natural germanium isotopes transform into unstable isotopes via neutron capture, which subsequently decay into dopants [83], as shown in Fig. 2.3. The relevant reactions are:

$$\begin{aligned} {}^{70}\mathrm{Ge}\,(21\%) + n &\rightarrow {}^{71}\mathrm{Ge} \\ {}^{71}\mathrm{Ge} &\rightarrow {}^{71}\mathrm{Ga}\,(\text{Acceptor}) \end{aligned} \tag{2.5}$$

$$\begin{aligned} {}^{74}\mathrm{Ge}\,(36\%) + n &\rightarrow {}^{75}\mathrm{Ge} \\ {}^{75}\mathrm{Ge} &\rightarrow {}^{75}\mathrm{As}\,(\text{Donor}) \end{aligned} \tag{2.6}$$

$$\begin{aligned} {}^{76}\mathrm{Ge}\,(7.4\%) + n &\rightarrow {}^{77}\mathrm{Ge} \\ {}^{77}\mathrm{Ge} &\rightarrow {}^{77}\mathrm{As} \\ {}^{77}\mathrm{As} &\rightarrow {}^{77}\mathrm{Se}\,(\text{Double donor}) \end{aligned} \tag{2.7}$$

The germanium irradiation for CUORICINO was performed at the University of Missouri Research Reactor (MURR). After a waiting period of at least six months for the activation products to decay, the germanium wafers were cut into $3 \times 3 \times 1$ mm pieces and made into thermistors.

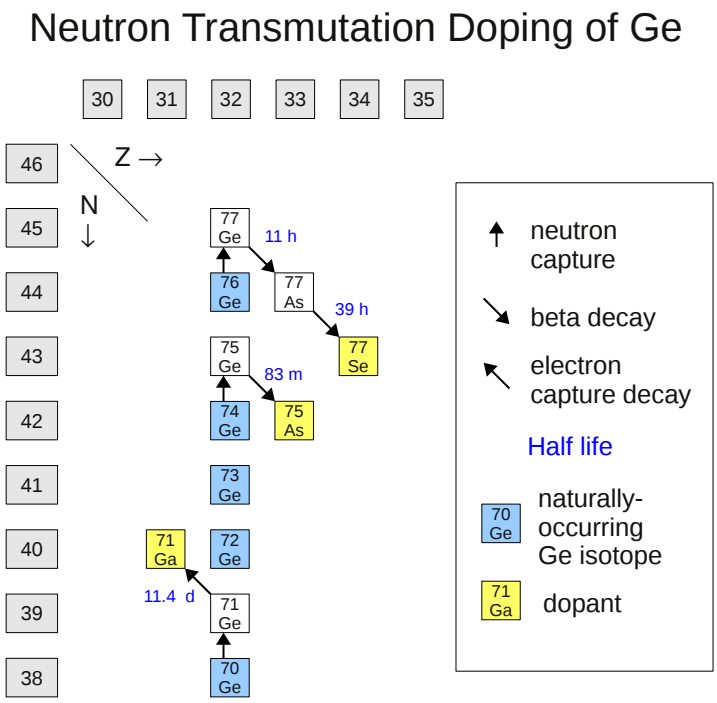

Figure 2.3: Reactions involved in neutron transmutation doping of germanium.

In NTD germanium thermistors, conduction occurs when electrons tunnel, or "hop" between dopant atoms by absorbing or emitting the energy difference via phonons. At low temperatures, because there are fewer high energy phonons available, electrons may have to tunnel a long distance to find an unoccupied site with an energy near that of an available phonon. This is called the "variable range hopping" regime [84], and the resistance of the thermistors in this regime is given as a function of temperature (T) by:

$$R(T) = R_0 \exp\left(\frac{T_0}{T}\right)^p, \tag{2.8}$$

where $p = 1/2$ and R_0 and T_0 are experimentally determined parameters which depend on the doping level, the properties of the Ge lattice, and the stresses applied to the sample. For CUORICINO thermistors, the operating resistance is on the order of 100 MΩ at 10 mK.

The thermistors were attached to the crystals using nine 0.5 mm diameter spots of Araldit Rapid epoxy, arranged in a 3×3 grid, which provided a thermal link between the thermistor and the crystal. Using glue spots rather than a continuous film of glue reduces the strain due to thermal contraction, which can change the resistance of the thermistors and degrade their performance. Electrical connections to the thermistors were made via 50 μm diameter gold wires which were bonded to metallic contacts on the thermistors.

2.1.3 Resistive heaters

In addition to the NTD thermistor, an extremely temperature-stable silicon resistor with a resistance of ∼50–100 kΩ was glued to each CUORICINO TeO_2 crystal. These resistors were used as joule heaters to inject a fixed amount of energy into the detectors at regular (∼305 s) intervals as a way to monitor variations in the gain [85]. An ultra-stable pulser was used to apply short-duration voltage pulses to the heaters. The pulses had a much shorter duration than the response time of the bolometers, simulating the nearly instantaneous energy deposition due to a particle interaction in the crystal. These heater pulses were then used in the offline analysis to correct for changes in the gain due to temperature drifts, as described in Sect. 3.2.

2.2 The CUORICINO detector

The individual bolometer units described in the previous section were arranged in modules of four or nine crystals, which were then stacked to form a tower, as shown in Fig. 2.4. The detector tower contained 44 ($5 \times 5 \times 5$) cm^3 "large" crystals and 18 ($3 \times 3 \times 6$) cm^3 "small" crystals, for a total of 62 bolometers with a total active mass of 40.7 kg of TeO_2. Two of the small crystals were enriched to ∼82% in ^{128}Te and another two were enriched to ∼75% in ^{130}Te. These four enriched crystals were used for the $2\nu\beta\beta$ measurement which is the topic of this thesis.

The TeO_2 crystals were supported by frames made of oxygen-free high conductivity (OFHC) copper, which served both as a mechanical support structure and as a heat sink. OFHC copper was chosen for its low radioactivity and the fact that copper's thermal expansion coefficient is well-matched to that of TeO_2. The gold wires for the thermistors and heater resistors were connected to wiring on the outside of the tower via copper crimp connectors which were inserted into copper tubes glued into through-holes in the copper frames. In this way, the wires were thermally connected to, but electrically insulated from the copper frames. The crystals were also weakly thermally connected to the copper frames by Teflon fittings, which helped to hold the crystals firmly in place without applying too much strain during cooling.

All materials used in the CUORICINO detector were screened for radioactivity, and subjected to strict cleaning and handling procedures to avoid contamination. The detector was assembled in a cleanroom directly above the CUORICINO cryostat, in a glovebox flushed with clean N_2 to exclude radon.

2.2.1 Cryostat and shields

The CUORICINO tower was cooled to an operating temperature of $\sim$8 mK in a commercial dilution refrigerator manufactured by Oxford Instruments. The temperature of the tower was kept very stable by a heating element and an NTD thermistor glued to the copper frame and operated in a feedback loop, as described in [86].

The detector was enclosed in several layers of shielding, as shown in Fig. 2.5. From the inside out, the layers are as follows:

1. top Roman lead shield
2. 50 mK copper irradiation shield
3. 600 mK copper irradiation shield
4. Lateral and bottom Roman lead shield
5. Inner Vacuum Chamber (IVC) (4.2 K) vacuum-tight irradiation shield
6. Outer Vacuum Chamber (OVC)
7. 10 cm low-activity lateral lead shield (<20 Bq/kg in ^{210}Pb)
8. 10 cm standard lateral lead shield.
9. Plexiglas box (flushed with pure nitrogen to eliminate radon)
10. Lateral neutron shield (borated polyethylene, 10 cm minimum thickness)
11. Top external lead shield

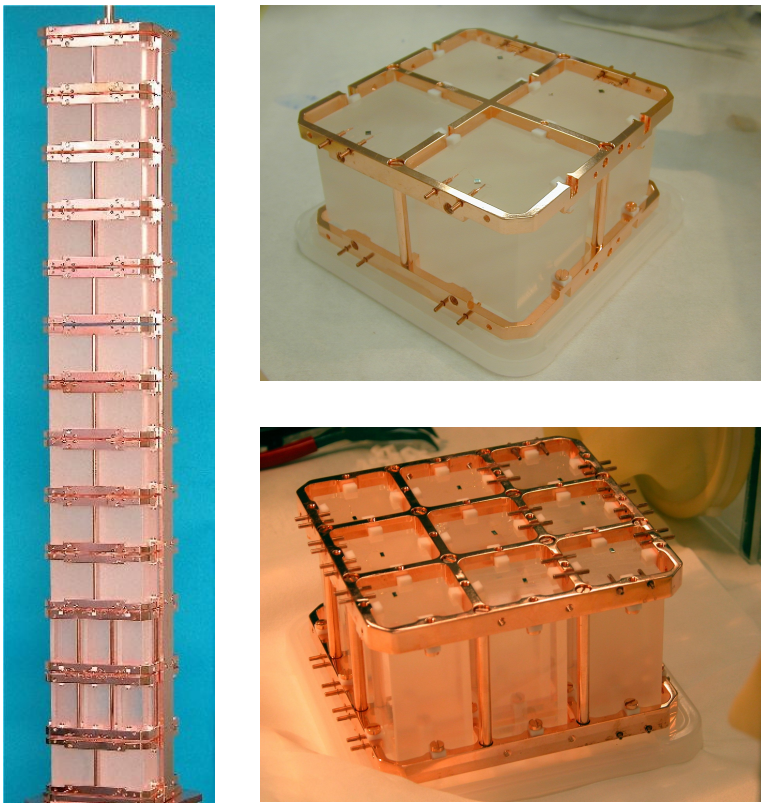

Figure 2.4: Left: Assembled CUORICINO tower. Right top: module of four $5 \times 5 \times 5$ cm^3 bolometers. Right bottom: module of nine $3 \times 3 \times 6$ cm^3 bolometers.

12. Faraday cage

Here, "Roman" lead refers lead recovered from an ancient Roman shipwreck. Because the time since the lead was separated from other elements is much longer than the 22.3 y half-life of ^{210}Pb, the resulting lead is extremely low-activity in ^{210}Pb (< 0.004 Bq/kg).

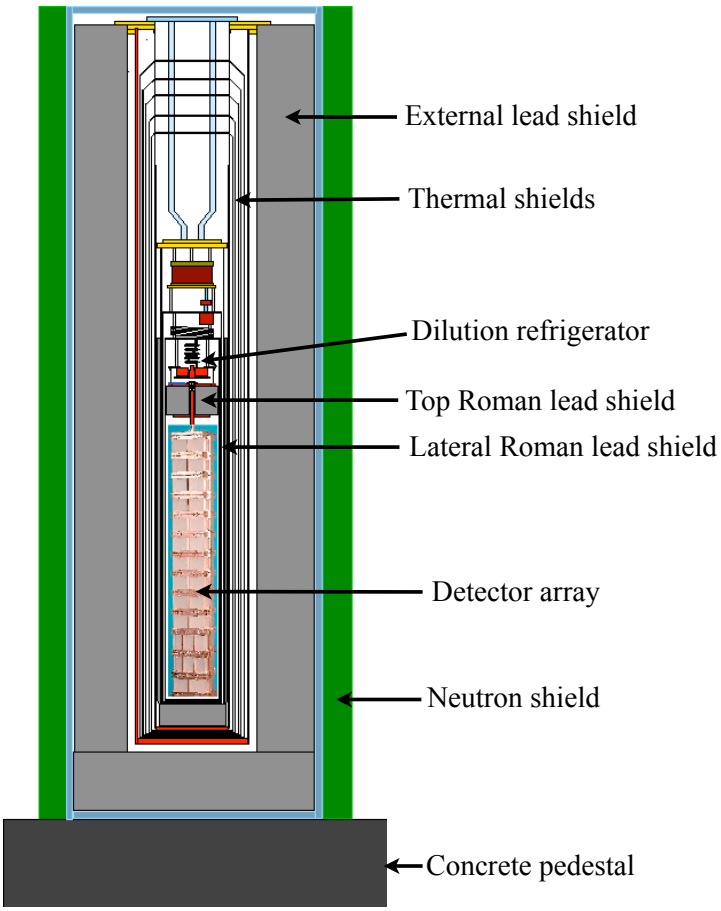

Figure 2.5: Layout of CUORICINO cryostat and shields.

2.2.2 Laboratory environment

The CUORICINO experiment was situated in Hall A of the Laboratori Nazionali del Gran Sasso (LNGS) in Italy (Fig. 2.6). The laboratory is located underneath the Gran Sasso mountain, at an average depth of approximately 3650 m.w.e., which corresponds to an effective vertical depth of 3100 m.w.e. relative to a flat overburden [87]. This overburden reduces the total muon flux to $\sim 2.6 \times 10^{-8}$ cm^{-2} s^{-1}.

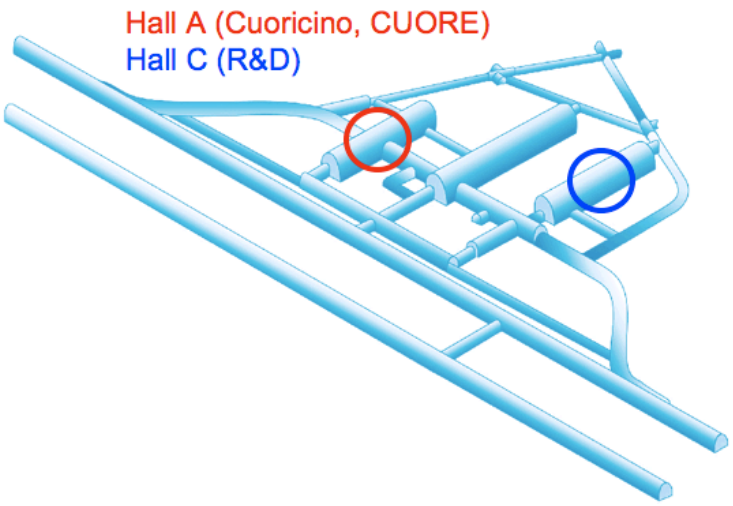

Figure 2.6: Location of CUORICINO in the LNGS underground facility.

Natural radioactivity in the rock walls is a potential source of background for experiments at LNGS. According to recent measurements [88], the gamma flux in hall A of LNGS is $\sim$0.3 cm^{-2} s^{-1}. The neutron flux in the laboratory is $\sim 4 \times 10^{-6}$ cm^{-2} s^{-1}, primarily due to spontaneous fission and (α,n) reactions ([89], [90], [91]). In addition, radon emanating from the rock can cause elevated backgrounds in the detector. For this reason, the detector was enclosed in a Plexiglas box which was continually flushed with boil-off N_2 while the detector was running.

2.2.3 Electronics and DAQ

The readout electronics for CUORICINO performed three basic functions: thermistor biasing, signal amplification, and filtering. The thermistor biasing circuit is shown in Fig. 2.7. Two load resistors with a total resistance R_L were placed symmetrically in series with the thermistor ($R_{\rm Th}$). The load resistors were chosen to have $R_L \gg R_{\rm Th}$ so that an applied bias voltage $V_{\rm Bias}$ would produce an approximately constant current flowing through the thermistor, $I = V_{\rm Bias}/(R_L + R_{\rm Th}) \approx V_{\rm Bias}/R_L$. The voltage on the thermistor is then proportional to the thermistor resistance, which is a function of temperature:

$$V_{\rm Th}(T) = IR_{\rm Th}(T) \approx \left(\frac{V_{\rm Bias}}{R_L}\right) R_{\rm Th}(T). \tag{2.9}$$

The bias current heats the thermistor via joule heating and thereby changes its resistance in a phenomenon known as electrothermal feedback. For small values of the bias voltage, this effect is negligible, and the relationship between the bias current and the thermistor voltage is nearly linear. However, for larger values of the bias current, the $I - V$ curve begins to

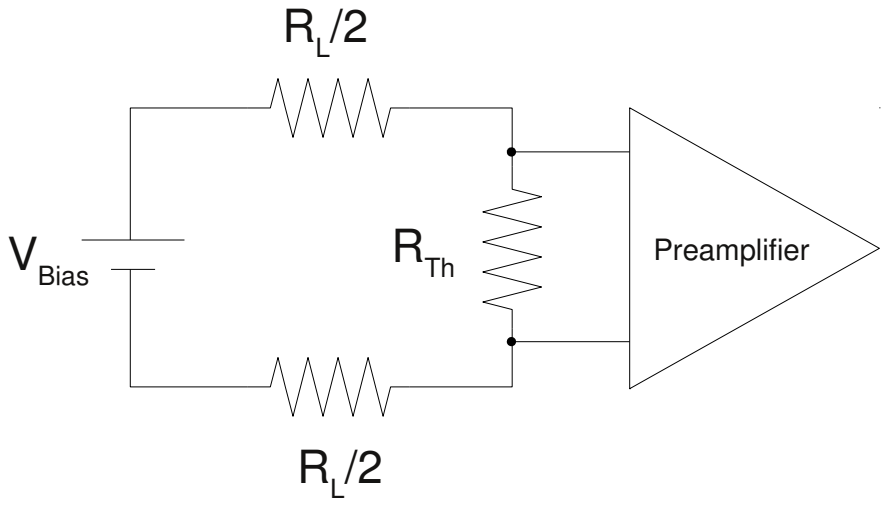

Figure 2.7: Circuit used for biasing of CUORICINO thermistors.

display non-ohmic behavior as the slope increases non-linearly and eventually reaches an inversion point, after which increasing the bias current actually decreases the voltage across the thermistor (Fig. 2.8). The optimal value of the bias voltage is that for which the signal to noise ratio is maximized. In practice, this is found by scanning through different values of the bias voltage and choosing the one which maximizes the signal pulse amplitude.

The voltage on the thermistor was sent to a preamplifier [92], which was at room temperature for most channels, but for some channels was attached to the 4 K plate of the dilution refrigerator, for the purpose of studying possible sources of noise. The signal then underwent a second stage of amplification with programmable gain, before being sent to a programmable 6-pole Bessel low-pass filter for anti-aliasing. The adjustable settings of the electronics, including bias voltage, amplifier gain, Bessel filter roll-off, and voltage offset, were remotely controllable and optimized for each bolometer [93]. The signal was digitized by a 16 bit ADC with a range of 0–10 V, with a sampling frequency of 125 Hz.

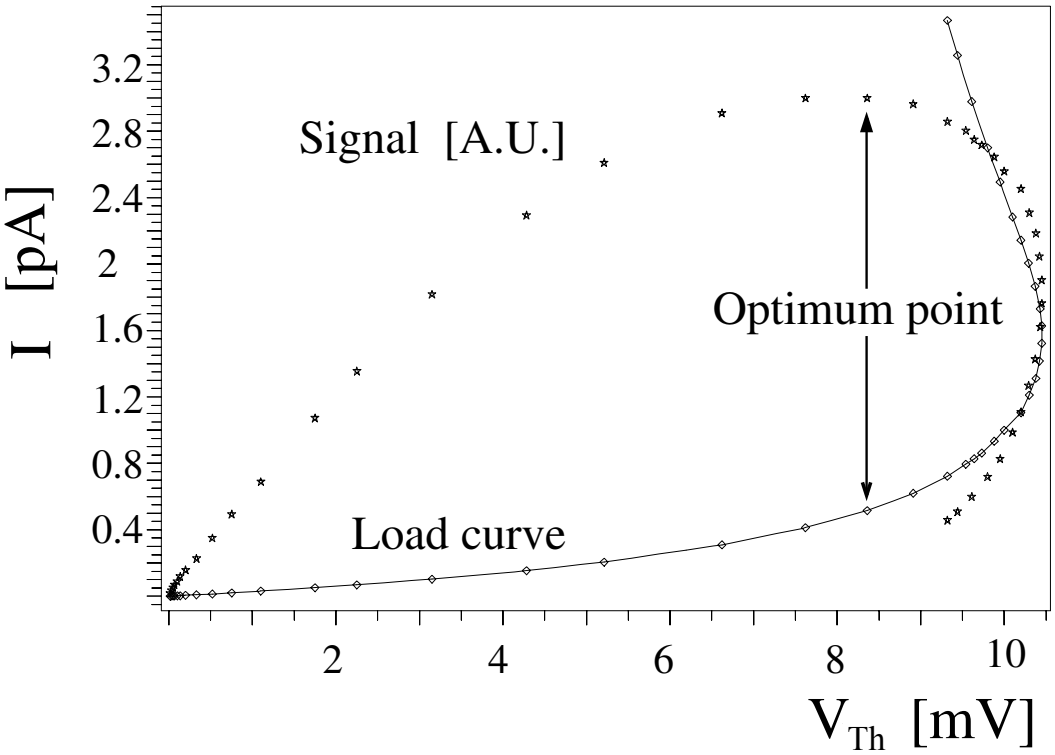

Figure 2.8: $I - V$ curve ("load curve") for a semiconductor thermistor, superimposed by a measurement of the signal pulse height (in arbitrary units) for different values of the bias voltage. The optimum point is the point for which the signal to noise ratio is maximized.

Chapter 3

First level data analysis and event reconstruction

The raw data for CUORICINO consist of measurements of the voltage on the thermistor of each bolometer, digitized and and sampled every 8 ms by the CUORICINO DAQ. The DAQ software applied a threshold trigger to the data; a trigger was generated whenever the thermistor voltage exceeded a fixed threshold, set individually for each bolometer. The trigger thresholds were set to be as low as possible without generating an unreasonably high event rate due to noise fluctuations. The threshold voltage corresponds to 30–50 keV for most channels.

For each trigger, one event was written to disk. Each event contains 512 thermistor voltage samples encompassing the 4 second window from 1 second before to 3 seconds after the trigger fired. Additionally, the channel number, trigger time, and a unique event number were saved to the event.

The CUORICINO data are organized into runs, each lasting approximately one day, which are further organized into "datasets," each lasting approximately one month. A dataset is a group of runs which all have the same calibration. Ideally, a dataset consists of one or more initial calibration runs, followed by a series of ordinary runs, followed by one or more final calibration runs. The final calibration of one dataset may be used as the initial calibration of the next; therefore, calibration runs may belong to more than one dataset. Some datasets have only an initial or final calibration because the dataset was interrupted by problems with the cryostat or electronics.

The raw data were processed to compute useful quantities such as energy, pulse shape parameters, and coincidence information for each event. A custom C++ based analysis framework called Diana was used for this first-level data processing in CUORICINO. The Diana framework provides a standardized event class and data storage format, as well as a system for running analysis code in a modular fashion controlled by plain-text configuration files.

3.1 Amplitude evaluation

When a particle deposits energy in the detector, it produces a temperature pulse whose amplitude is proportional to the energy deposited. The simplest way to estimate the pulse amplitude is to take the maximum voltage of the pulse minus the baseline voltage from before the trigger fired. However, this method is extremely vulnerable to noise fluctuations, since it uses only one data point to find the maximum voltage, rather than using information from the entire pulse.

In order to reduce the vulnerability of the amplitude evaluation to noise, an optimum filter algorithm was used, based on the technique described in [94]. The filter weights each frequency component based on its signal to noise ratio in order minimize the effect of noise on the measurement.

This method is based on the assumption that the voltage pulse recorded in the detector can be expressed as

$$V(t) = b + a \cdot s(t - t_0) + n(t), \tag{3.1}$$

where a is the pulse amplitude, b is the baseline voltage of the detector, t_0 is the time of the pulse onset, $s(t)$ is the signal shape of a generic pulse, which is independent of the pulse amplitude, and $n(t)$ is stochastic noise. The assumption that the pulse shape is independent of amplitude is not exactly true, but is a good approximation. Deviations from this ideal behavior are compensated by nonlinearity in the calibration function, described in Sect. 3.3.

The baseline b is obtained by averaging the voltage samples in the $\sim$1 second pre-pulse interval. Additionally, the optimum filter algorithm requires as input:

1. The ideal signal shape, $s(t)$, which is obtained by performing a pointwise average of a large number of high-energy pulses which pass some basic pulse-shape selection cuts.

2. The average noise power spectrum, $N(\omega)$, obtained by averaging the power spectrum (squared magnitude of the Fourier transform) of many noise samples. The noise samples were acquired by a special "noise" trigger which fired at random times during the data acquisition, with the requirement that no physical triggers were present within the noise acquisition window.

The average pulse shape and average noise power spectrum are computed separately for each bolometer; representative examples are shown in Fig. 3.1. The transfer function of the optimum filter, $H(\omega)$, is constructed from the Fourier transform of the average pulse shape, $S(\omega)$, and the average noise power spectrum as follows:

$$H(\omega) = \frac{S^*(\omega)}{N(\omega)} e^{-i\omega t_M}, \tag{3.2}$$

where t_M is the time of the pulse maximum.

This filter effectively puts less weight on frequency components with a low signal-to-noise ratio and more weight on frequency components with a high signal-to-noise ratio. After the

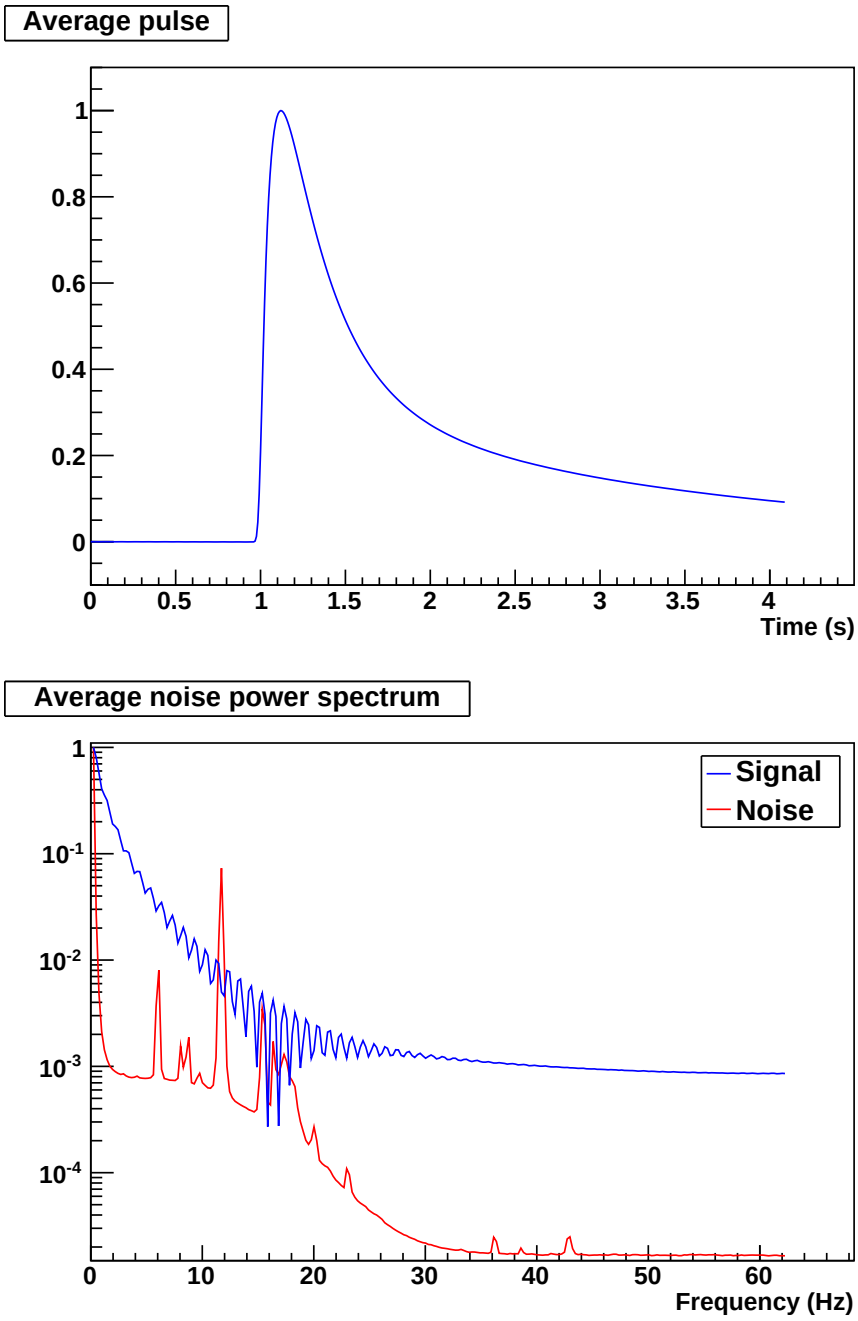

Figure 3.1: Top: Average pulse for CUORICINO Channel 1. Bottom: Average noise power spectrum (red) and Fourier transform of the average pulse (blue) for CUORICINO Channel 1, scaled to be equal at the lowest frequency.

acquired data sample is Fourier transformed and filtered, it is transformed back into the time domain (Fig. 3.2), where the maximum value of the optimum filter output corresponds to the pulse amplitude. In order to more precisely evaluate the maximum value, which may fall between discrete data samples, a parabolic interpolation is used, by analytically finding the maximum of a parabola which is constrained to pass through the maximum point of the optimum filter output and its nearest neighbor points to the right and left.

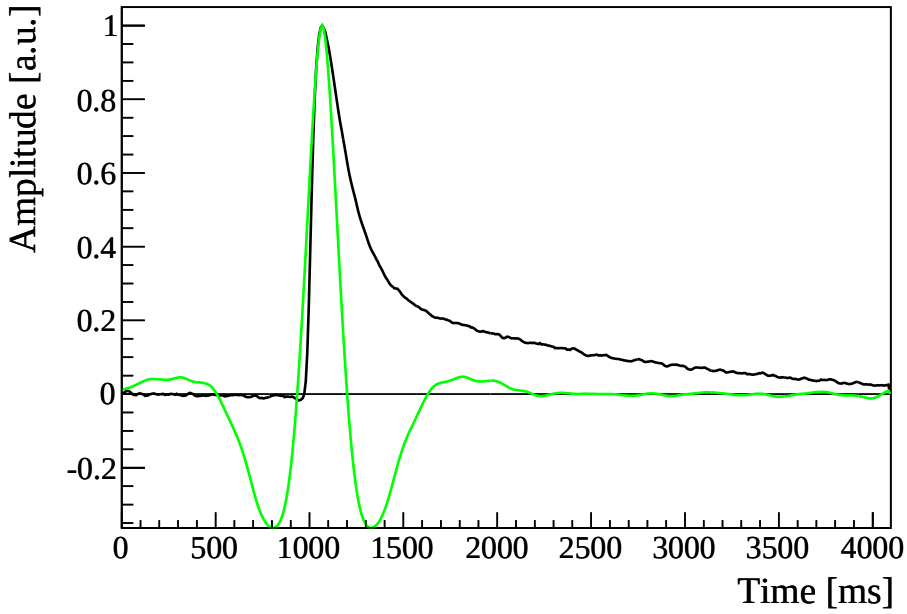

Figure 3.2: A typical CUORICINO pulse (black) and its optimum filter output in the time domain (green).

An alternative way of measuring the pulse amplitude is by summing over the frequency components of the optimum filter output in the frequency domain. This method will differ from the amplitude evaluation in the time domain for the case of a pulse which deviates from the ideal pulse shape. The frequency domain amplitude is therefore used in the pulse shape analysis described in Sect. 3.4.

3.2 Gain instability correction

The gain of a bolometric detector depends on the operating temperature, due to the temperature dependence of the thermistor response, crystal heat capacity, and thermal conductances between detector elements. In order to maintain an optimal energy resolution, it

is necessary to correct for this change in the gain as the temperature of the detector drifts over time [85].

The strategy used in CUORICINO was to inject pulses of fixed energy into the detectors using resistive heaters glued to the surface of each bolometer. A voltage pulse was applied to each heater at a regular interval of ∼305 seconds in order to monitor the variation in the gain and establish its dependence on temperature.

The baseline voltage in the pre-pulse interval (b) was taken as a measure of the temperature of the detector at the time of the pulse. The relationship between the heater amplitude (a_h) and the baseline voltage was empirically found to be quite linear, even over a large range of baselines. A linear fit to the scatter plot of a_h versus b was performed to determine the function $a_h(b)$ (Fig. 3.3(a)).

The temperature-dependent gain of the detector relates the measured amplitude of a heater pulse a_h to its energy, E_h, which is a constant:

$$a_h(b) = G(b)E_h. \tag{3.3}$$

The gain stabilization method relies on the assumption that the gain $G(b)$ is independent of the energy of the pulse, which is true to a good approximation (small deviations from this assumed behavior can be compensated by nonlinearity in the calibration function). Then the amplitude of an ordinary pulse in the detector is given by

$$a = G(b)E = a_h(b)\frac{E}{E_h}. \tag{3.4}$$

The ratio $a/a_h(b)$ should then be independent of the baseline and proportional to the energy of the event. The stabilized amplitude is defined as:

$$a_s = 5000 \cdot \left(\frac{a}{a_h(b)}\right). \tag{3.5}$$

The factor of 5000 is included for convenience, so that one unit of stabilized amplitude is on the order of 1 keV. The effect of the gain stabilization procedure is shown in Fig. 3.3(b).

In general, the stabilization fit is performed once for each run and channel. However, sometimes the amplitude versus baseline trend changes abruptly in the middle of the a run. In that case, the run may be broken into parts, each of which is stabilized separately. For this purpose, an algorithm developed by collaborator Adam Bryant was used, which employs a "brute force" method to determine whether and how to split the run into parts. The algorithm splits the run at every possible point and performs separate linear fits to the resulting segments; the split with the lowest summed square error from both fit lines is chosen as the best point to split the run. This procedure is repeated to find the optimal way to split the data into three or four sections, instead of just two. Next the algorithm estimates the error σ on each point by setting the χ^2 per degree of freedom equal to one for each scenario and choosing the minimum value of σ found, σ_{min}. Using this σ_{min} as the error on each point, the p-value for each scenario is computed, and the scenario is chosen with the minimum number of split points and a p-value greater than 1%. Figure 3.4 shows a CUORICINO run which was split into three parts for stabilization.

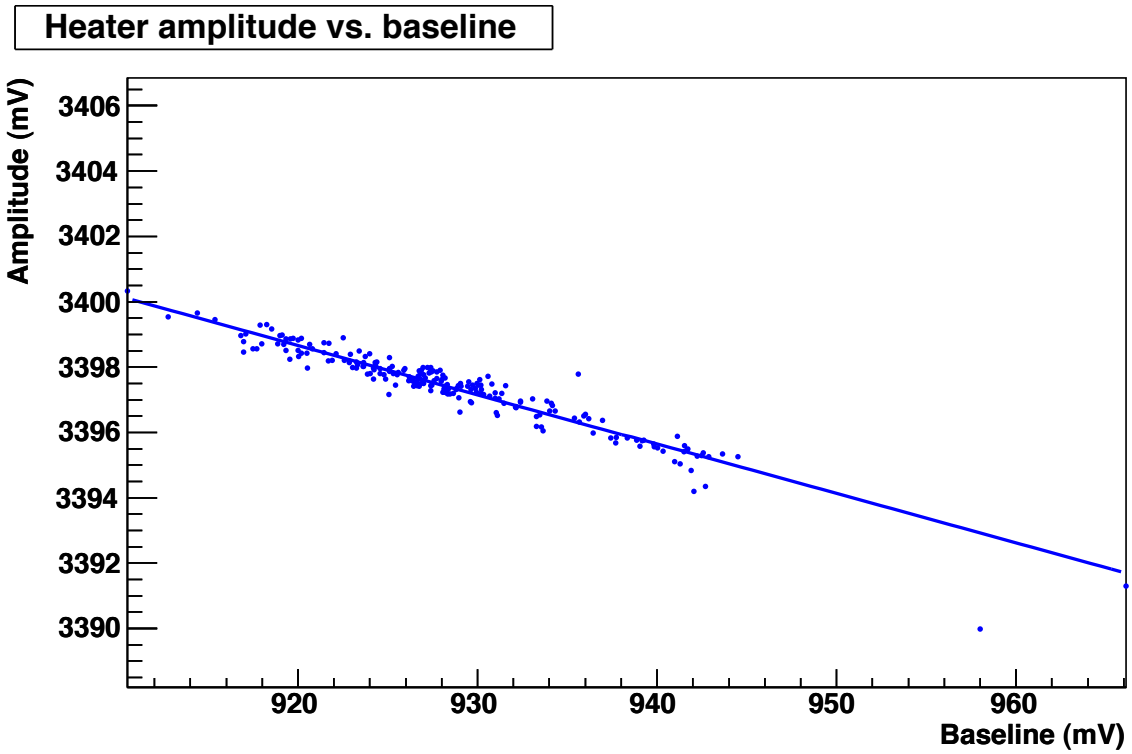

(a) Heater amplitude versus baseline voltage, with linear fit.

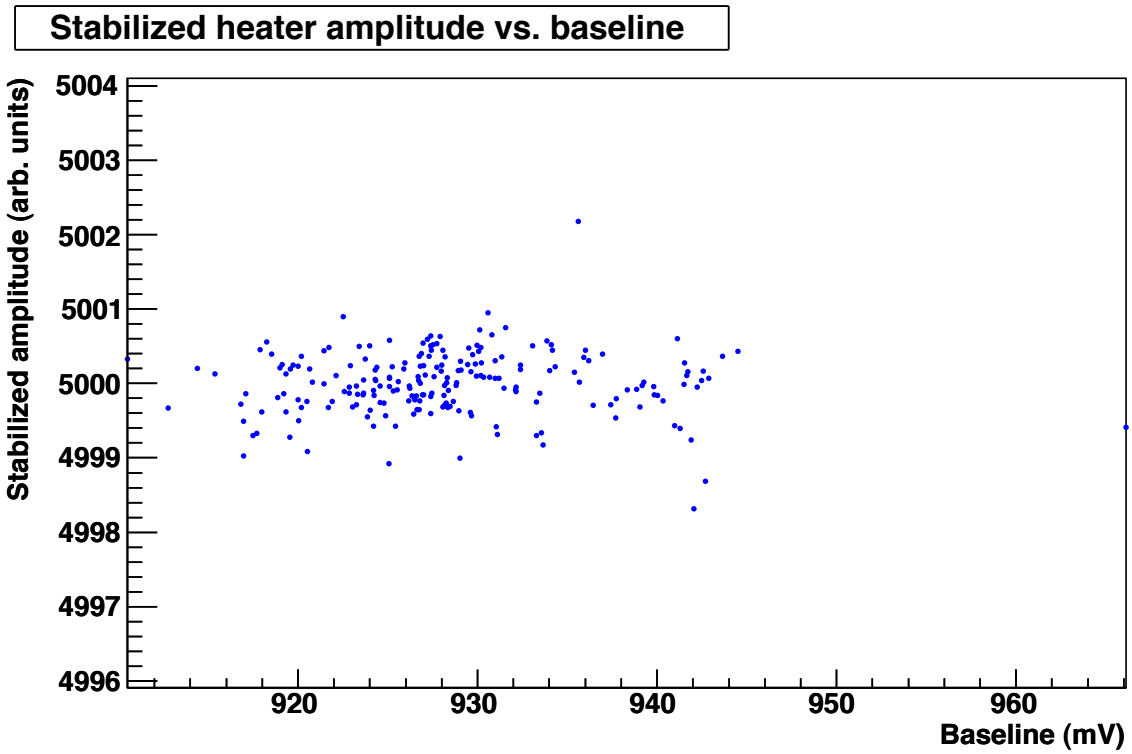

(b) Stabilized heater amplitude versus baseline voltage

Figure 3.3: Heater amplitude versus baseline, before and after the gain instability correction was applied. The data shown are from CUORICINO run 1214, channel 8. Figure from Adam Bryant.

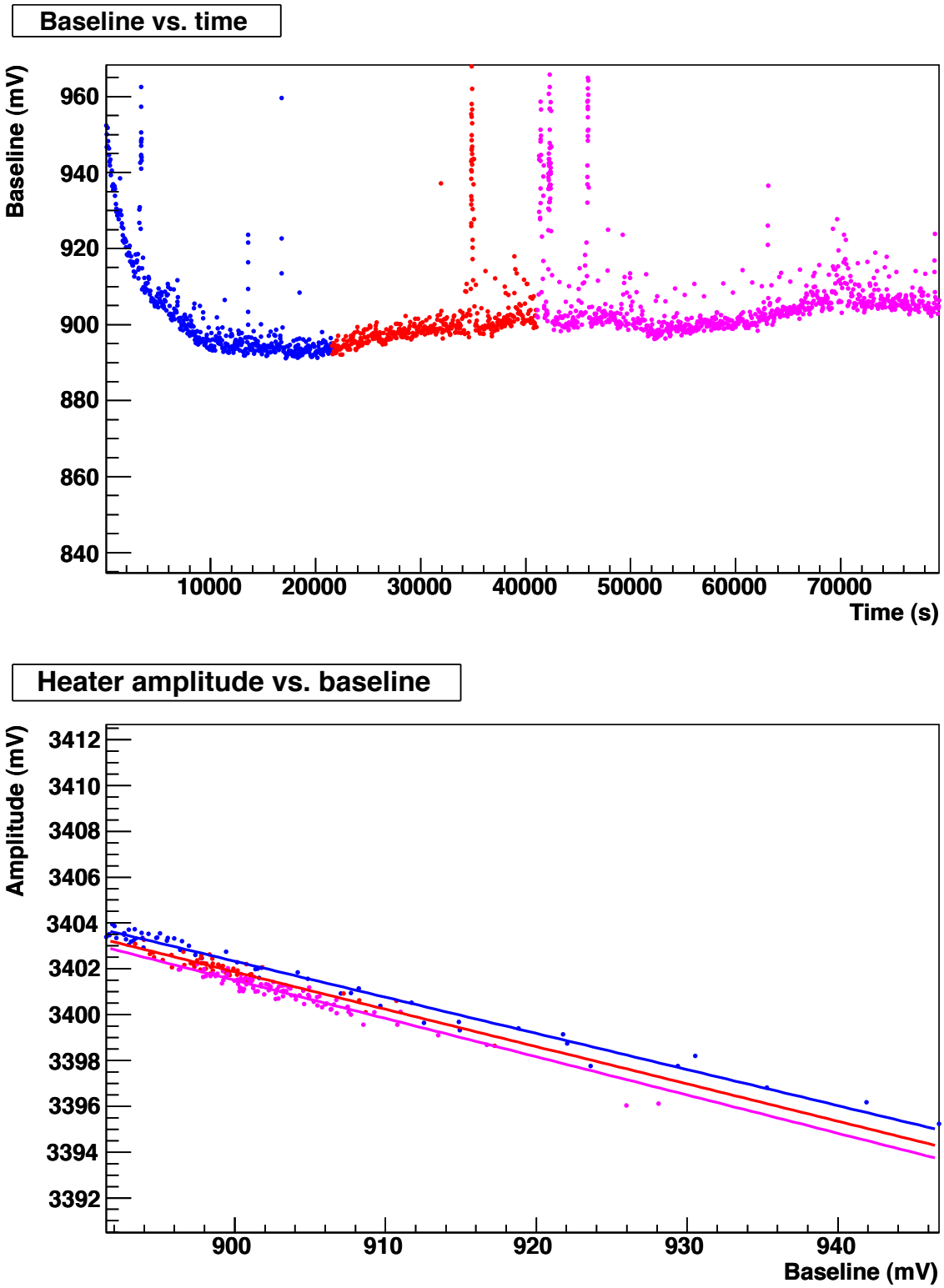

Figure 3.4: Example of a run which was broken into three parts for stabilization. The data shown are from CUORICINO run 1209, channel 8. Figure from Adam Bryant.

3.3 Energy calibration

The purpose of the energy calibration is to find the relationship between the stabilized amplitude of an event (a_s), and its energy (E). This relationship is approximately linear, but there are several sources of non-linearity in the detector response, such as the temperature dependence of the bolometer's heat capacity and the exponential response of the thermistors. In the standard CUORICINO $0\nu\beta\beta$ analysis, the detector response was modeled by a 3rd order polynomial, which can be viewed as the first terms of a Taylor expansion of the true calibration function:

$$E = c_0 + c_1\, a_s + c_2\, a_s^2 + c_3\, a_s^3. \tag{3.6}$$

However, this function diverges very quickly when extrapolated to energies above the highest calibration point. Another function has been used in past CUORICINO analyses which studied the higher energy region where alpha decays occur (3–5 MeV). This function is a second-order log polynomial, given by:

$$\ln(E/(1\text{ keV})) = c_0 + c_1 \ln a_s + c_2\, (\ln a_s)^2, \tag{3.7}$$

and is phenomenologically found to have better properties on extrapolation to the alpha region of the spectrum.

The energy calibration was accomplished by the insertion of a gamma source (thoriated tungsten wires) on opposite sides of the cryostat, between the external lead shields and the OVC. Even after the gain stabilization correction is applied, the energy-amplitude relationship of the detector can drift over time. In order to account for drift, the detector was calibrated approximately once per month. Ideally, a calibration of at least two days was performed at the beginning and end of each data set; however, this was not always the case.

For each data set, the data from the initial and final calibrations were combined, if both were present. Each channel may have a different amplitude-energy relationship, so a separate calibration spectrum was produced for each channel. A representative stabilized amplitude spectrum is shown in Fig. 3.5(a). Gamma lines from the decay chain of ^{232}Th are visible in the spectrum; the strongest of these, listed in Table 3.1, are used for calibration.

The calibration lines are divided into two classes: primary and secondary. The primary peaks are the strongest and are clearly present in virtually every calibration spectrum. The secondary peaks are weaker and may or may not be discernible in a given calibration spectrum, depending on the length of exposure, source/crystal position, and channel resolution.

The calibration algorithm begins by fitting the primary peaks. The peak locations may be determined by two methods. One possibility is to supply an existing calibration file, referred to as a "seed" file (for example, the calibration from the previous data set). If the energy calibration has not shifted too much, the old calibration function can be inverted to find the approximate stabilized amplitude corresponding to the energy of each primary peak. If no seed file is available, the program will attempt to identify the primary peaks in the spectrum using a pattern-matching strategy described in Appendix A.

Once the program has an initial guess for the locations of the primary peaks, it proceeds to fit them as described in Sect. 3.3.1. The nominal energy of each primary peak is plotted

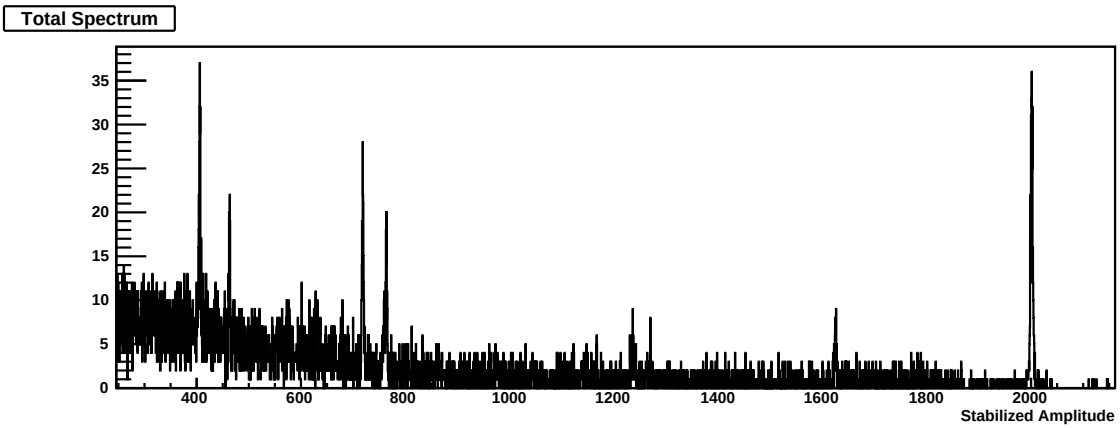

(a) Calibration spectrum

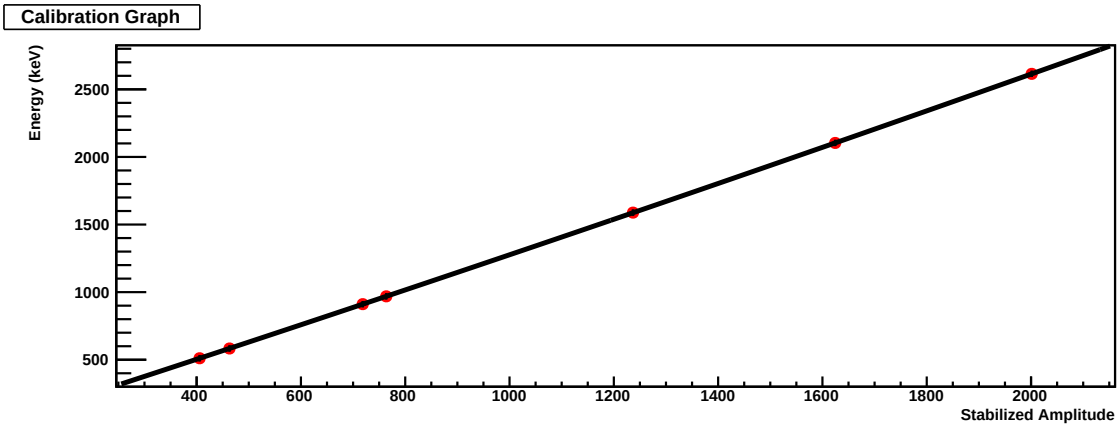

(b) Calibration function fit to graph

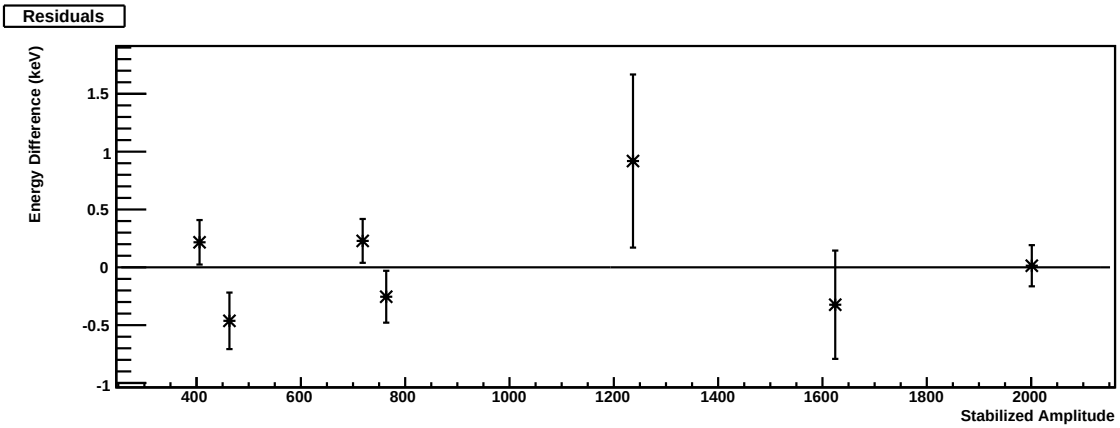

(c) Residuals of calibration fit

Figure 3.5: Calibration spectrum and fit function.

Table 3.1: Gamma lines used for calibration.

Source	Energy (keV)	Line shape	Classification
^{208}Tl	2614.533	Gaussian	Primary
^{208}Tl single escape	2103.533	Gaussian	Secondary
^{208}Tl double escape ^{228}Ac	1592.533 1588.19	Double Gaussian	Secondary
^{228}Ac ^{228}Ac	968.971 964.766	Double Gaussian	Primary
^{228}Ac	911.204	Gaussian	Primary
^{208}Tl	583.191	Gaussian	Secondary
annihilation gamma ^{208}Tl	511.0* 510.77	Gaussian	Primary

*The energy used for the fit is 511.0 keV. Simulations indicate that the 510.77 keV line contributes only about 6%. This will need to be re-evaluated for CUORE since the sources will be inside the shields.

versus the mean stabilized amplitude returned by the fit; this graph is then fit with an interpolation function[1], as shown in Fig. 3.6. The interpolation function is then inverted to find the approximate location of each secondary peak. The secondary peaks are each fit individually, and the results of all the individual peak fits are combined into a calibration graph, as shown in Fig. 3.5(b).

The calibration graph is a plot of the nominal energy of each peak versus the fitted stabilized amplitude. It includes horizontal error bars, which represent the error on the mean of each peak returned by the fitter. These error bars are used to weight the fit of the calibration function to the calibration graph. The resulting calibration fit for each channel is saved to a file and used to convert the stabilized amplitudes into energies.

3.3.1 Peak fitting

The peaks in the calibration spectrum were fit using either a single or double Gaussian line shape with a linear background. The fit function was parameterized as follows:

$$F_{\text{single}}(x) = f_{\text{bkg}} B(x) + (1 - f_{\text{bkg}})\, G_1(x) \tag{3.8}$$

$$F_{\text{double}}(x) = f_{\text{bkg}} B(x) + (1 - f_{\text{bkg}})\, ((1 - A_2) G_1(x) + A_2 G_2(x)) \tag{3.9}$$

where

$$B(x) = \left(\frac{1}{x_{\max} - x_{\min}}\right)\left(1 + m\left(x - \frac{x_{\min} + x_{\max}}{2}\right)\right), \tag{3.10}$$

[1]In general, the calibration function itself is used as the interpolation function, but if there are more degrees of freedom in the calibration function than successfully fit primary peaks, then a.) a second order polynomial or b.) a second order polynomial with the constant term fixed to zero may be used.

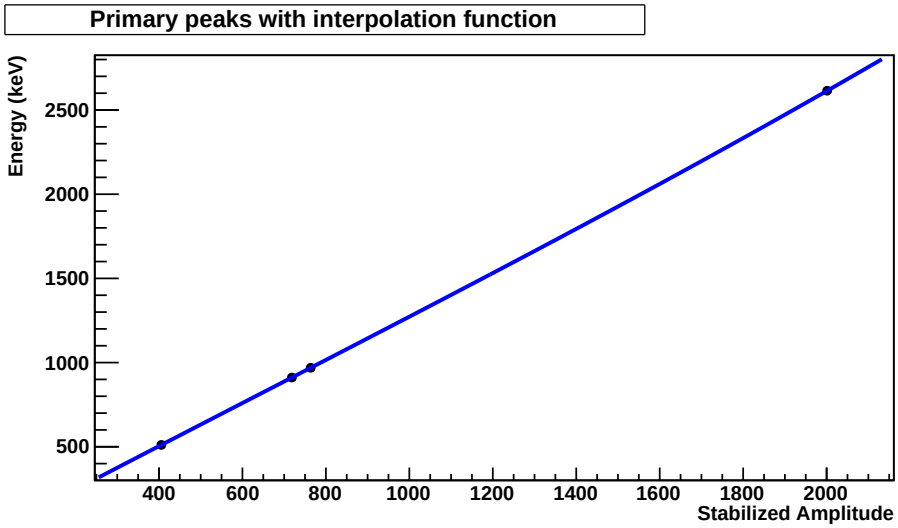

Figure 3.6: Primary peaks fit by interpolation function.

$$G_1(x) = \frac{1}{\sigma\sqrt{2\pi}} e^{-(x-\mu)^2/(2\sigma^2)}, \tag{3.11}$$

$$G_2(x) = \frac{1}{\sigma\sqrt{2\pi}} e^{-(x-\mu\cdot R_\mu)^2/(2\sigma^2)}, \tag{3.12}$$

and the fit parameters are defined in Table 3.2. Examples of fitted peaks can be found in Figs. 3.7 and 3.8.

The data are fit by this fit function using the following procedure.

1. A starting guess for the peak mean is obtained (from seed file, interpolation function, or automatic peak-finding routine, as described in Sect. 3.3 and Appendix A).

2. A "big" window of width $\pm W$ around this starting guess is defined. This can be done in one of two ways:

   (a) If CORC has already been run for the data (discussed in Sect. 4.2.1), the program can obtain the heater peak resolution for the channel from the CORC database. Then, W is defined as 7 times the CORC heater resolution.

   (b) If the resolution from CORC is not available, the default value is used, which is an amplitude range approximately corresponding to 40 keV.

   If the big window spans more than 2/3 of the distance to the nearest neighboring calibration peak, the window is set to that value.

3. The data within $\pm W$ of the initial guess are histogrammed in 80 bins. The maximum bin is chosen as the new guess for the peak mean, μ_0. This is set as the initial value for μ in the fit function.

Table 3.2: Fit parameters used for calibration peaks. Those marked with * are used only in the double Gaussian fit.

Variable	Free/Fixed	Description
f_{bkg}	Free	Fraction of counts in background
A_2	Fixed/Free*	Relative peak amplitude. Obtained from branching ratios b, if known, by $A_2 = b_2/(b_1 + b_2)$. Otherwise left free in fit.
$x_{\max}$	Fixed	Fit range maximum
$x_{\min}$	Fixed	Fit range minimum
m	Free	Slope of linear background
σ	Free	Width of peak
μ	Free	Mean of peak
R_μ	Fixed*	Ratio of peak means. It is approximated by the ratio of the energies of the peaks.

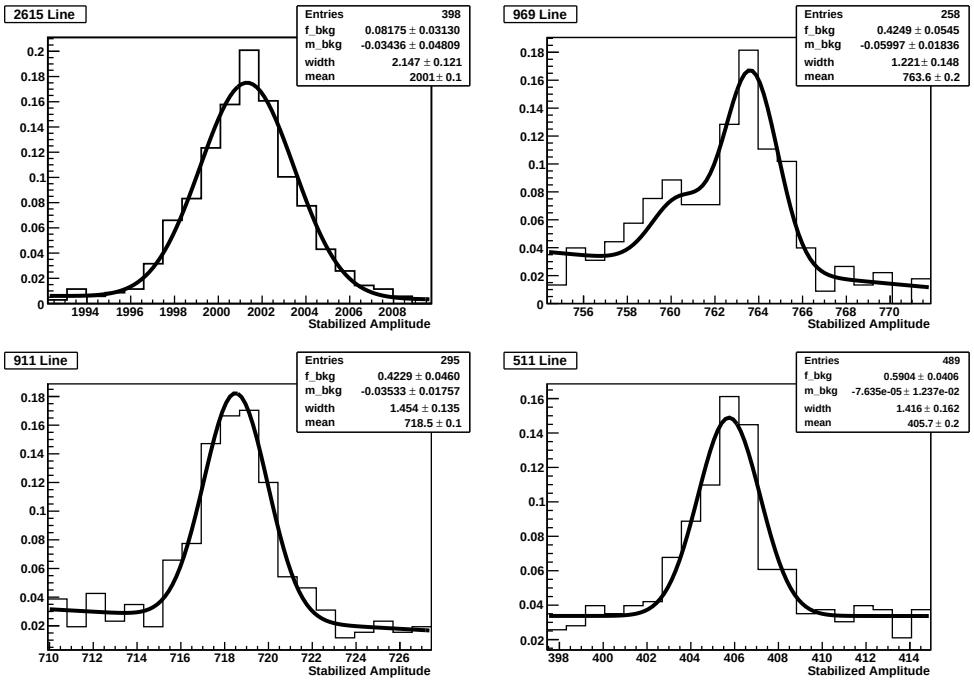

Figure 3.7: Fitted primary peaks.

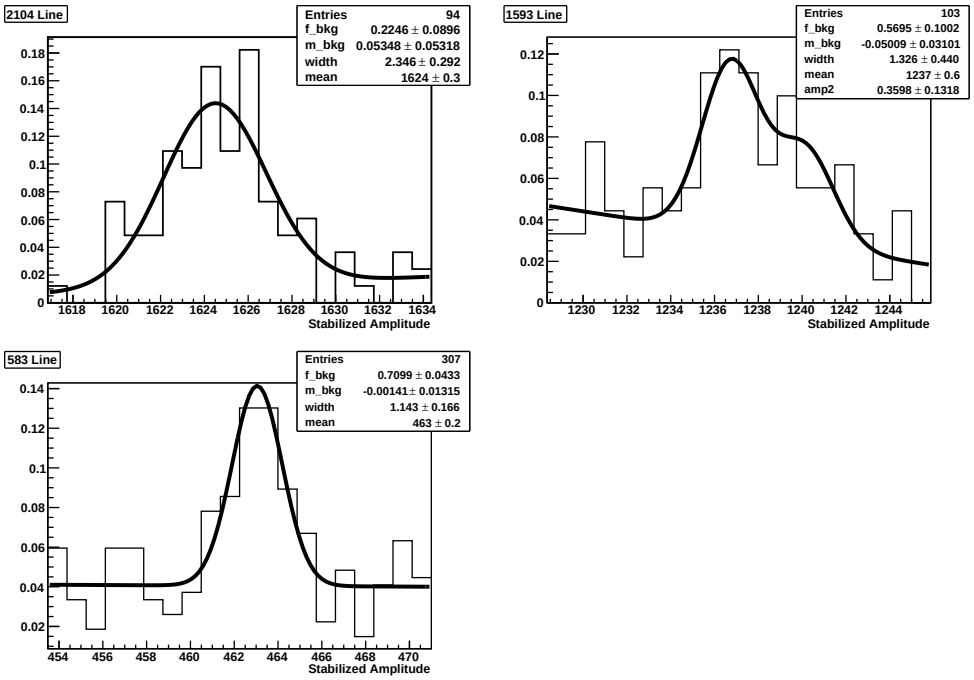

Figure 3.8: Fitted secondary peaks.

4. A "small" window of width $\pm w$ is defined around the new central value. This window will be 5 sigma if using CORC or $\sim$15 keV otherwise. Again, the window is not allowed to exceed 2/3 of the distance to the nearest neighboring peak. The fit parameters $x_{\max}$ and $x_{\min}$ are fixed at $\mu_0 \pm w$.

5. The line shape in Table 3.1 is fit to the data on the range $\mu_0 \pm w$ using an unbinned maximum likelihood fit.

A statistical significance test is applied to decide whether or not to use the peak for calibration. The number of signal events in the peak is defined as $n_{\text{sig}} = N(1 - f_{\text{bkg}})$, where N is the total number of points in the fit region. We require $n_{\text{sig}} \geq 6$ and $n_{\text{sig}}/\sqrt{N} \geq 1.5$ for the peak to be accepted. If a peak is accepted, the fitted mean, μ, of the peak is then used in the energy-amplitude calibration fit.

For the standard CUORICINO $0\nu\beta\beta$ analysis, the calibration function used to fit the energy-amplitude plot is a third-order polynomial (Eq. (3.6)). However, for the $2\nu\beta\beta$ analysis, a second-order log polynomial (Eq. (3.7)) was used instead, because it is more stable under extrapolation to the alpha region (3–10 MeV). For the $2\nu\beta\beta$ analysis, the ability to properly reconstruct the backgrounds from alpha decays is more important than increasing the precision of the energy calibration in the $2\nu\beta\beta$ region, because of the slowly varying nature of the $2\nu\beta\beta$ signal. However, even with the more stable log polynomial calibration,

the lack of any calibration points above the 2615 keV line makes the calibration at higher energies extremely unreliable.

3.3.2 Alpha region recalibration

After all the CUORICINO data had been calibrated by the usual gamma calibration method described above, an additional calibration step was taken for energies above 3900 keV. This secondary calibration was based on peaks from alpha decays of radioactive contaminants of the crystals and surrounding materials. Because the rate of alpha events in the detector was very low, it was not possible to perform the alpha calibration independently for each dataset; rather, the calibration was performed separately for each channel, using the total sum of CUORICINO data.

The peaks in the spectrum above 3900 keV can be accounted for by alpha decays in the ^{238}U and ^{232}Th decay chains. All the alpha decays from these chains with an energy between 3900 and 7100 keV and a branching ratio greater than 5% were used for the calibration and are listed in Table 3.3. The energy calibration is not linear; however, the spectrum was broken into four regions, each of which may be approximated with a linear calibration to within the experimental error. The energy regions used were 3900–4500 keV, 4500–5100 keV, 5100–5900 keV and 5900–7100 keV. The alpha lines and energy regions used are shown in Fig. 3.9.

Table 3.3: Alpha lines used for alpha region re-calibration [11].

Energy Region	Source	Q value (keV)	Alpha Energy (keV)	Secondary Alpha Energy (keV)	Branching Ratios (%/%)
1	^{232}Th	4083	4012	3947	78/21
	^{238}U	4270	4198	4151	79/21
2	^{230}Th	4770	4687	4620	76/23
	^{234}U	4857	4775	4722	71/28
	^{226}Ra	4871	4784	4601	94/06
3	^{210}Po	5407	5304		
	^{228}Th	5520	5423	5340	72/27
	^{222}Rn	5590	5489		
	^{224}Ra	5788	5685	5449	95/05
4	^{218}Po	6115	6002		
	^{212}Bi	6207	6051	6090	25/10
	^{220}Ra	6404	6288		
	^{216}Po	6909	6778		

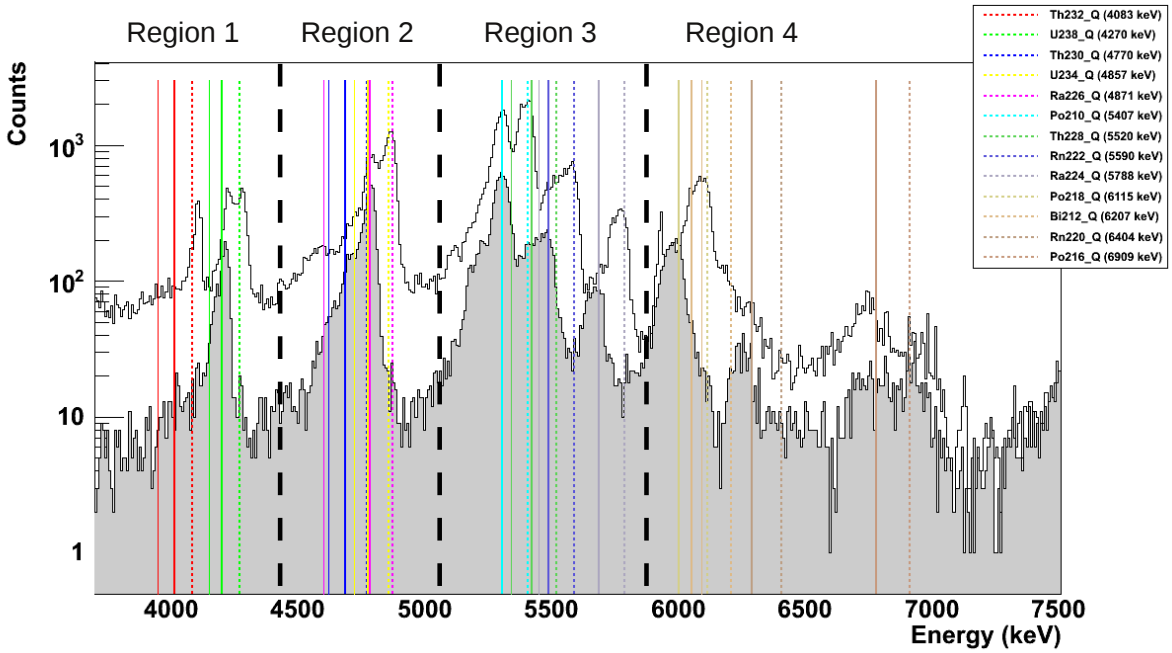

Figure 3.9: Alpha peaks in the CUORICINO spectrum, before recalibration, summed on all channels. The white spectrum contains multiplicity 1 events, while the grey spectrum contains multiplicity 2 events (events which occurred in coincidence with an event on another bolometer). The thick black dashed lines show how the spectrum was divided into 4 regions. The thin dashed lines correspond to Q values of alpha decays, and the thin solid lines represent the alpha energies of those decays.

A model of the alpha spectrum was constructed using a software package called RooFit [95], which is an extension of the ROOT data analysis toolkit [96]. In the case of surface contaminations, the shape of the alpha peaks is not expected to be gaussian, but to have a low energy tail due to alphas which deposit only part of their energy in the crystal. Therefore, each alpha line was modeled with a "crystal ball" probability density function (PDF), which is a gaussian with a power law tail on the low energy side, defined by [97]:

$$f(x;\alpha,n,\mu,\sigma) = \begin{cases} \exp\left(-\frac{(x-\mu)^2}{2\sigma^2}\right), & \text{for} \frac{x-\mu}{\sigma} > -|\alpha| \\ \left(\frac{n}{|\alpha|}\right)^n e^{-\alpha^2/2} \left(\frac{n}{|\alpha|} - |\alpha| - \frac{x-\mu}{\sigma}\right)^{-n} & \text{for} \frac{x-\mu}{\sigma} < -|\alpha| \end{cases} \tag{3.13}$$

A fit of the spectrum was performed separately for each channel and energy region, with a PDF which includes a linear background and a crystal ball function representing each alpha peak found in Table 3.3. The mean of each peak was fixed to its known energy, but a linear energy correction ($E_{\text{true}} = \epsilon_0 + \epsilon_1 E$) was introduced globally for each energy region; finding this energy correction was the goal of the fit. Besides the two parameters of the linear energy correction, ϵ_0 and ϵ_1, other free parameters were as follows:

- 2 parameters to describe the linear background;
- 3 peak shape parameters α, n, and σ (these parameters were constrained to be the same for all peaks in a given energy region); and
- 1 free parameter per peak representing the number of events in the peak (except for decays with multiple alpha energies, for which the intensity of the secondary alpha peak was fixed by the branching ratios of the decays).

The model PDF was fit to the spectrum using a binned extended maximum likelihood fit. The results of the fit for the enriched crystals are shown in Figs. 3.10–3.13.

Once the spectra had been fit, the energy correction parameters ϵ_0 and ϵ_1 were used to recalibrate the energy of all events for a given channel and energy region. The effects of this recalibration are shown in Fig. 3.14.

3.4 Pulse shape analysis

The goal of the pulse shape analysis is to eliminate:

1. spurious pulses, i.e. events that trigger the data acquisition, but are not due to a particle interaction in the bolometer absorber; and
2. deformed pulses, which may be due to a particle interaction, but are degraded by noise or pileup such that the amplitude can not be accurately evaluated.

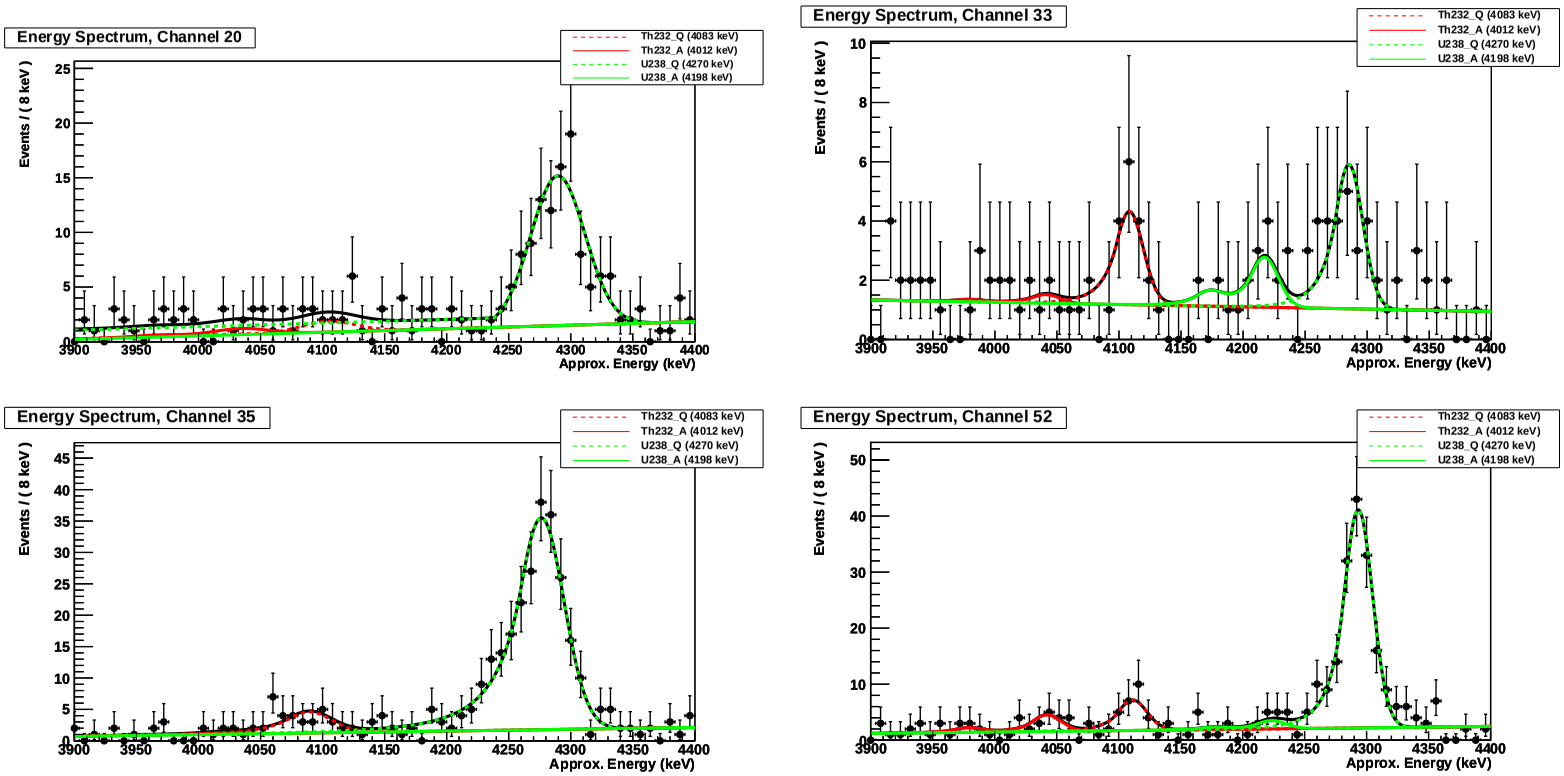

Figure 3.10: Fit of alpha lines in region 1. Dotted lines show peaks at the Q values, while solid lines show peaks at the alpha energies of the decays. From low to high energy, this region includes decays from ^{232}Th and ^{238}U.

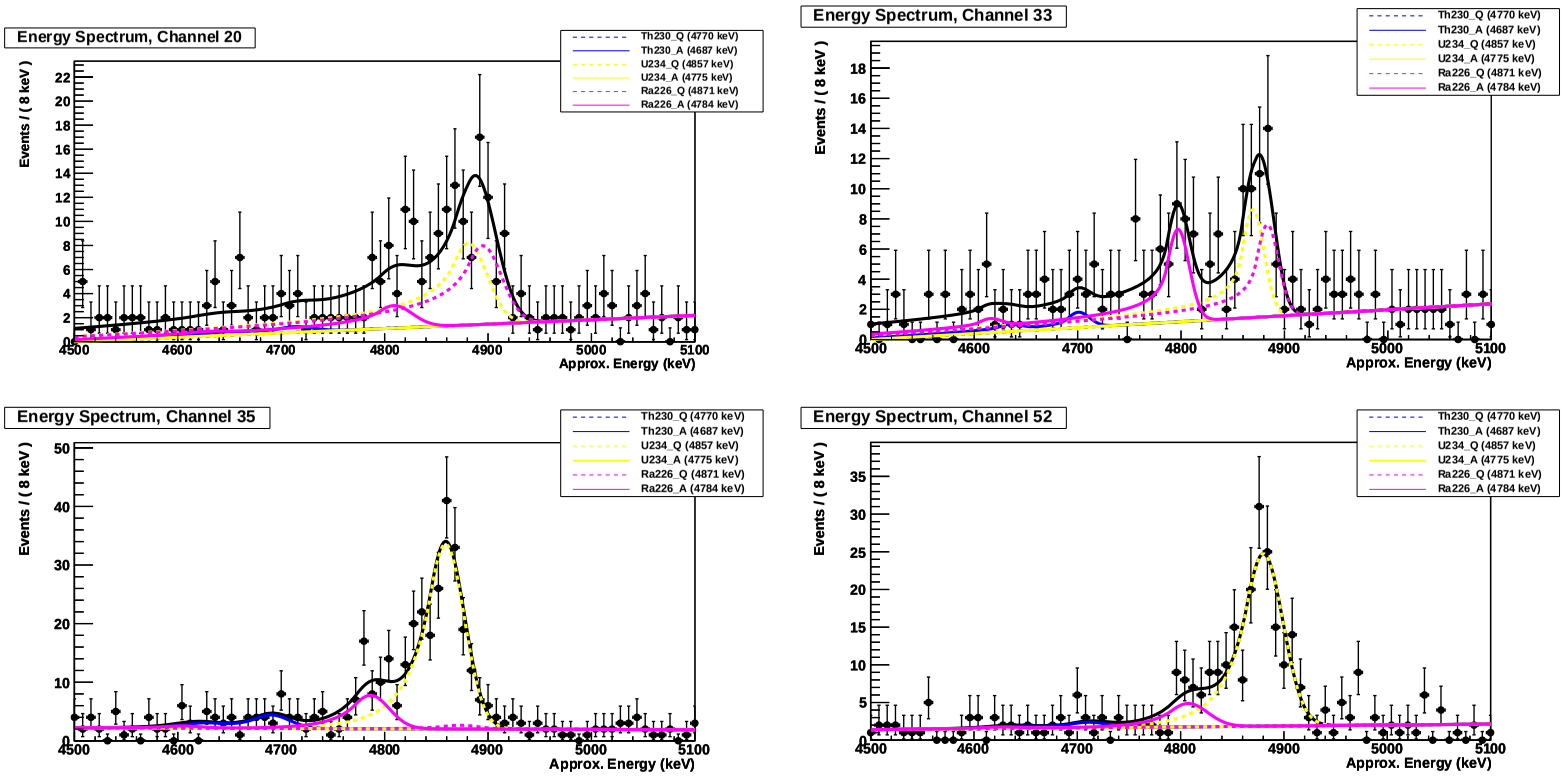

Figure 3.11: Fit of alpha lines in region 2. Dotted lines show peaks at the Q values, while solid lines show peaks at the alpha energies of the decays. From low to high energy, this region includes decays from ^{230}Th, ^{234}U, and ^{226}Ra.

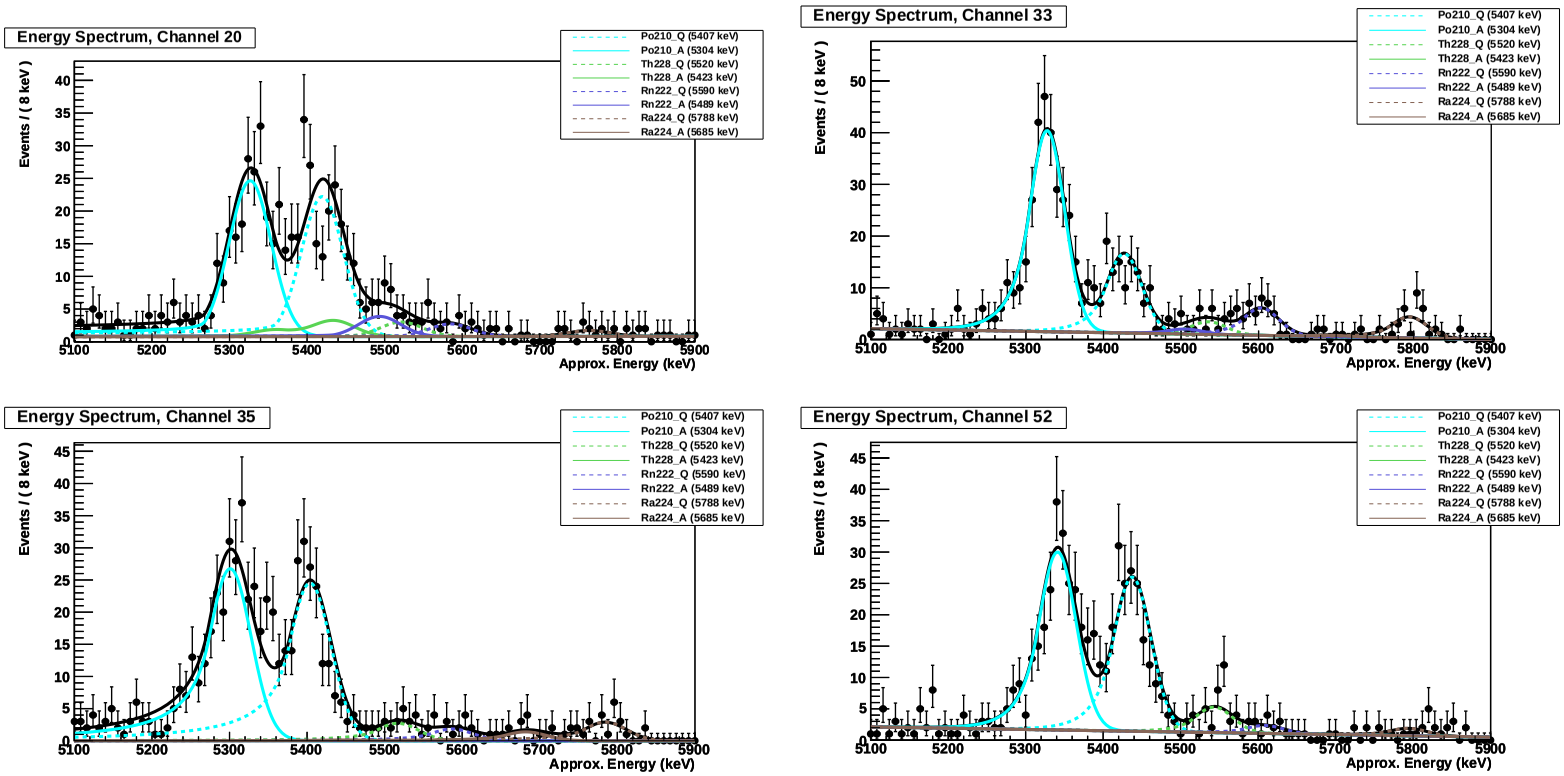

Figure 3.12: Fit of alpha lines in region 3. Dotted lines show peaks at the Q values, while solid lines show peaks at the alpha energies of the decays. From low to high energy, this region includes decays from ^{210}Po, ^{228}Th, ^{222}Rn, and ^{224}Ra.

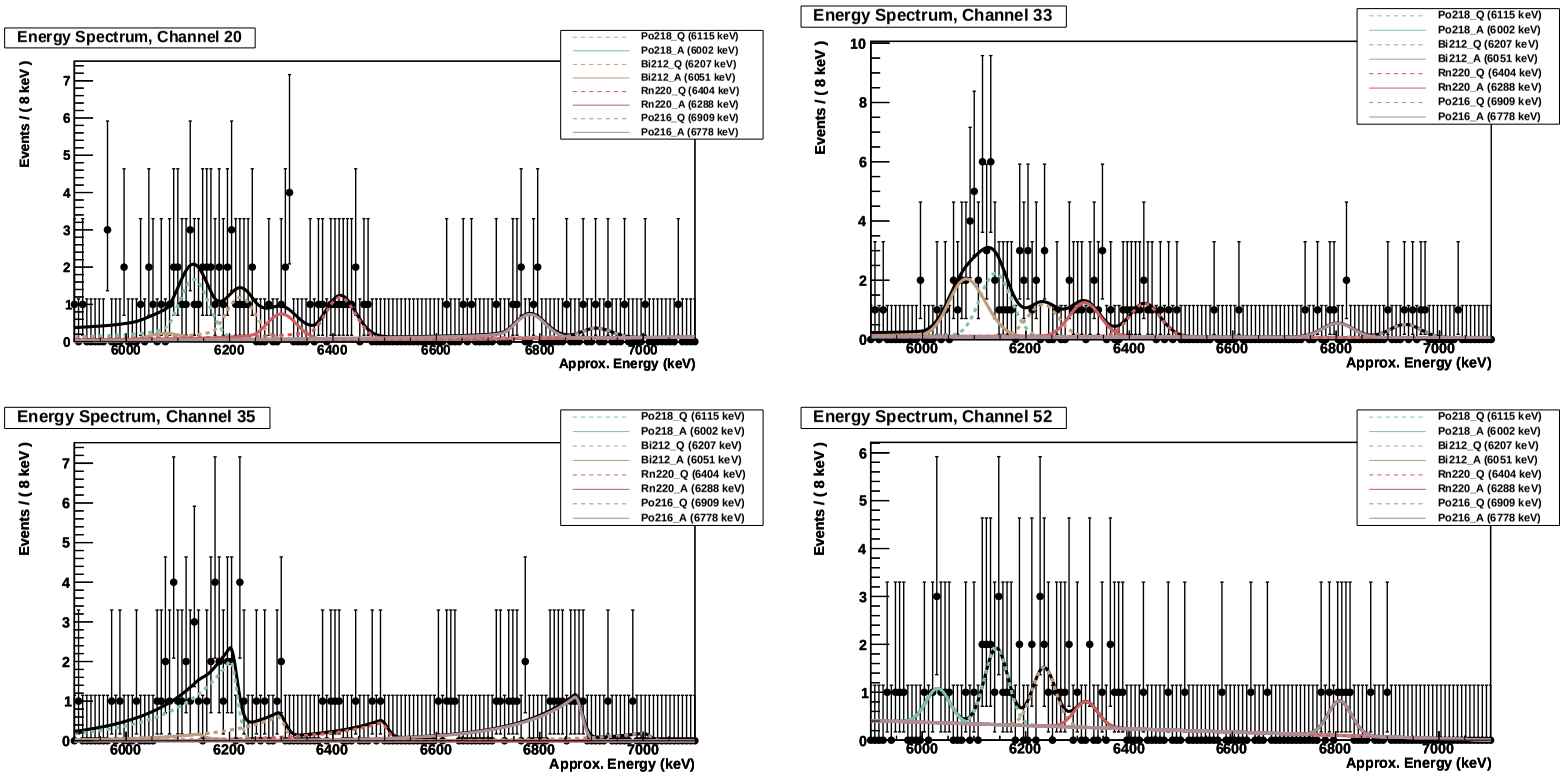

Figure 3.13: Fit of alpha lines in region 4. Dotted lines show peaks at the Q values, while solid lines show peaks at the alpha energies of the decays. From low to high energy, this region includes decays from ^{218}Po, ^{212}Bi, ^{220}Rn, and ^{216}Po.

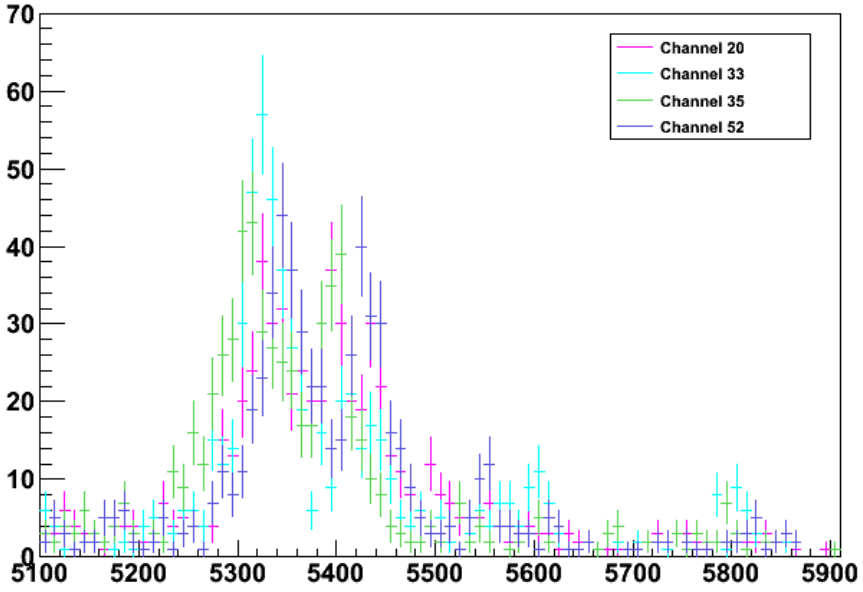

(a) Uncorrected spectrum

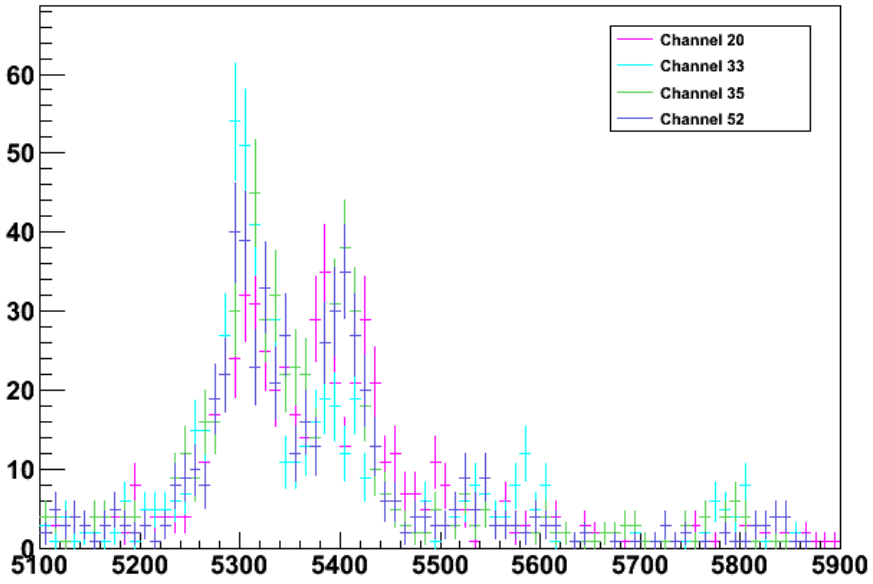

(b) Recalibrated spectrum

Figure 3.14: Energy spectrum of enriched crystals before and after alpha energy recalibration.

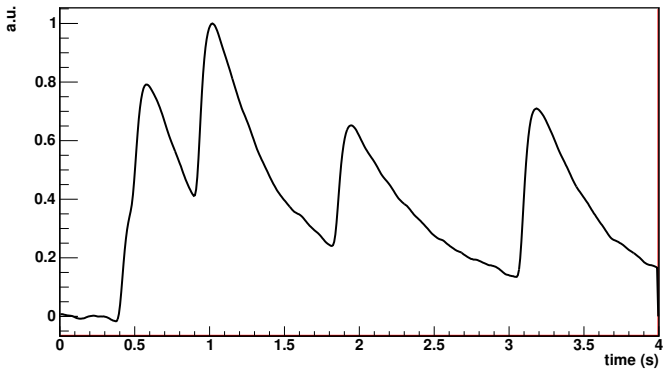

(a) Pileup of pulses

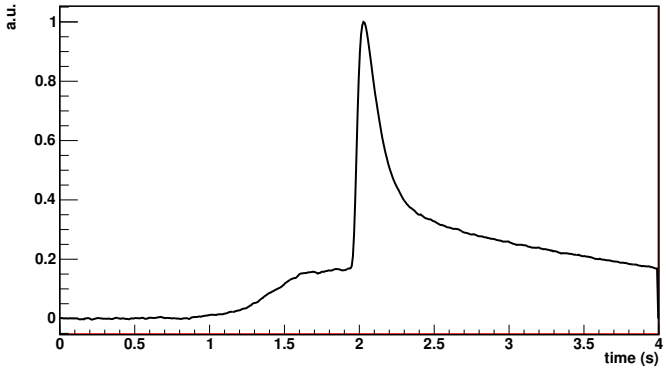

(b) Pileup of a pulse with a non-particle event

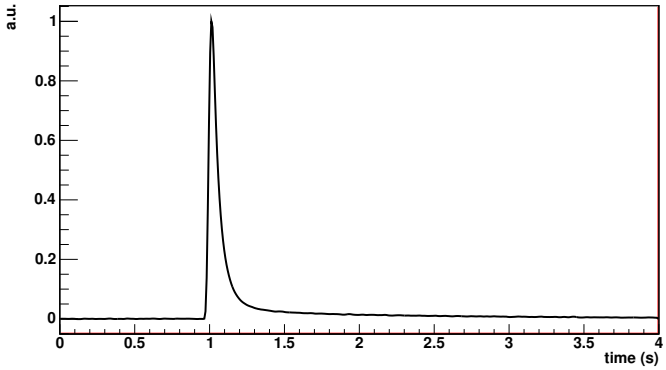

(c) An atypically narrow voltage spike.

Figure 3.15: Examples of pulses rejected by the pulse shape analysis. Figure from Marco Carrettoni.

Some examples of spurious and deformed pulses are shown in Fig. 3.15.

In CUORICINO these types of pulses were rejected using a pulse shape analysis method developed by collaborator Marco Carrettoni. The analysis was based on a pulse shape parameter called the "Optimum Filter Test" (OFT), defined as $OFT = a_{TD}/a_{FD}$, where a_{TD} and a_{FD} are evaluations of the pulse amplitude in the time domain and the frequency domain, respectively, as described in Sect. 3.1. For pulses with a shape close to the ideal shape, these amplitudes should match well, but for abnormally-shaped pulses they will differ.

Unfortunately the OFT parameter has a complicated dependence on energy, which makes it impossible to set a simple cutoff value that will be valid for all pulses. Therefore, a procedure was used to linearize the OFT parameter and remove its energy dependence.

First, an interpolation function $f_{OFT}(E;\boldsymbol{\theta})$ was fit to the OFT versus energy curve to find the best fit parameters, $\boldsymbol{\theta}_{best}$, using a robust regression technique which is less sensitive to outliers than a least-squares fit. This is important because the presence of large clusters of outliers due to non-physical events would significantly skew a standard least-squares fit. The fit was performed with three different interpolation functions, shown in Fig. 3.16). Next, the OFT parameter was linearized using the transformation:

$$\widehat{OFT}(E) = \frac{OFT}{f_{OFT}(E;\boldsymbol{\theta}_{best})}. \tag{3.14}$$

At this point, the interpolation function was chosen which produced the least energy-dependent $\widehat{OFT}(E)$.

Finally, the variance was normalized by dividing the plot of $\widehat{OFT}$ versus E into equal slices in the log of the energy and finding the mean m_i and standard deviation σ_i of the $\widehat{OFT}$ of events in each slice (Fig. 3.17(a)). Then a pulse shape parameter P was constructed as:

$$P = \frac{\widehat{OFT} - m_i}{\sigma_i}, \tag{3.15}$$

so that P corresponds to the number of standard deviations away from the mean an event's pulse shape parameter falls (Fig. 3.17(b)). The resulting parameter is reasonably energy independent and consistent across bolometers, so that a single cut on P can discriminate badly-shaped pulses for all energies and channels. More details on the pulse shape analysis can be found in [98]. For this analysis, a cut of $P < 2$ was used (see Sect. 4.1.4).

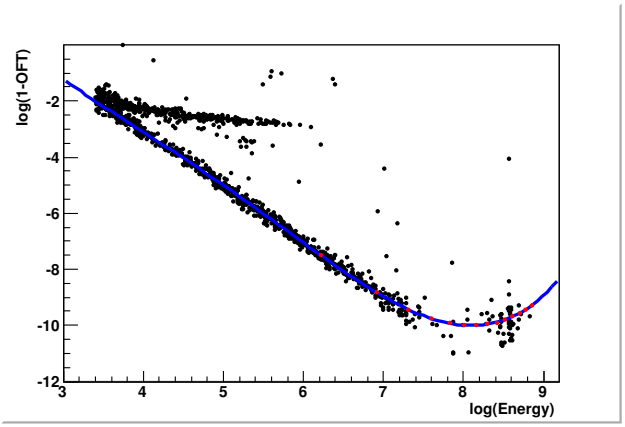

(a) Interpolation with a 4th order polynomial

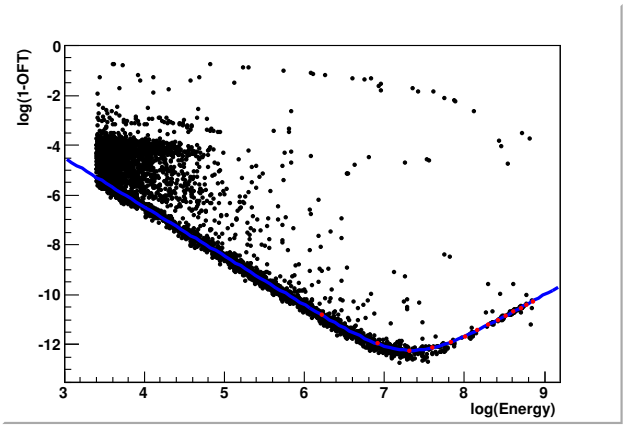

(b) Interpolation with the integral of a sigmoid function

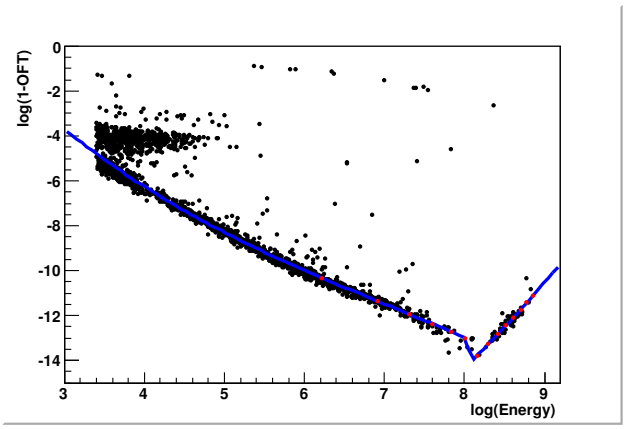

(c) Interpolation with a discontinuous 2nd order polynomial

Figure 3.16: Examples of the OFT parameter's dependence on energy, fit by different interpolation functions, $f_{OFT}(E)$. The energy scale is from 30–7000 keV; red dots identify intervals of 500 keV. Figure from Marco Carrettoni.

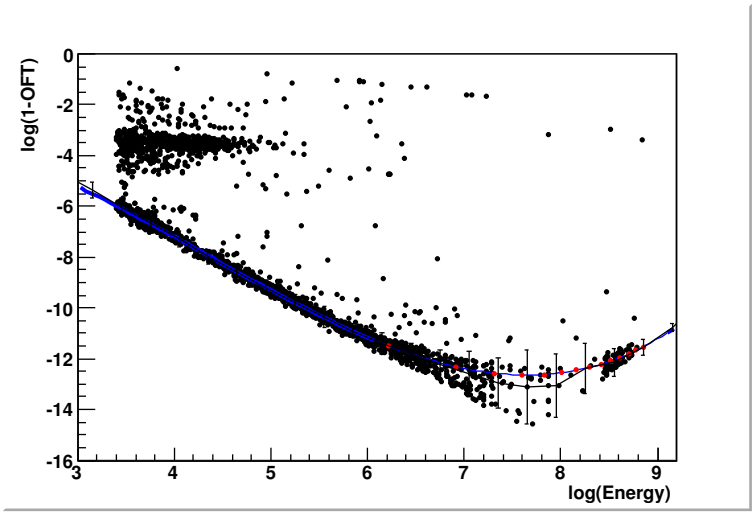

(a) Scatter plot showing the mean and standard deviation of OFT (represented by vertical error bars) for bins of equal width in $\log(E)$.

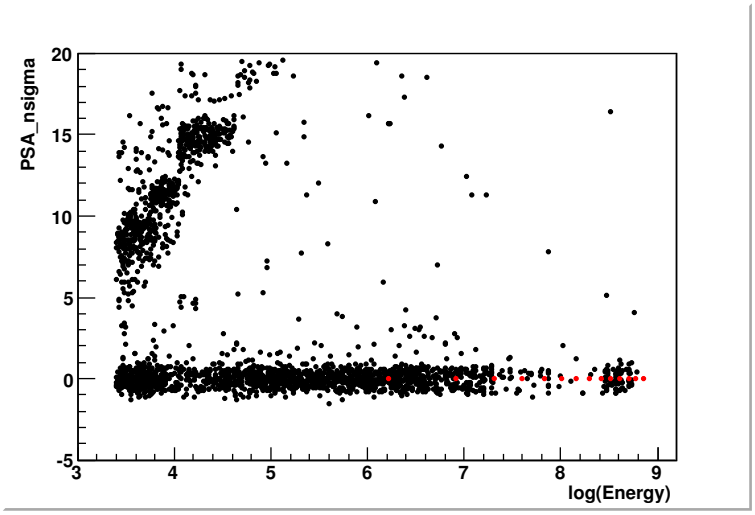

(b) Energy distribution of the pulse shape parameter P (denoted "PSA_nsigma" in figure)

Figure 3.17: Procedure used to construct the pulse shape parameter P (denoted "PSA_nsigma" in the figure) by linearizing and normalizing OFT. The energy scale is from 30–7000 keV; red dots identify intervals of 500 keV. Figure from Marco Carrettoni.

Chapter 4

Background model and $2\nu\beta\beta$ fit

In order to measure the $2\nu\beta\beta$ rate in CUORICINO, the component of the energy spectrum due to $2\nu\beta\beta$ must be distinguished from the backgrounds. In CUORICINO, this was accomplished by using crystals enriched in ^{128}Te (and depleted in ^{130}Te) as background monitors, so that the shared backgrounds could be subtracted from another pair of crystals enriched in ^{130}Te. Fig. 4.1 shows the layout of the enriched crystals, which were located on the 12th floor of the CUORICINO tower.

The basic procedure followed was to bin the data from the enriched crystals into histograms, subtract the spectrum of the 128-enriched crystals from the 130-enriched crystals, and fit the resulting spectrum for the $2\nu\beta\beta$ signal. Unfortunately, although most of the experimental backgrounds were shared between the detectors, there were some non-uniformities which led to residual backgrounds in the subtracted spectrum. In particular, some peaks from known alpha decays were clearly present.

In order to account for the effects of these residual backgrounds, Monte-Carlo simulations were performed introducing radioactive contaminations at different locations. The resulting simulated spectra were fit to the data along with the signal component, and the $2\nu\beta\beta$ rate was extracted.

The $2\nu\beta\beta$ decay analysis was performed in a semi-blind fashion, by not computing the total live time of the measurement (and therefore precise half-life) until all the analysis procedures were established. The values for all the cuts described in the following section were determined before unblinding the final half-life value.

4.1 Cuts

Before the fit was performed, variety of cuts were applied to the data in order to reduce backgrounds. The general goal of these cuts was to maximize the ratio of the number of signal counts to the square root of the number of background counts in the region of interest, thereby maximizing the sensitivity of the $2\nu\beta\beta$ measurement.

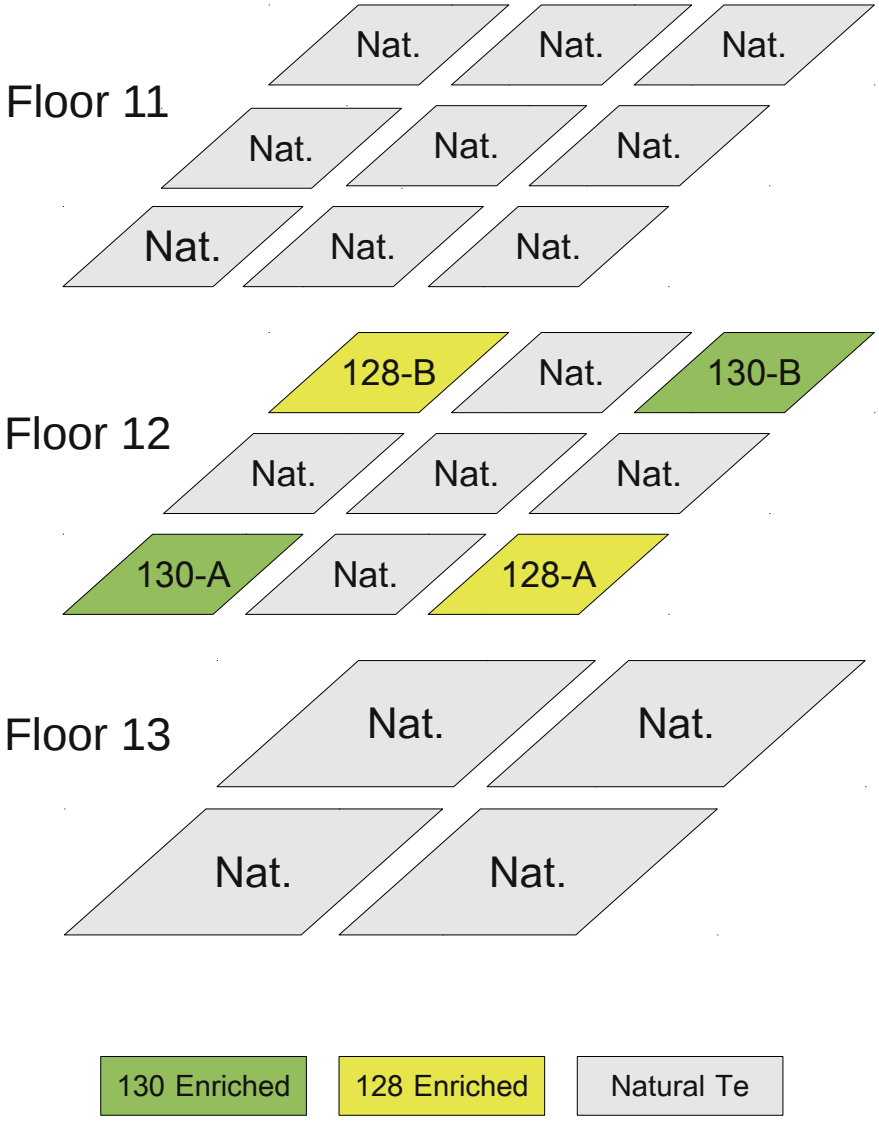

Figure 4.1: Layout of the bottom three floors of the CUORICINO tower.

4.1.1 Energy threshold

Since the shape of the spectrum is fit along with the residual background contributions, in principle, there is no disadvantage to including all the data down to zero energy. However, because the background increases exponentially at low energies, and the signal becomes very small, there is little to be gained by extending the fit to very low energies. Moreover, there are additional systematic effects to be considered at low energy. For example, the energy corresponding to the trigger threshold varies from channel to channel, as does the efficiency of the pulse shape cut near threshold. Because the analysis relies on subtracting the spectra of different bolometers, these variations in performance at low energy could result in a spurious signal that would interfere with the $2\nu\beta\beta$ measurement. Therefore, it is advantageous to set an energy threshold for the $2\nu\beta\beta$ analysis.

In order to avoid biasing the analysis, only 1/5 of the data (runs divisible by 5) was used to optimize the energy threshold. After dividing the data into 1 keV bins, the signal in each bin was taken to be proportional to the signal PDF evaluated at the bin center ($S_i = f(E_i)$), and the background was estimated by the total number of events in the bin which passed all other analysis cuts (B_i). The contribution to the sensitivity from each bin is then $S_i/\sqrt{B_i}$, and the total sensitivity X was obtained by summing the contribution from all bins above the energy threshold:

$$X = \sum_{i=i_{min}}^{n} \frac{S_i}{\sqrt{B_i}} \tag{4.1}$$

The sensitivity is plotted as a function of the energy threshold in Fig. 4.2. An energy threshold of 500 keV was chosen for this analysis, since that is around the point where the sensitivity plateaus, and well above the energies where the systematic uncertainties described above are significant.

4.1.2 Radon

Radon (specifically ^{222}Rn) is a radioactive noble gas naturally produced in the decay chain of ^{238}U. It is present in the environment of the underground laboratory at LNGS, where it emanates from the rock walls of the experimental halls. The CUORICINO cryostat was surrounded by a Plexiglas box flushed with pure nitrogen (Sect. 2.2) for the purpose of radon abatement. Unfortunately, this system was not always operational during the course of CUORICINO data-taking, leading to some periods in which elevated radon levels are evident in the data.

^{222}Rn decays through several steps to ^{214}Bi (Fig. 4.15), which undergoes beta decay accompanied by numerous characteristic gamma lines. These gamma lines are the clearest indicator of the presence of radon in CUORICINO (Fig. 4.3). In order to track the relative radon level over time, an estimator of the radon level (L_{Rn}) was constructed by taking the sum of the number of counts in the four strongest ^{214}Bi lines normalized by the sum of counts in the three strongest stable background lines not associated with ^{222}Rn (Table 4.1). The yield in each peak was determined by a gaussian plus linear background fit to the energy

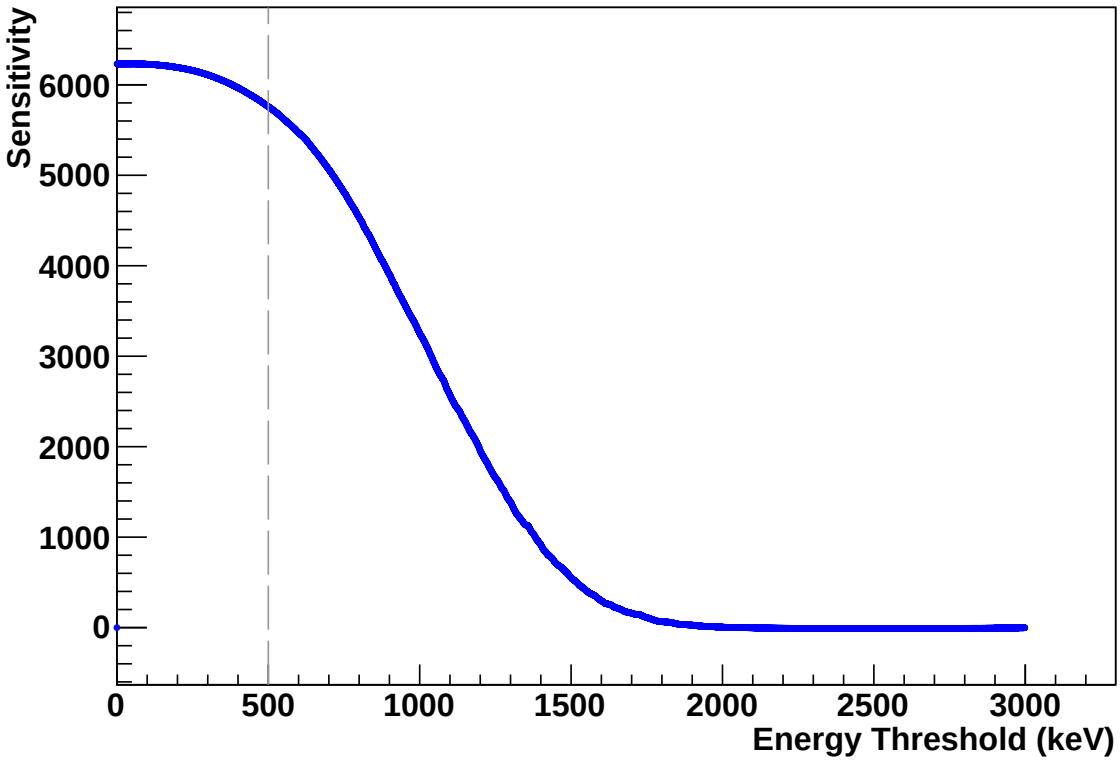

Figure 4.2: Experimental sensitivity (arbitrary units) as a function of energy threshold. An energy threshold of 500 keV (marked with dotted line) was chosen for use in the analysis.

Table 4.1: Lines used to estimate the level of ^{222}Rn in CUORICINO [11]

	Source	Energy (keV)	Branching Ratio (%)
Radon Indicators	^{214}Bi	609.31	46.1
	^{214}Bi	1120.29	15.1
	^{214}Bi	1764.49	15.4
	^{214}Bi	2204.21	5.08
Reference Lines	^{228}Ac	911.20	25.8
	^{40}K	1460.83	11
	^{208}Tl	2614.53	99

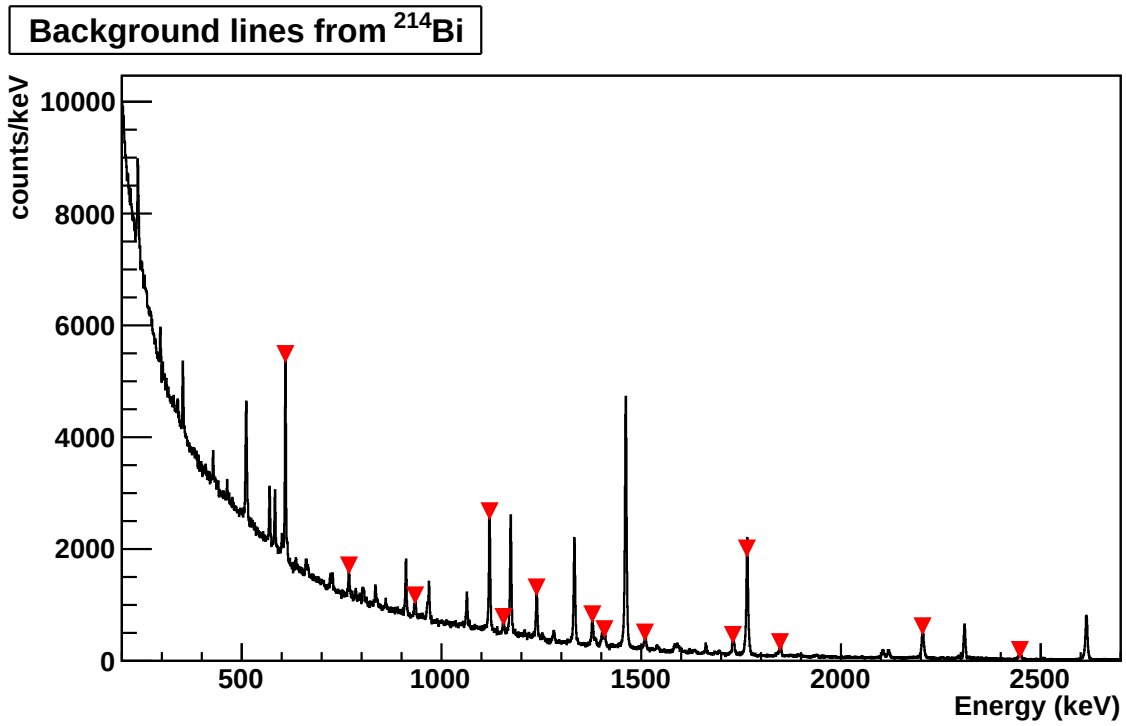

Figure 4.3: Most prominent γ lines associated with the β decay of ^{214}Bi (marked with red triangles).

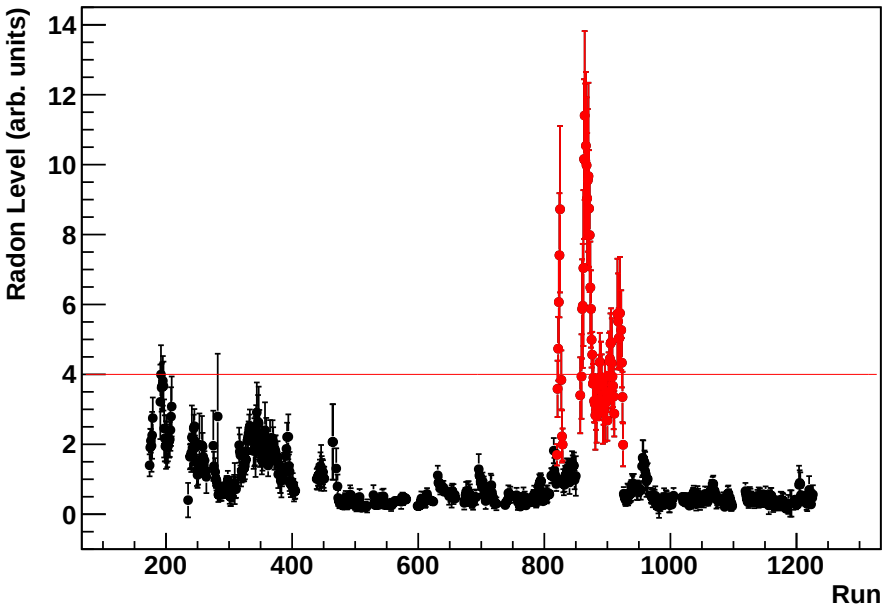

Figure 4.4: Radon level measured by the detector for each CUORICINO run. Line is drawn at a radon level of 4 for reference. Runs in red were excluded from the $2\nu\beta\beta$ analysis.

spectrum in the neighborhood of each peak. Then, if Y_E is the yield under the peak at each energy E, the estimator L_{Rn} is given by

$$L_{\mathrm{Rn}} = \frac{Y_{609} + Y_{1120} + Y_{1764} + Y_{2204}}{Y_{911} + Y_{1460} + Y_{2615}} \quad . \tag{4.2}$$

In order to determine the radon level over time, each run was combined with the two runs immediately before and two runs immediately after it to increase statistics. The radon level L_{Rn} was computed for each such overlapping set of 5 runs. A plot of L_{Rn} versus run number is shown in Fig. 4.4..

The effect of the radon level on the measurement sensitivity was evaluated as follows: the number of signal events S was assumed to be proportional to the total live time of included runs, and the number of background events B was approximated by the total number of events between the energy threshold (500 keV) and the Q value (2530 keV) which pass all other analysis cuts. Then the measurement sensitivity was estimated as $S/\sqrt{B}$ for different values of the maximum allowed radon level (Fig. 4.5). Since the background due to radon should be approximately uniform over the entire detector, the radon level cutoff value was optimized based on the data from the non-enriched crystals.

As seen in Fig. 4.5, the maximum sensitivity is attained at a radon cutoff of 3.5–4. There were two main time periods exceeding a radon level of 4 over the course of the CUORICINO

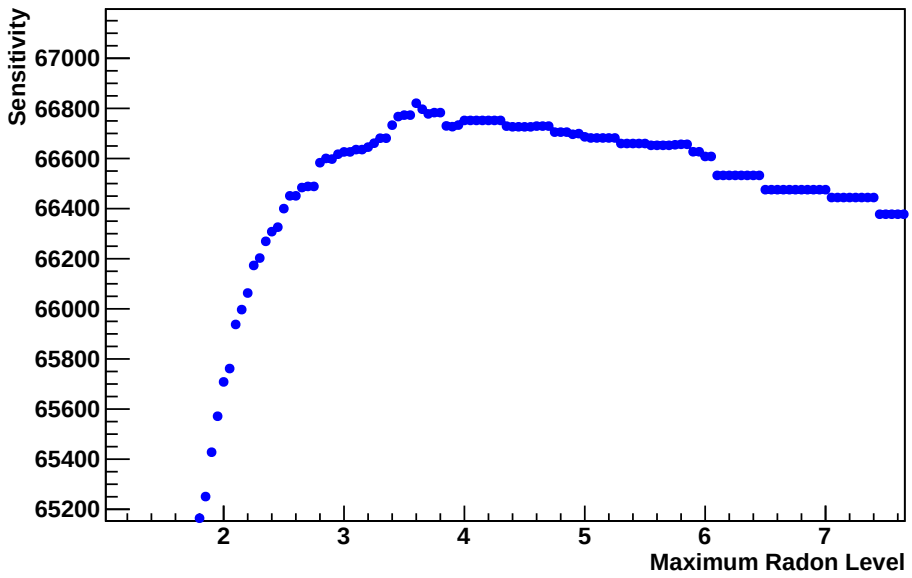

Figure 4.5: Sensitivity of $2\nu\beta\beta$ measurement as a function of maximum allowed radon level.

experiment, most likely due to a failure of the system designed to flush the experimental volume with clean N_2; these periods, comprised of runs 820–829 and 857–925 were therefore excluded from the analysis (Fig. 4.4).

4.1.3 Detector performance in early runs

For a period of time in the earlier CUORICINO runs, one of the bolometers enriched in ^{128}Te (referred to as 128-A) exhibited an anomalously low rate of events at low energy (less than 500 keV), as shown in Fig. 4.6. In this time period, an excess of coincidence events was also observed for the 130-enriched bolometers relative to the 128-enriched ones, probably due to this loss of efficiency for detecting low energy events in 128-A. The event rate above 500 keV does not appear to be affected by this loss of efficiency; however, the average event rate is elevated in the early runs, and appears to be steadily decreasing until it reaches a plateau around run 450. This higher event rate could be due to elevated levels of radon in the vicinity of the detector, as indicated by Fig. 4.4; it could also be due to the presence of cosmogenic or other short-lived radioactive contaminants that decayed away after the start of CUORICINO. Due to these anomalies in the data, runs 174–450 (corresponding to the first 1/4 of the detector exposure time) were not included in the analysis.

One other notable feature of Fig. 4.6 is the presence of spikes in the event rate for low energy (<500 keV) events. These spikes are likely due to vibrations or electronic noise, which are unlikely to significantly affect the $2\nu\beta\beta$ fit because they are below the energy

threshold of 500 keV used for the fit. The accidental coincidence rate will increase during noisy time periods, but the cumulative loss of efficiency to accidental coincidences, measured as described in Sect. 4.2.3, is still less than 1%.

4.1.4 Pulse shape

An algorithm for identifying pulses which do not match the expected shape for signal events was applied to the data as described in Sect. 3.4. This algorithm produces a pulse shape parameter P which is much less energy dependent than the raw pulse shape parameters, allowing a single cut on P to be made at all energies.

Like the energy threshold cut (Sect. 4.1.1), the pulse shape cut was optimized based on 1/5 of the data to avoid biasing the analysis. For a given value of the pulse shape cut, the signal is proportional to the signal efficiency, $\epsilon_{\rm sig}$, and the background is proportional to the background efficiency, $\epsilon_{\rm bkg}$. The signal and background efficiencies were evaluated at several different energies using prominent peaks in the background spectrum. For each peak, the events accepted by the cut and the events rejected by the cut were fit simultaneously by a gaussian plus linear background, as shown in Fig. 4.7. The parameters $\epsilon_{\rm sig}$, and $\epsilon_{\rm bkg}$ were included directly in the simultaneous fit, such that signal yield for accepted events is $\epsilon_{\rm sig}N_{\rm sig}$ and the signal yield for the rejected events is $(1-\epsilon_{\rm sig})N_{\rm sig}$, where $N_{\rm sig}$ is the total number of signal events determined by the fit. Similarly, the background yields for accepted and rejected events are $\epsilon_{\rm bkg}N_{\rm bkg}$ and $(1-\epsilon_{\rm bkg})N_{\rm bkg}$, respectively.

The sensitivity was estimated from the signal and background efficiency as $\epsilon_{\rm sig}/\sqrt{\epsilon_{\rm bkg}}$. A plot of the sensitivity versus the maximum value of the pulse shape parameter P is shown in Fig. 4.8 for several different energies. Based on this result, a maximum value of $P_{\rm max} = 2$ was chosen for the pulse shape cut, which is the same value used in the standard CUORICINO analysis.

Given a pulse shape cut of $P < 2$, the efficiency was computed at several different energies with the technique described above, for each channel, using the entire dataset. The result is shown in Fig. 4.9.

4.1.5 Pileup with heaters

Pileup of pulses (the presence of more than one pulse within 4 second data acquisition window) is undesirable because it interferes with the ability of the optimum filter algorithm (Sect. 3.1) to accurately determine the pulse amplitude.

The probability that a pulse will occur within an interval ΔT of another pulse on the same channel is given by $1 - e^{r\Delta T}$, where r is the event rate on that channel. For a pileup window of $\sim$6 seconds (3 seconds before or after the pulse) and a typical single channel event rate of $\approx$1 mHz, the probability of an event piling up with another event is $\approx 0.6\%$.

The pulse shape cut eliminates most of the pileup events; the remaining fraction of events affected by pileup is negligible for the purposes of this analysis, as it is much smaller than other systematic and statistical uncertainties.

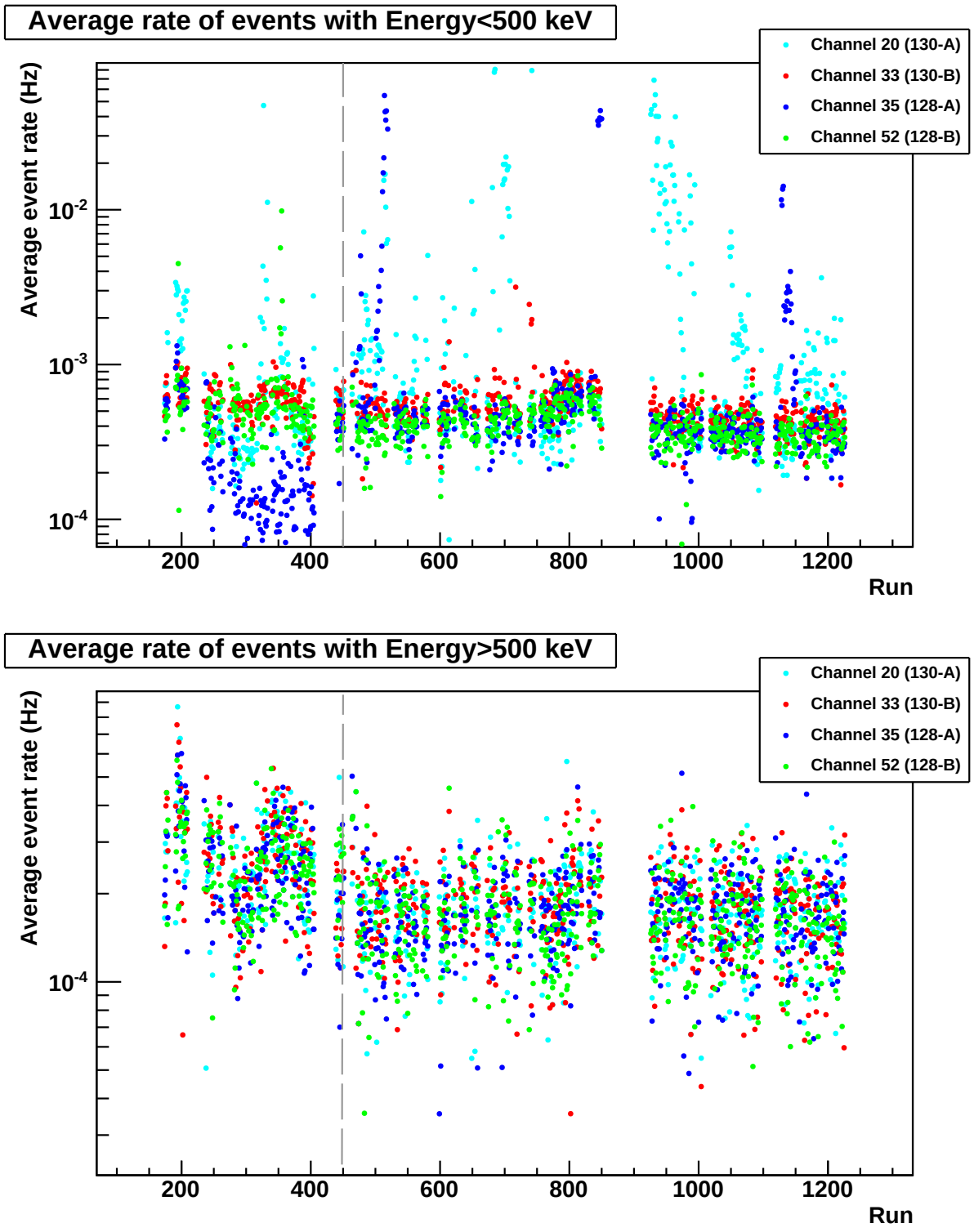

Figure 4.6: Average rate of events in the enriched bolometers above and below 500 keV. The dotted line indicates run 450; only runs after the line were included in the analysis.

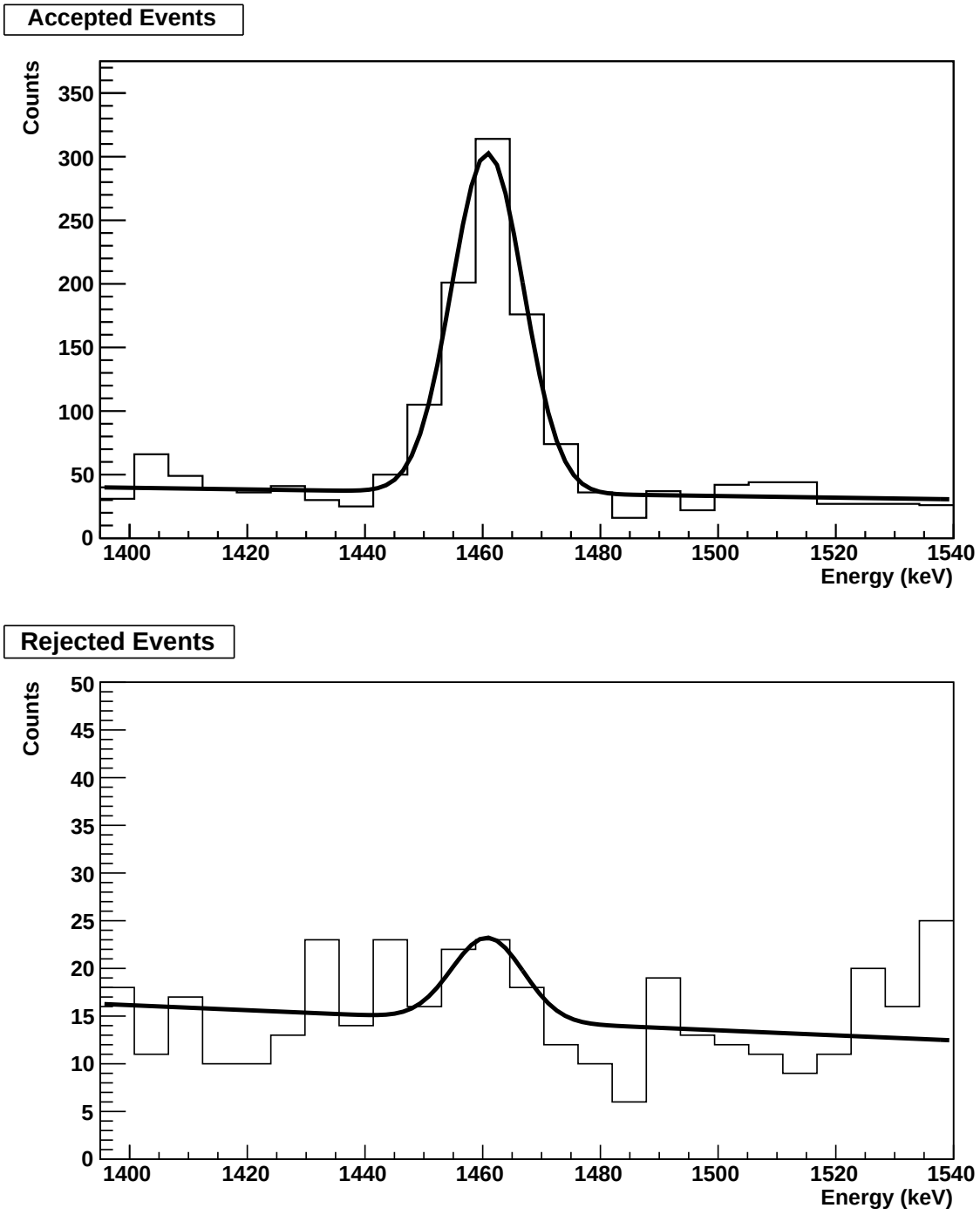

Figure 4.7: Simultaneous fit of accepted and rejected events used to determine the efficiency of the pulse shape cut. The fit returned a signal efficiency of of $97 \pm 1\%$ and a background efficiency of $71 \pm 1\%$..

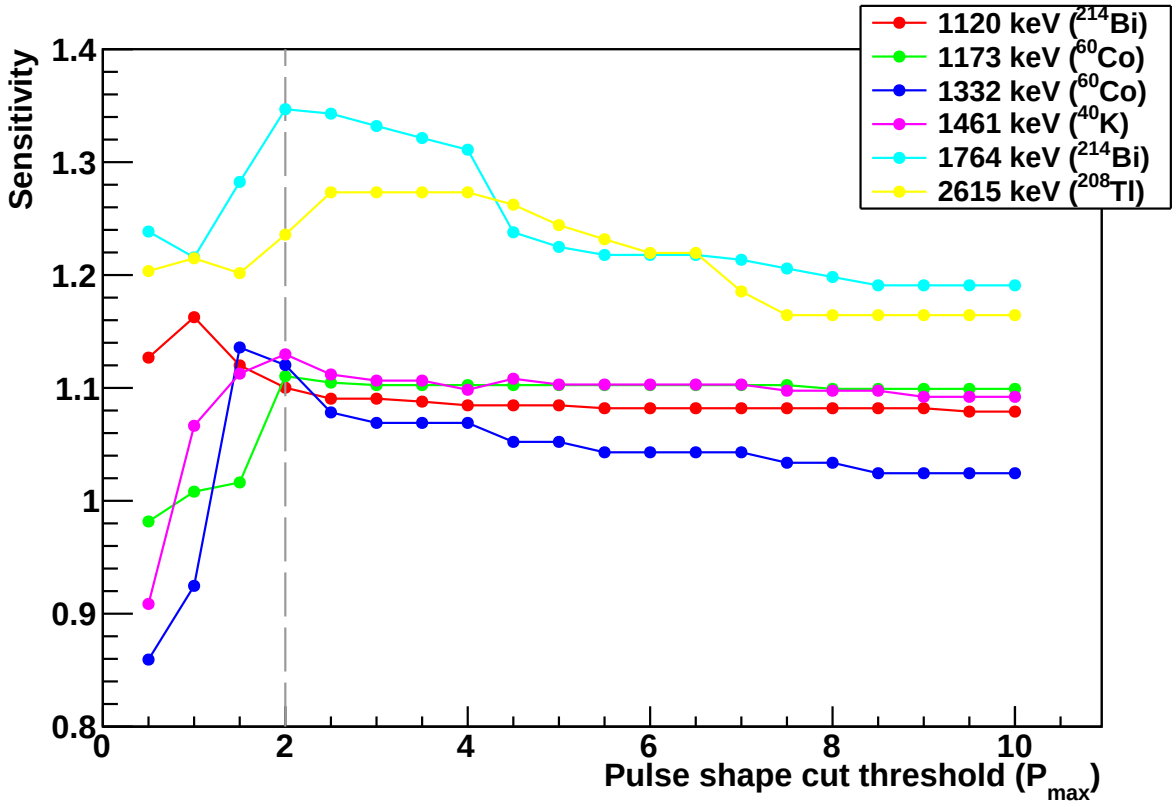

Figure 4.8: Experimental sensitivity as a function of pulse shape cut. A pulse shape threshold of $P_{\max} = 2$ was chosen for this analysis, marked with the gray dashed line.

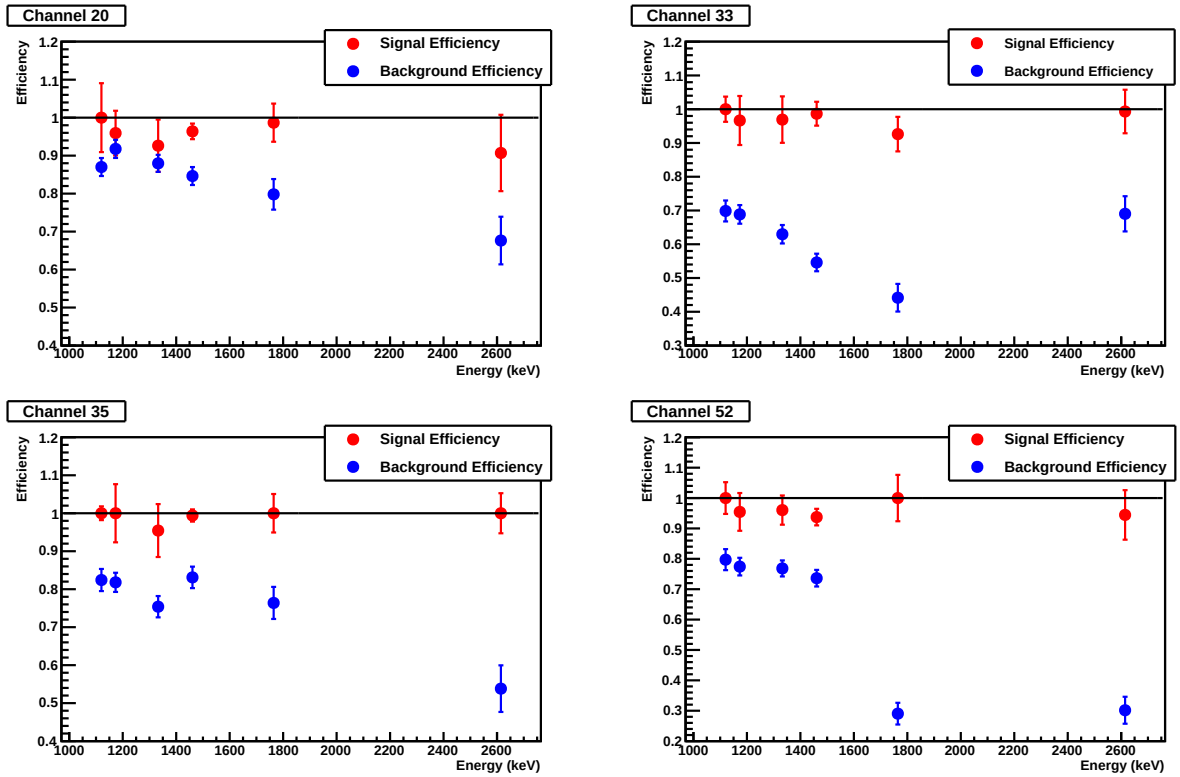

Figure 4.9: Efficiency of pulse shape cut $P < 2$ for signal and background.

In addition to pileup occurring between two ordinary (signal) events, a signal event may pile up with the pulsers used for gain stabilization (heater events), described in Sect. 3.2). Since the heaters fire at known times, the interval around each heater event can be vetoed and the consequent dead time can be calculated exactly. A dead time was imposed of 3.1 seconds before and 4 seconds after each heater pulse. The heaters fire once every 305 seconds, yielding an effective efficiency of $(305 - 7.1)/305 \approx 97.7\%$.

4.2 Construction of the subtracted spectrum

4.2.1 Data quality checks and removal of bad intervals of data

A number of checks were performed to ensure that the data included in the analysis were acquired during periods when the detector was operating normally. A tool called CUORE Online/Offline Run Check (CORC) was used identify problems with the detector operation, as described in [99]. The software computed basic quantities used to characterize the detector performance, such as the event rate and RMS baseline fluctuation for each channel, and stored those quantities in a database. The types of intervals which were considered "bad" for this analysis were the following:

Detector saturated Thermistor voltage too high or low, out of ADC range.

Inverted polarity Thermistor bias voltage reversed, causing pulses to appear upside-down.

No triggered events No signal events recorded in an anomalously long time interval, probably due to incorrect DAQ or electronics settings.

Noisy Excessive noise.

Unable to calibrate Calibration spectrum has no discernible peaks and cannot be calibrated.

Intervals marked with one of these flags in the CORC database not included in the analysis and their duration was subtracted from the total detector live-time. For the background subtraction to work correctly, all channels involved must have the same live-time. Furthermore, because the analysis considers coincidences between bolometers as a way to characterize the crystal surface contaminations, it is important that all the crystals adjacent to the crystals of interest are also functioning properly for the entire live-time. Therefore, bad intervals were removed in conjunction for all crystals in floors 11-13, such that if any crystal in those three floors had a bad interval, that interval was removed for all the channels. In this way, data were only included for which all 4 enriched bolometers and all their neighbors were functioning normally.

4.2.2 Resolution equalization

Subtracting the spectra of two detectors with different energy resolution can lead to artifacts in the residual spectrum. Therefore, a correction was made to equalize the resolution between the detectors. First, the average resolution of each detector was computed based on six gamma peaks in the region of interest, listed in Table 4.2. Each peak was fit with a gaussian plus linear background, with all parameters floating. The fit results are shown in Fig. 4.10(a).

Table 4.2: Lines used to compute the average resolution of each detector [11]

Source	Energy (keV)
^{214}Bi	1120.29
^{60}Co	1173.24
^{60}Co	1332.5
^{40}K	1460.83
^{214}Bi	1764.49
^{208}Tl	2614.53

The average measured resolution of each channel is listed in Table 4.3. A smearing was applied to each of the channels $i = \{33, 35, 52\}$ with a width

$$\sigma_i^{\text{correction}} = \left[\sigma_{20}^2 - (\sigma_i^{\text{measured}})^2\right]^{1/2}, \tag{4.3}$$

by adding to the energy of each event on channel i a random number sampled from a gaussian distribution of width $\sigma_i^{\text{correction}}$. Effectively, this procedure worsened the energy resolution of each channel to match the worst channel (channel 20). Because the $2\nu\beta\beta$ spectrum is extremely broad, a slight worsening of the energy resolution does not significantly affect the measurement sensitivity. The results of the resolution equalization are shown in Table 4.3 and Fig. 4.10(b).

Table 4.3: Average measured energy resolution (1σ) of each enriched bolometer in the $2\nu\beta\beta$ region of interest, before and after a correction was applied to equalize the resolutions.

Crystal	Channel	Energy Resolution (keV)	
		Before	After
130-A	20	7.73	7.73
130-B	33	4.46	7.31
128-A	35	4.82	7.23
128-B	52	3.53	5.93

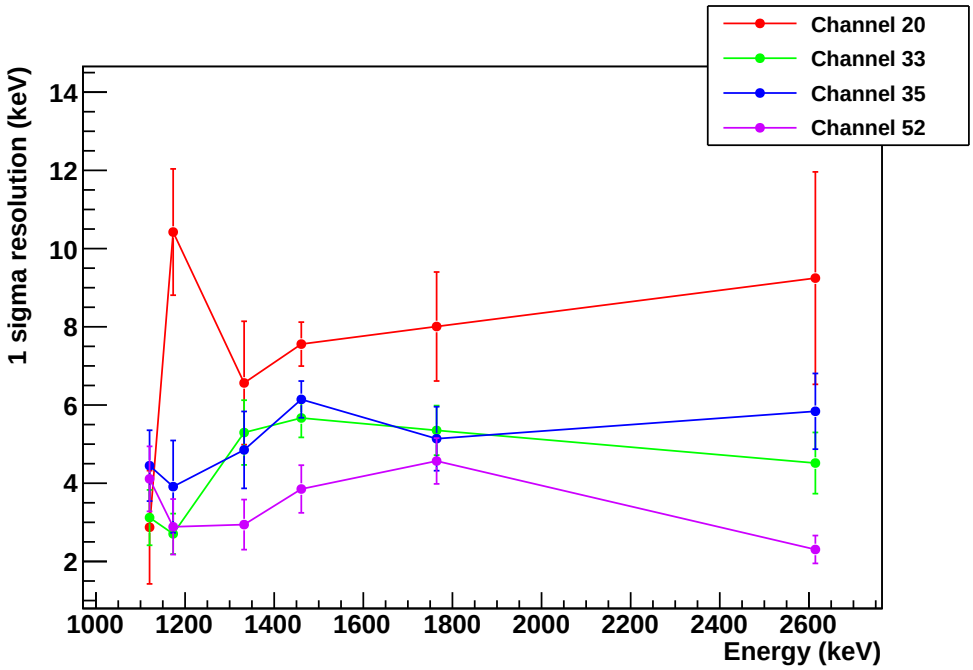

(a) Measured resolutions before resolution equalization correction

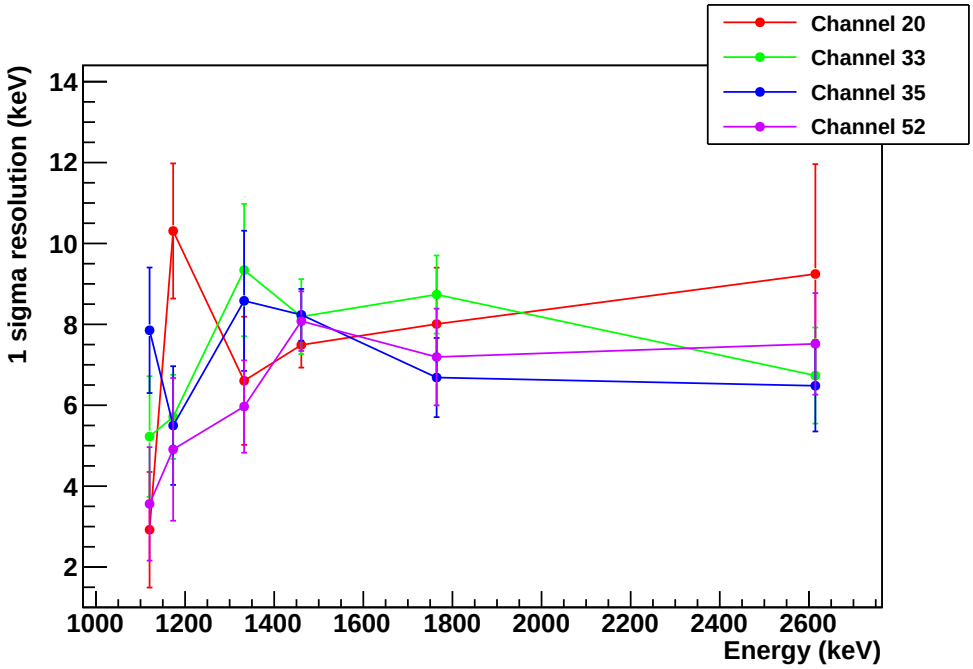

(b) Measured resolutions after resolution equalization correction

Figure 4.10: Resolution of the enriched bolometers as determined from fits of the gamma peaks listed in Table 4.2.

4.2.3 Coincidences

Most of the time, if a double beta decay occurs within a detector crystal, both electrons will be fully absorbed in the crystal where the decay occurred. On the other hand, many backgrounds, such as surface alphas, Compton-scattered photons, and cosmic ray muons or showers, may deposit their energy in multiple crystals almost simultaneously. For this reason, studying coincidences between events in different detectors can be a powerful tool for characterizing the backgrounds and discriminating signal from background.

For the purpose of studying coincidences, events were grouped into multiplets. A multiplet was defined as a set of signal (non-heater) events on different bolometers for which each event occurred within 100 ms of the previous event, and all events passed the following cuts:

- Minimum energy threshold: $E > 60\,\mathrm{keV}$
- Pulse shape cut: $(P < 3)$

Events were then classified by their multiplicity, i.e. the number of events in the multiplet containing that event.

Three spectra were produced:

Multiplicity 1 (M1) Energy spectrum of single-crystal events which did not occur in coincidence with any other events.

Multiplicity 2 (M2) Energy spectrum of events which occurred in coincidence with one other event on a different crystal.

Multiplicity 2 total energy (M2Tot) Spectrum of the total energy of pairs of events occurring in coincidence.

When performing a coincidence analysis, there is some chance of events being mistakenly assigned a higher multiplicity due to accidental (random) coincidences. The probability of an accidental coincidence between two events is given by

$$P(\text{accidental}) = 1 - e^{-2r\Delta t} \tag{4.4}$$

where r is the overall event rate and Δt is the time window used to define a coincidence (any event occurring within $\pm\Delta t$ of a given event is defined to be "in coincidence" with that event). Therefore, the fraction of events involved in accidental coincidences should be

$$1 - e^{-2r\Delta t} \approx 2r\Delta t \approx 1\% \tag{4.5}$$

for typical values of $r = 56\,\mathrm{mHz}$ and $\Delta t = 100\,\mathrm{ms}$.

To evaluate the probability of accidental coincidence more precisely, a simultaneous fit was performed of the ^{40}K line at 1461 keV in the anticoincidence (Multiplicity = 1) and coincidence (Multiplicity > 1) spectra. The 1461 keV gamma line comes from the electron-capture decay of ^{40}K, and is not expected to occur in coincidence with any other physical

event. Therefore, if this line is present in the coincidence spectrum, it is due to accidental coincidences. In this fit, the "signal" was represented by a gaussian line shape centered at 1461 keV, and the background was represented by a first order polynomial. The signal yields in the coincidence and anticoincidence spectra were proportional to $P^{\rm sig}_{\rm coinc}$ and $(1 - P^{\rm sig}_{\rm coinc})$, respectively. Similarly, the background yields were proportional to $P^{\rm bkg}_{\rm coinc}$ and $(1 - P^{\rm bkg}_{\rm coinc})$.

The fit, shown in Fig. 4.11, returned values of $P^{\rm sig}_{\rm coinc} = (0.3 \pm 0.9)\%$ and $P^{\rm bkg}_{\rm coinc} = (21 \pm 1)\%$ for the probability of coincidences in the signal and background components of the spectrum. The value $P^{\rm sig}_{\rm coinc}$ may be interpreted as the probability of accidental coincidences in the detector. Because this value was much smaller than the other statistical and systematic uncertainties of the experiment, it was not considered in the analysis.

4.2.4 Adaptive binning algorithm

When performing fits to binned data, it is beneficial to choose appropriately sized bins. If the bins are much smaller than the scale of the signal variation, the bin to bin fluctuations will be increased without adding any meaningful information to the fit. On the other hand, if the bins are too large, useful information about the spectrum shape will be lost.

Unfortunately, the characteristic scale over which the signal varies is not constant. The $2\nu\beta\beta$ signal is slowly varying over the entire energy region from 0 to 2528 keV; however, the alpha peaks form much more quickly varying structures at higher energy. In order to accommodate the variation in signal size and shape at different energies, the following adaptive binning procedure was used.

1. Base binning: For the alpha region, a base binning of 20 keV was used, since this is on the order of the energy resolution in the alpha region. For the $2\nu\beta\beta$ signal region, a larger binning of 40 keV was used, due to the slowly varying nature of the signal.

2. Minimum bin content: The spectra of the four enriched crystals were summed into a histogram using the base binning. Starting from zero and working up to 8000 keV, if any bin had fewer than 50 counts, it was combined with the next bin until the number of counts was ≥ 50. This minimum bin content was chosen to be large enough that the error on the bin content may be safely approximated as gaussian.

3. ^{190}Pt peak: The energy region from 3200 – 3600 keV was placed in one large bin to contain the peak produced by α decay of ^{190}Pt, for reasons discussed in Sect. 4.3.1.

4. Scaling by bin width: The number of events in each bin (n_i) was divided by the bin width (w_i) to produce a representation of the event rate density in counts/keV, so that the bin content c_i was given by $c_i = n_i/w_i$.

5. Error bars: If there are n_i events in bin i, the uncertainty on n_i is given by $\sigma_{n_i} = \sqrt{n_i}$. Since the bin contents c_i are scaled by the bin width w_i, the error bar on the bin content is given by $\sigma_{c_i} = (1/w_i)\sqrt{n_i}$.

The resulting histograms are shown before and after subtraction in Figs. 4.12–4.14.

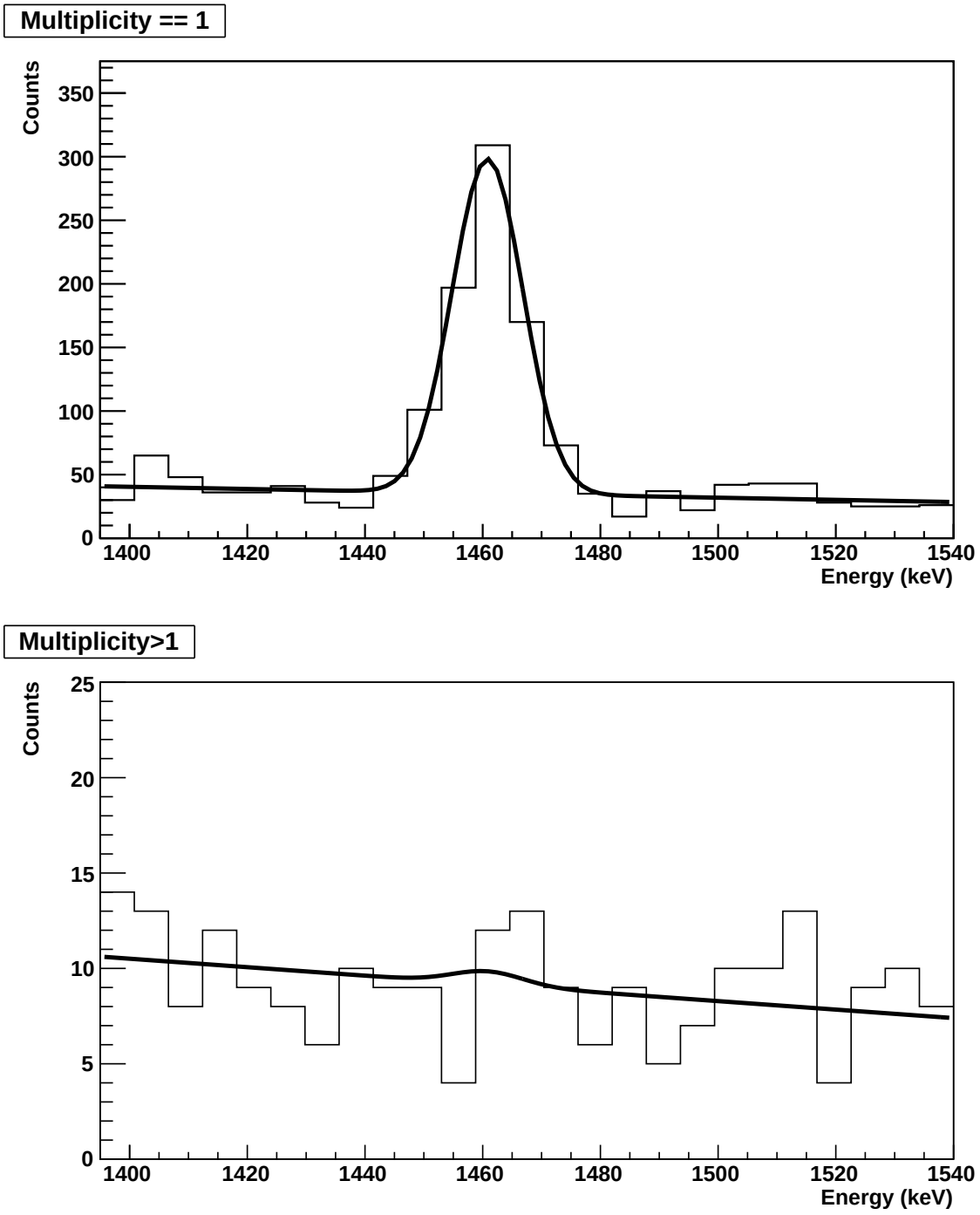

Figure 4.11: Simultaneous fit of coincidence and anticoincidence spectra used to determine the probability of accidental coincidences. The fit returned an accidental coincidence probability of $0.3 \pm 0.9\%$.

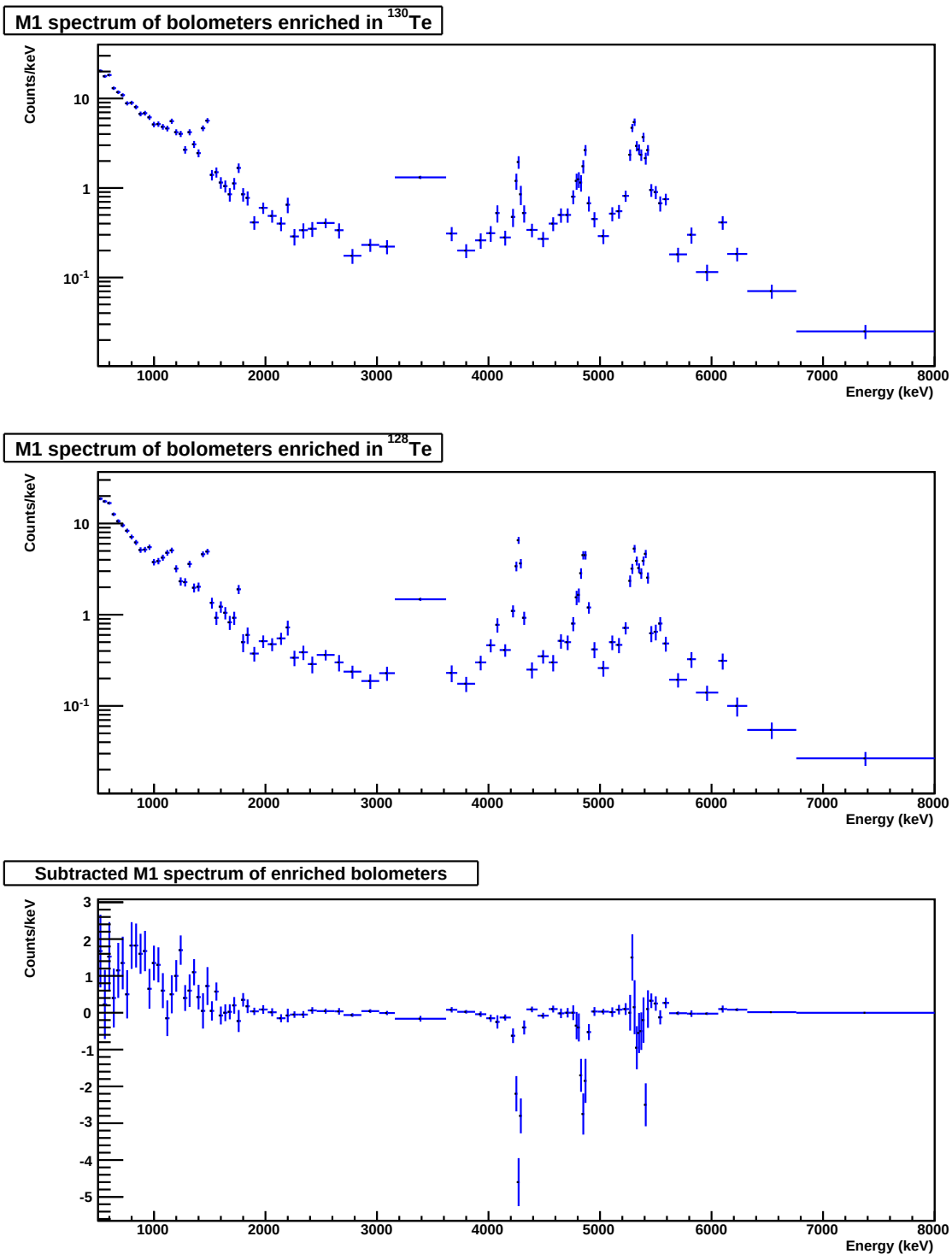

Figure 4.12: Histogram of multiplicity 1 (M1) events in the enriched bolometers. The bottom histogram is produced by subtracting the M1 spectrum of the 128-enriched bolometers from that of the 130-enriched bolometers.

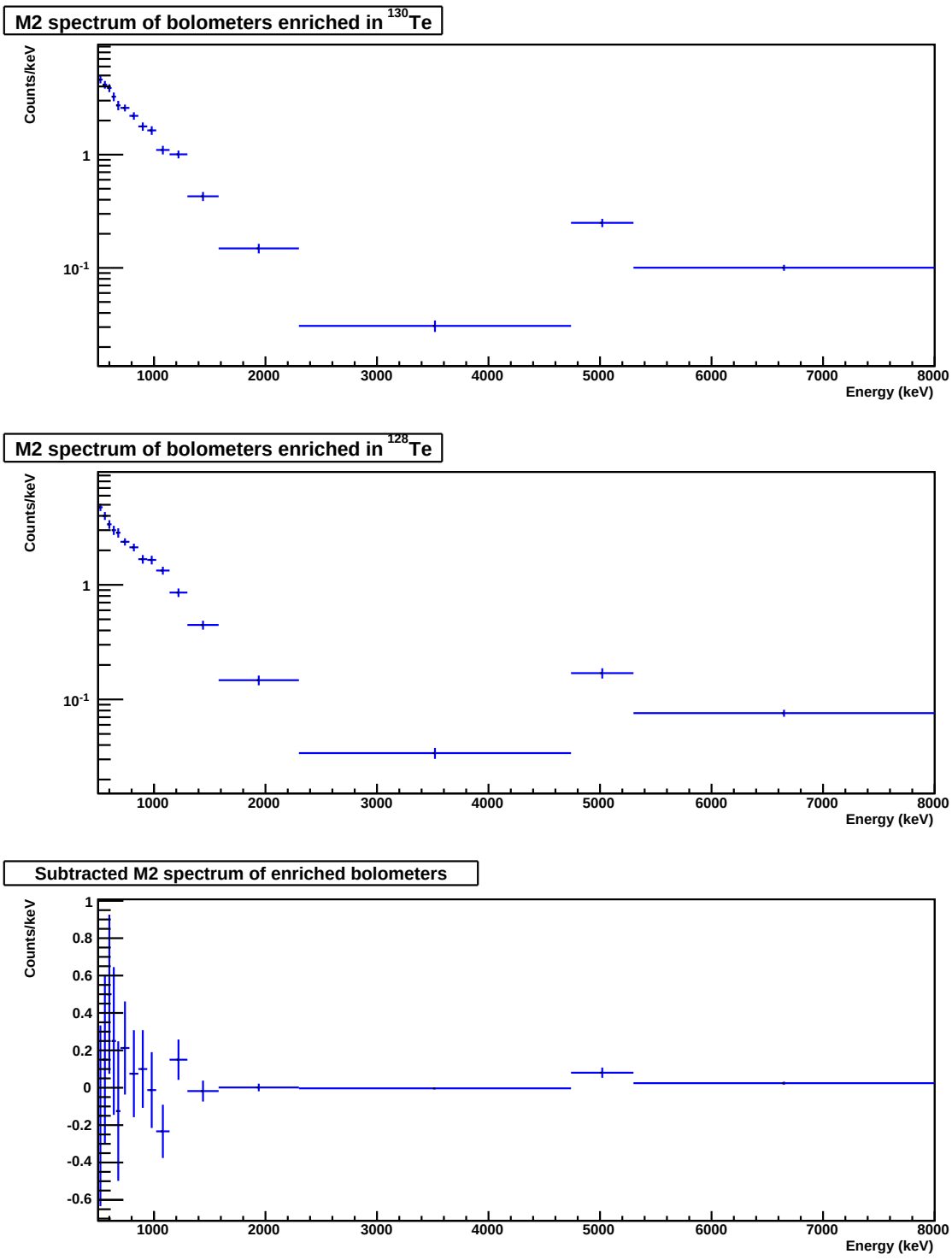

Figure 4.13: Histogram of multiplicity 2 (M2) events in the enriched bolometers. The bottom histogram is produced by subtracting the M2 spectrum of the 128-enriched bolometers from that of the 130-enriched bolometers.

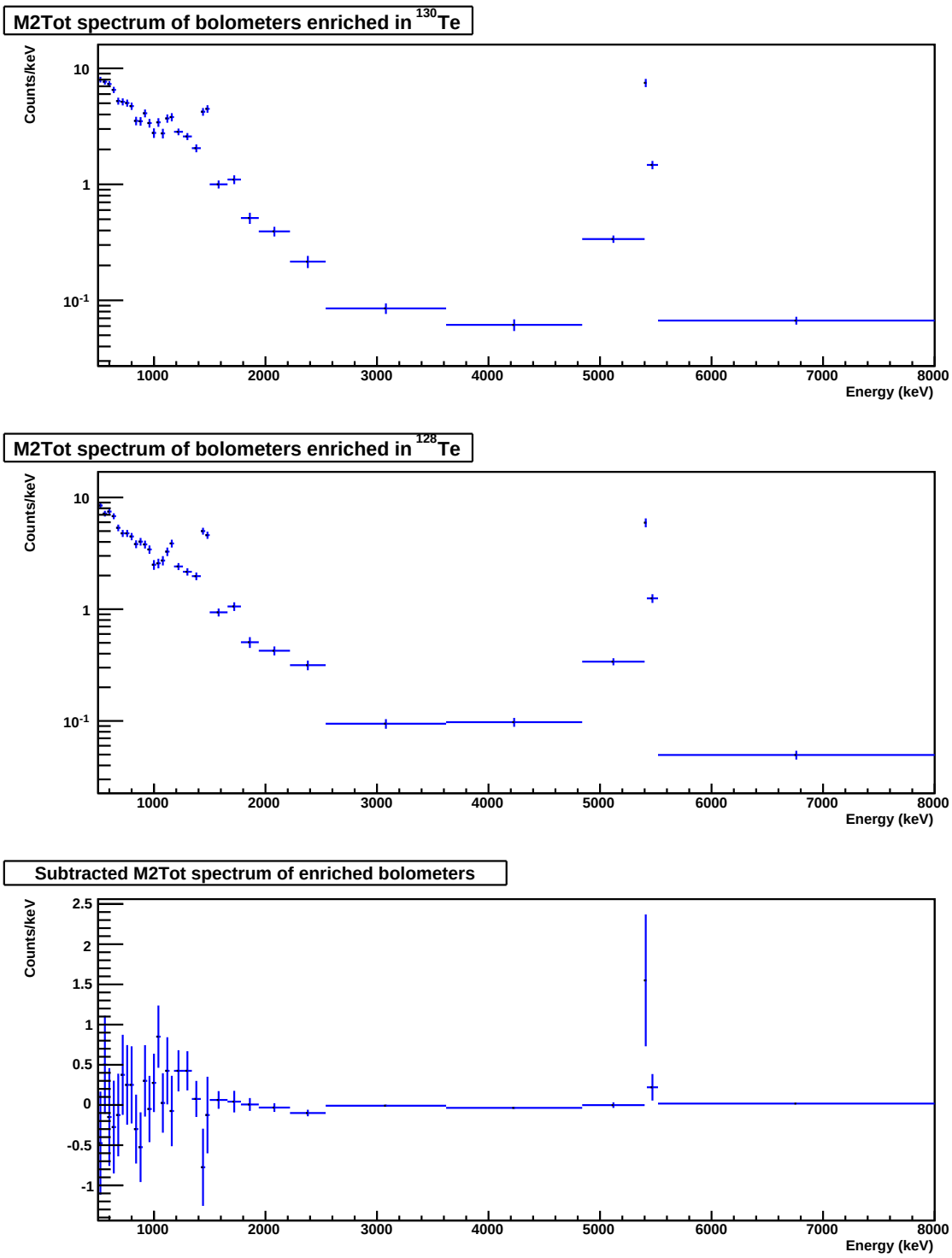

Figure 4.14: Histogram of the total energy of multiplicity 2 pairs of events (M2Tot) in the enriched bolometers. The bottom histogram is produced by subtracting the M2Tot spectrum of the 128-enriched bolometers from that of the 130-enriched bolometers.

4.3 Sources of background

There are a number of sources which can produce background in the CUORICINO detector, listed below.

Bulk and surface contaminations Contaminations of the detector and surrounding materials with naturally-occurring radioactive isotopes, mainly ^{40}K and isotopes in the ^{238}U and ^{232}Th decay chains.

Cosmogenic activation of detector materials Long-lived activation products of Te, Cu, and other materials (including Te isotopes, ^{60}Co, ^{124}Sb, ^{125}Sb, and ^{3}H).

Cosmic rays Cosmic ray muons and showers.

Environmental neutrons Neutrons from spontaneous fission, (α,n) reactions and cosmic ray interactions in the LNGS environment.

Environmental gammas Gammas from natural radioactivity in the LNGS environment (primarily ^{40}K and ^{238}U and ^{232}Th chains).

Most of these sources of background affect all the CUORICINO bolometers uniformly, and can therefore be eliminated by subtracting the spectra of the enriched bolometers as described in the previous sections. However, in the subtracted spectrum shown in Fig. 4.12, there are clearly some residual backgrounds which are not completely canceled by the background subtraction. In particular, there are a number of pronounced peaks in the alpha region of the spectrum (3000-8000 keV). Due to the short range of alpha particles, these peaks must come from contaminations located in the crystals or the immediately adjacent materials. Moreover, the presence of peaks at the alpha decay Q values implies a contamination located in the crystals themselves, since the full energy of the decay was captured in the crystals.

In the $2\nu\beta\beta$ region of interest (ROI), on the other hand, there are no statistically significant peaks remaining after background subtraction. The peaks in this region are due to gammas, which have a longer range and are more likely to come from farther away in the cryostat, shields, or surrounding environment, leading to more uniform coverage of the crystals.

However, even though there are no visible gamma peaks in the ROI after background subtraction, there may still be a residual contribution to the continuum from betas and degraded alphas. Since they do not form peaks, these contributions must be inferred based on the alpha peaks which are visible at higher energies. With the exception of the line from ^{190}Pt at 3250 keV, all the visible alpha peaks can be accounted for by decays in the ^{238}U and ^{232}Th decay chains (Figs. 4.15 and 4.16).

Because most of the decays in these two chains have half-lives which are much shorter than the duration of the CUORICINO experiment, there are only a few places where the decay chain could be out of secular equilibrium. For the purposes of this analysis, the ^{238}U

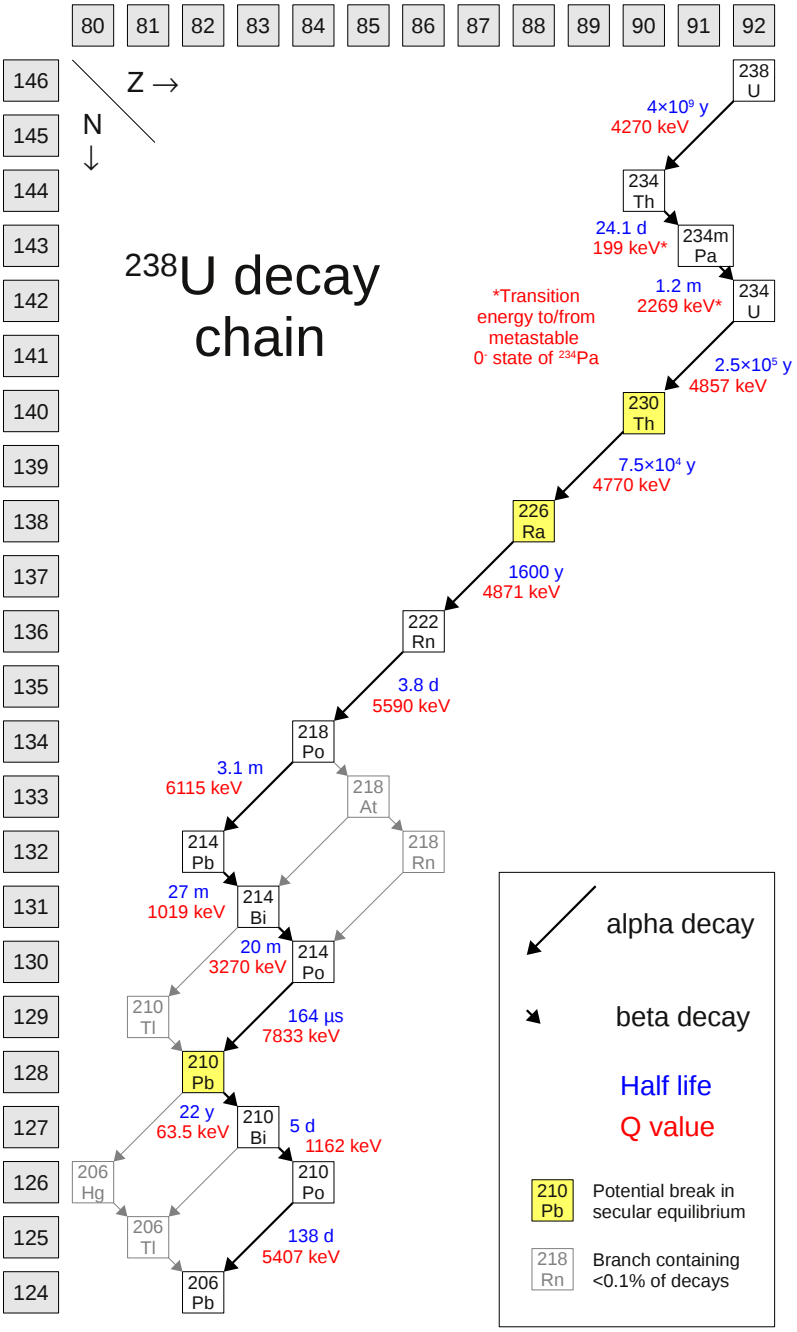

Figure 4.15: Overview of the ^{238}U decay chain. Isotopes marked in yellow are where the decay chain was broken for the purposes of this analysis, as described in the text. Half lives and decay energies taken from [11].

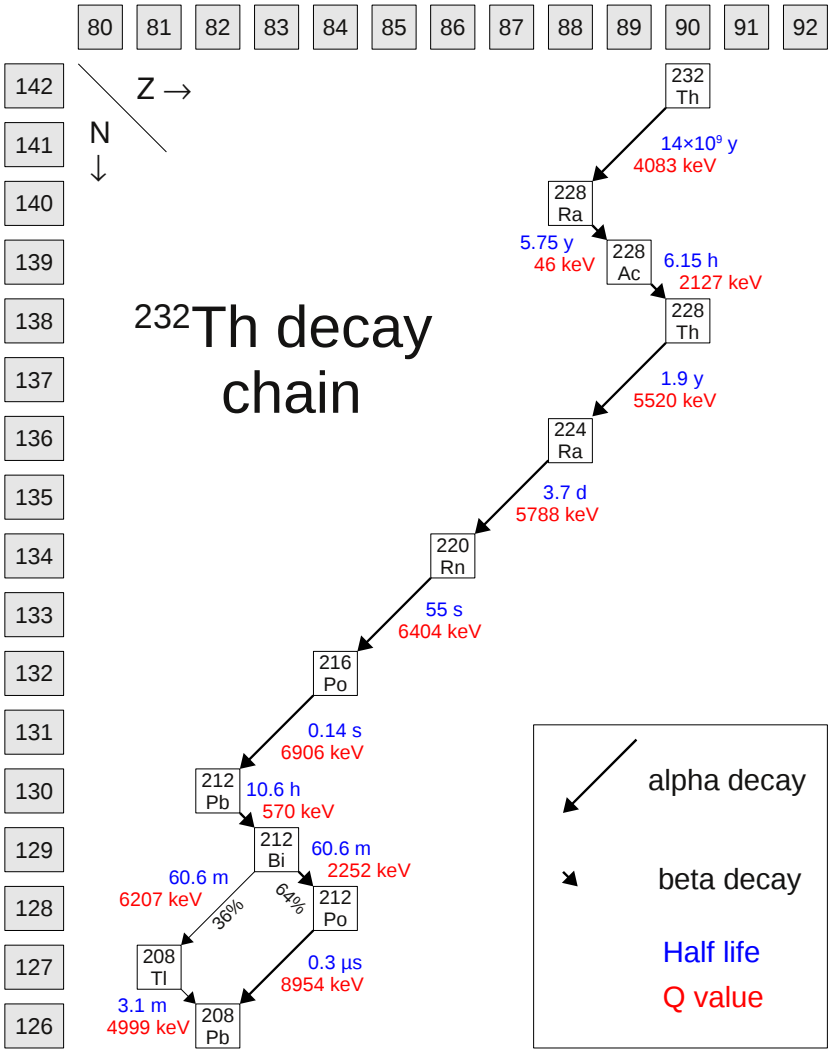

Figure 4.16: Overview of the ^{232}Th decay chain. Half lives and decay energies taken from [11]

decay chain was broken at three places, such that the segments ^{238}U$\rightarrow^{230}$Th, ^{230}Th$\rightarrow^{226}$Ra, ^{226}Ra$\rightarrow^{210}$Pb, and ^{210}Pb$\rightarrow^{206}$Pb were considered independently. In principle, there could also be a break in the chain at ^{234}U; however, this is less likely, since ^{238}U and ^{234}U should be affected similarly by any chemical processes that would add or remove contaminants from the crystals.

The ^{232}Th decay chain was taken to be entirely in secular equilibrium. The chain could potentially be broken at ^{228}Ra ($T_{1/2}$ = 5.75 y) or ^{228}Th ($T_{1/2}$ = 1.9 y), but allowing for these breaks in equilibrium does not significantly affect the outcome of the analysis due to the small number of events attributable to the ^{232}Th chain and the fact that the half-lives involved are relatively short.

The shape of the spectrum recorded in the detector due to the presence of a given alpha emitter is strongly dependent on the location of the contaminating material. A surface contamination produces a very different signature in the detector than a bulk contamination of the crystals. Furthermore, the depth of the surface contamination affects the shape of the alpha peaks and the ratio of peak to continuum backgrounds. The general characteristics of alpha backgrounds due to bulk and surface contaminations are described below:

Bulk contamination of crystals

- Appears in M1 spectrum with negligible contribution to M2 spectrum
- Peak at Q value of alpha decay
- Alpha peaks have a symmetric shape

Surface contamination of crystals

- Peaks appear in M1 and M2 spectra
- Peak at alpha energy in M2 spectrum and at Q value in M2Tot spectrum
- Asymmetric peaks (low energy tail due to partial loss of alpha energy before escape)

Surface contamination of facing materials

- Peaks appear only in M1 spectrum
- Peaks at alpha energy (not Q value)
- Asymmetric peaks (low energy tail due to partial loss of alpha energy before escape)

The alpha peaks in the residual spectrum can be well described considering only contributions from bulk and surface contaminations of the crystals. In order to account for different possible depths of crystal surface contamination, Monte Carlo simulations were performed introducing surface contaminations with characteristic depths ranging from 5 nm to 200 μm. These simulations were used to build a fit function as described in Sect. 4.4.1.

4.3.1 Platinum peak

^{190}Pt is a naturally occurring isotope of platinum with an abundance of 0.01%. It decays via alpha emission with a Q value of 3250 keV to ^{186}Os, a long-lived isotope with $T_{1/2} = 2.0 \times 10^{15}$ y [11]. Platinum may be introduced into the crystals during production, as the crystals are grown in Pt crucibles.

A peak exists in the energy spectrum of all the CUORICINO bolometers in the vicinity of 3250 keV which is attributed to the presence of ^{190}Pt. There are no other long-lived alpha emitters with an energy within $\sim$ 100 keV of the observed peak which could provide a plausible alternative source for these events.

The 3250 keV peak exhibits some anomalous features. Firstly, it does not appear at exactly the same energy on all channels Fig. 4.17 It has a high energy tail, which is more pronounced on some channels than others. This high energy tail appears to be due to anomalies in the pulse shape causing an error in the evaluation of the pulse amplitude. As shown in Fig. 4.18, the evaluated energy of events in this peak is correlated with the pulse shape parameter P.

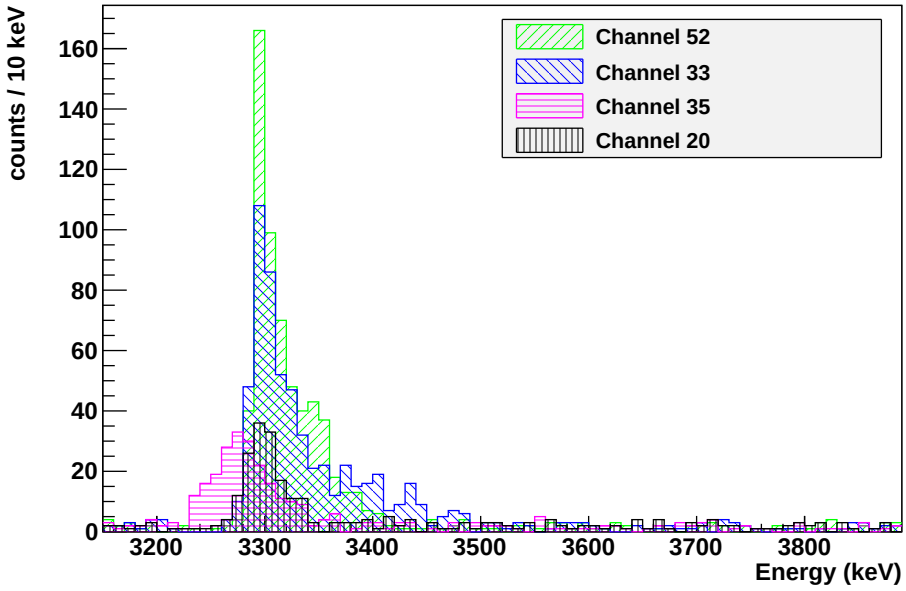

Figure 4.17: Discrepancy in the apparent energy of the ^{190}Pt alpha line between channels (the nominal energy is 3250 keV).

Because the peak appears only in the M1 spectrum, it is likely to be due to a bulk (rather than surface) contamination of the crystals. One hypothesis for the anomalous pulse shape of the ^{190}Pt events is that the platinum forms discrete inclusions inside the crystals, having different thermal properties than the host TeO_2. This could cause the energy emitted in a

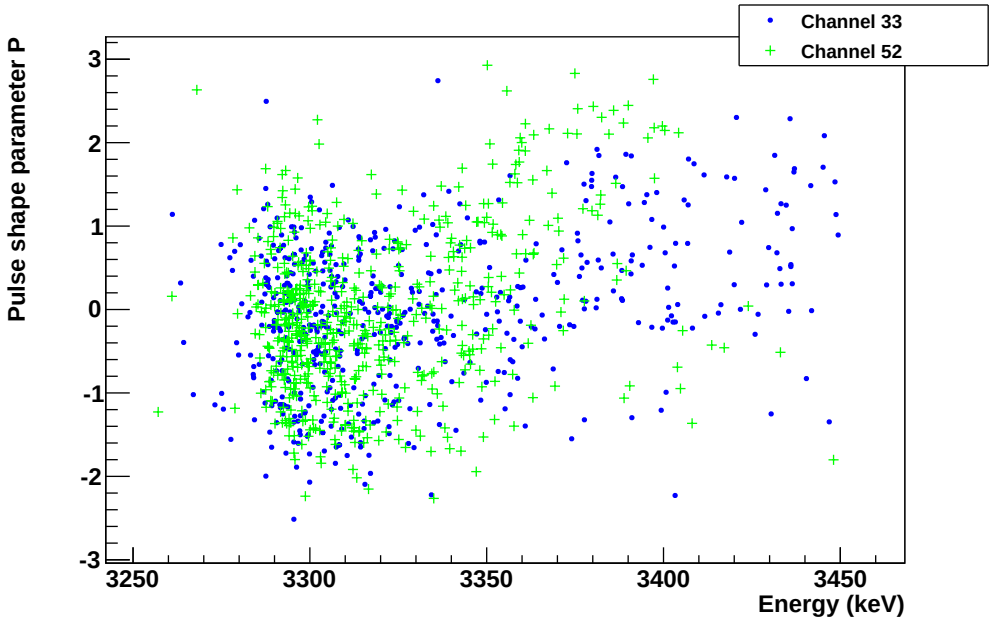

Figure 4.18: Correlation of the evaluated energy of events in the ^{190}Pt alpha line with the pulse shape parameter P.

decay to be absorbed differently, leading to a subtle difference in the pulse shape of those events.

In order to compensate for the inconsistencies in shape and energy of the peak between channels, a single large bin was used from 3200–3600 keV, encompassing the bulk of the peak on all channels.

Because this decay emits only a single alpha particle, which is almost always fully contained within the crystal and is unaccompanied by any gamma or beta decays, it contributes virtually no background in the double beta decay region of interest. It is included in the fit for completeness, along with the other identified background components.

4.4 Fit procedure

4.4.1 Constructing fit PDFs from Monte Carlo simulation

Each component of the residual background described in Sect. 4.3 was simulated using a Monte Carlo simulation based on GEANT4, a C++ based physics simulation toolkit widely used in particle physics [100]. The simulation software, described extensively in [101], included a detailed representation of the CUORICINO detectors, cryostat, and shields, and used a physics list based on the standard Low Background Experiments (LBE) physics list

for GEANT4. This software is the standard software used for CUORICINO background simulations, and has been well tested and vetted against experimental data.

The simulation allowed radioactive contaminations to be introduced at various locations in the detector and surrounding materials. Each simulated decay chain began with a single parent isotope placed at a random location in the detector, according to the distribution specified. Bulk contaminations were uniformly distributed in a given detector part, while surface contaminations were distributed with an exponential density profile (truncated at a depth of 1 mm). For each simulated parent nucleus, all the successive decay products were simulated using the appropriate branching ratios and half-lives, until a stable decay product was reached or a break in the decay chain was specified. For each interaction depositing energy in a crystal, the simulation recorded the detector number, the amount of energy deposited, and the time of the event relative to other events in the same chain.

After the raw data from the simulation was recorded, a second program was used to put the data in a form as similar as possible to the experimental data. This program accounted for the following effects:

Absolute timing The simulation software only recorded relative times between subsequent decays in a chain, but in order to analyze the simulated data using the same methods applied to the experimental data, events need to be assigned absolute times. This was accomplished by assigning the first event in each chain a random time, such that the average rate of chain-initiating events was 1 μHz. This rate was chosen to be very low so that the probability of accidental coincidences in the simulated data would be negligible.

Time resolution The time resolution of the CUORICINO detector was ∼20 ms. Any energy depositions in the same crystal occurring within 20 ms of each other were combined into a single event.

Energy resolution A gaussian smearing with a (1σ) width of 17 keV was applied. This is the average energy resolution of the enriched bolometers in the alpha region, which, for surface and bulk contaminations of the crystals, is the region where peaks are seen.

Coincidences A coincidence analysis was performed in the same manner as for the experimental data (coincidence window of 100 ms and energy threshold of 60 keV), as described in Sect. 4.2.3.

Monte Carlo simulations were performed for the $2\nu\beta\beta$ signal and background sources listed in Table 4.4. Surface contaminations were simulated at characteristic depths of 5 nm, 10 nm, 20 nm, 50 nm, 100 nm, 200 nm, 500 nm, 1 μm, 2 μm, 5 μm, 10 μm, 20 μm, 50 μm, 100 μm, and 200 μm. Spectra produced from the simulations are shown in Figs. 4.19 – 4.26. The radioactive sources were localized on one individual crystal representing the geometric location of the enriched crystals (due to the symmetric placement of the enriched crystals, they are geometrically equivalent). For the case of ^{210}Pb$\rightarrow^{206}$Pb, an additional contribution was simulated located on a crystal neighboring the enriched crystals, to account for an

observed excess of ^{210}Po activity in one of the adjacent crystals in the detector. Events originating in this crystal are largely responsible for the prominent ^{210}Po peak in the residual coincidence spectra (Figs. 4.13 and 4.14).

Table 4.4: List of simulated contributions to the energy spectrum. Surface contaminations were simulated using an exponential density profile with characteristic depths ranging from 5 nm to 200 µm.

Source	Location
$2\nu\beta\beta$ signal	Bulk only
^{238}U$\rightarrow^{230}$Th	Bulk and surface
^{230}Th$\rightarrow^{226}$Ra	Bulk and surface
^{226}Ra$\rightarrow^{210}$Pb	Bulk and surface
^{210}Pb$\rightarrow^{206}$Pb	Bulk and surface
^{210}Pb$\rightarrow^{206}$Pb	Neighbor crystal bulk and surface
^{232}Th chain	Bulk and surface
^{190}Pt	Bulk only

The energy of the simulated events was histogrammed using the same binning as the data histograms, for each of the three coincidence spectra (M1, M1, M2Tot). Each bin's contents were divided by the bin width and each histogram was normalized to the number of decay chains generated in the simulation, i.e. the value in bin i was given by

$$f_i = \frac{m_i}{w_i \cdot M}, \tag{4.6}$$

where m_i is the number of events in the bin, w_i is the width of the bin and M is the number of parent decays generated in the simulation. This histogram can be taken as a representation of the probability density function (PDF) for energy deposition in the crystals due to a particular radioactive source and depth profile.

Separate histograms were produced for each depth of contamination simulated. These histograms were then combined into a single PDF, parameterized by the depth, where the PDF value was interpolated between different simulated depths linearly in the log of the depth. In other words, the value of f_i at an arbitrary depth d, between two simulated depths d^+ and d^-, was given by:

$$f_i(d) = f_i(d^-) + \left(f_i(d^+) - f_i(d^-)\right)\left(\frac{\log(d) - \log(d^-)}{\log(d^+) - \log(d^-)}\right). \tag{4.7}$$

For the purposes of interpolation, bulk contaminations were assigned a depth of 2 cm.

There is an uncertainty associated with the value of the PDF in each bin due to the finite number of Monte Carlo samples used to construct the histogram. The uncertainty on the bin content for a histogram at a given simulated depth is

$$\sigma_{f_i} = \frac{\sqrt{m_i}}{w_i \cdot M}. \tag{4.8}$$

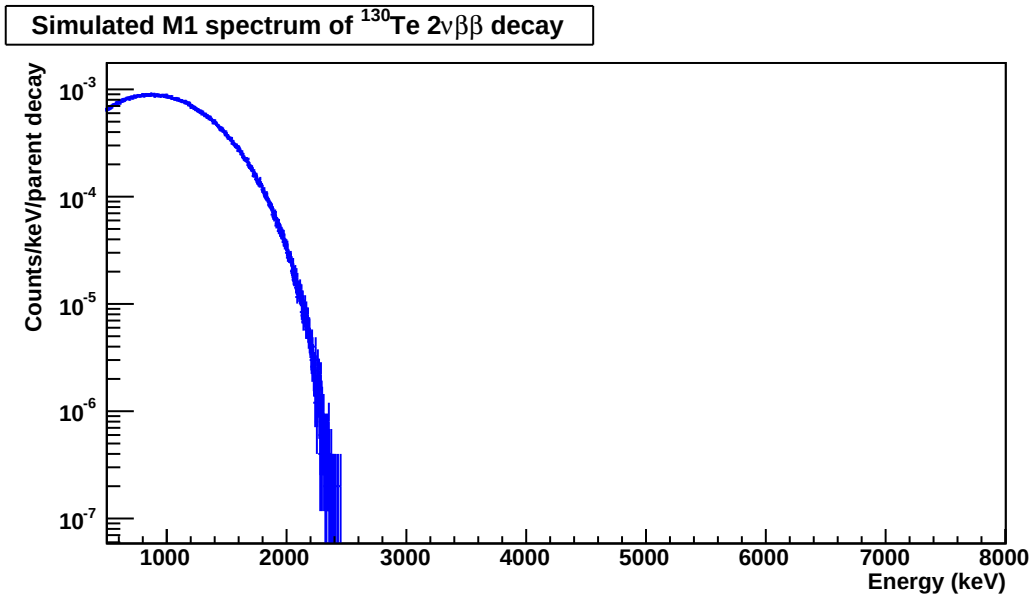

Figure 4.19: Output of the Monte Carlo simulation showing the spectrum produced by $2\nu\beta\beta$ of ^{130}Te in the enriched crystals.

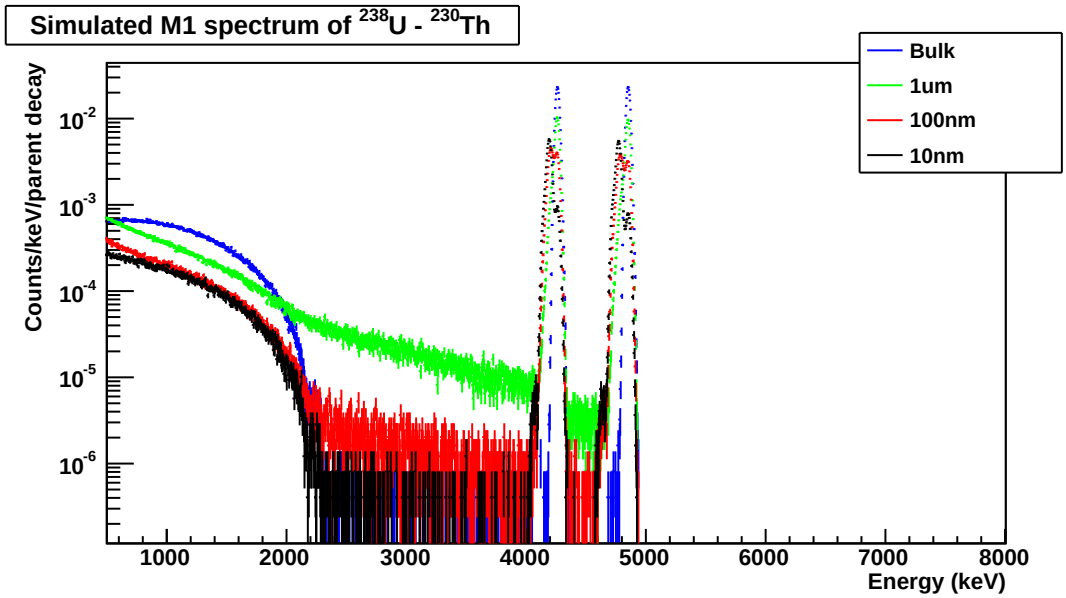

Figure 4.20: Output of the Monte Carlo simulation showing the spectrum produced in an enriched crystal by bulk or surface contaminations of that crystal by ^{238}U in secular equilibrium with its decay products down to ^{230}Th.

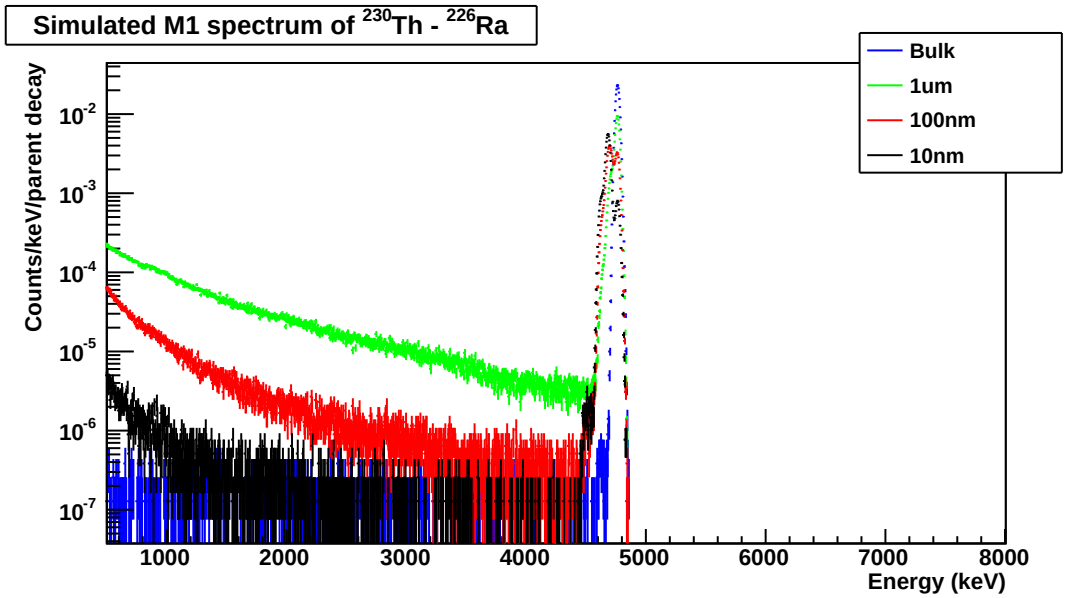

Figure 4.21: Output of the Monte Carlo simulation showing the spectrum produced in an enriched crystal by bulk or surface contaminations of that crystal by ^{230}Th decaying to ^{226}Ra.

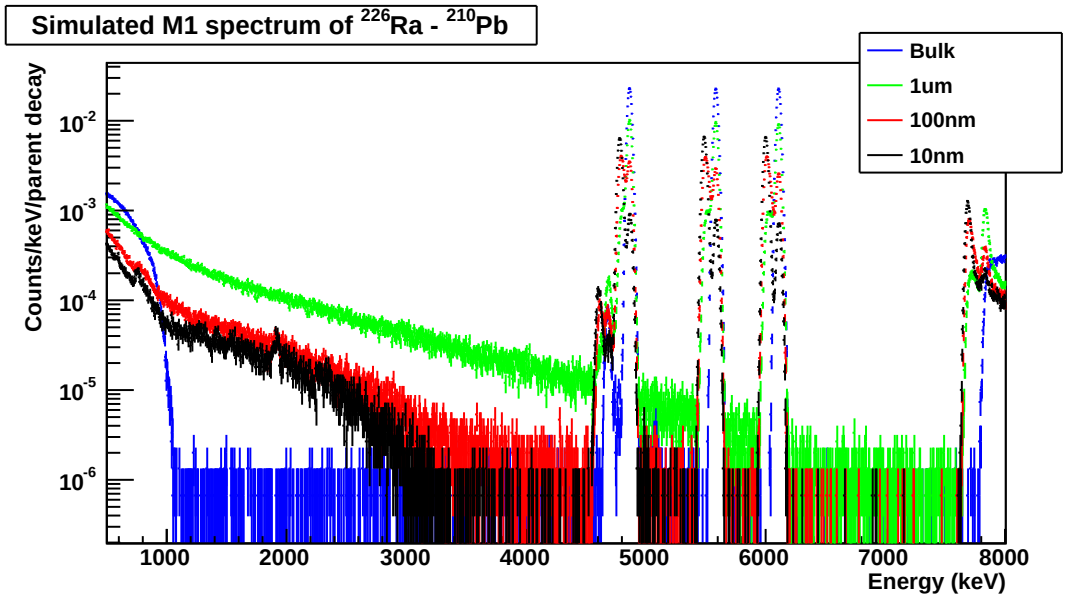

Figure 4.22: Output of the Monte Carlo simulation showing the spectrum produced in an enriched crystal by bulk or surface contaminations of that crystal by ^{226}Ra in secular equilibrium with its decay products down to ^{210}Pb.

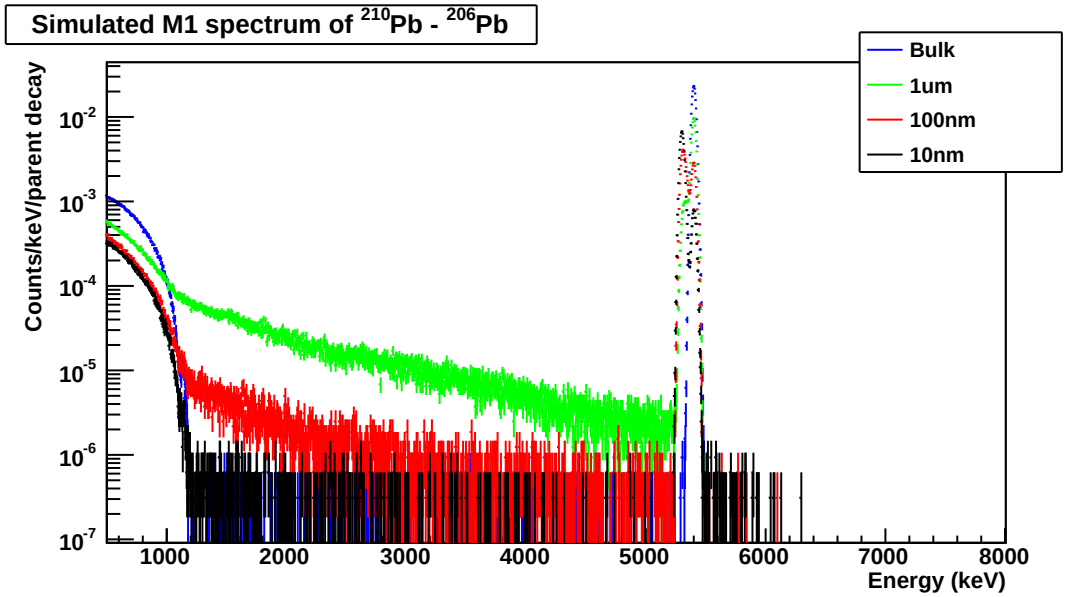

Figure 4.23: Output of the Monte Carlo simulation showing the spectrum produced in an enriched crystal by bulk or surface contaminations of that crystal by ^{210}Pb in secular equilibrium with its decay products.

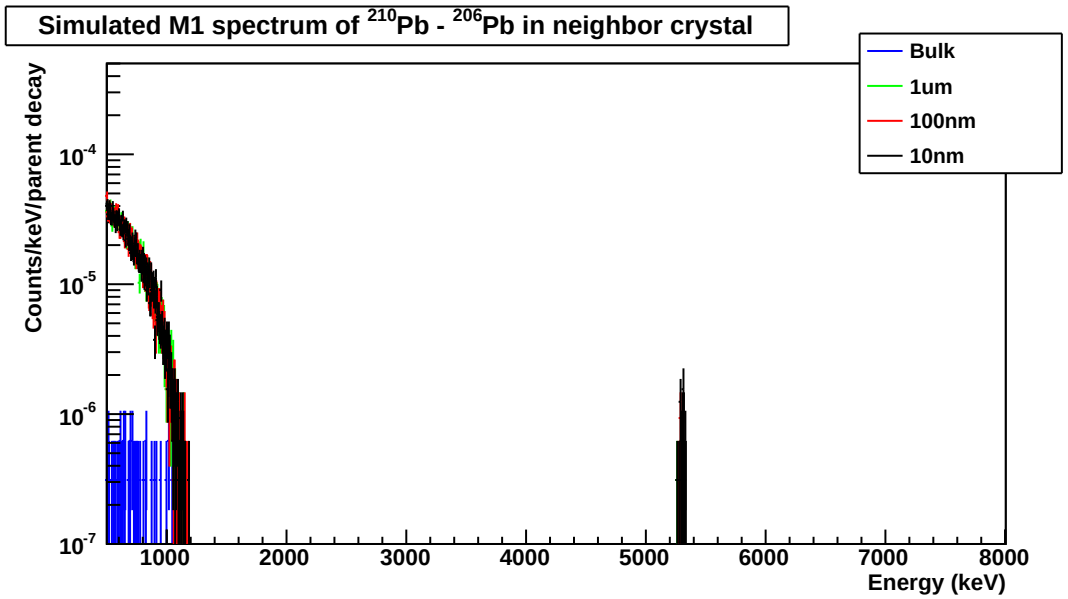

Figure 4.24: Output of the Monte Carlo simulation showing the spectrum produced in an enriched crystal by bulk or surface contaminations of a neighboring crystal by ^{210}Pb in secular equilibrium with its decay products.

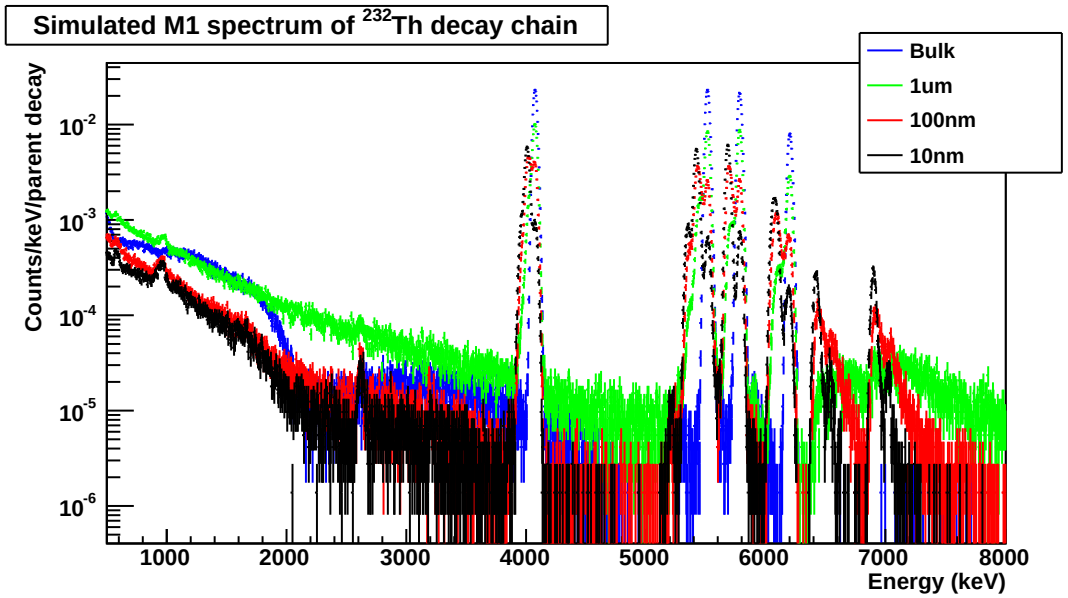

Figure 4.25: Output of the Monte Carlo simulation showing the spectrum produced in an enriched crystal by bulk or surface contaminations of that crystal by ^{232}Th and its decay products, in secular equilibrium.

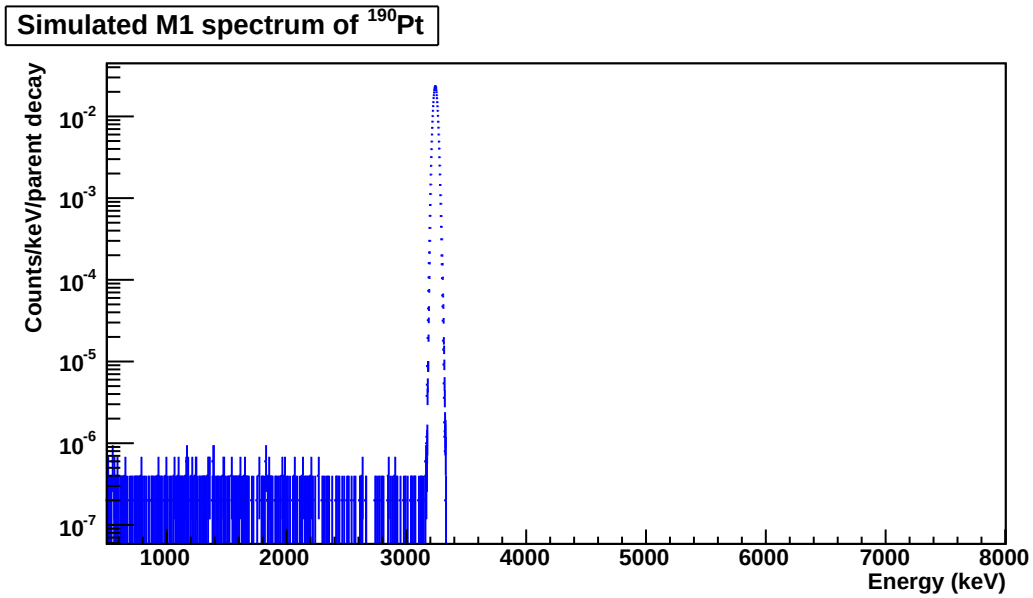

Figure 4.26: Output of the Monte Carlo simulation showing the spectrum produced in an enriched crystal by a bulk contamination of that crystal by ^{190}Pt.

The uncertainty was also interpolated for arbitrary depths, as described above.

4.4.2 Fit routine

A least squares fit was performed to fit the function described in Sect. 4.4.1 to the data. The fit was performed simultaneously on all three subtracted spectra (M1, M2, and M2Tot), using a modified χ^2 to account for the error introduced by the finite number of samples used to construct the fit function from Monte Carlo simulations.

Recall from section Sect. 4.2 that the data are described by a set of bins $\{i\}$ with content

$$c_i = \frac{1}{w_i}(n_i^{130} - n_i^{128}), \tag{4.9}$$

where n_i^{130} and n_i^{128} are the number of events in bin i in the 130-enriched spectrum and the 128-enriched spectrum, respectively, and w_i is the width of the bin. The uncertainty on the bin content, σ_{c_i} is then given by

$$\sigma_{c_i} = \frac{1}{w_i}\sqrt{n_i^{130} + n_i^{128}}. \tag{4.10}$$

The fit function F was a linear combination of the individual signal and background PDFs f constructed from Monte Carlo simulations as described in Sect. 4.4.1. The value of F in each bin i was given by:

$$\begin{aligned} F_i(\boldsymbol{\theta}) &= n_{2\nu\beta\beta} f_i^{2\nu\beta\beta} + n_{190\mathrm{Pt}} f_i^{190\mathrm{Pt}} + n_{232\mathrm{Th}} f_i^{232\mathrm{Th}}(d_{232\mathrm{Th}}) \\ &+ n_{238\mathrm{U}} f_i^{238\mathrm{U}}(d_{238\mathrm{U}}) + n_{230\mathrm{Th}} f_i^{230\mathrm{Th}}(d_{230\mathrm{Th}}) + n_{226\mathrm{Ra}} f_i^{226\mathrm{Ra}}(d_{226\mathrm{Ra}}) \\ &+ n_{210\mathrm{Pb}} f_i^{210\mathrm{Pb}}(d_{210\mathrm{Pb}}) + n_{210\mathrm{Pb\text{-}n}} f_i^{210\mathrm{Pb\text{-}n}}(d_{210\mathrm{Pb\text{-}n}}), \end{aligned} \tag{4.11}$$

where $\boldsymbol{\theta}$ represents the fit parameters: n_{source}, the number of decays, and d_{source}, the depth of the contamination, for each source listed in Table 4.4. The parameters were estimated by minimizing the following χ^2 function:

$$\chi^2 = \sum_i^{N_{\mathrm{bins}}} \frac{(c_i - F_i(\boldsymbol{\theta}))^2}{\sigma_{c_i}^2 + \sigma_{F_i(\boldsymbol{\theta})}^2}, \tag{4.12}$$

where $\sigma_{F_i(\boldsymbol{\theta})}^2$ was obtained by combining the statistical error on each component of the fit function ($\sigma_{f_i}^2$) , as defined in Sect. 4.4.1.

4.4.3 Fit results

The results of the fit are shown in Figs. 4.27–4.29. The normalized residuals are shown in Fig. 4.30. The fit returned a value of $n_{2\nu\beta\beta} = 1364 \pm 133$ for the number of $2\nu\beta\beta$ signal events. The best fit values for all the fit parameters are listed in Table 4.5.

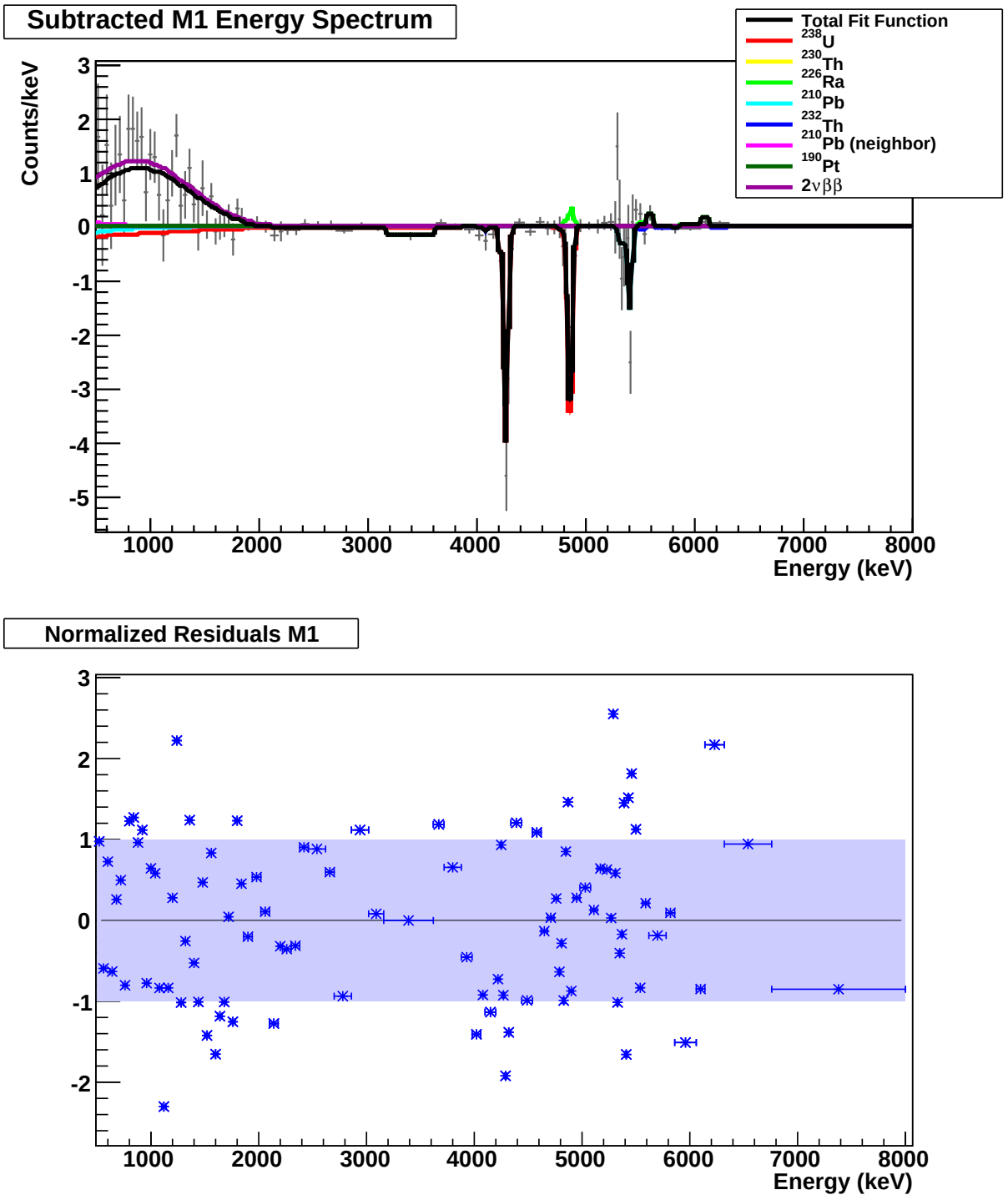

Figure 4.27: Fit of the simulated spectrum components to the Multiplicity 1 (M1) spectrum. The fit was performed simultaneously on the M1, M1, and M2Tot spectra.

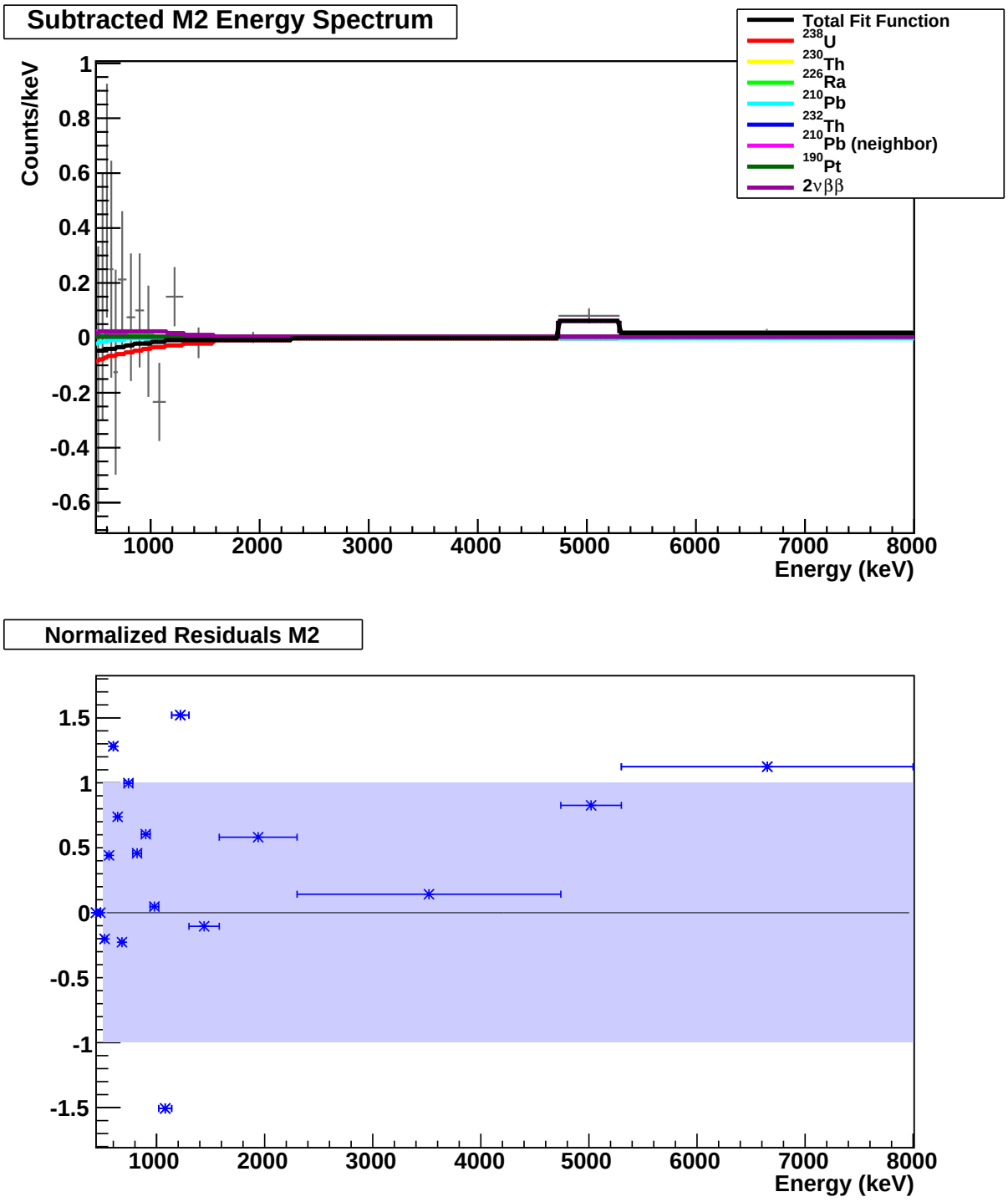

Figure 4.28: Fit of the simulated spectrum components to the Multiplicity 2 (M2) spectrum. The fit was performed simultaneously on the M1, M1, and M2Tot spectra.

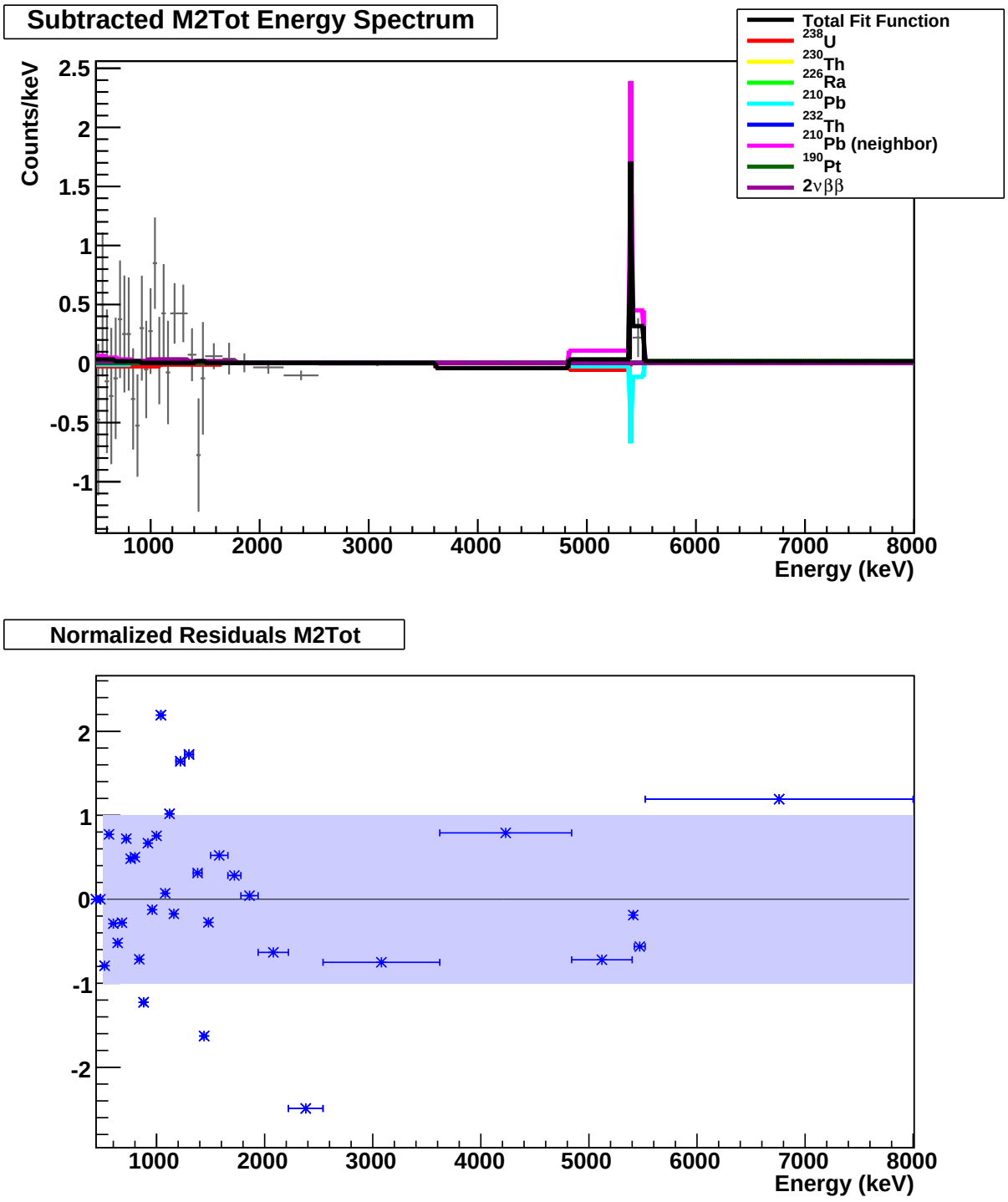

Figure 4.29: Fit of the simulated spectrum components to the Multiplicity 2 total energy spectrum (M2Tot). The fit was performed simultaneously on the M1, M1, and M2Tot spectra.

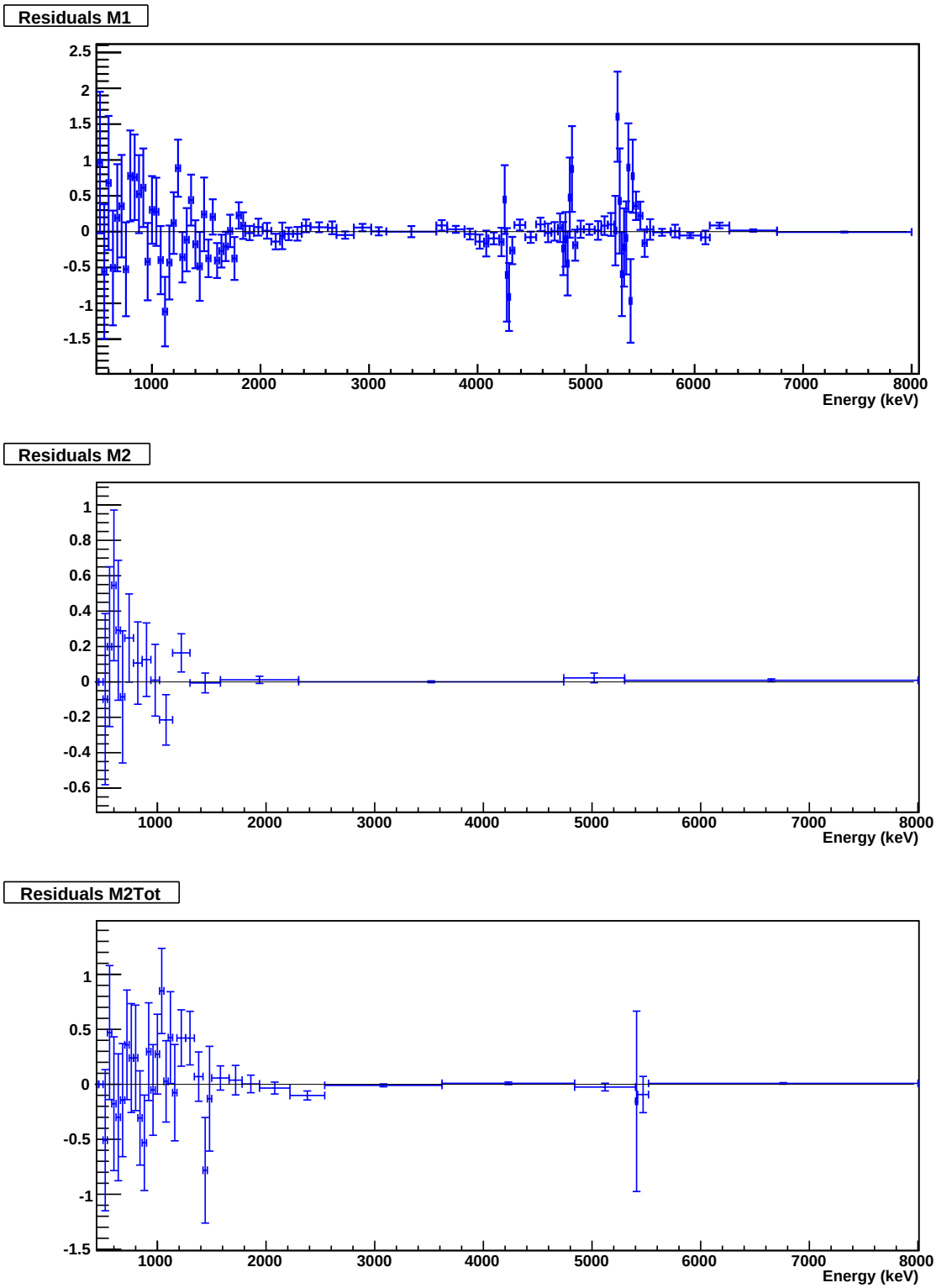

Figure 4.30: Residuals from the simultaneous fit to the M1, M1, and M2Tot spectra.

Table 4.5: Results of the $2\nu\beta\beta$ fit.

Parameter	Fit result	unit
$n_{238\text{U}}$	-328±34	
$d_{238\text{U}}$	2.4±0.9	μm
$n_{230\text{Th}}$	-0.8±11	
$d_{230\text{Th}}$	10±5	mm
$n_{226\text{Ra}}$	50.±17	
$d_{226\text{Ra}}$	0.40±0.34	μm
$n_{210\text{Pb}}$	-214±58	
$d_{210\text{Pb}}$	0.50±0.02	μm
$n_{232\text{Th}}$	-4±6	
$d_{232\text{Th}}$	10±5	mm
$n_{210\text{Pb-n}}$	1770±350	
$d_{210\text{Pb-n}}$	6±17	nm
$n_{190\text{Pt}}$	-71±36	
$n_{2\nu\beta\beta}$	1364±133	
χ^2/NDF	138.4/131 = 1.06	
P-value	0.31	

4.5 Systematic errors

In addition to the statistical error returned by the fit, there are several possible sources of systematic error. The main sources of systematic error are related the background model used to account for the imperfect subtraction of the background between the enriched crystals.

4.5.1 Systematic error from background model and fit

Each component in the background model represents an excess of some radioactive contamination in one pair of enriched crystals over the other pair. In principle, there are an infinite number of possible distributions of contaminants which could produce residual backgrounds in the crystals. To construct a background model with a manageable number of free parameters, the following simplifying assumptions were made:

- The only sources which contribute significantly to the background are ^{190}Pt and isotopes in the ^{238}U and ^{232}Th decay chains, which are assumed to be in secular equilibrium except as noted in Sect. 4.3.
- Significant contributions to the residual background only come from crystal bulk or surface contaminations.
- Each background component exists as an exponentially-distributed surface contamination with a single characteristic depth, or as a uniformly distributed bulk contamination

(A single source may not have multiple depths).

These assumptions reduced the number of background components considered, and reduced the number of free parameters per background source to two (activity and depth).

There were additional steps in constructing the fit PDF from the simulated data which could potentially introduce systematic error, such as the choice of energy resolution to apply to the simulation, the interpolation between simulated depth points, and the use of finite width bins to approximate the probability density.

One way to measure the cumulative effect of these approximations is to repeat the analysis on the non-enriched crystals, which should yield a null result, as should alternative combinations of the enriched crystals. Five alternative combinations of crystals were analyzed, shown in Fig. 4.31, and the results of the fits are listed in Table 4.6. The full fit results are shown in Appendix C.

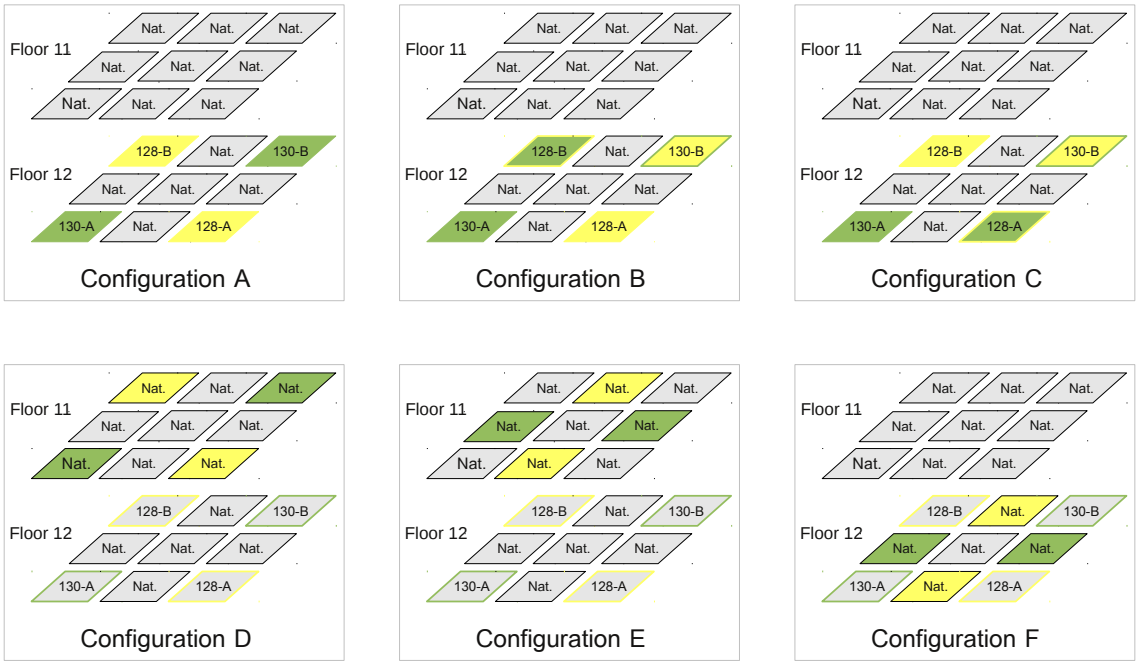

Figure 4.31: Different combinations of bolometers used to evaluate the systematic error of the fit method. For each configuration shown, the spectrum of the two bolometers shown in yellow was summed and subtracted from the summed spectrum of the two bolometers shown in green. Configuration A corresponds to the ordinary $2\nu\beta\beta$ analysis. The other configurations should all produce null results.

The value of $n_{2\nu\beta\beta}$ returned by the fit was within 2 sigma of zero for each of the alternate configurations tested. The results are summarized in Fig. 4.32. In order to estimate the systematic error on the fit procedure, the average result for the combinations of natural

Table 4.6: Results of performing the $2\nu\beta\beta$ fit on different combinations of crystals as shown in Figure 4.31, in order to evaluate the systematic error of the fit procedure. All fits in this table are expected to yield $n_{2\nu\beta\beta} = 0$.

Parameter	Config. B	Config. C	Config. D	Config. E	Config. F
$n_{238\text{U}}$	14±41	145±36	-71±10	13±7	22±24
$d_{238\text{U}}$ (nm)	3±400	2660±2570	1e7±8e6	2e5±1e7	5±18
$n_{230\text{Th}}$	-84±60	7±11	-55±17	-88±30	-104±17
$d_{230\text{Th}}$ (nm)	270±260	1e7±6e6	1e7±8e6	4±9	1e7±7e6
$n_{226\text{Ra}}$	-28±103	-13±6	15±7	23±17	9±6
$d_{226\text{Ra}}$ (nm)	6e3±3e5	1e7±6e6	2.0e5±0.6e5	1±200	1e7±7e6
$n_{210\text{Pb}}$	-280±70	-130±890	-14±26	35±48	-908±78
$d_{210\text{Pb}}$ (nm)	3±14	1±2800	1e7±9e6	2000±3000	144±26
$n_{232\text{Th}}$	10.±88	26±28	54±17	66±17	-19±11
$d_{232\text{Th}}$ (nm)	2e4±1e7	1±182	340±330	48±70	1.2e6±5.4e6
$n_{210\text{Pb-n}}$	415±655	-946±2970	570±270	950±370	1200±700
$d_{210\text{Pb-n}}$ (nm)	2000±2200	1000±3400	1±100	1±80	4900±5000
$n_{190\text{Pt}}$	-12±36	-543±36	18±11	10±13	-1±16
$n_{2\nu\beta\beta}$	43±142	54±131	108±119	23±109	-131±123
χ^2	179	194	150	156	228
NDF	133	131	120	115	134
χ^2/NDF	1.34	1.48	1.25	1.36	1.70

crystals (Configurations D–F) was taken, $\langle n_{2\nu\beta\beta} \rangle = 0 \pm 68$. Since the average result was less than the fit uncertainty, the combined fit uncertainty was taken as the systematic error on the fit method.

The final result for the number of $2\nu\beta\beta$ events in the 130-enriched crystals is then $n_{2\nu\beta\beta} = 1364 \pm 133(\text{stat}) \pm 68(\text{syst})$.

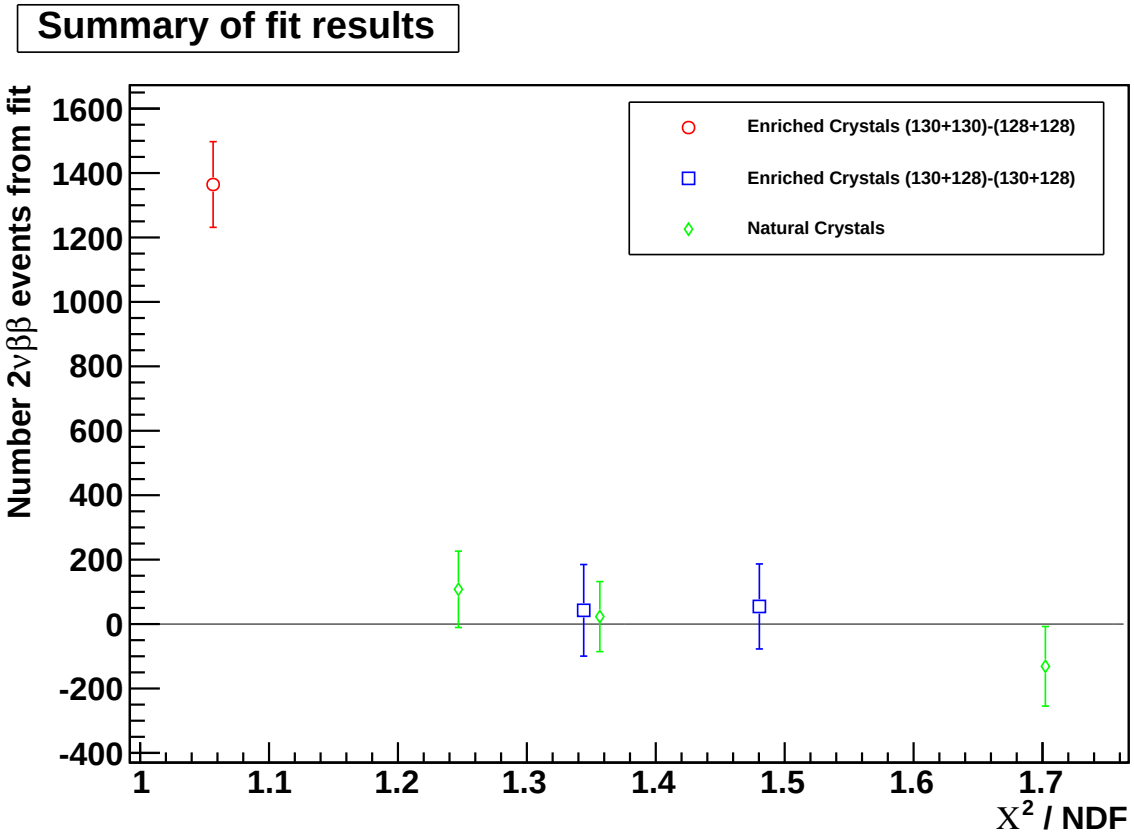

Figure 4.32: Fit results for different combinations of crystals. The average value returned by the natural crystals was taken as a representation of the systematic error.

4.5.2 Systematic error from choice of signal shape

The PDF used to model the $2\nu\beta\beta$ energy spectrum in the Monte Carlo simulation, which was then used to generate the fit function, was obtained using the non-relativistic Primakoff-Rosen approximation for the Coulomb interaction between the nucleus and the outgoing electrons. This approximation allows the phase space integral to be evaluated analytically and therefore greatly improves the speed of the Monte-Carlo simulation. However, it also constitutes a potential source of systematic error.

In order to evaluate the systematic error introduced by this approximation, the spectrum shape, $S(T)$ was calculated including the relativistic Coulomb correction, as described in Appendix B. Here, T refers to the total kinetic energy of the emitted electrons. The distribution $S(T)$ was sampled every 20 keV from 500 keV to the Q value, matching the fit range and binning used for the experimental data. The Primakoff-Rosen spectrum $S^{\mathrm{PR}}(T)$ was then fit to the sampled points, with an overall normalization constant N as the only free parameter in the fit. The fit, shown in Fig. 4.33, returned a value of $N = 0.9926$. In other words, if the data are truly drawn from the parent distribution $S(T)$, then using the function $S^{\mathrm{PR}}(T)$ for the fit will underestimate the size of the signal by 0.7%. In order to correct for this effect, the number of signal events returned by the fit should be divided by N.

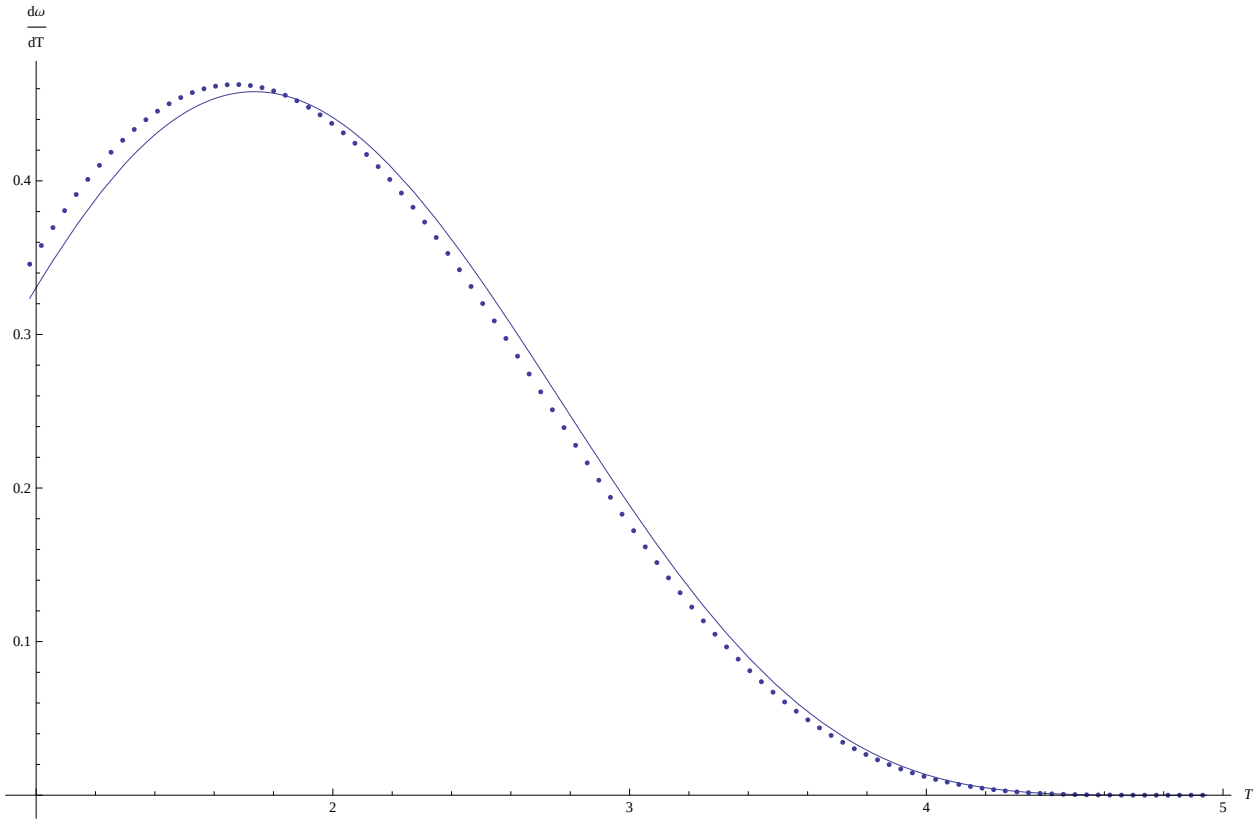

Figure 4.33: Fit of the Primakoff-Rosen spectrum shape $S^{\mathrm{PR}}(T)$ (solid line) to the spectrum $S(T)$ (data points) calculated using relativistic Coulomb corrections.

4.6 Evaluation of the $2\nu\beta\beta$ half-life

The half-life $T^{2\nu}_{1/2}$ can be computed from the number of decay events returned by the fit as follows:

$$T^{2\nu}_{1/2} = \frac{\log(2)\eta T N}{n_{2\nu\beta\beta}}, \tag{4.13}$$

where η is the efficiency for observing $2\nu\beta\beta$ events, $T = 1.276$ y is the live-time of the detector, and N is the number of parent nuclei (in this case, the difference in the number of ^{130}Te nuclei between the 130-enriched and the 128-enriched crystals). The efficiency is the product of the efficiency due to the pulse shape cut and the heater-pileup cut times the renormalization factor due to the spectrum shape: $\eta = 0.97 \cdot 0.977 \cdot 0.9926 = 0.941$. The efficiency of the anti-radon cut is included in the live time evaluation, and the effects of the energy threshold cut and escape of β particles from the crystal are already accounted for in the construction of the fit PDF from the Monte Carlo.

The number of ^{130}Te nuclei can be computed from the crystal masses and enrichments, given in Table 4.7. The net number of ^{130}Te nuclei (obtained by subtracting the number found in the 128-enriched crystals from the 130-enriched crystals) is $N = 2.67 N_A$.

Table 4.7: Enriched crystal masses and enrichments. The enrichment levels were measured by mass spectroscopy of small fragments taken from the grown crystals. The ^{130}Te content in mol was calculated assuming that the remainder of the Te which was neither ^{130}Te or ^{128}Te was ^{126}Te.

Channel	Crystal	^{130}Te (atomic %)	^{128}Te (atomic %)	Mass TeO_2 (g)	^{130}Te (mol)
20	130-A	77.9	14.0	340.86	1.65
33	130-B	72.2	16.6	337.99	1.51
35	128-A	10.2	85.4	338.80	-0.216
52	128-B	13.0	79.3	334.71	-0.272
Net ^{130}Te					2.67

Therefore, the measured half-life for the $2\nu\beta\beta$ of ^{130}Te is

$$T^{2\nu}_{1/2} = \left(\frac{\log(2) \cdot 0.941 \cdot 2.67 N_A}{1364} \right) \cdot 1.276\,\text{y} = [9.81 \pm 0.96(\text{stat}) \pm 0.49(\text{syst})] \times 10^{20}\,\text{y} \tag{4.14}$$

Chapter 5

Conclusion

5.1 Comparison with previous measurements

The value obtained for the $2\nu\beta\beta$ half-life is slightly longer than the previous two results obtained from direct measurement. The results from this measurement, the NEMO-3 experiment [76], and the Mi-DBD experiment [75] (which was the precursor to CUORICINO) are summarized in Table 5.1. The "Combined error" column in the table comes from adding the statistical and systematic errors in quadrature. In the analysis that follows, the upwards error on the Mi-DBD measurement is used, since that is the direction in which it differs from the other two results. The measurements are compared graphically, along with the results from geochemical measurements, in Fig. 5.1.

Table 5.1: Results from the three experiments to date which have measured the $2\nu\beta\beta$ half-life of ^{130}Te via direct detection of the decay electrons. For the purposes of analyzing the statistical compatibility of these measurements, the statistical and systematic errors were combined by adding in quadrature.

Measurement	$T_{1/2}$	Statistical error	Systematic error	Combined error
	(10^{20} y)			
This work	9.81	$\pm$0.96	$\pm$0.49	$\pm$1.07
NEMO-3 [76]	7.0	$\pm$0.9	$\pm$1.1	$\pm$1.42
Mi-DBD [75]	6.1	1.4	+2.9 -3.5	+3.22 -3.77

This work disagrees with the recent NEMO-3 result by

$$\Delta_{T_{1/2}} = T_{1/2}(\text{This work}) - T_{1/2}(\text{NEMO-3}) = (2.8 \pm 1.8) \times 10^{20}\,\text{y}, \tag{5.1}$$

which is a discrepancy of 1.6 sigma. The disagreement with the Mi-DBD result is $\Delta_{T_{1/2}} = 3.7 \pm 3.4$, or 1.1 sigma.

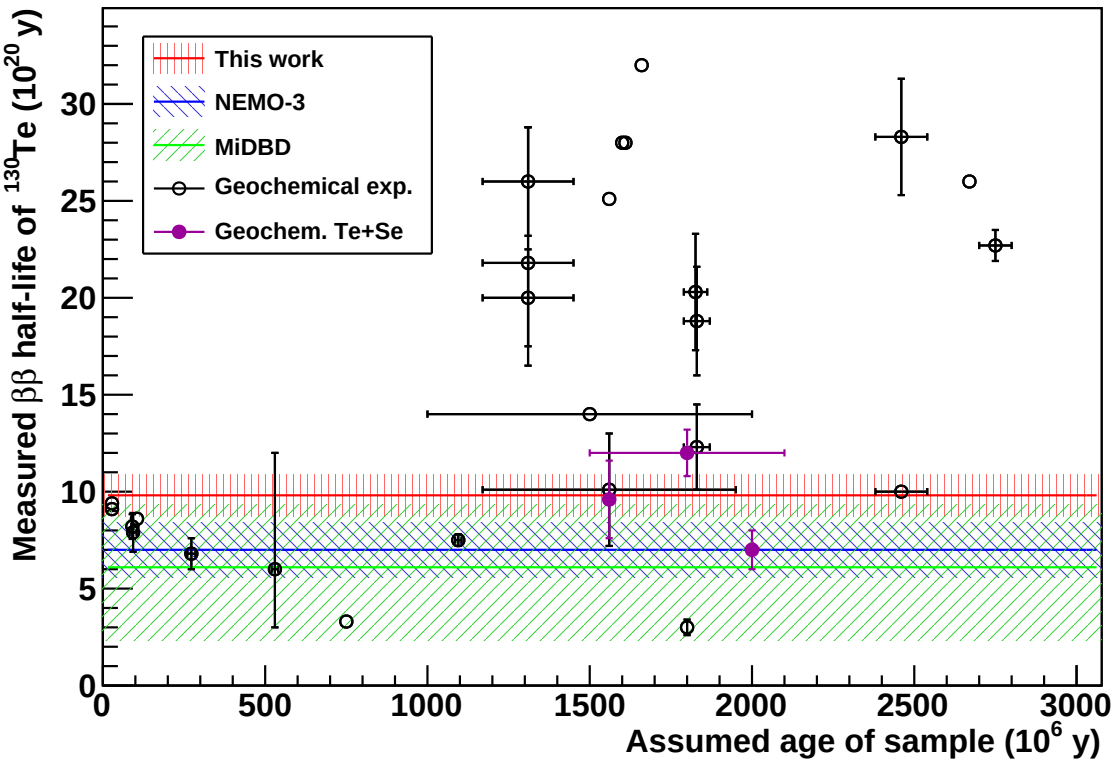

Figure 5.1: Comparison of experimental results from direct detection experiments (colored bands) and geochemical measurements (points). The direct detection experiments are listed in Table 5.1 and the geochemical measurements are listed in 1.3. The purple solid circles correspond to geochemical measurements of the ratio of the $\beta\beta$ half-life of ^{82}Se to ^{130}Te (Table 1.4). These measurements may be more reliable than other geochemical experiments because the gas retention age of the sample should cancel.

Combining all three results in Table 5.1 yields an average value of:

$$T_{1/2}^{avg} = 8.6 \pm 0.8 \times 10^{20}\,\mathrm{y} \tag{5.2}$$

In order to assess the compatibility of these three measurements, the chi-square was computed, under the assumption that the maximum likelihood estimator $T_{1/2}^{avg}$ was the true value of the half-life. The chi-square is $\chi^2 = 3.14$, which corresponds to a p-value of 21%. This is the probability that three randomly sampled measurements with gaussian errors given by the "Combined error" values from Table 5.1 would have a χ^2 greater or equal to the value obtained.

5.2 ^{128}Te half life

The $2\nu\beta\beta$ half-life of ^{128}Te is several orders of magnitude longer than that of ^{130}Te, mainly due to the relatively low Q-value of 866 keV (recall that the phase space factor $G^{2\nu}$ scales roughly as Q^{11}). For this reason, it is not currently possible to measure the decay in direct detection experiments. However, some geochemical experiments have been able to measure the ^{130}Te to ^{128}Te half-life ratio R with good precision, such as [43] and [44], which found values of $R = (3.52 \pm 0.11) \times 10^{-4}$ and $R = (3.74 \pm 0.10) \times 10^{-4}$, respectively. Using the average value of these two measurements,

$$R \equiv \frac{T_{1/2}^{130}}{T_{1/2}^{128}} = (3.64 \pm 0.07) \times 10^{-4}, \tag{5.3}$$

we can compute the value of $T_{1/2}^{128}$ from the value of $T_{1/2}^{130}$ measured by CUORICINO:

$$T_{1/2}^{128} = (2.69 \pm 0.30) \times 10^{24}\,\mathrm{y}. \tag{5.4}$$

Alternatively, using the average value of the ^{130}Te half-life measured by direct detection experiments (Eq. (5.2)), we obtain

$$(T_{1/2}^{128})^{avg} = (2.36 \pm 0.22) \times 10^{24}\,\mathrm{y}. \tag{5.5}$$

5.3 Comparison with theory

According to the equation

$$\frac{1}{T_{1/2}^{2\nu}} = G^{2\nu}(Q, Z)|M^{2\nu}|^2 \tag{5.6}$$

(see Sect. 1.2.1), the nuclear matrix element for $2\nu\beta\beta$ may be obtained from the half-life using the calculated value for the phase-space factor $G^{2\nu}$. Taking the value of $G^{2\nu}$ from

Table 1.2, we find the experimentally-determined matrix element corresponding to the value of $T^{130}_{1/2}$ measured by CUORICINO:

$$|M^{2\nu}| = 0.0146 \pm 0.0008 \tag{5.7}$$

or, using the average experimental half-life value $T^{avg}_{1/2}$ from Eq. (5.2),

$$|M^{2\nu}_{avg}| = 0.0155 \pm 0.0007. \tag{5.8}$$

Because not all $2\nu\beta\beta$ calculations are performed using the approximation (Eq. (1.15)) which allows the factorization of the phase-space integral and nuclear matrix element, I prefer to compare the experimental results to the computed half-life values directly, rather than comparing values for the matrix elements $|M^{2\nu}|$. Figure 5.2 shows a representative sample of half-life calculations in different models. It is apparent that there are large disagreements between models, as well as between theory and experiment.

As discussed in Sect. 1.2.3, early calculations such as the ISM result in Fig. 5.2, tended to severely underestimate the half-life for $2\nu\beta\beta$. Later calculations in the QRPA model were able to better account for the observed rate suppression, in large part due to the introduction of a particle-particle spin-isospin force, whose strength is given by the parameter g^{pp}. Because both $M^{2\nu}$ and $M^{0\nu}$ depend sensitively on the value of g^{pp}, many recent QRPA calculations do not predict the value of $M^{2\nu}$, but rather use the experimental value as an input to fix g^{pp}, which is then used to compute $M^{0\nu}$ [36]. In this way, the updated experimental value for $T^{2\nu}_{1/2}$ may be used to improve $M^{0\nu}$ calculations in the QRPA framework.

5.4 Background to $0\nu\beta\beta$ measurements

The tail of the $2\nu\beta\beta$ spectrum is an unavoidable background to any $0\nu\beta\beta$ measurement. For measurements with extremely good energy resolution, such as CUORICINO ($\sim 0.1\%$ 1σ resolution at 2.5 MeV), this background is negligibly small. However, for experiments with worse energy resolution, the background from $2\nu\beta\beta$ may be significant. Given the measured rate of $2\nu\beta\beta$ decay, we can estimate the size of its background contribution as a function of an experiment's energy resolution.

We start with the $2\nu\beta\beta$ energy spectrum in the Primakoff-Rosen approximation (Eq. (1.19)). Because this approximate spectrum converges to the true spectrum as it approaches the $\beta\beta$ endpoint, it is adequate for estimating backgrounds in the $0\nu\beta\beta$ region of interest (ROI). The probability density function (PDF) for $2\nu\beta\beta$ as a function of total electron energy, $F(E)$, is then convolved with a Gaussian of width σ, $G(E;\sigma)$, to obtain a PDF for the energy observed in the detector, $C(E;\sigma)$, as shown in Fig. 5.3.

For the purposes of this study, the $0\nu\beta\beta$ ROI will be taken as the region within $\pm 1\sigma$ of the Q value. The fraction of $2\nu\beta\beta$ background events which fall in the ROI ($f^{2\nu}_{\rm ROI}$) is then equal to the integral

$$f^{2\nu}_{\rm ROI}(\sigma) = \int_{Q-\sigma}^{Q+\sigma} C(E;\sigma)\mathrm{d}E. \tag{5.9}$$

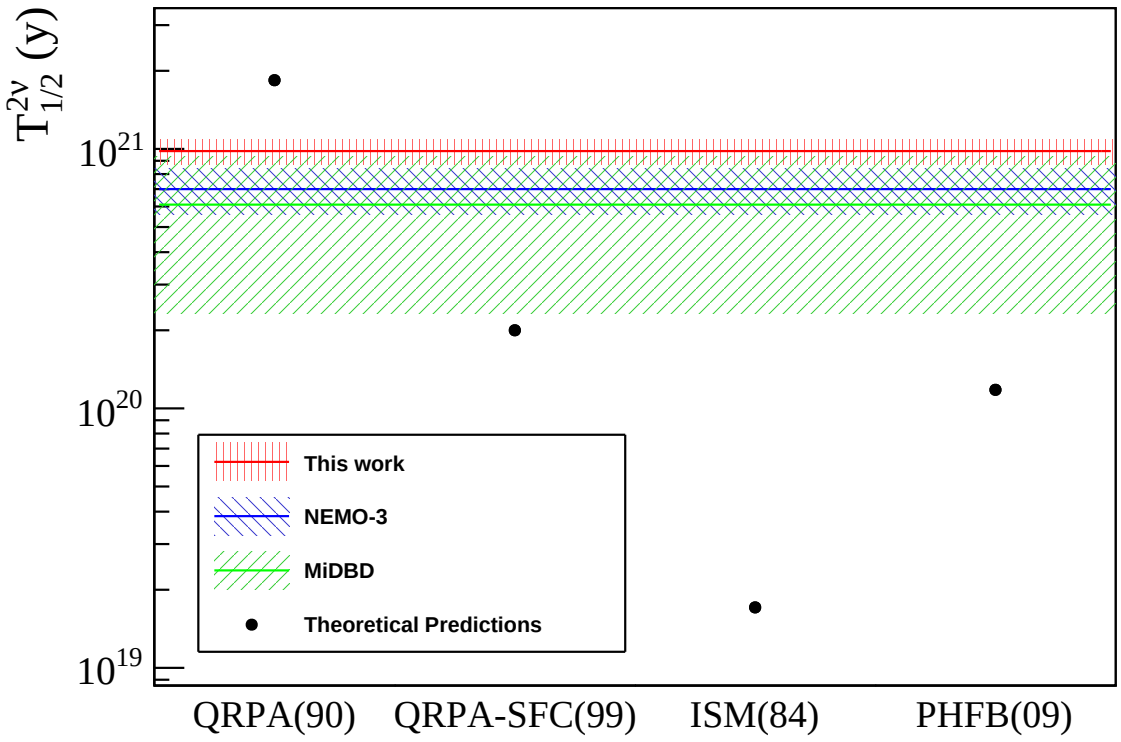

Figure 5.2: Comparison of experimental results from direct detection experiments (colored bands) and a sample of representative theoretical half-life predictions (dots), labeled by model and year on the x-axis. The calculated values are taken from the following references: QRPA [40], ISM: [38], QRPA-SFC: [41], and PHFB: [31]. The PHFB half-lives were obtained from the reported matrix elements using the phase space factors $G^{2\nu}$ listed in Table 1.2. A more detailed discussion of these different calculation methods can be found in Sect. 1.2.3.

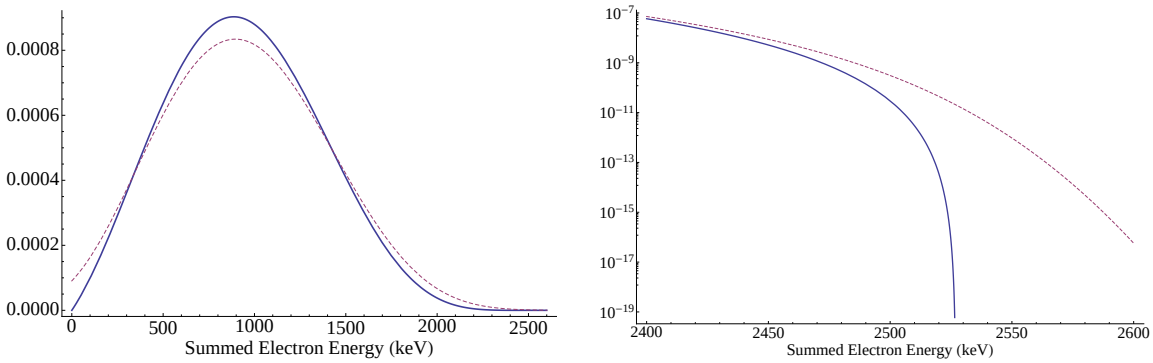

Figure 5.3: The convolution $C(E;\sigma)$ (dashed line) of the $2\nu\beta\beta$ spectrum $F(E)$ (solid line) and a Gaussian of width σ representing the detector resolution. The left panel shows the entire spectrum with a resolution of 200 keV, and the right panel shows the spectrum near the endpoint, with a resolution of 20 keV.

Similarly, the fraction of $0\nu\beta\beta$ events which fall in the ROI is simply equal to the integral of a gaussian from $-\sigma$ to σ: $f^{0\nu}_{\rm ROI} \simeq 0.683$. Given $2\nu\beta\beta$ decay rate $\Gamma^{2\nu}$, measured in this work, we can estimate lowest decay rate $\Gamma^{0\nu}$ that could be measured by a $0\nu\beta\beta$ experiment with energy resolution σ by setting the ratio of signal to irreducible $2\nu\beta\beta$ background in the ROI equal to one:

$$\Gamma^{0\nu} f^{0\nu}_{\rm ROI} = \Gamma^{2\nu} f^{2\nu}_{\rm ROI}(\sigma), \tag{5.10}$$

or, inverting this equation,

$$T^{0\nu}_{1/2} = \frac{0.683}{f^{2\nu}_{\rm ROI}(\sigma)} T^{2\nu}_{1/2}. \tag{5.11}$$

Here, $T^{0\nu}_{1/2}$ is an estimate of the achievable half-life sensitivity of an experiment with energy resolution σ, plotted in Fig. 5.4. As this figure shows, for an experiment like CUORICINO, with an energy resolution of $\sigma \sim 3$ keV, it would be possible to measure a $T^{0\nu}_{1/2}$ around 10 orders of magnitude longer than the present CUORICINO limit ($\sim 3\times10^{24}$ y) if background from $2\nu\beta\beta$ were the only limiting factor. For experiments with an energy resolution on the order of 100–200 keV in the ROI (such as NEMO-3), on the other hand, $2\nu\beta\beta$ backgrounds begin to be significant for values of $T^{0\nu}_{1/2}$ at or just beyond the present CUORICINO limit.

Of course, $\beta\beta$ experiments such as NEMO-3 do not simply count events in the ROI, but rather utilize sophisticated fitting methods, including information from the single electron spectra and the angular distribution of decay electrons. These techniques improve the sensitivity beyond the naïve approach presented here; nevertheless, Fig. 5.4 provides insight into the substantial challenge such experiments face to overcome the background from $2\nu\beta\beta$.

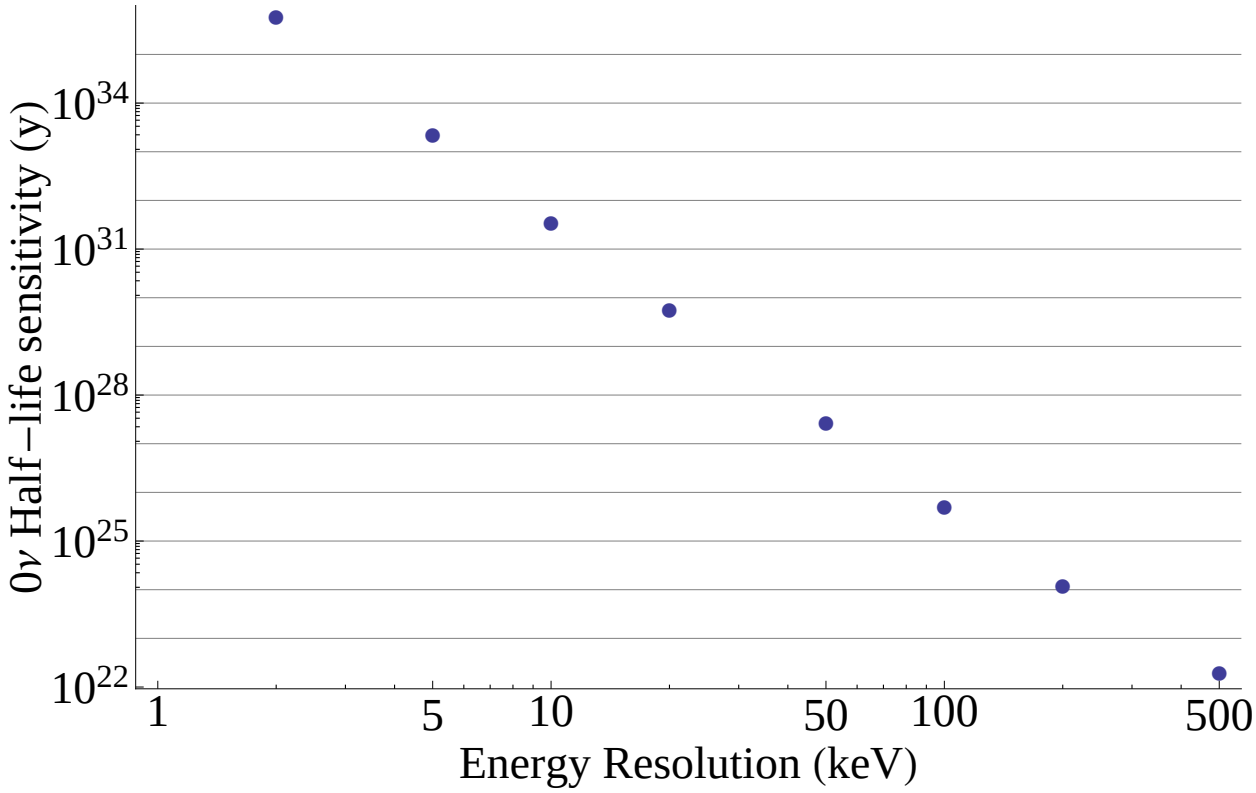

Figure 5.4: Impact of the irreducible $2\nu\beta\beta$ background on the ^{130}Te $0\nu\beta\beta$ half-life sensitivity of an experiment as a function of energy resolution. The vertical axis represents the $0\nu\beta\beta$ half-life corresponding to a signal to background ratio of 1 in the $0\nu\beta\beta$ ROI, assuming the only background comes from $2\nu\beta\beta$.

5.5 Prospects for future measurements

The measurement presented in this work represents the most precise determination of the $2\nu\beta\beta$ half life of ^{130}Te to date, and is in reasonably good agreement with previous measurements. Although there is still an experimental uncertainty on the order of 10% on the half-life, this uncertainty is small compared to the theoretical uncertainties surrounding $\beta\beta$ decay. For this reason, the urgency of improving the $2\nu\beta\beta$ half-life measurement may be considered to be relatively low.

There are currently no plans to include differentially enriched crystals in future experiments in the CUORE line. This means that the type of measurement described in this work, relying on background subtraction from crystals depleted in ^{130}Te, will not be possible in planned future experiments. The background reduction goal for CUORE is a factor of 20 relative to CUORICINO in the $0\nu\beta\beta$ region of interest. Assuming that this goal were met and extended to cover the $2\nu\beta\beta$ region of interest as well, the signal to background ratio for a $2\nu\beta\beta$ measurement in CUORE would be on the order of 1:1. In that case, a $2\nu\beta\beta$ measurement in CUORE is conceivable, although it would have to rely more heavily on Monte-Carlo simulations to quantify the backgrounds than did this measurement.

The main challenge for future experiments aiming to improve on the measurement of the ^{130}Te $2\nu\beta\beta$ half-life will be, as for all $\beta\beta$ measurements, achieving the extraordinarily low backgrounds necessary to observe this rare decay.

Bibliography

[1] F. Boehm and P. Vogel, *Physics of Massive Neutrinos*, 2nd edition, Cambridge University Press, 1992.

[2] L. Bonolis, *Bruno Pontecorvo: From slow neutrons to oscillating neutrinos*, Am. J. Phys., **73**, 487 (2005).

[3] R. Davis, D. S. Harmer, and K. C. Hoffman, *Search for Neutrinos from the Sun*, Phys. Rev. Lett., **20**, 1205 (1968).

[4] Q. R. Ahmad *et al.*, *Direct Evidence for Neutrino Flavor Transformation from Neutral-Current Interactions in the Sudbury Neutrino Observatory*, Phys. Rev. Lett., **89**, 011301 (2002).

[5] S. Abe *et al.* (The KamLAND Collaboration), *Precision Measurement of Neutrino Oscillation Parameters with KamLAND*, Phys. Rev. Lett., **100**, 221803 (2008).

[6] Y. Fukuda *et al.*, *Evidence for Oscillation of Atmospheric Neutrinos*, Phys. Rev. Lett., **81**, 1562 (1998).

[7] E. Aliu *et al.* (The K2K Collaboration), *Evidence for Muon Neutrino Oscillation in an Accelerator-Based Experiment*, Phys. Rev. Lett., **94**, 081802 (2005).

[8] K. Nakamura *et al.* (Particle Data Group), *Review of Particle Physics*, J. Phys. G, **37** (2010), URL `http://pdg.lbl.gov/`.

[9] B. Kayser, F. Gibrat-Debu, and F. Perrier, *The Physics of Massive Neutrinos*, World Scientific, 1989.

[10] S. M. Bilenky, C. Giunti, and W. Grimus, *Phenomenology of neutrino oscillations*, Prog. Part. Nucl. Phys., **43**, 1 (1999).

[11] S. Chu, L. Ekström, and R. Firestone, *WWW Table of Radioactive Isotopes* (1999), URL `http://nucleardata.nuclear.lu.se/nucleardata/toi/`.

[12] K. Rosman and P. Taylor, *Isotopic compositions of the elements 1997*, Pure Appl. Chem., **70**, 217 (1998).

[13] G. Audi, A. H. Wapstra, and C. Thibault, *The 2003 atomic mass evaluation: (II). Tables, graphs and references*, Nucl. Phys. A, **729**, 337 (2003), the 2003 NUBASE and Atomic Mass Evaluations.

[14] S. Rahaman *et al.*, *Q value of the 100Mo Double-Beta Decay*, Phys. Lett., **B662**, 111 (2008).

[15] N. D. Scielzo *et al.*, *Double-β-decay Q values of $Te130$, $Te128$, and $Te120$*, Phys. Rev. C, **80**, 025501 (2009).

[16] M. Redshaw *et al.*, *Masses of $Te130$ and $Xe130$ and Double-β-Decay Q Value of $Te130$*, Phys. Rev. Lett., **102**, 212502 (2009).

[17] M. Redshaw *et al.*, *Mass and Double-Beta-Decay Q Value of $Xe136$*, Phys. Rev. Lett., **98**, 053003 (2007).

[18] M. Goeppert-Mayer, *Double Beta-Disintegration*, Phys. Rev., **48**, 512 (1935).

[19] K. Muto and H. V. Klapdor, *Neutrinos*, pages 183–237, Graduate Texts in Contemporary Physics, Springer-Verlag, 1988.

[20] H. Primakoff and S. P. Rosen, *Double beta decay*, Rept. Prog. Phys., **22**, 121 (1959).

[21] J. Schechter and J. W. F. Valle, *Neutrinoless double-β decay in $SU(2) \times U(1)$ theories*, Phys. Rev. D, **25**, 2951 (1982).

[22] A. Strumia and F. Vissani, *Implications of neutrino data circa 2005*, Nucl. Phys. B, **726**, 294 (2005).

[23] F. Šimkovic *et al.*, *$0\nu\beta\beta$-decay nuclear matrix elements with self-consistent short-range correlations*, Phys. Rev. C, **79**, 055501 (2009).

[24] J. Menéndez *et al.*, *Disassembling the nuclear matrix elements of the neutrinoless $\beta\beta$ decay*, Nucl. Phys. A, **818**, 139 (2009).

[25] J. P. Schiffer *et al.*, *Nuclear Structure Relevant to Neutrinoless Double β Decay: ^{76}Ge and ^{76}Se*, Phys. Rev. Lett., **100**, 112501 (2008).

[26] B. P. Kay *et al.*, *Nuclear structure relevant to neutrinoless double β decay: The valence protons in ^{76}Ge and ^{76}Se*, Phys. Rev. C, **79**, 021301 (2009).

[27] J. Menéndez *et al.*, *Occupancies of individual orbits, and the nuclear matrix element of the ^{76}Ge neutrinoless $\beta\beta$ decay*, Phys. Rev. C, **80**, 048501 (2009).

[28] F. Šimkovic, A. Faessler, and P. Vogel, *nuclear matrix elements and the occupancy of individual orbits$0\nu\beta\beta$*, Phys. Rev. C, **79**, 015502 (2009).

[29] T. Bloxham *et al.*, *Pair correlations in the neutrinoless double-β decay candidate ^{130}Te*, Phys. Rev. C, **82**, 027308 (2010).

[30] J. Barea and F. Iachello, *Neutrinoless double-β decay in the microscopic interacting boson model*, Phys. Rev. C, **79**, 044301 (2009).

[31] R. Chandra *et al.*, *Multipolar correlations and deformation effect on nuclear transition matrix elements of double-β decay*, Europhys. Lett., **86**, 32001 (2009).

[32] K. Chaturvedi *et al.*, *Nuclear deformation and neutrinoless double-β decay of $Zr94, 96$, $Mo98, 100$, $Ru104$, $Pd110$, $Te128, 130$, and $Nd150$ nuclei within a mechanism involving neutrino mass*, Phys. Rev. C, **78**, 054302 (2008).

[33] P. K. Rath *et al.*, *Uncertainties in nuclear transition matrix elements for neutrinoless $\beta\beta$ decay within the projected-Hartree-Fock-Bogoliubov model*, Phys. Rev. C, **82**, 064310 (2010).

[34] T. R. Rodríguez and G. Martínez-Pinedo, *Energy Density Functional Study of Nuclear Matrix Elements for Neutrinoless $\beta\beta$ Decay*, Phys. Rev. Lett., **105**, 252503 (2010).

[35] V. Rodin *et al.*, *Erratum to: Assessment of uncertainties in QRPA $0\nu\beta\beta$-decay nuclear matrix elements [Nucl. Phys. A 766 (2006) 107]*, Nucl. Phys. A, **793**, 213 (2007).

[36] V. Rodin *et al.*, *Assessment of uncertainties in QRPA $0\nu\beta\beta$-decay nuclear matrix elements*, Nucl. Phys. A, **766**, 107 (2006).

[37] F. Šimkovic *et al.*, *Relation between the $0\nu\beta\beta$ and $2\nu\beta\beta$ nuclear matrix elements reexamined*, Phys. Rev. C, **83**, 015502 (2011).

[38] W. C. Haxton and G. J. Stephenson, *Double beta decay*, Prog. Part. Nucl. Phys., **12**, 409 (1984).

[39] P. Vogel and M. R. Zirnbauer, *Suppression of the two-neutrino double-beta decay by nuclear-structure effects*, Phys. Rev. Lett., **57**, 3148 (1986).

[40] A. Staudt, K. Muto, and H. V. Klapdor-Kleingrothaus, *Calculation of 2ν and 0ν Double-Beta Decay Rates*, Europhys. Lett., **13**, 31 (1990).

[41] C. Barbero *et al.*, *Weak magnetism in two neutrino double beta decay*, Phys. Lett. B, **445**, 249 (1999).

[42] O. Civitarese and J. Suhonen, *Use of summation methods in the calculation of nuclear double beta decay processes*, Phys. Rev. C, **47**, 2410 (1993).

[43] T. Bernatowicz *et al.*, *Precise determination of relative and absolute $\beta\beta$-decay rates of ^{128}Te and ^{130}Te*, Phys. Rev. C, **47**, 806 (1993).

[44] M. T. F. da Cruz *et al.*, *Thick-target yields of iodine isotopes from proton interactions in Te, and the double-β decays of* ^{128,130}Te, Phys. Rev. C, **48**, 3106 (1993).

[45] M. Fehr, M. Rehkamper, and A. Halliday, *Application of MC/ICP/MS to the precise determination of tellurium isotope compositions in chondrites, iron meteorites and sulfides*, Int. J. Mass Spectrom., **232**, 83 (2004).

[46] M. G. Inghram and J. H. Reynolds, *Double Beta-Decay of* Te^{130}, Phys. Rev., **78**, 822 (1950).

[47] M. E. Wieser and J. R. de Laeter, *Evidence of the double β decay of zirconium-96 measured in* 1.8×10^9 *year-old zircons*, Phys. Rev. C, **64**, 024308 (2001).

[48] H. Hidaka, C. V. Ly, and K. Suzuki, *Geochemical evidence of the double β decay of* ^{100}*Mo*, Phys. Rev. C, **70**, 025501 (2004).

[49] N. Takaoka and K. Ogata, *The Half-life of* ^{130}*Te Double β-decay*, Z. Naturforsch., Teil A, **21**, 84 (1966).

[50] E. Gerling, Y. Shukolyukov, and G. Ashkinadze, *Determination of the Rate of the* ^{130}*Te Double β^- Decay*, Sov. J. Nucl. Phys., **6**, 226 (1968).

[51] T. Kirsten, W. Gentner, and O. A. Schaeffer, *Massenspektrometrischer Nachweis von -Zerfallsprodukten*, Z. Phys. A, Hadrons and Nuclei, **202**, 273 (1967).

[52] T. Kirsten *et al.*, *Experimental Evidence for the Double-Beta Decay of* Te^{130}, Phys. Rev. Lett., **20**, 1300 (1968).

[53] E. A. Jr., B. Srinivasan, and O. Manuel, *Xenon in Kirkland lake tellurides*, Earth Planet. Sci. Lett., **5**, 478 (1968).

[54] B. Srinivasan, E. C. Alexander, and O. K. Manuel, *Xenon isotopes in tellurobismuthite, Boliden, Sweden*, J. Inorg. Nucl. Chem., **34**, 2381 (1972).

[55] B. Srinivasan, E. C. Alexander, and O. K. Manuel, *Te 130 -Xe 130 Age Determinations of Tellurium Minerals*, Econ. Geol., **67**, 592 (1972).

[56] E. W. Hennecke, O. K. Manuel, and D. D. Sabu, *Double beta decay of* ^{128}*Te*, Phys. Rev. C, **11**, 1378 (1975).

[57] T. Kirsten, H. Richter, and E. Jessberger, *Rejection of Evidence for Nonzero Neutrino Rest Mass from Double Beta Decay*, Phys. Rev. Lett., **50**, 474 (1983).

[58] T. Kirsten *et al.*, *New Geochemical Double Beta Decay Measurements on Various Selenium Ores and Remarks Concerning Tellurium Isotopes*, in T. Kotani, H. Ejiri, and E. Takasugi, editors, *Nuclear Beta Decays and Neutrino*, pages 81–92, World Scientific, 1986.

[59] J. F. Richardson *et al.*, *Double beta decay of tellurium-130*, Nucl. Phys. A, **453**, 26 (1986).

[60] W. J. Lin *et al.*, *Double beta-decay of 82Se and 130Te*, Nucl. Phys. A, **457**, 285 (1986).

[61] W. J. Lin *et al.*, *Geochemically measured half-lives of 82Se and 130Te*, Nucl. Phys. A, **481**, 477 (1988).

[62] T. Bernatowicz *et al.*, *Neutrino mass limits from a precise determination of $\beta\beta$-decay rates of ^{128}Te and ^{130}Te*, Phys. Rev. Lett., **69**, 2341 (1992).

[63] N. Takaoka, Y. Motomura, and K. Nagao, *Half-life of ^{130}Te double-β decay measured with geologically qualified samples*, Phys. Rev. C, **53**, 1557 (1996).

[64] N. Takaoka, Y. Motomura, and K. Nagao, *Noble gases in tellurium and associated minerals and double-beta decay of tellurium-130.*, J. Mass Spectrom. Soc. Jpn., **44**, 63 (1996).

[65] H. V. Thomas *et al.*, *Geochemical constraints on the half-life of Te130*, Phys. Rev. C, **78**, 054606 (2008).

[66] A. S. Barabash and the Nemo Collaboration, *NEMO 3 double beta decay experiment: Latest results*, J. Phys. Conf. Ser., **173**, 012008 (2009).

[67] A. Barabash, *Possible evidence for a time variation of the weak-interaction constant from double-beta-decay experiments*, Phys. Atom. Nucl., **63**, 1210 (2000).

[68] S. Murty and K. Marti, *Nucleogenic noble gas components in the Cape York iron meteorite*, Geochim. Cosmochim. Acta, **51**, 163 (1987).

[69] A. Meshik *et al.*, *130Te and 128Te double beta decay half-lives*, Nucl. Phys. A, **809**, 275 (2008).

[70] B. Srinivasan *et al.*, *Double Beta Decay of Selenium-82*, Econ. Geol., **68**, 252 (1973).

[71] H. V. Klapdor-Kleingrothaus *et al.*, *Evidence for Neutrinoless Double Beta Decay*, Mod. Phys. Lett., **A16**, 2409 (2001).

[72] C. E. Aalseth *et al.*, *Comment on 'Evidence for Neutrinoless Double Beta Decay'*, Mod. Phys. Lett., **A17**, 1475 (2002).

[73] A. S. Barabash, *Precise half-life values for two-neutrino double-β decay*, Phys. Rev. C, **81**, 035501 (2010).

[74] E. Andreotti *et al.*, *130Te neutrinoless double-beta decay with CUORICINO*, Astropart. Phys., **34**, 822 (2011).

[75] C. Arnaboldi *et al.*, *A calorimetric search on double beta decay of 130Te*, Phys. Lett. B, **557**, 167 (2003).

[76] R. Arnold *et al.* (NEMO-3 Collaboration), *Measurement of the $\beta\beta$ Decay Half-Life of Te130 with the NEMO-3 Detector*, Phys. Rev. Lett., **107**, 062504 (2011).

[77] E. Andreotti *et al.*, *Search for β^+/EC double beta decay of 120Te*, Astropart. Phys., **34**, 643 (2011).

[78] E. Guardincerri, *Sviluppo del sistema di acquisizione per CUORE e analisi di eventi a bassa energia in Cuoricino*, Ph.D. thesis, Università degli Studi di Genova (2006).

[79] C. Kittel, *Introduction to Solid State Physics*, John Wiley & Sons, Inc., 1986.

[80] M. Barucci *et al.*, *Measurement of Low Temperature Specific Heat of Crystalline TeO2 for the Optimization of Bolometric Detectors*, J. Low. Temp. Phys., **123**, 303 (2001).

[81] Y. Chu *et al.*, *Growth of the high quality and large size paratellurite single crystals*, J. Cryst. Growth, **295**, 158 (2006).

[82] C. Arnaboldi *et al.*, *Production of high purity TeO2 single crystals for the study of neutrinoless double beta decay*, J. Cryst. Growth, **312**, 2999 (2010).

[83] E. E. Haller, *Isotopically engineered semiconductors*, J. Appl. Phys., **77**, 2857 (1995).

[84] D. McCammon, *Semiconductor Thermistors*, Appl. Phys., **99**, 35 (2005), `arXiv:physics/0503086v1`.

[85] A. Alessandrello *et al.*, *Methods for response stabilization in bolometers for rare decays*, Nucl. Instrum. Meth. A, **412**, 454 (1998).

[86] C. Arnaboldi *et al.*, *The temperature stabilization system of CUORICINO: an array of macro bolometers*, IEEE Trans. Nucl. Sci., **52**, 1630 (2005).

[87] D.-M. Mei and A. Hime, *Muon-induced background study for underground laboratories*, Phys. Rev. D, **73**, 053004 (2006).

[88] M. Haffke *et al.*, *Background measurements in the Gran Sasso Underground Laboratory*, Nucl. Instrum. Meth. A, **643**, 36 (2011).

[89] P. Belli *et al.*, *Deep underground neutron flux measurement with large BF_3 counters*, Nuovo Cim. A (1971-1996), **101**, 959 (1989).

[90] F. Arneodo *et al.*, *Neutron background measurements in the Hall C of the Gran Sasso Laboratory*, Nuovo Cim., **A112**, 819 (1999).

[91] H. Wulandari *et al.*, *Neutron flux at the Gran Sasso underground laboratory revisited*, Astropart. Phys., **22**, 313 (2004).

[92] G. Pessina, *Room temperature differential voltage sensitive preamplifier for large mass bolometric detectors*, Nucl. Instrum. Meth. A, **444**, 132 (2000).

[93] A. Alessandrello *et al.*, *A programmable front-end system for arrays of bolometers*, Nucl. Instrum. Meth. A, **444**, 111 (2000).

[94] E. Gatti and P. Manfredi, *Processing the signals from solid-state detectors in elementary-particle physics*, Riv. Nuovo Cim. (1978-1999), **9**, 1 (1986).

[95] *RooFit*, URL `http://roofit.sourceforge.net/`.

[96] *ROOT: A Data Analysis Framework*, URL `http://root.cern.ch`.

[97] W. Verkerke and D. Kirkby, *RooFit Users Manual*, v2.07 edition (2006), URL `http://roofit.sourceforge.net/docs/`.

[98] M. Carrettoni, *Data Analysis for Neutrinoless Double Beta Decay*, Ph.D. thesis, Università Milano Bicocca (2011).

[99] A. Bryant, *A Search for Neutrinoless Double Beta Decay of* ^{130}*Te*, Ph.D. thesis, University of California, Berkeley (2010).

[100] S. Agostinelli *et al.*, GEANT*4–a simulation toolkit*, Nucl. Instrum. Meth. A, **506**, 250 (2003).

[101] S. Capelli, *Background analysis of the experiments MiDBD, CUORICINO and CUORE*, Ph.D. thesis, Università Milano Bicocca (2005).

[102] H. Behrens and J. Jänecke, *Numerical Tables for Beta-Decay and Electron Capture*, volume 4 of *Numerical Data and Functional Relationships in Science and Technology*, Springer-Verlag, 1969.

Appendix A

Automatic calibration peak finding method

If no starting values are provided to the calibration program, a peak search is performed to try to identify the primary calibration peaks. The following procedure is used:

1. The data are histogrammed. For the first iteration, the bin width is set to one amplitude unit, but it will be modified in subsequent iterations. The scale of the stabilized amplitudes is set by the energy of the stabilization heater pulses, which is defined to be 5000 stabilized amplitude units. Therefore, the range of amplitudes to be searched is determined by the range of calibration peak energies and by the approximate heater energy (for CUORICINO, the heater energy is taken to be 5000 keV for all channels, but the user may specify an input file containing these values for non-CUORICINO detectors).

2. A ROOT TSpectrum object is used to search for candidate calibration peaks. For the first pass, the number of candidate peaks ($n_{\text{candidate}}$) is equal to the number of primary calibration peaks (n_{primary}) plus 2. For each subsequent iteration ($i = 0, 1, 2, \text{etc.}$), the number of candidate peaks is increased by one, i.e. $n_{\text{candidate}} = n_{\text{primary}} + 2 + i$.

3. A pattern-matching algorithm is applied to attempt to identify the primary peaks from the candidate peaks.

   (a) All possible combinations of n_{primary} candidate peaks with the correct energy ordering are generated.

   (b) Each combination of candidate peaks is plotted versus the primary peak energies and fit with a test function, $T(x) = ax + bx^2$.

   (c) The chi-squares of the test fits are compared. The combination of candidate peaks with the lowest chi-square value is selected as the best combination.

4. If the best combination has a chi-square less than a fixed value (for CUORICINO, $\chi^2 < 200$ was used), those candidate peaks are taken to be the primary peaks, and their locations (from the TSpectrum object) are passed back to the main calibration program to be used as the starting guess.

   If the best combination does not have a low enough chi-square, the algorithm returns to step 1, but increases the number of candidate peaks by one and adjusts the histogram binning based on the previous results. Up to 7 iterations were allowed for CUORICINO. If after 7 iterations the primary peaks still have not been identified, the peak locations must be specified by the user with a GUI tool.

Appendix B

Calculation of $2\nu\beta\beta$ spectrum shape

The following derivation is based on the discussion found in the 1984 review article by Haxton and Stephenson [38]. We begin with the expression for the differential decay rate found in Eq. 15 of that article. Neglecting factors which are independent of the electron energies (and therefore do not affect the shape of the spectrum), the differential decay rate can be written as:

$$\frac{\mathrm{d}\omega}{\mathrm{d}k_1\mathrm{d}k_2\mathrm{d}\cos\theta} \sim \mathcal{F}(Z,\varepsilon_1)\mathcal{F}(Z,\varepsilon_2)k_1^2k_2^2(W_0-\varepsilon_1-\varepsilon_2)^5(1-\beta_1\beta_2\cos\theta). \tag{B.1}$$

Here, $k_{1,2}$ are the electron momenta, $\varepsilon_{1,2}=\sqrt{k_{1,2}^2+m_e^2}$ are the electron energies, $\beta_i = k_i/\varepsilon_i$, and θ is the opening angle between the two emitted electrons. The total energy release is $W_0 = Q + 2m_e$, and $\mathcal{F}(Z,\varepsilon_i)$ is the Fermi factor, which describes the Coulomb interaction between the electrons and the final state nucleus.

For convenience, we will set $m_e = 1$ and all put all energies in units of the electron mass. Integrating over $\cos\theta$ and changing variables from momentum to energy yields

$$\frac{\mathrm{d}\omega}{\mathrm{d}\varepsilon_1\mathrm{d}\varepsilon_2} \sim \mathcal{F}(Z,\varepsilon_1)\mathcal{F}(Z,\varepsilon_2)\varepsilon_1\varepsilon_2\sqrt{(\varepsilon_1^2-1)(\varepsilon_2^2-1)}\,(\varepsilon_1+\varepsilon_2-W_0)^5\,. \tag{B.2}$$

The Fermi factor $\mathcal{F}$ is often approximated by a non-relativistic expression introduced by Primakoff and Rosen [20], which allows Eq. (B.2) to be integrated analytically.

$$\mathcal{F}^{\mathrm{PR}}(Z,\varepsilon) = \left(\frac{\varepsilon}{k}\right)\frac{2\pi Z\alpha}{1-e^{-2\pi Z\alpha}}. \tag{B.3}$$

A more accurate relativistic expression is obtained by taking "the square of the ratio of the Dirac scattering solution for a point charge Z to a plane wave, evaluated at the nuclear surface" (Eq. A4 from [38]):

$$\mathcal{F}^{\mathrm{R}}(Z,\varepsilon) = 2(1+\gamma)(2kR_0)^{2(\gamma-1)}e^{\pi\eta}\left|\frac{\Gamma(1+i\eta)}{\Gamma(2\gamma+1)}\right|^2, \tag{B.4}$$

where $\eta = \alpha Z/\beta$, $\gamma = \sqrt{1-(\alpha Z)^2}$, and R_0 is the nuclear radius, which was approximated by $R_0 = 1.2A^{1/3}$.

The accuracy can be further improved by including screening corrections, which can be found in Table III of [102]. For the purpose of this calculation, which is to determine how the choice of spectrum shape affects the decay rate evaluation, the screening corrections were found to have a negligible effect (about an order of magnitude less than the effect of using the relativistic expression). Therefore, the following discussion will use the relativistic Fermi factor $\mathcal{F} = \mathcal{F}^{\mathrm{R}}$ with no screening correction.

We would like to plot the differential decay rate as a function of the summed energy of the two electrons, so we perform a change of variables:

$$\begin{aligned} E_{(+)} &= \varepsilon_1 + \varepsilon_2 \\ E_{(-)} &= \varepsilon_1 - \varepsilon_2. \end{aligned} \tag{B.5}$$

Furthermore, it is conventional to use the kinetic energy rather than the total energy, since that is what is measured in the detector. The total kinetic energy of the two electrons is

$$T = E_{(+)} - 2, \tag{B.6}$$

and the Q value Q is the maximum possible value of T.

After changing variables, again neglecting constant factors, we can write:

$$\begin{aligned} \frac{\mathrm{d}\omega}{\mathrm{d}T\mathrm{d}E_{(-)}} &\sim (E_{(-)} - T - 2)\sqrt{(E_{(-)} - T - 4)(E_{(-)} - T)} \\ &\times (E_{(-)} + T + 2)\sqrt{(E_{(-)} + T + 4)(E_{(-)} + T)} \\ &\times (T-Q)^5 \mathcal{F}(Z, \frac{T+2-E_{(-)}}{2})\mathcal{F}(Z, \frac{T+2+E_{(-)}}{2}) \\ &\equiv I(T, E_{(-)}) \end{aligned} \tag{B.7}$$

Integrating over $E_{(-)}$ then yields the differential decay rate as a function of the total kinetic energy of the electrons:

$$\frac{\mathrm{d}\omega}{\mathrm{d}T} \sim \int_{-T}^{T} I(T, E_{(-)})\mathrm{d}E_{(-)}. \tag{B.8}$$

When using the Primakoff-Rosen approximation for the Fermi factor, $\mathcal{F}^{\mathrm{PR}}$, this integral can be performed analytically, and evaluates to:

$$\left(\frac{\mathrm{d}\omega}{\mathrm{d}T}\right)^{\mathrm{PR}} \sim T(Q-T)^5(T^4 + 10T^3 + 40T^2 + 60T + 30) \tag{B.9}$$

However, when using the relativistic Fermi factor $\mathcal{F}^{\mathrm{R}}$, the integral must be evaluated numerically; a plot of the result is shown in Fig. B.1, along with the Primakoff-Rosen approximate spectrum for comparison.

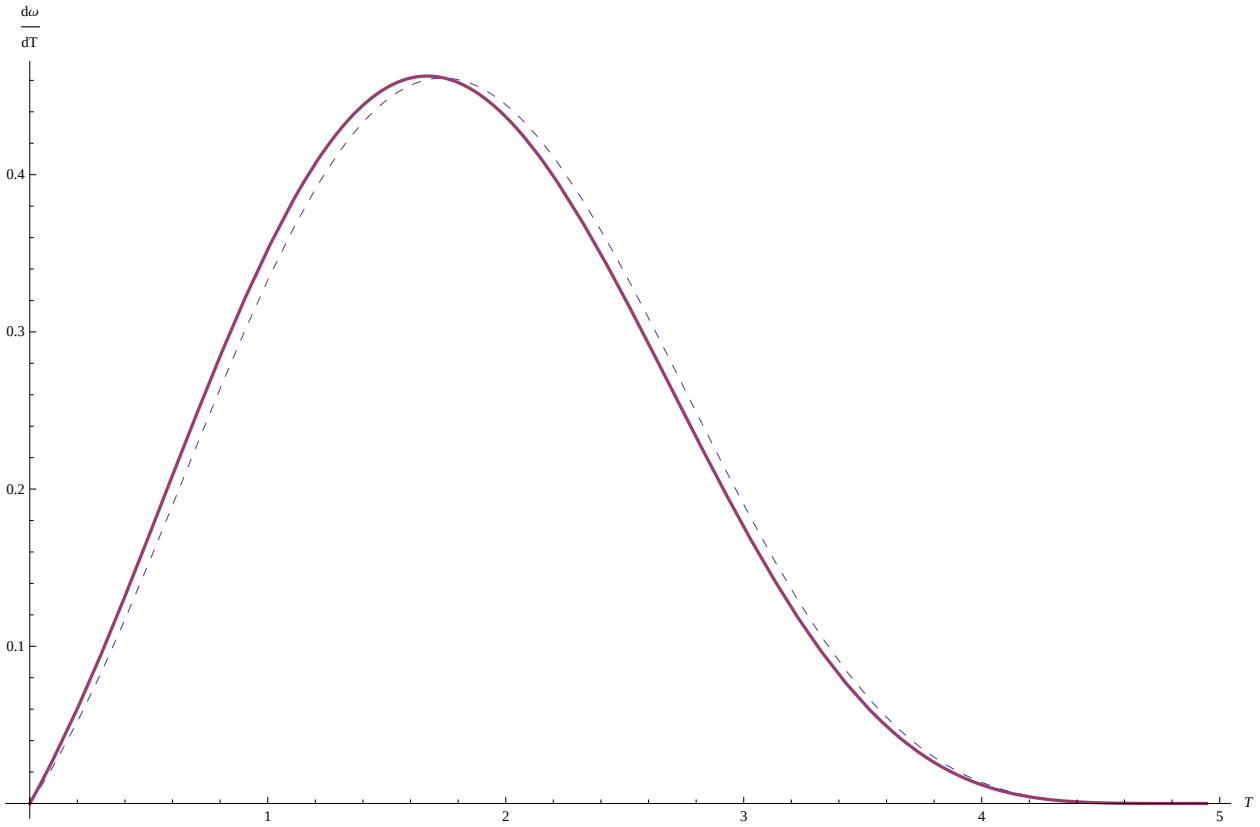

Figure B.1: The differential decay rate for the $2\nu\beta\beta$ of ^{130}Te as a function of the total electron kinetic energy (T), evaluated using a relativistic expression for the Fermi factor (solid line), and using the non-relativistic Primakoff-Rosen approximation (dashed line). The functions have been normalized for the purpose of comparison, and the energy is in units of electron mass.

Appendix C

Full fit results for evaluation of systematic errors

In order to evaluate the systematic error of the analysis procedure, the analysis was repeated for alternative configurations of crystals as specified in Fig. 4.31.

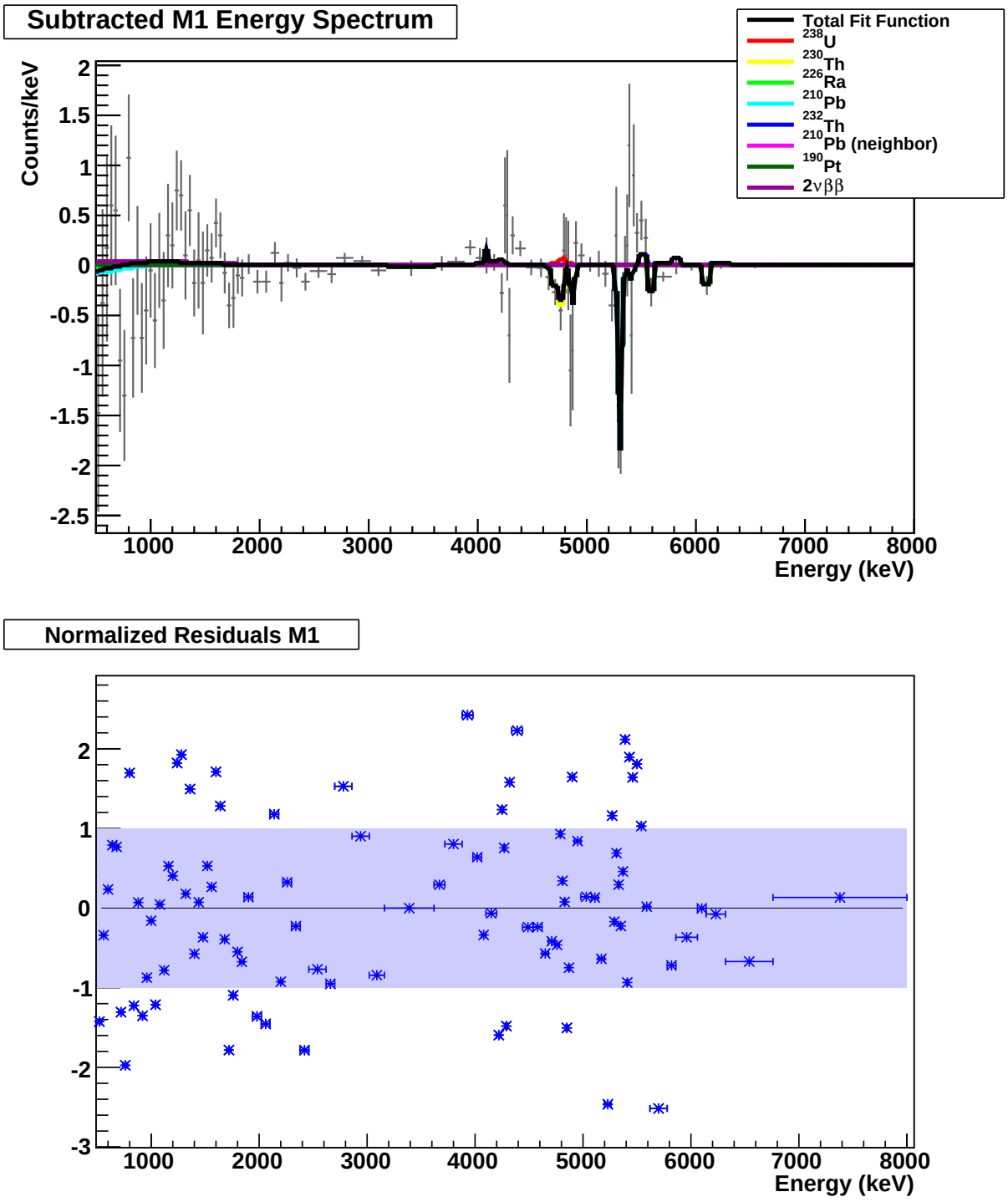

Figure C.1: Fit of the simulated spectrum components to the Multiplicity 1 (M1) spectrum for crystal configuration B. The fit was performed simultaneously on the M1, M1, and M2Tot spectra.

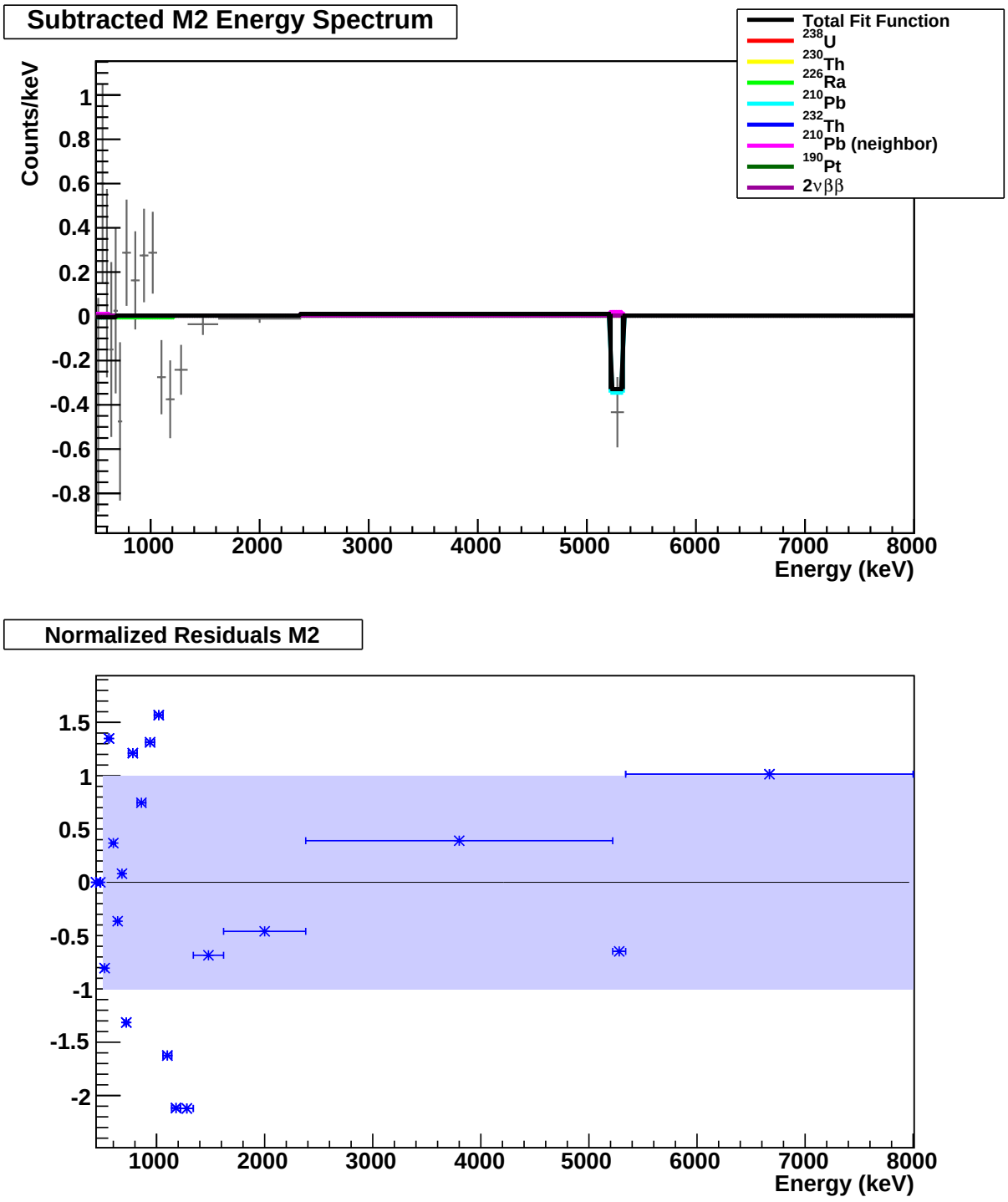

Figure C.2: Fit of the simulated spectrum components to the Multiplicity 2 (M2) spectrum for crystal configuration B. The fit was performed simultaneously on the M1, M1, and M2Tot spectra.

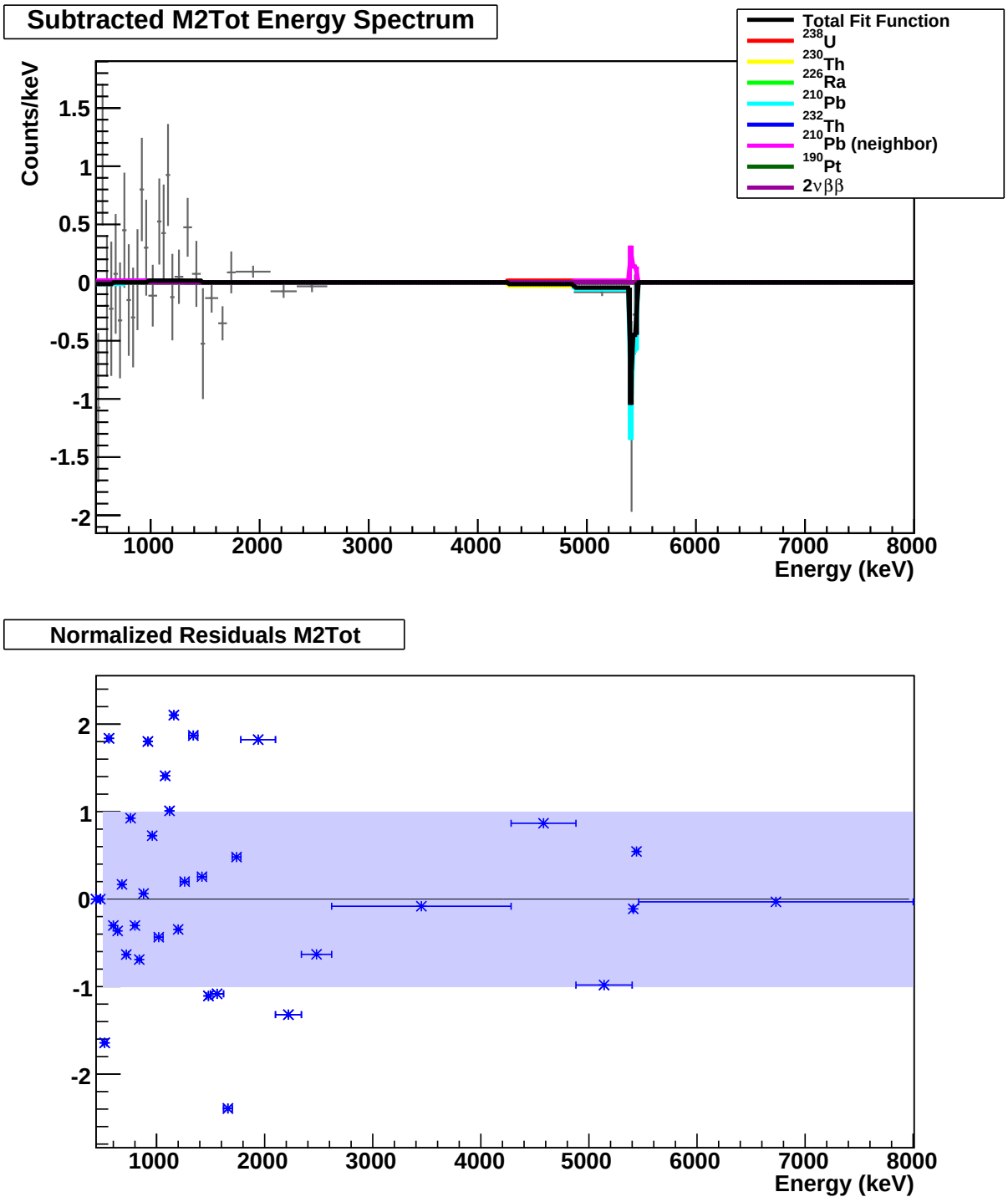

Figure C.3: Fit of the simulated spectrum components to the Multiplicity 2 total energy spectrum (M2Tot) for crystal configuration B. The fit was performed simultaneously on the M1, M1, and M2Tot spectra.

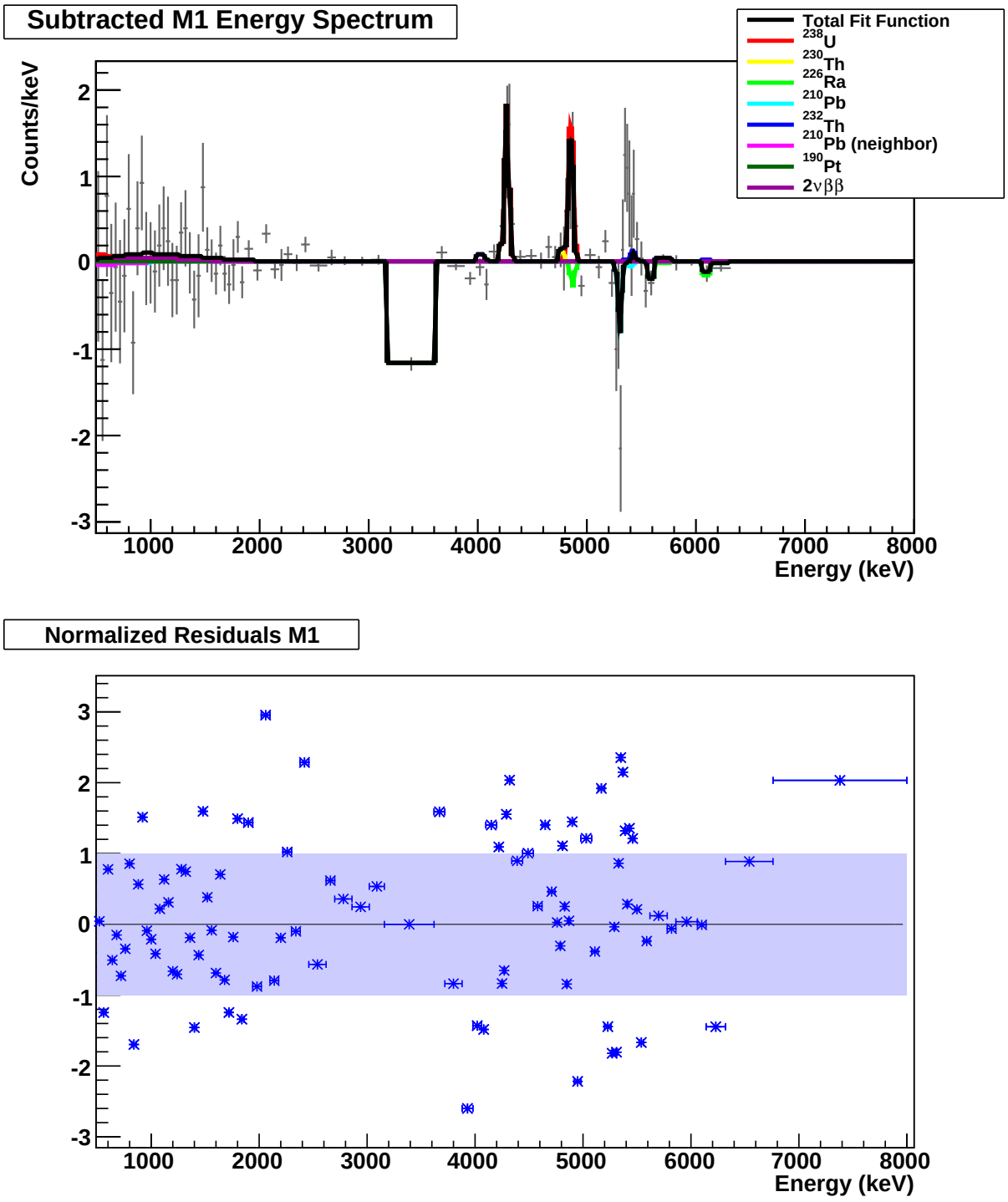

Figure C.4: Fit of the simulated spectrum components to the Multiplicity 1 (M1) spectrum for crystal configuration C. The fit was performed simultaneously on the M1, M1, and M2Tot spectra.

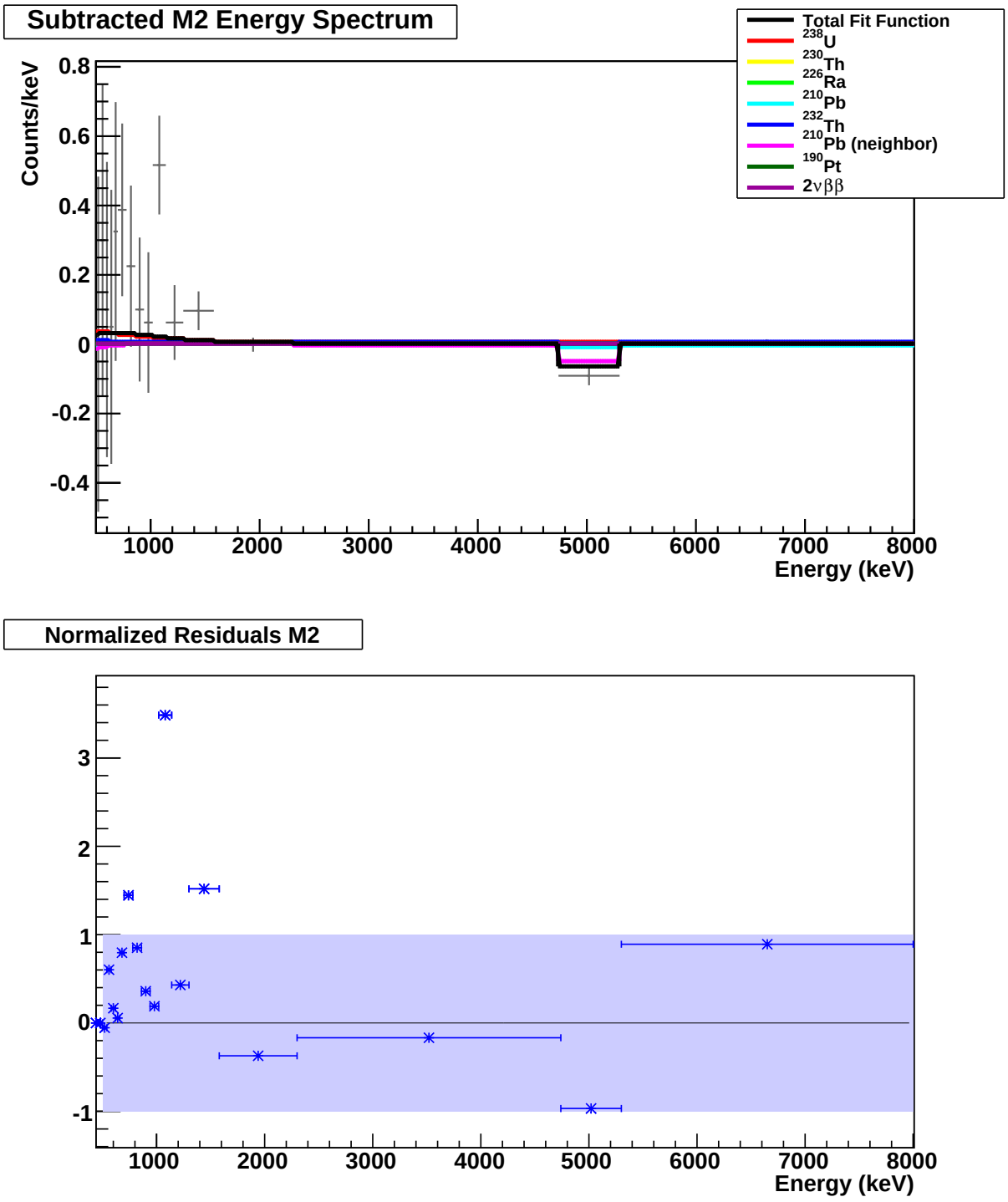

Figure C.5: Fit of the simulated spectrum components to the Multiplicity 2 (M2) spectrum for crystal configuration C. The fit was performed simultaneously on the M1, M1, and M2Tot spectra.

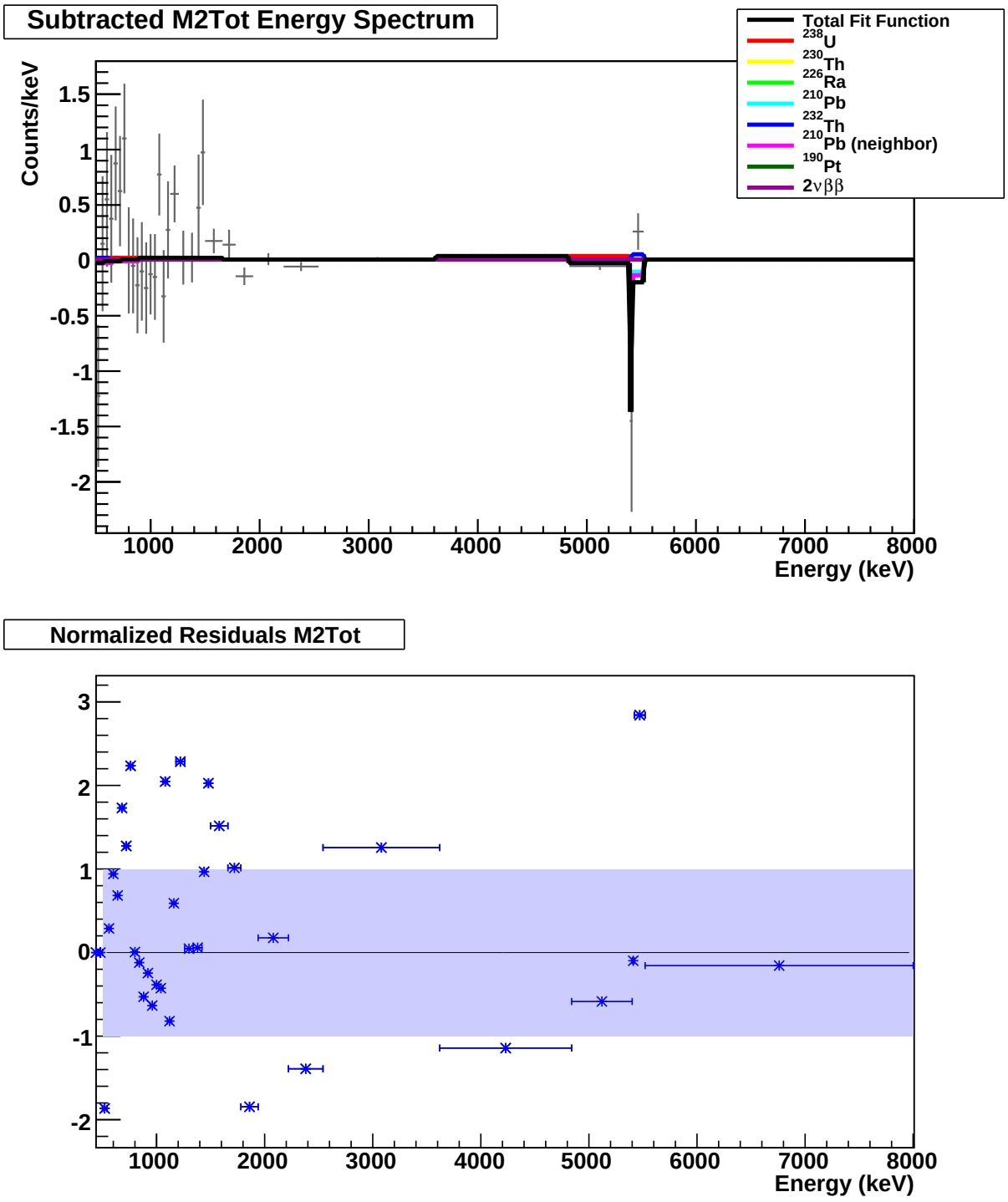

Figure C.6: Fit of the simulated spectrum components to the Multiplicity 2 total energy spectrum (M2Tot) for crystal configuration C. The fit was performed simultaneously on the M1, M1, and M2Tot spectra.

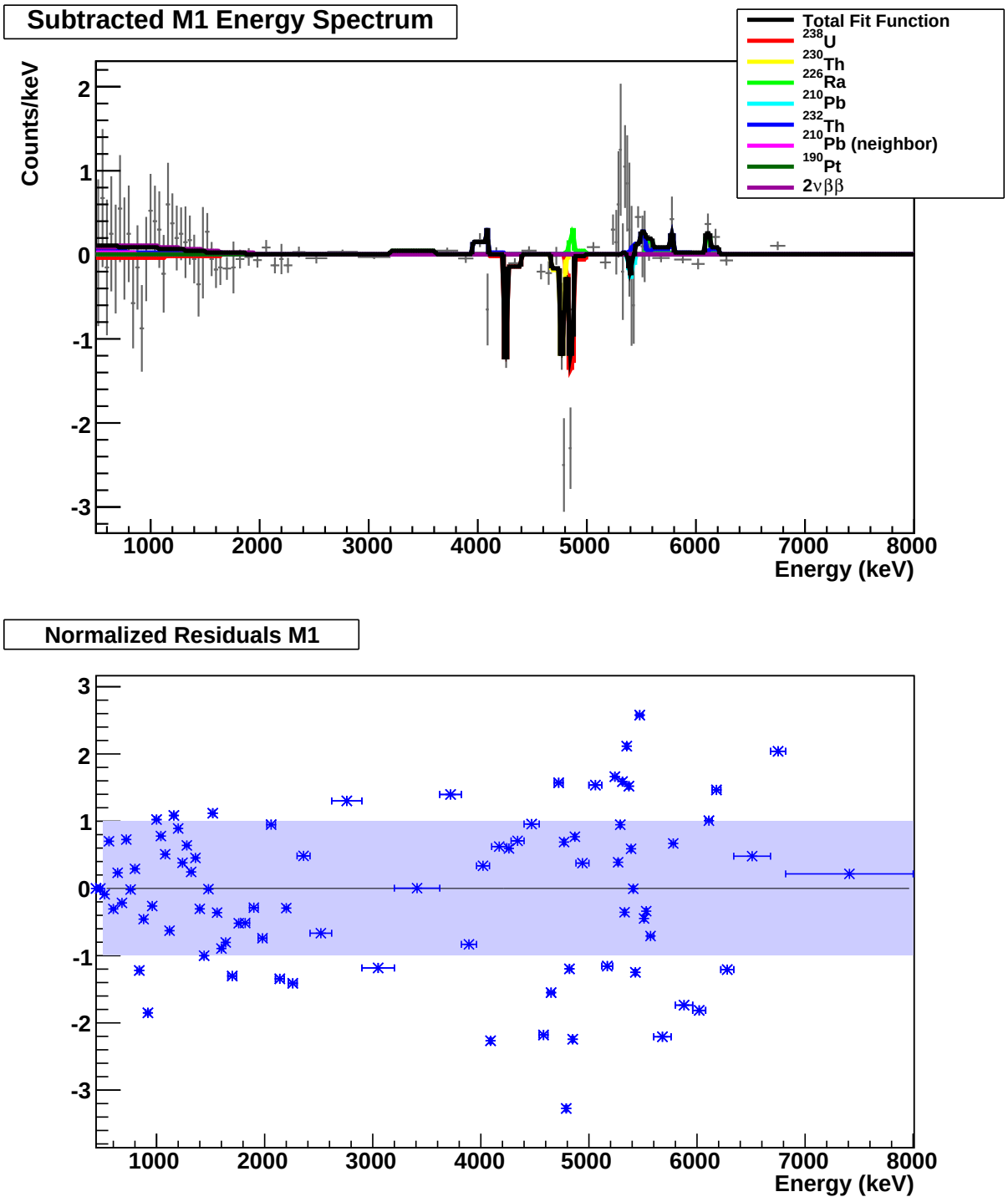

Figure C.7: Fit of the simulated spectrum components to the Multiplicity 1 (M1) spectrum for crystal configuration D. The fit was performed simultaneously on the M1, M1, and M2Tot spectra.

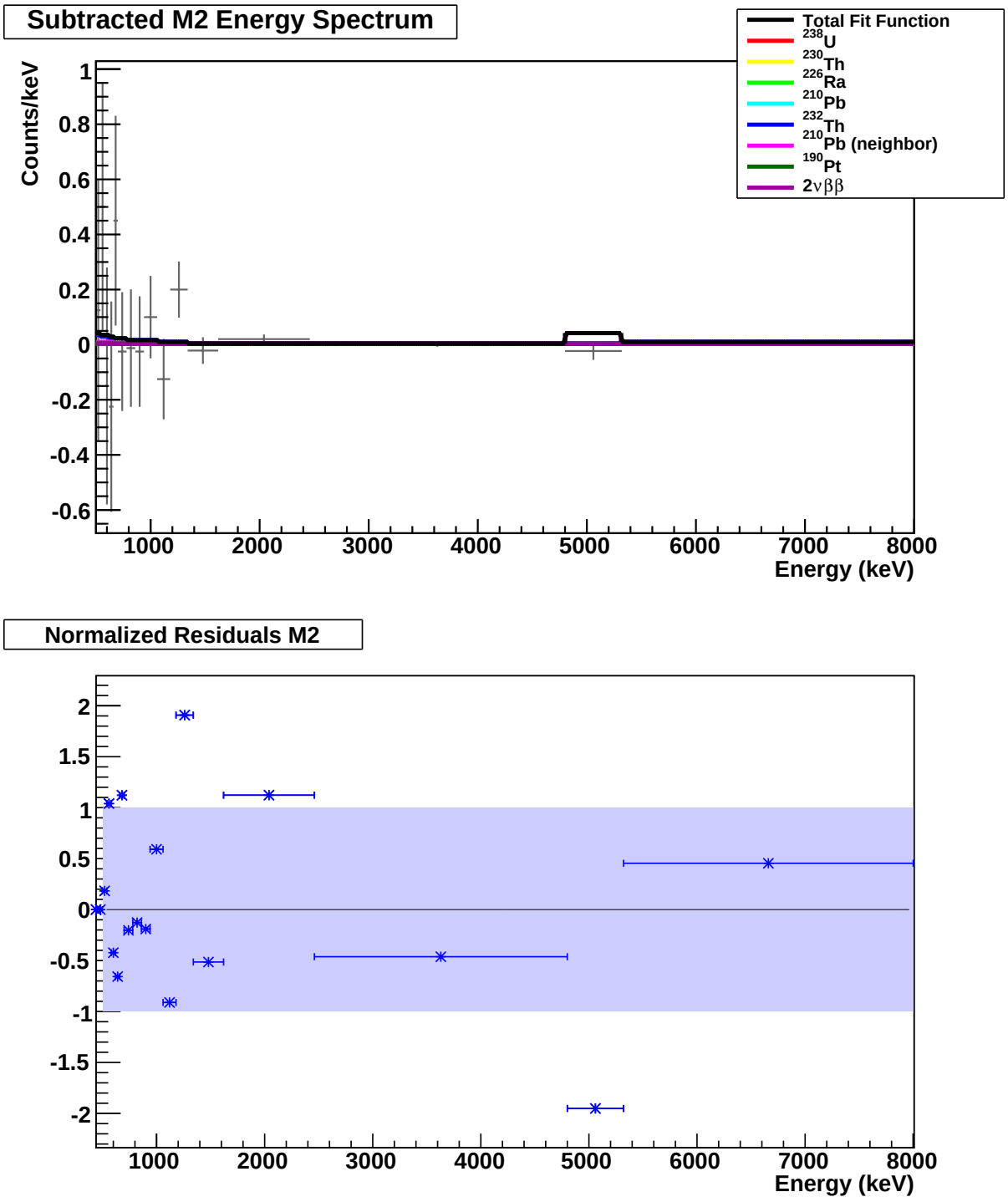

Figure C.8: Fit of the simulated spectrum components to the Multiplicity 2 (M2) spectrum for crystal configuration D. The fit was performed simultaneously on the M1, M1, and M2Tot spectra.

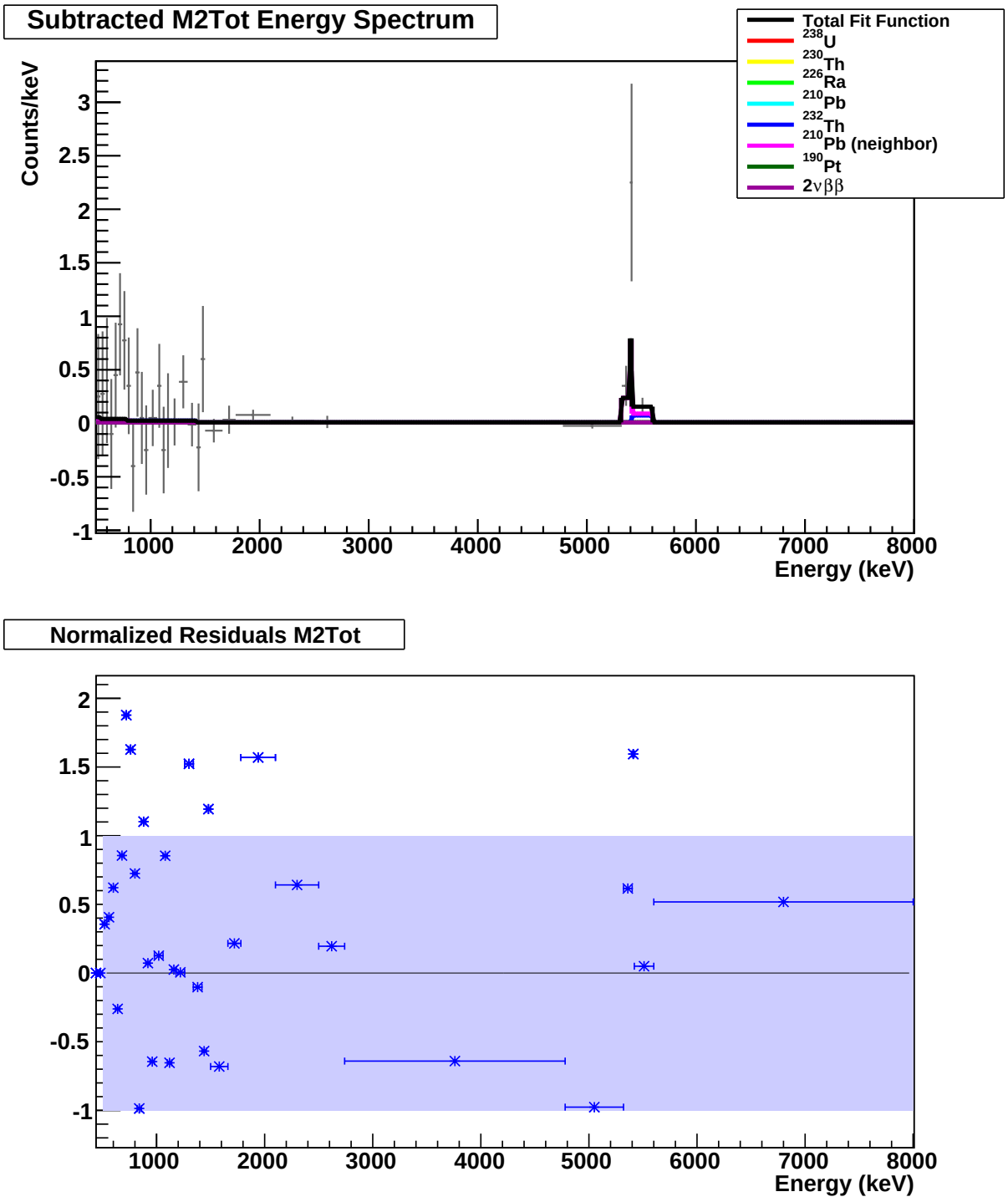

Figure C.9: Fit of the simulated spectrum components to the Multiplicity 2 total energy spectrum (M2Tot) for crystal configuration D. The fit was performed simultaneously on the M1, M1, and M2Tot spectra.

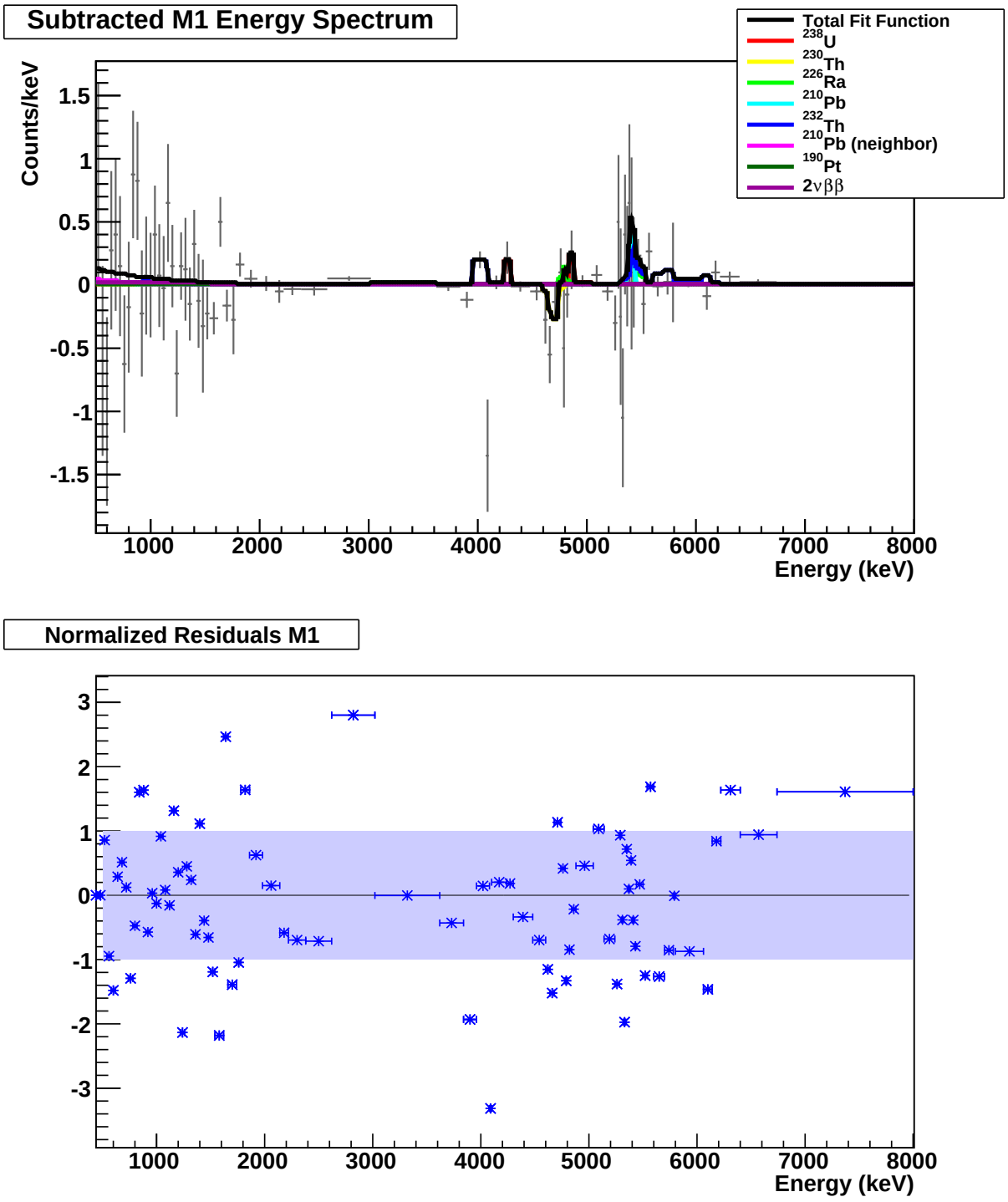

Figure C.10: Fit of the simulated spectrum components to the Multiplicity 1 (M1) spectrum for crystal configuration E. The fit was performed simultaneously on the M1, M1, and M2Tot spectra.

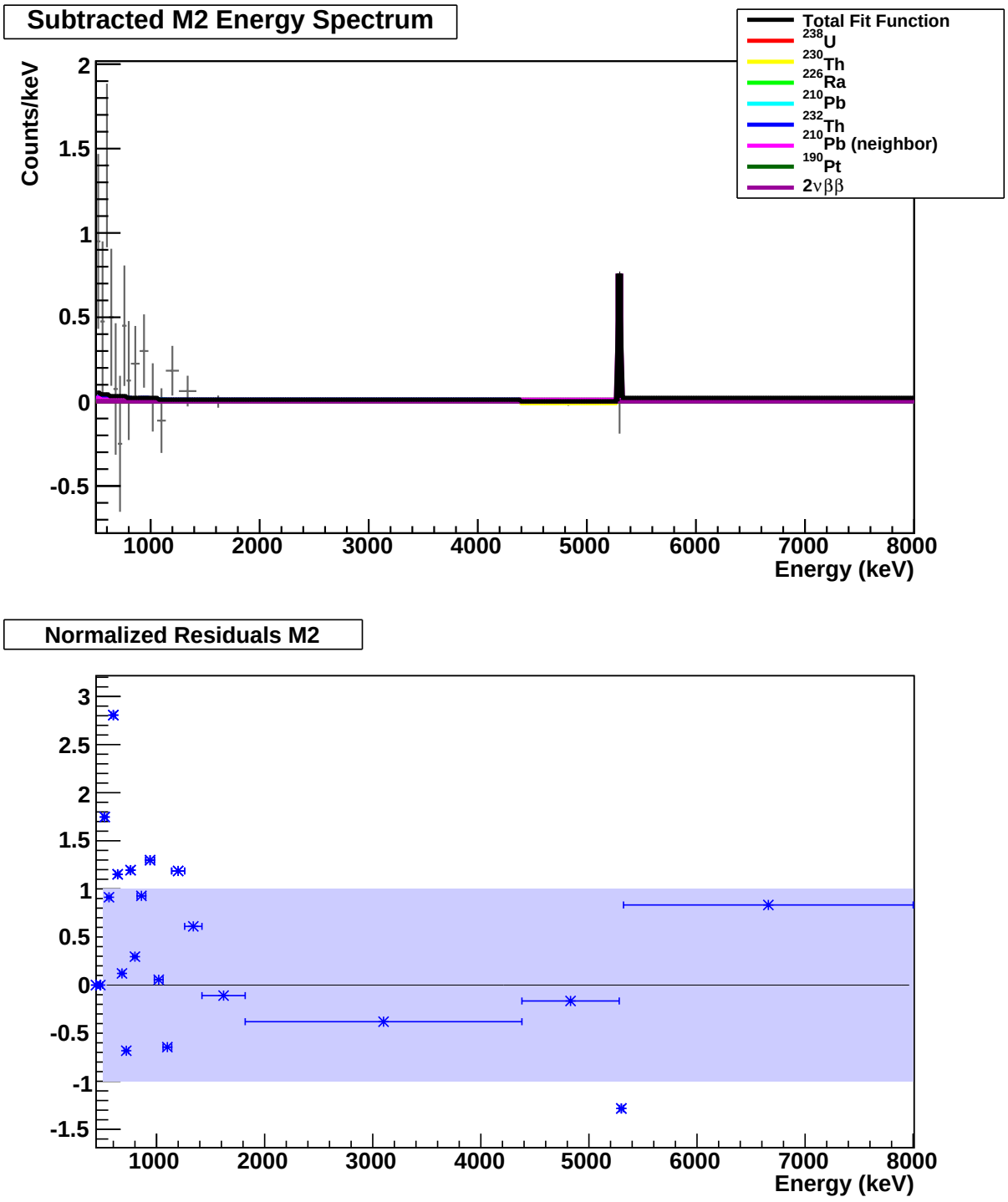

Figure C.11: Fit of the simulated spectrum components to the Multiplicity 2 (M2) spectrum for crystal configuration E. The fit was performed simultaneously on the M1, M1, and M2Tot spectra.

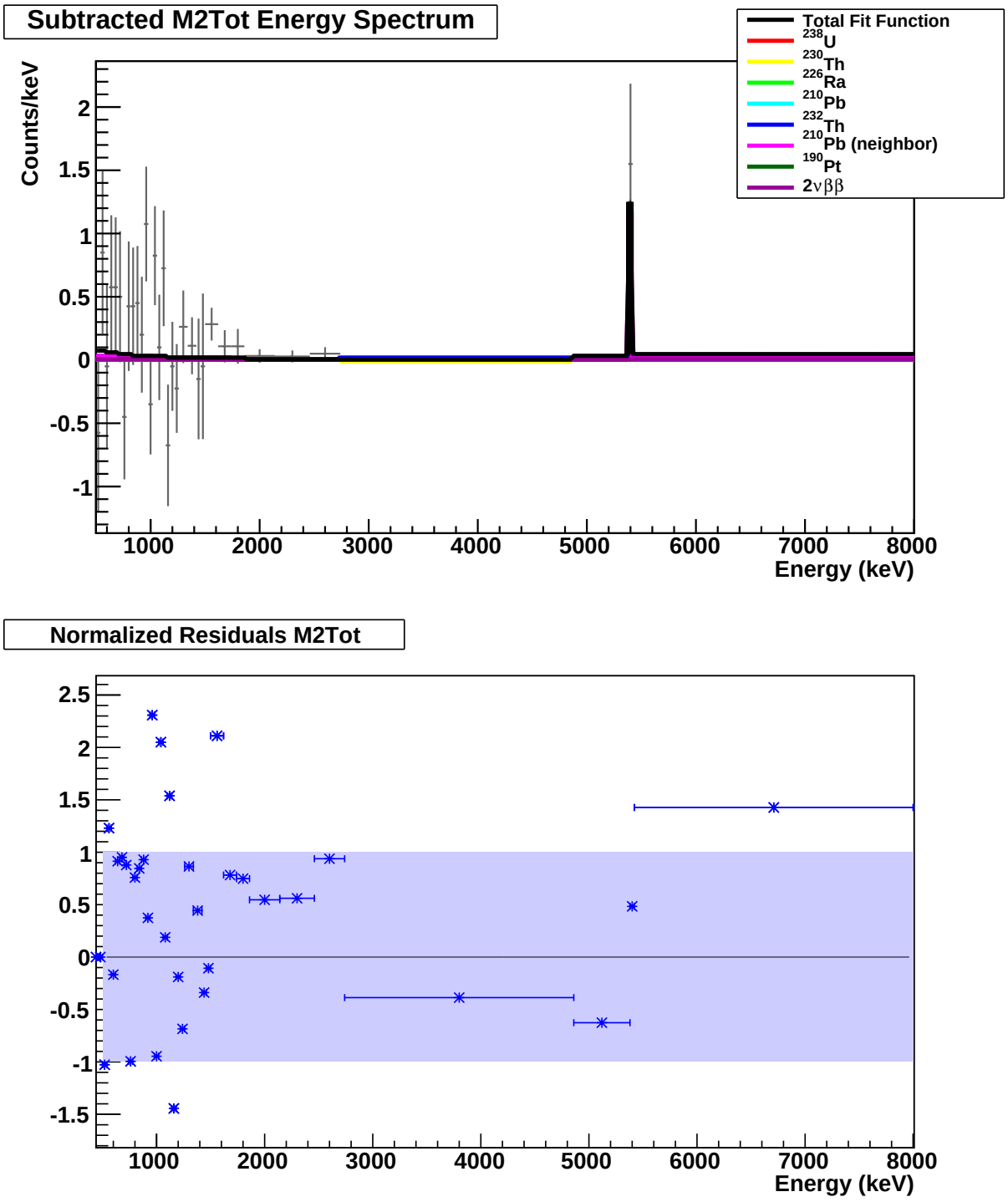

Figure C.12: Fit of the simulated spectrum components to the Multiplicity 2 total energy spectrum (M2Tot) for crystal configuration E. The fit was performed simultaneously on the M1, M1, and M2Tot spectra.

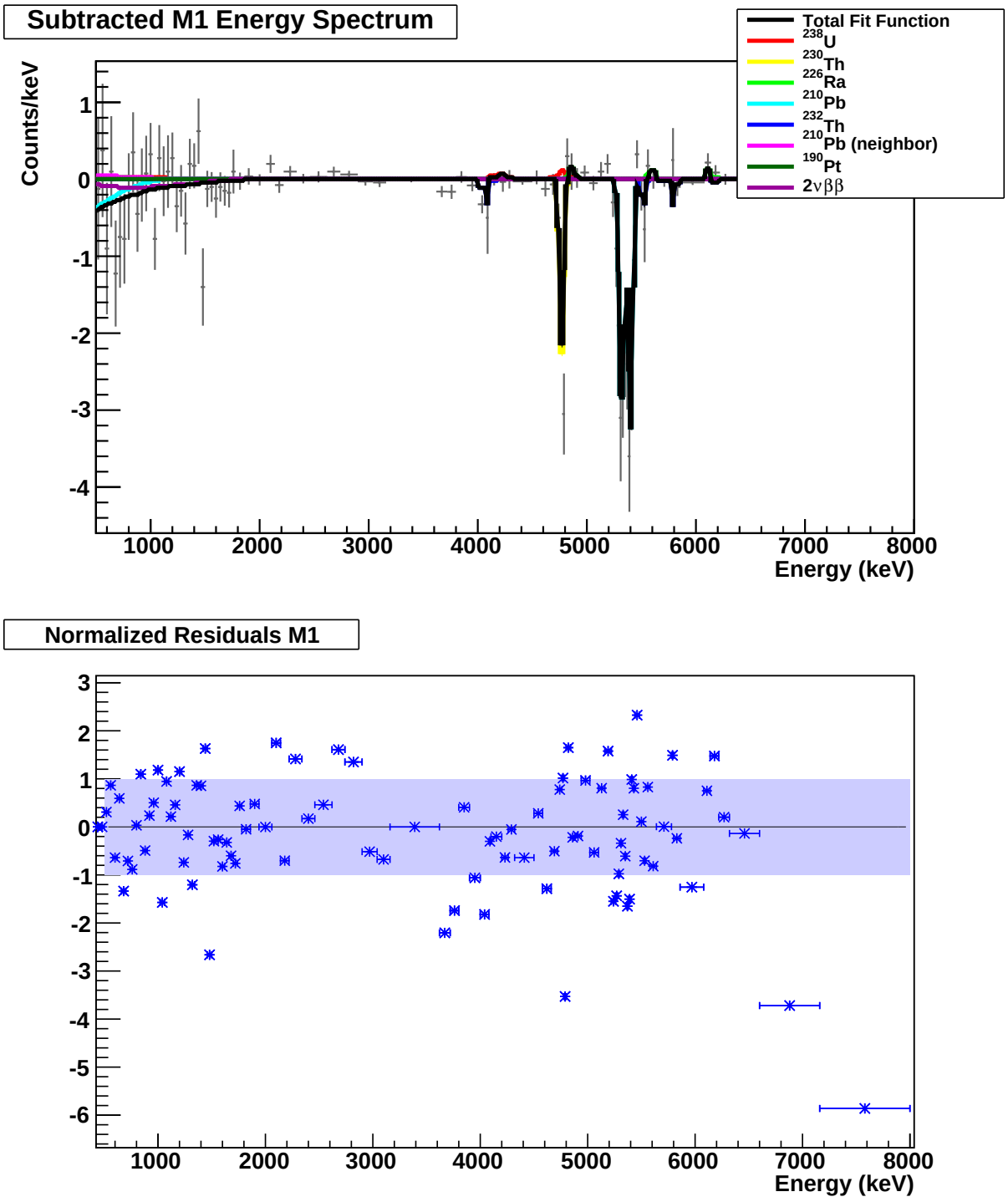

Figure C.13: Fit of the simulated spectrum components to the Multiplicity 1 (M1) spectrum for crystal configuration F. The fit was performed simultaneously on the M1, M1, and M2Tot spectra.

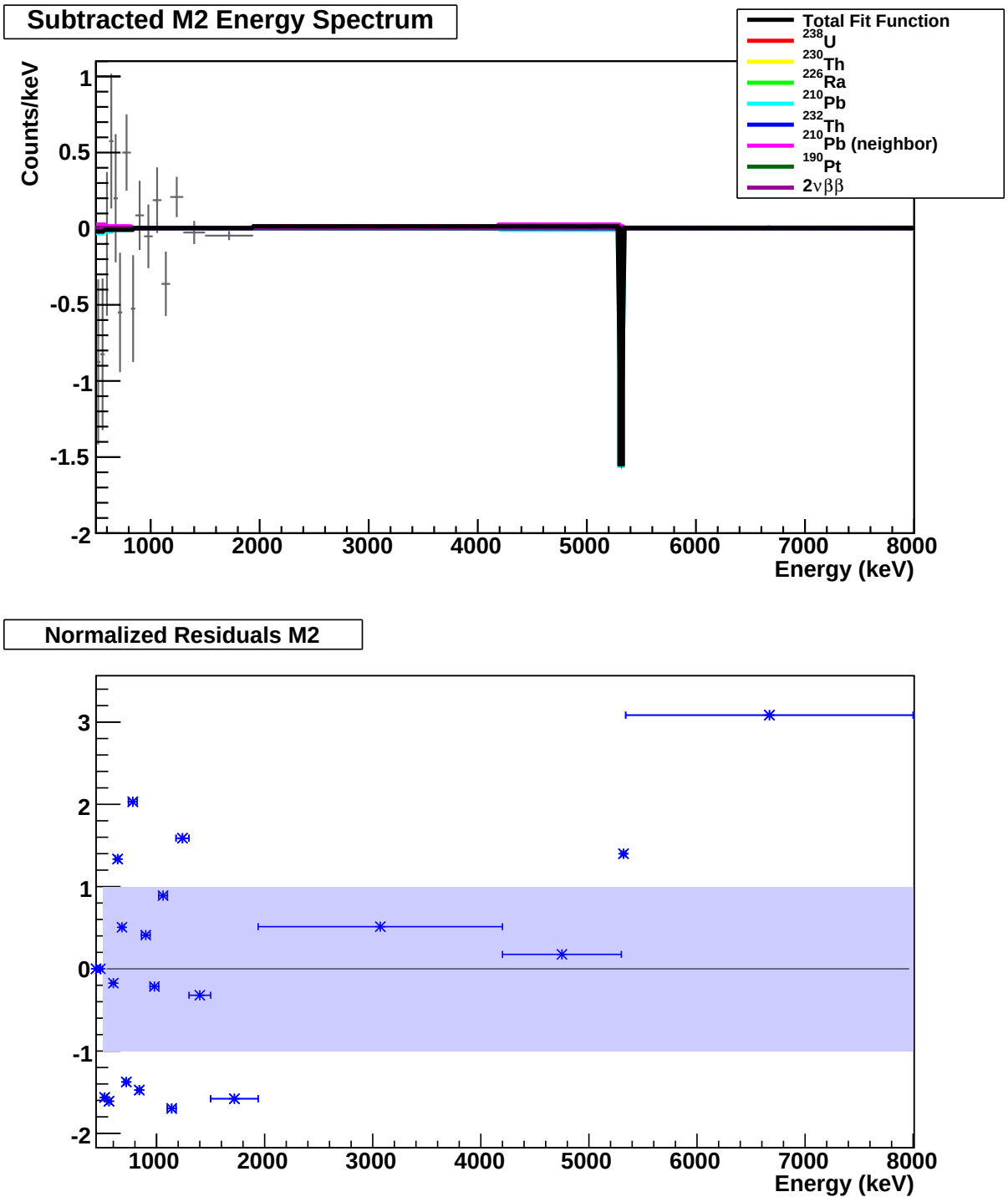

Figure C.14: Fit of the simulated spectrum components to the Multiplicity 2 (M2) spectrum for crystal configuration F. The fit was performed simultaneously on the M1, M1, and M2Tot spectra.

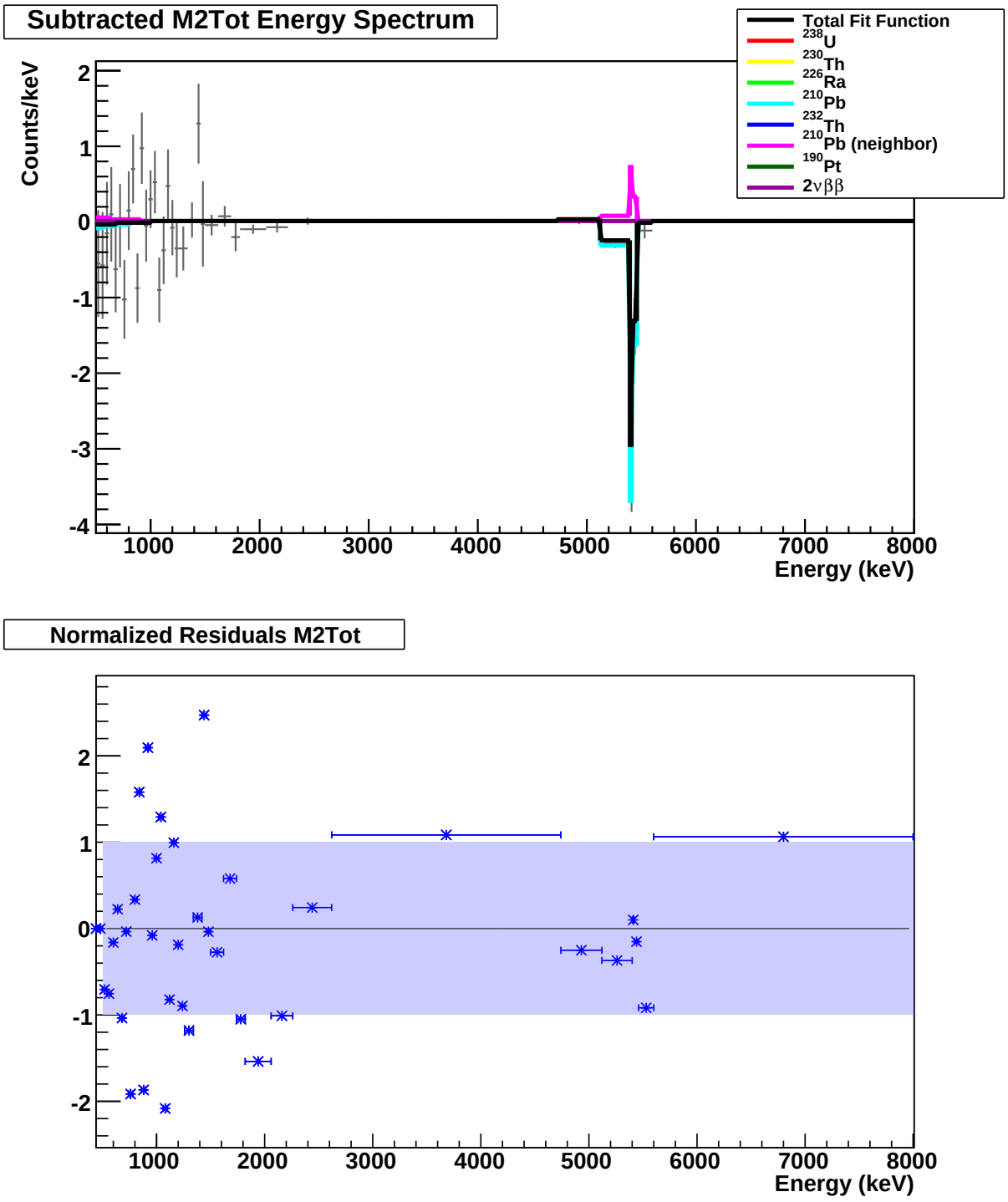

Figure C.15: Fit of the simulated spectrum components to the Multiplicity 2 total energy spectrum (M2Tot) for crystal configuration F. The fit was performed simultaneously on the M1, M1, and M2Tot spectra.